Development and use of compact instruments for tropospheric investigations based on optical spectroscopy from mobile platforms

Thèse présentée en vue de l'obtention du grade de docteur en sciences

Alexis Merlaud

Mars 2013

Composition du jury:

Xavier Urbain (UCL): promoteur

Michel Van Roozendael (BIRA-IASB): co-promoteur

Alain Cornet (UCL): co-promoteur

Martine De Mazière (BIRA-IASB)

Didier Fussen (BIRA-IASB)

Pierre Defrance (UCL): Président du Jury

Johan Mellqvist (Chalmers)

Although this may seem a paradox, all exact science is dominated by the idea of approximation. When a man tells you that he knows the exact truth about anything, you are safe in inferring that he is an inexact man.

Bertrand Russell, The Scientific Outlook, 1931

Acknowledgements

The studies presented hereafter are the result of my interactions with a large number of people, to which I express my full gratitude. First, I would like to thank Michel Van Roozendael, who has supervised me at the Belgian Institute for Space Aeronomy (BIRA-IASB). Michel has set me on right track using his scientific expertise and creativity. He was always available for discussion and his constructive criticism has improved my work over the years. I also thank Martine De Mazière and Didier Fussen for useful discussions and for having taken the time to evaluate my manuscript. I collectively thank the three aforementioned persons for their scientific rigor, their humanity, and for maintaining a pleasant research environment at BIRA-IASB. My promoters at Université catholique de Louvain (UCL), Xavier Urbain and Alain Cornet, provided their points of view as physicists on my work, this was both interesting and fruitful. I have really appreciated their active assistance, especially for the tough last steps of writing. I take this opportunity to thank here all the people who have evaluated my writings along the time span of this PhD: the journal editors Jan W. Bottenheim and Udo Frieß, the anonymous referees, and the two other members of the jury: Johan Mellqvist and Pierre Defrance.

Before the results could be evaluated, it was necessary to develop the instruments and to collect and analyze the data. Caroline Fayt has not only written incredibly stable acquisition programs, she has also brought many ideas and above all her good humor and optimism. The engineering skills and dynamism of Jeroen Maes, together with the mechanical know-how of Tom Egerickx, Marc Neven, and Geert Hemerijckx, enabled the creation of instruments that are both compact and robust enough to be operated from ultralight aircraft. Francis Scolas provided support and clever advice in electronics, as did Christian Hermans regarding optics and spectroscopic measurements. My participation to the POLARCAT experiment (chapter 5) was made possible by Kathy Law and Gérard Ancellet. For this chapter, I also thank Aurélien Bourdon and Hubert Bellec from Safire and Emilie Serf from EUFAR. Many people have helped me on the analysis of the dataset collected during POLARCAT, including Matthieu Pommier, Boris Quennehen, Corinne Vigouroux, Nicolas Theys, Andreas Stohl, François Hendrick, and

Filip Vanhellemont. Regarding the participation in the Earth Challenge expedition (chapter 6), I am grateful to Olivier Ronveaux, Michel de Maegd, Xavier Toledo-Fuentes and Jeroen van Gent. Most of the Mobile-DOAS measurements presented in chapter 7 were performed with enthusiasm by my friend Anabel-Lise Le Roux. The development of SWING (chapter 8) has taken place in the framework of a collaboration between BIRA-IASB, the University of Galati, and Reev River Aerospace, thanks to the involvement of our Romanian colleagues: Daniel-Eduard Constantin, Lucian P. Georgescu, Mirela Voiculescu, Gabriel Murariu, and Florin Mingireanu. I also thank Hugo Maes, the ultralight aircraft pilot who has performed the test flights for this payload. Appendix A directly results from a discussion with Robert J. Spurr, while appendix B originates from discussions with many colleagues mentioned here, and the useful feedback of Clive D. Rodgers.
Many other people have contributed to this PhD. Emmanuel Dekemper and I have shared the same office for over 6 years. He has heroically endured my mood swings and has even accepted to check a draft of this manuscript. So did Valentin Duflot, *collègue et néanmoins ami*. I am indebted to him for too many things to list but they include his help for chapter 5 and appendix B. Despite his tight schedule, Fabien Darrouzet always offered a kind and helping hand, often after hours. I had useful discussions with many other persons, who all brought something to this PhD, being an idea, a fresh insight, an escape, or at least a good dinner game: Romain Maggiolo, Nuno Pereira, Sébastien Viscardy, Gaia Pinardi, Yannick Willame, Valérie Wilquet, Lori and Pat Neary, Trissevgeni Stavrakou, Isabelle De Smedt, Christophe Lerot, Ana Franco, Sébastien Henrotin, Aurore Marchand, my brother Julien Merlaud, Alessandra Scaffidi, Nonne Prisle, Anders Strandberg, Sorcha Edwards, François Vander Stappen, Benoit Carpent, Johanna Grolig, Vincent Mathieu, Evelyn Doering, Pierre Lebec, Justine Spits, Jean Bricmont, Maxime Stapelle, Rachel Drummond, Arnaud Mahieux, Eric Constant, Thomas Danckaert, and all the people I forgot to mention...
Most importantly, I thank Cristina Brailescu for her support and patience these last months, as well as for being herself.
This book is dedicated to the memory of my father and to my mother, who did everything to help me become what I wanted to be.

Brussels, March 2013.

Abstract

This thesis presents the development of four different remote-sensing instruments dedicated to atmospheric research and their use in field campaigns between 2008 and 2012. The instruments are based on uv-visible spectrometers and installed respectively on a scientific aircraft (Safire ATR-42), ultralight aircraft, and cars. One of the instruments is targeted to operate from an Unmanned Aerial Vehicle (UAV). The Differential Optical Absorption Spectroscopy (DOAS) technique is used to quantify the molecular absorption in the spectra of scattered sky light. These absorptions are then interpreted by modeling the radiative transfer in the atmosphere. Depending on the instrument, different information on trace gases and aerosols are retrieved: vertical distributions, tropospheric columns, or maps of surface abundances.

Airborne platforms enable new measurement geometries, leading for instance to a high sensitivity in the free troposphere. On the other hand, a miniaturization effort is required, especially for the instruments onboard ultralight aircraft and UAV. Reaching the limited size, weight, and power consumption is possible through the use of compact spectrometers and computers, together with custom built electronics circuits and housings. The inversion strategies are optimized for each instrument with proper error budgets and the results are compared with other datasets when available.

In April 2008, the Airborne Limb Scanning DOAS (ALS-DOAS) was first used on the ATR-42 to derive NO_2 and aerosol extinction profiles during the POLar study using Aircraft, Remote sensing, surface measurements and models, of Climate chemistry, Aerosols and Transport (POLARCAT). It revealed in particular that NO_2, despite its typical lifetime of a few hours, may be transported from mid-latitude Europe to the Arctic. This is not visible in satellite data since the involved concentrations are under the detection limit. The Ultralight Motorized-DOAS (ULM-DOAS) was operated during the Earth Challenge expedition in April, October, and December 2009. This expedition provided an opportunity to perform measurements from an ultralight between Australia and Belgium, crossing areas were few local measurements have been reported, such as Bangladesh, Rajasthan, Saudi Arabia, and Libya. The ULM-DOAS measurements of tropospheric NO_2

columns mostly fall within the confidence interval of satellite data but indicate that the NO_2 columns over Riyadh may be underestimated by the Ozone Monitoring Instrument (OMI). In addition, the ULM-DOAS data provided a confirmation for the recent finding of a soil signature in the spectra recorded above desert. The Mobile-DOAS, operated from a car, was developed and first operated during the Cabauw Intercomparison Campaign of Nitrogen Dioxide measuring Instruments (CINDI) in the Netherlands during June and July 2009. Routine measurements in 2010 and 2011, mostly across Belgium yielded a large database of measurements which was compared with a chemical transport model (CHIMERE). The geometric approximation was not used to evaluate the database, since air mass factors calculations indicate that the associated uncertainties are larger than expected from previous studies. Finally, the UAV payload, the Small Whiskbroom Imager for trace gases monitoriNG (SWING) was tested from an ultralight aircraft in July and October 2012. One major objective of the UAV measurements is the mapping of NO_2 columns at high spatial resolution allowing to subsample satellite measurements within the extent of a typical ground pixel. This has yet to be achieved.

Contents

List of Figures

List of Tables

Chapter 1

Introduction

To estimate the height of the atmosphere, the 11th century astronomer Ibn Mu'adh used his eyes during sunset, simple trigonometric formulas, and assumptions on other parameters such as the radius of the earth (Lehn and van der Werf, 2005). From the duration of the twilight, he guessed the maximum angle of depression of the Sun, and from there the highest altitude at which light could be scattered by hypothetical suspended vapors in the atmosphere. The number he reached, around 80 km, remained the academic value for five centuries. Refraction was not taken into account in Ibn Mu'adh description of the interaction of light with matter. In 1604, Kepler introduced this effect to correct Ibn Mu'adh calculation, reducing drastically the altitude of the top of the atmosphere to 4 km. Ironically, even with the refraction properly taken into account, Kepler's retrieval of the height of the atmosphere was not much more accurate than the value of Ibn Mu'adh. This was mainly due to a wrong conception of the shape of the atmosphere, shared by the two astronomers. They considered a sharp boundary between an homogeneous atmosphere and an outside ether, while the air density, as we now know, decreases exponentially with altitude.

Ten centuries after Ibn Mu'adh, the scattered skylight still provides new and interesting information on the earth atmosphere. It is in particular possible to retrieve trace gas abundances in the uv-visible through the Differential Optical Absorption Spectroscopy (DOAS) (Platt and Stutz, 2008). The principle of differential absorption has been introduced for the first measurements of the ozone total column in the 1920's by Fabry and Buisson (Dobson, 1968). However, modern DOAS measurements really started in the 1970s with ground-based zenith-sky observations of stratospheric gas columns (NO_2 (Noxon, 1975), ozone (Pommereau and Goutail, 1988), OClO (Solomon et al., 1989), ...). More recently, DOAS was further developed for chemical investigations of the troposphere, by means of the Multi-Axis DOAS (MAX-DOAS) technique (Hönninger et al., 2004), which by combining multiple viewing directions, allows to derive information on

the vertical distribution of gases in the lower troposphere. Ground-based DOAS instruments are now operated at many locations around the planet as part of monitoring infrastructures such as the Network for the Detection of Atmospheric Composition Change (NDACC)[1]. From the 1990s, the DOAS instruments were mature enough to be installed on satellites. These space-based experiments (GOME, SCIAMACHY, OMI) are particularly valuable since they reveal the global fields of important trace gases such as NO_2 (Boersma et al., 2004), SO_2 (Loyola et al., 2008), formaldehyde (De Smedt et al., 2008), glyoxal (Lerot et al., 2010) and BrO (Theys et al., 2011).

Satellite and ground-based data have intrinsic limitations. The stations from NDACC or other networks are unevenly distributed with large areas poorly sampled, such as Africa. On the other hand, satellites offer global coverage but at the expense of poorer sensitivities and limited ground resolutions. The best instrument in this last respect is currently the Ozone Monitoring Instrument (OMI) whose pixel size is 13x24km^2. Such a scale is too coarse to study the high spatial frequencies of short-lived species like tropospheric NO_2 in urban areas. As a comparison, the spatial resolution of the local chemistry and transport models is three orders of magnitude lower, at the level of individual streets (Cosemans and Mensink, 2005). These high resolution models may have very practical importance for public health policies but they can not be validated with fixed ground-based measurements nor with satellite data. Another common limitation of satellite and ground based instruments is their poor ability to retrieve profile information. The MAX-DOAS method is mainly sensitive to the lower troposphere (Vlemmix et al., 2011), while satellite measurements separate only the total measured column into its stratospheric and tropospheric contributions.

The difficulty to retrieve profile information for a given species does not mean that its vertical distribution can be neglected when measuring its total column, whether from a satellite or from ground. DOAS is a remote sensing technique which uses the spectrum of the sun light to quantify the atmospheric abundance of absorbers. The measured absorptions are thus integrated along an optical path which needs to be estimated accurately. This is done by modeling the radiative transfer in the atmosphere, which depends on various geophysical parameters such as the solar position, the ground albedo and the scattering by aerosols. But understanding accurately the radiation transfer is only one part of the problem, as it was already the case with the early remote sensing of the height of the atmosphere by Ibn Mu'adh and Kepler. To interpret correctly the measured absorptions in terms of vertical columns, one also needs the position of the absorbers along the light path, and thus their vertical distribution. These vertical distributions are poorly known for most of the species. This is the case even for tropospheric NO_2

[1] `http://ndacc-uvvis-wg.aeronomie.be/`)

close to the sources (Dieudonné, 2012), which is easily and widely measured with DOAS or in-situ instruments.

In this thesis, we concentrate on the development of DOAS instruments from various mobile platforms to contribute to fill the gaps between ground-based and satellite data. Several mobile DOAS measurements have already been reported from cars (e.g. Galle et al. (2003), Johansson et al. (2009b), Rivera et al. (2010), Wagner et al. (2010)) or airplanes (e.g. Heue et al. (2005), Prados-Roman et al. (2011)), especially since the advent of compact grating spectrometers. The instruments presented here are simple, low-cost, and miniaturized systems designed for integration in ultralight and Unmanned Aerial Vehicles (UAVs), allowing for measurements to be in remote and poorly sampled areas. The data analysis schemes were also optimized for each instrument.

Relevant background information on the atmosphere is presented in chapter 2. Tropospheric NO_2 has been a common target for our instruments so we describe it in more detail. In chapter 3, the physical principles of DOAS and the algorithms used in practice to analyze the spectra are introduced. Chapter 4 presents the general instrumental aspects of scattered light DOAS including their characterizations. Chapter 5 presents the Airborne Limb Scanning DOAS (ALS-DOAS), which was operated from the SAFIRE ATR-42 and contributed to the POLARCAT project which studied the transport of pollution to Arctic. This instrument was used to derive profiles of NO_2 and aerosols. Chapter 6 presents a more compact instrument, the ULM-DOAS, which was installed on an ultralight aircraft during an expedition between Australia and Belgium. The measurements were used in particular to derive tropospheric columns of NO_2 around megacities like Karachi and Riyadh. In chapter 7, we describe an instrument operated from a car, the Mobile-DOAS, which was first used during the Cabauw Intercomparison Campaign of Nitrogen Dioxide measuring Instruments (CINDI) campaign in the Netherlands and then routinely in Belgium. These measurements shows the high horizontal gradients in polluted areas and the large database makes them interesting for comparisons with chemistry and transport models. Chapter 8 presents the development of a compact imaging system dedicated to Unmanned Aerial Vehicles. Chapter 9 concludes this study with an overview of the findings and the perspectives regarding the instruments and the data analysis.

Chapter 2

Some aspects of the Earth atmosphere

This chapter describes the geophysical context of our studies. The first section presents some basic properties of the Earth's atmosphere: its composition and vertical structure, the importance of trace gases and aerosols, and the transport mechanisms of air masses. In the second section, we focus on a particular trace gas, nitrogen dioxide (NO_2), a common target of the different instruments developed through this work. We describe the importance of NO_2 both for the chemistry of the troposphere and for air quality, its emissions and removal processes, and the general patterns of its spatial and temporal distribution.

2.1 Atmospheric composition and dynamics

2.1.1 Trace gases and aerosols

Nitrogen (N_2) and oxygen (O_2) account together for 99 % of the volume of the present Earth atmosphere. The remaining one percent is made up of trace gases among which the most abundant are Argon (Ar) and water vapor (H_2O), the latter lying close to the surface and highly variable (0 to 4 %). The volume mixing ratio (vmr) of all other atmospheric species are expressed in parts per million (ppm), parts per billion (ppb), or parts per trillion (ppt). Despite their small amounts, trace gases have a major impact on the physical and chemical properties of the Earth system. This is illustrated by the following elements, revealed by atmospheric research in the last decades:

1. *stratospheric ozone and its depletion*: ozone (O_3) is a relatively abundant trace gas between 20 and 30 km altitude, with volume mixing ratios reaching a few ppm (see figure 2.3). This ozone layer shields the Earth surface

from energetic solar radiation. Since the 1980s, a depletion has been observed at high latitudes in spring, most clearly visible above Antarctica. This phenomenon is now explained by catalytic reactions involving 1 ppb of chlorine, originating from anthropogenic chlorofluorocarbons (CFCs). International legislation contributed to a drastic reduction of CFCs emissions. However, due to their long lifetime, the seasonal thinning of stratospheric ozone may continue for several decades (WMO, 2011).

2. *climate forcing due to greenhouse gases*: the greenhouse gases (H_2O, CO_2, CH_4, N_2O ...) are transparent to the visible light from the Sun but trap the infrared radiation reemitted by the Earth. This results in an increase of 30 K in the ground temperature, enabling the presence of liquid water. The rise of the concentration of these gases in the industrial age, which has accelerated in the 1950's is a major concern for the global climate. A doubling of CO_2 level, currently at 390 ppm, is expected to yield a 3 K increase in the surface temperature, the latter reaching values unexperienced by mankind since the Neolithic revolution (IPCC, 2007).

3. *air quality*: some trace gases (O_3, NO_x, CO, SO_2, ...) exhibit harmful effects from small quantities. For instance, ground-level ozone yields significant crop reduction from 50 ppb (figure 2.1). At low altitude, ozone abundance depends on the presence of volatile organic compounds and nitrogen oxides (see Sec. 2.2.2), the latter being mostly related to fuel combustion. Historical records indicate that, in the 19th century, characterized by significantly lower fuel consumption than today, the ozone levels may have been as low as 10 ppb (Volz and Kley, 1988).

The work presented in this thesis mainly deals with air quality, but the problems are tightly linked. Indeed, the stratospheric cooling associated with greenhouse gas increase may enhance ozone depletion, while this depletion itself may lead to climate change (Kang et al., 2011). Climate change, in turn, affects the surface concentrations in various ways, such as modifying the radiative flux available for photochemistry.

Two other quantities are useful, beside the mixing ratio, to describe gas abundance: the number density and the vertical column. The number density is given by the product of the volume mixing ratio and the air density, and usually expressed in molecules/cm^3. This unit is more relevant than volume mixing ratio when dealing with the optical properties of gases, such as those measured through this work. Integrating the number density along the vertical gives a vertical column, expressed in molecules/cm^2. The total column of a molecule x is its number density c_x integrated vertically over the full atmosphere:

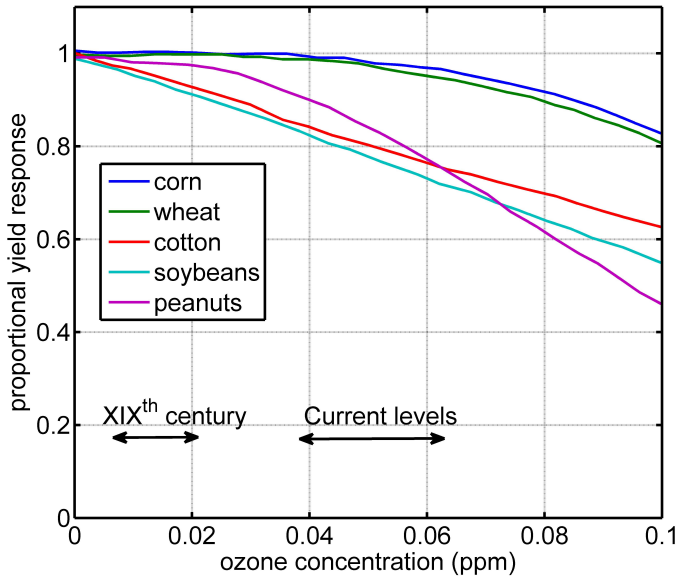

Figure 2.1: Surface ozone effects on crop production. Adapted from Heck et al. (1983).

$$C_x = \int_0^{TOA} c_x(z)\,\mathrm{d}z \tag{2.1}$$

For our applications, the top of the atmosphere (TOA) may be defined as the stratopause (see next Section). We often separate the total column in its tropospheric and stratospheric contributions.

Besides gases, liquid and solid particles are present in suspension in the atmosphere. Cloud droplets are the most visible, but other examples are sea water or desert dust blown by the wind, soot particles produced by combustion, or in the case of sulfate and nitrate aerosols, indirect product of gas emission in the atmosphere. Such particles are referred to as aerosols. Aerosols sizes range mostly from 0.01 to 15 μm, to compare with the size of a raindrop usually around 1 mm.

Aerosols are involved in the chemistry of the Earth system in different ways. To give two examples, nitrate and sulfate aerosols lower the pH of rain, while polar stratospheric clouds offer surface for heterogeneous reactions involved in ozone seasonal thinning. Regarding the Earth radiative budget, the impact of aerosol is more complicated than the one of greenhouse gases. The direct effect is a reduction of absorbed solar energy on ground due to higher global albedo. On the other hand, aerosols also act as cloud seeds and affect thus the size distribution and lifetime

of clouds, which also affect the global albedo.

Aerosols are also affecting climate by lowering the albedo of snow and ice. Light absorbing aerosol particles, such as black carbon, are transported to snow-covered areas and increase the amount of solar energy absorbed by the surface. This leads to an increase in temperature, which leads to a reduction of ice cover and an even more decreasing global albedo (figure 2.2). Aerosols deposition may thus trigger this positive feedback. It has been suggested that this phenomenon explains parts of the enhanced warming observed at the poles (Law and Stohl, 2007). Investigating the transport of aerosols to the Arctic was one of the objective of the first campaign in which we participated (Chap. 5).

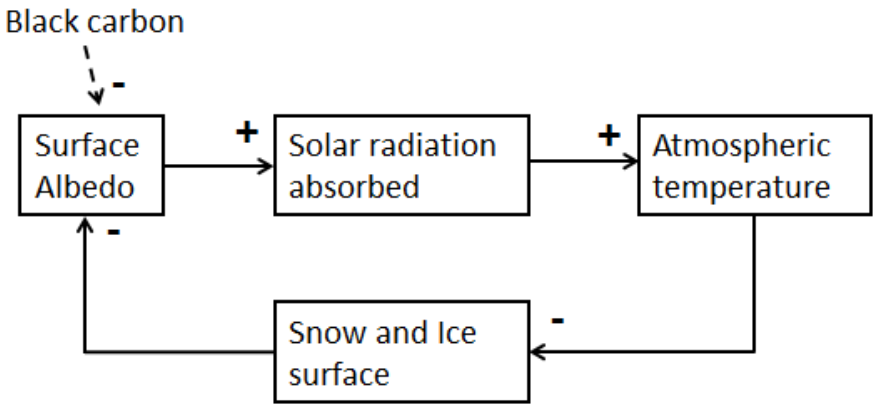

Figure 2.2: Effect of black carbon on ice sheets: black carbon deposit can trigger a positive feedback between ice cover and temperature.

Composition and size of aerosols, even in a given time and location, are always statistically distributed. An important optical quantity, both for the Earth radiative budget and for our measurements, is the aerosol extinction coefficient, expressed in km^{-1}. This coefficient describes the attenuation of light through an aerosol layer. One can draw a parallel between the concentration of a gas and its total column with the extinction of aerosols ($\mathcal{E}$) and the aerosol optical thickness (AOT), calculated as:

$$AOT = \int_0^{TOA} \mathcal{E}(z)\,\mathrm{d}z \tag{2.2}$$

The aerosol extinction profile was measured in the Arctic during the POLARCAT campaign and the AOT was derived from satellite data in order to analyze the measurements of the Earth Challenge expedition.

2.1.2 General vertical structure

Below 100 km altitude, turbulent mixing dominates over molecular diffusion. The vertical distributions of gases are thus determined by their production's place and lifetime rather than molecular weights. This explains why trace gases, which are often heavier than air, are found in the upper atmosphere (e.g. 48 g/mol for ozone and 46 g/mol for NO_2, as compared to the average molar mass of air, 29 g/mol). The lifetime of chemical species in the atmosphere varies from seconds (OH) to eons (Argon). Between these two extremes, mixing is also limited by the vertical temperature structure which defines layers in atmosphere with different characteristics.

Figure 2.3 presents these different layers and standard profiles of ozone and NO_2. Starting from the ground, the troposphere, where most meteorological phenomena occur, is characterized by a generally decreasing temperature (-6.5 K per km) up to the tropopause[1]. The tropopause marks an inversion: the temperature starts increasing with altitude throughout the stratosphere, reaching a maximum at the stratopause (50 km). The high temperatures in the stratosphere originate from the ozone absorption of ultraviolet solar radiation. A NO_2 layer is also present in the stratosphere, but is three orders of magnitude less dense than the ozone layer. The actual ozone and NO_2 profiles vary greatly with time and location, and for the latter the tropospheric contribution dominates the total column in polluted areas. Together, the stratosphere and troposphere represent 99.9 % of the atmosphere mass and are the relevant layers for this work. Above the stratopause, the temperature vertical gradient reverses again twice: it decreases in the mesosphere up to 80 km and increases again in the thermosphere due to absorption of strong UV radiation by N_2 and O_2.

The changes in temperature gradients lead to different vertical circulation patterns. An air parcel rising in the atmosphere expands due to the decrease in pressure. This expansion is associated with an adiabatic cooling. If the temperature decreases strongly with altitude, as it happens in the troposphere, the air parcel is still warmer than its surroundings, thus less dense, and continues to rise. This configuration is associated with convection transport and the atmosphere is said unstable. On the contrary, if the gradient is weakly negative or positive as in the stratosphere, the rising air parcel is denser than its surroundings and it sinks down: the atmosphere is said stable. The concept of potential temperature takes into account the adiabatic cooling: it is the temperature the air parcel would have if it was brought adiabatically to the standard conditions. The air being close enough to a perfect gas, the potential temperature θ is calculated as:

[1]The tropopause ranges from 7 km altitude above the poles to 20 km above the equator.

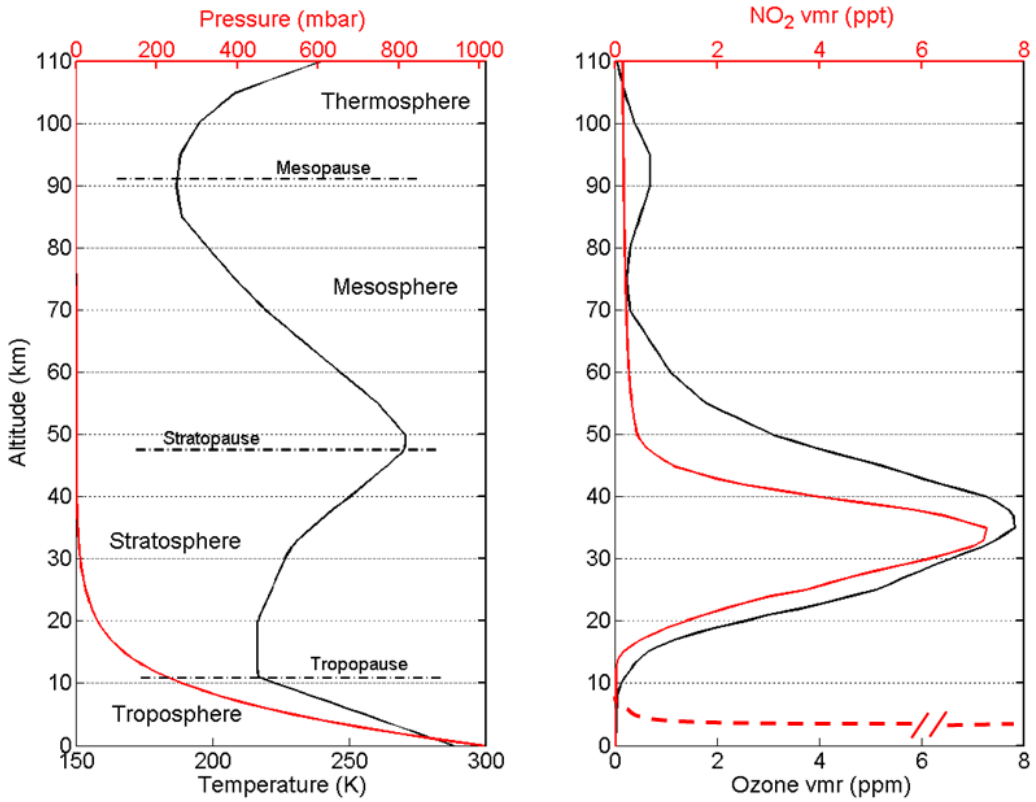

Figure 2.3: Vertical structure of a standard atmosphere (Anderson et al., 1986). The different layers are defined according to the temperature gradient. The right panel shows standard ozone and NO_2 profiles. Real profiles vary with time and location, in particular, for the NO_2, the tropospheric contribution (red dashed curve) may dominate the total column.

$$\theta = T(\frac{P_0}{P})^{\frac{R}{Cp}} \tag{2.3}$$

where P_0 and P are the pressures at ground and at the altitude of the air parcel, respectively, R the ideal gas constant, and Cp the specific heat capacity. Air tendency is to follow isentropes (lines of constant potential temperature, see figure 5.16), especially in the stratosphere where the adiabatic assumption is more realistic. In the troposphere, the potential temperature profile is nevertheless a good tool to estimate the atmospheric stability, as may be seen in figure 2.4, described in the next section.

2.1.3 A zoom in the troposphere

The temperature profile in the troposphere often shows small inversions between the surface and 4 km altitude. These inversions separate the turbulent atmospheric boundary layer, directly influenced by the surface, from the free troposphere. The boundary layer height experiences a diurnal cycle following the convection dependence with solar forcing. The inversion strength itself depends on local meteorological conditions and orography. In Brussels, winter inversions occur in cold and clear-sky days because the ground loses more quickly its heat than the atmosphere. In Los Angeles, the severe inversions correspond to warm desert air transported above the city across the Rocky Mountains.

Below the inversion, turbulence and convection efficiently mix the air, dispersing in particular the species emitted from the surface. The assumption of a well-mixed boundary layer, where the mixing ratios are constant in the vertical direction, is often used as an a priori knowledge to interpret measurements and we use it in the data analysis of the ULM-DOAS (chapter 6). However, it should be noted that the NO_2 profiles may be much more heterogeneous close to the sources (Dieudonné, 2012).

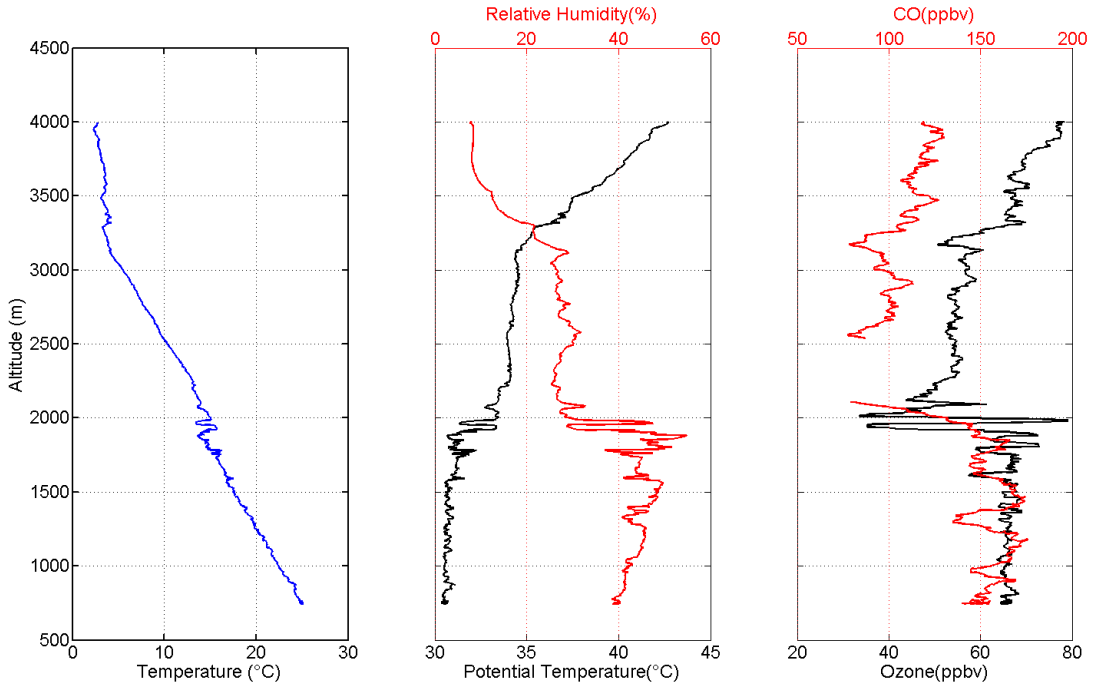

Figure 2.4: Sounding performed over Iasi, Romania (47.05N, 27.6E) between 12h42 and 13h07 UT on 16 July 2007.

Figure 2.4 presents a sounding performed from the SAFIRE ATR-42 aircraft in Romania during the EUFAR summer school in July 2007. The meteorological conditions during the flight and the previous days were clear-sky and a ground temperature above 35 °C, enabling a large convection. Two small inversions are visible on the sounding. The first one at 2 km corresponds to the boundary layer height. At the time of the sounding, its altitude was still increasing. The second inversion, at 3.2 km, is probably a footprint of the maximum height reached by the boundary layer the day before the sounding. The potential temperature, relative humidity, ozone and CO are rather constant inside the first two layers, apart from the inversions levels. The values of these different parameters are different from one layer to the other, indicating a probable different origin of the air masses. The constant potential temperatures in these two lowest layers explain the rather homogeneous volume mixing ratio, whereas above 3.2 km the potential temperature starts to rise constantly with altitude, indicating a stable free troposphere[2], which is consistent with all the measured parameters. In the next section, we describe the drivers of these air movements and the associated timescales.

2.1.4 Transport in the atmosphere

The driver of the air circulation is the difference of incoming solar energy due to the shape of the planet which creates convective movements from the equator to the poles. The resulting buoyancy on an air parcel is associated to three other forces: its weight, the Coriolis effect due to the planet rotation, and friction if the air parcel is close to the surface.

Figure 2.5 presents the general circulation patterns on Earth. The convective heat exchanges between the equator and the poles takes the form of three large cells in each hemisphere. The Hadley cells lie between the equator and 30° latitude. The solar radiation at the equator yields large convection systems associated with precipitations at the equator whereas the other extremity of the cell is associated with the largest deserts, partly because relative humidity decreases with temperature. The accurate positions of the northern and southern Hadley cells vary with the seasons but the contact zone close to the equator, the Intertropical Convergence Zone (ITCZ), limits the air circulation between the two hemispheres. From 60° toward higher latitudes, the polar cells reproduce the scheme of the Hadley cell. The Ferrel cell, acting like a ball bearing in the air circulation of the poles and the equator, rotates in the other direction and is responsible with the Coriolis effect for the westerlies experienced at mid-latitudes. The air originating

[2]The free troposphere is defined as the part of the troposphere which lies above the boundary layer.

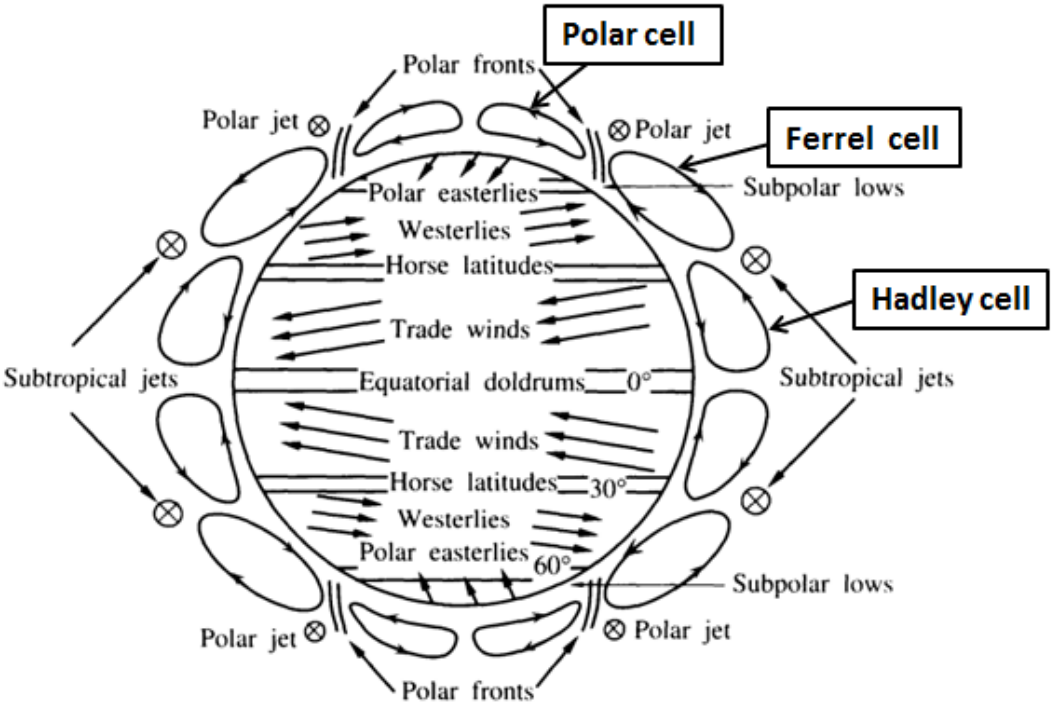

Figure 2.5: Global circulation patterns in the Earth atmosphere, adapted from Seinfeld and Pandis (1997).

from the mid-latitudes surfaces rises at the meeting of the Ferrel and polar cells which can lead to elevated pollution episodes in the free troposphere in Arctic. This transport path was studied in the POLARCAT experiment (chapter 5).

The ability of chemical species to follow the general air circulation depends on their lifetime, presented for important trace gases and aerosols in figure 2.6. The trace gases studied in this work are NO_x, tropospheric ozone, and CO. In addition, we also measured aerosol extinction profiles. Regarding NO_x, its lifetime of about a day spreads this species within the boundary layer but not much more. The three other compounds may travel around a hemisphere for one to several weeks (aerosols and ozone) or even months (CO). The most stable species on the figure are two important greenhouse gases (methane and nitrous oxide, a few decades) and CFCs (around 100 years), this latter compound being extremely stable, which explains both its attractiveness for industrial applications and its presence in the stratosphere. However, the importance of a chemical species is not only determined by its lifetime: the OH radical, at the other end of the figure, whose lifetime is a

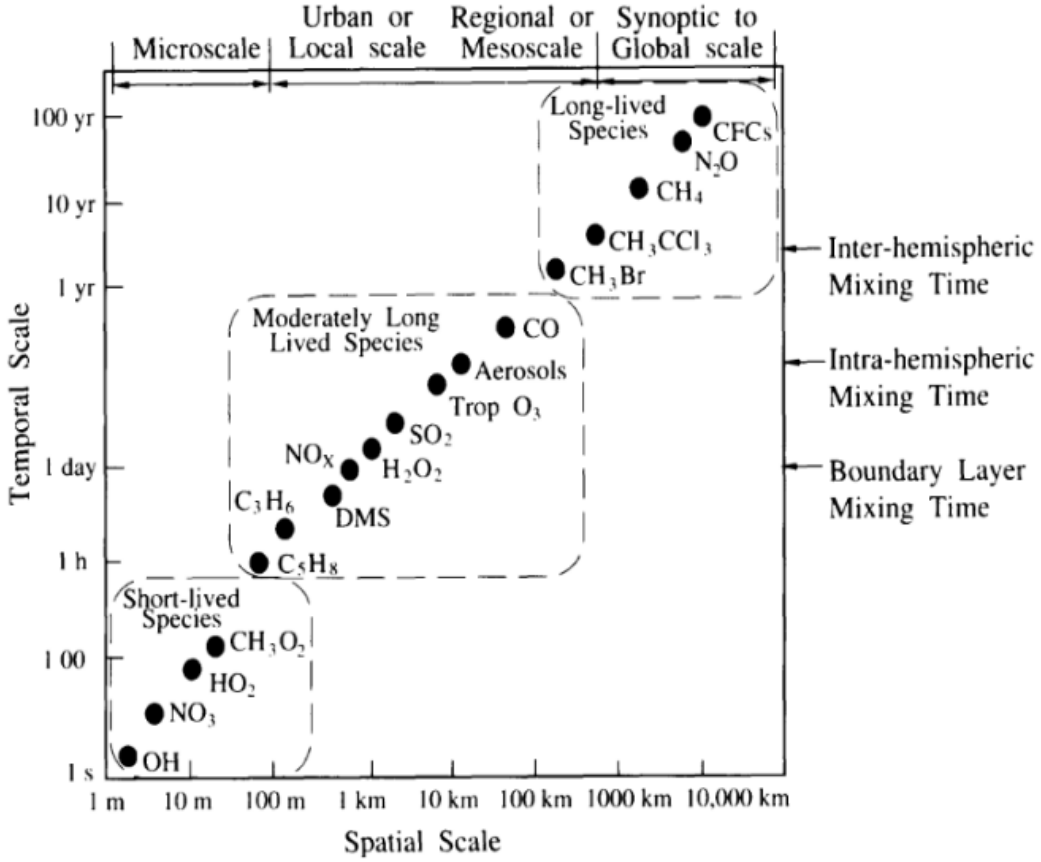

Figure 2.6: Transport times and ranges of atmospheric constituents (Seinfeld and Pandis, 1997).

second, has a considerable importance in atmospheric chemistry including in the NO_2 cycles as it will be explained in the next section.

2.2 Nitrogen oxides in the troposphere

The instruments developed in this work have all been applied to quantify NO_2 loadings in the troposphere, even if other geophysical quantities have been studied. Thus, this second part of geophysical background looks into the effects of NO_2 on air quality, its role in tropospheric chemistry, and the state-of-the art knowledge on its sources and sinks, and on its temporal and spatial distribution.

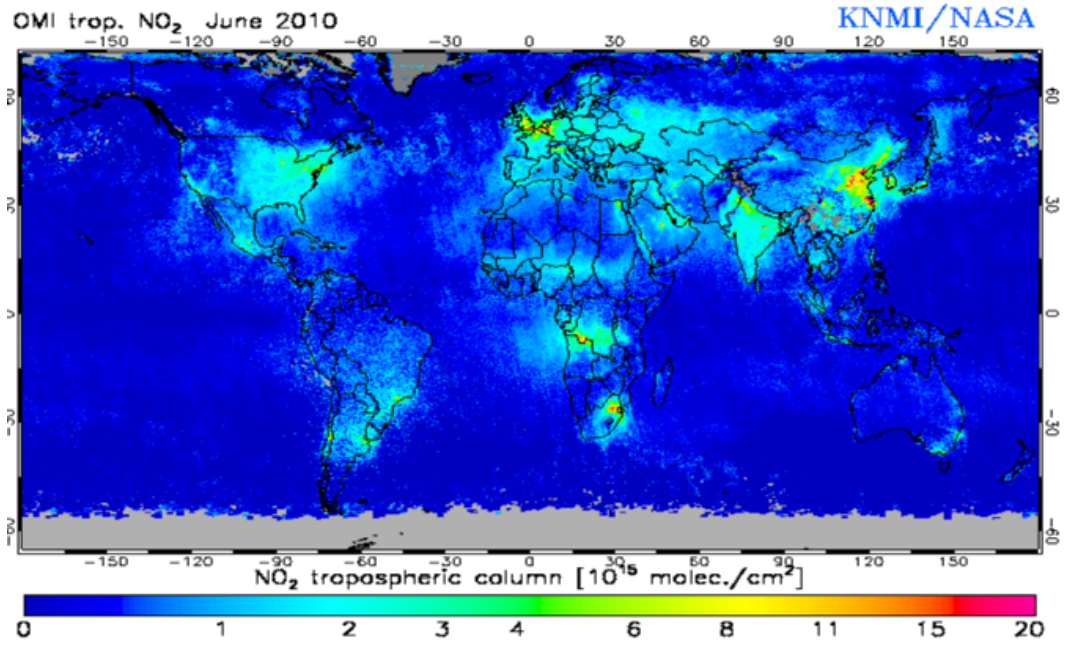

Figure 2.7: The global NO_2 field seen from the OMI satellite instrument in June 2010 (`www.temis.nl`).

2.2.1 NO_2 in air quality

NO_2 is a strong respiratory irritant at high concentrations, and the World Health Organization recommends a maximum 1-hour concentration of 200 $\mu g.m^{-3}$ and an annual average of 40 $\mu g.m^{-3}$ (WHO, 2003). Table 2.1 indicates how these concentrations are converted in vmr and tropospheric vertical columns. The direct effects on the respiratory system are not fully understood and epidemiological studies disagree on the existence of a specific health effect at typical urban levels. Correlations with the mortality rate were discovered, independently of other measured pollutants, but the effect of unmeasured species can not be ruled out (Chiusolo et al., 2011; Latza et al., 2009). In addition, experiments on humans in controlled environments indicate an amplifying effect of NO_2 in the allergic response of asthmatic subjects (Barck et al., 2005).

Moreover, NO_2 is a precursor of other irritants which form particularly in the photochemical smog seen above many cities. Smog contains, besides nitrogen compounds, volatile organic compounds from unburnt fuel, aerosols and ozone. Ozone is a strong oxidant, whose independent impact on health has been clearly established (WHO, 2003). The role of NO_2 in ozone formation will be detailed in the next section, but some severe irritants are produced in the process, including

Table 2.1: WMO recomendations for maximum levels of NO_2 for one hour and yearly average exposition. The (tropospheric) vertical column is calculated assuming a 500 m thick well-mixed boundary layer.

Dimension (unit)	Max. 1-hour	Max. 1-year
Concentration ($\mu g/m^3$)	200	40
Number density (molec./cm^3)	2.6e^{12}	5.2e^{11}
Volume mixing ratio (ppb)	100	20
Vertical column (molec./cm^2)	1.3e^{17}	2.6e^{16}

aldehydes and peroxyacyl nitrates.

Rain acidity also increases with NO_2 atmospheric concentration. Due to dissolved CO_2, rain water is naturally weakly acid, with a pH of about 5.6. NO_2 and sulfur dioxide (SO_2) lower this value due to the formation of nitric (HNO_3) and sulfuric acids (H_2SO_4). The effects are observable on vegetation and infrastructure. Concerning aquatic organisms, the tolerance on low pH depends on the species, but a more severe issue arises due to the release of aluminium dissolved by acid flowing on soils (Jacob, 1999).

2.2.2 NO_2 and tropospheric ozone

The only reaction producing ozone in the atmosphere is the combination of a free oxygen atom with an oxygen molecule (reaction 2.4).

$$O + O_2 + M \longrightarrow O_3 + M \tag{2.4}$$

In the above reaction and in those which follow, M may be N_2 or O_2 and stabilizes the formation of the produced chemical.

In the stratosphere, free oxygen atoms originate from the photolysis of O_2. This can not happen in the troposphere as the required radiative energy is not available. Stratospheric ozone may cross the tropopause but this mechanism is too weak to explain the ozone values at low altitudes. The free oxygen atom of reaction 2.4 originates in the troposphere from the photolysis of NO_2 (reaction 2.5), which happens at longer wavelengths than the photolysis of O_2.

$$NO_2 + h\nu \longrightarrow NO + O^* \tag{2.5}$$

NO_2 itself is formed rapidly after NO through its reaction with O_3

$$NO + O_3 \longrightarrow NO_2 + O_2 \tag{2.6}$$

Due to this rapid conversion, NO and NO_2 are commonly referred to as NO_x.

This cycle between ozone and NO_x enables to calculate a concentration of ozone depending on the ratio of $\frac{NO_2}{NO}$ and the reactions rate constants. This calculation often underestimates the ozone concentration, because reaction 2.6 is not the only oxidation path from NO to NO_2.

In the presence of volatile organic compounds (VOCs) originating from hydrocarbons, the hydroperoxyl radical (HO_2) replaces ozone (see reaction 2.11) in the oxidation of NO, enabling thus O_3 to accumulate. The oxidation of a hydrocarbon of general formula RH, where R is a chain of carbon and hydrogen atoms (e.g. CH_3 for methane), starts with the hydroxyl radical OH, the most effective scavenger in the atmosphere and is followed by several reactions (Sportisse, 2007):

$$RH + OH \longrightarrow R + H_2O \tag{2.7}$$

$$R + O_2 + M \longrightarrow RO_2 + M \tag{2.8}$$

$$RO_2 + NO \longrightarrow RO + NO_2 \tag{2.9}$$

$$RO + O_2 \longrightarrow R'CHO + HO_2 \tag{2.10}$$

$$HO_2 + NO \longrightarrow OH + NO_2 \tag{2.11}$$

The net effect is, thus, the oxidation of RH into a higher oxidation state, R′CHO, associated with ozone production:

$$RH + 4\,O_2 + 2h\nu \xrightarrow{HOx,NOx} R'CHO + 2\,O_3 + H_2O \tag{2.12}$$

This oxydation chain is initiated by HO_x (OH and HO_2) and catalyzed by NO_x.

Examples of R′CHO are formaldehyde (H_2CO), or glyoxal ($C_2H_2O_2$), two measurable species in the UV-visible with the DOAS technique. The catalyzed oxidation carries on with photolysis processes until the organic compounds are fully converted into CO_2. Note that the oxidation of CO also produces tropospheric ozone, though the ozone production efficiency is weaker than for hydrocarbons.

Termination occurs when HO_x or NO_x are removed, which happens mostly through:

$$NO_2 + OH + M \longrightarrow HNO_3 + M \tag{2.13}$$

or

$$HO_2 + HO_2 \longrightarrow H_2O_2 + O_2 \tag{2.14}$$

The above reactions point out the role of two parameters in ozone production: the available light and the ratio of NO_x to Volatile Organic Compound (VOC). Light is necessary to photolyze NO_2 (reaction 2.5) before ozone production. This explains both why the ozone maxima occur in summer during clear-sky days, and why NO_2 abundance is higher in winter, as it can be seen for China on figure 2.10. At the same time, for NO_x to act as a catalyst, NO_2 must be regenerated through reaction 2.11. This mechanism is competitive with the termination of HO_x (reaction 2.14) when VOC concentrations are high. The ratio of VOC to NO_x is thus a second key-element in the ozone formation.

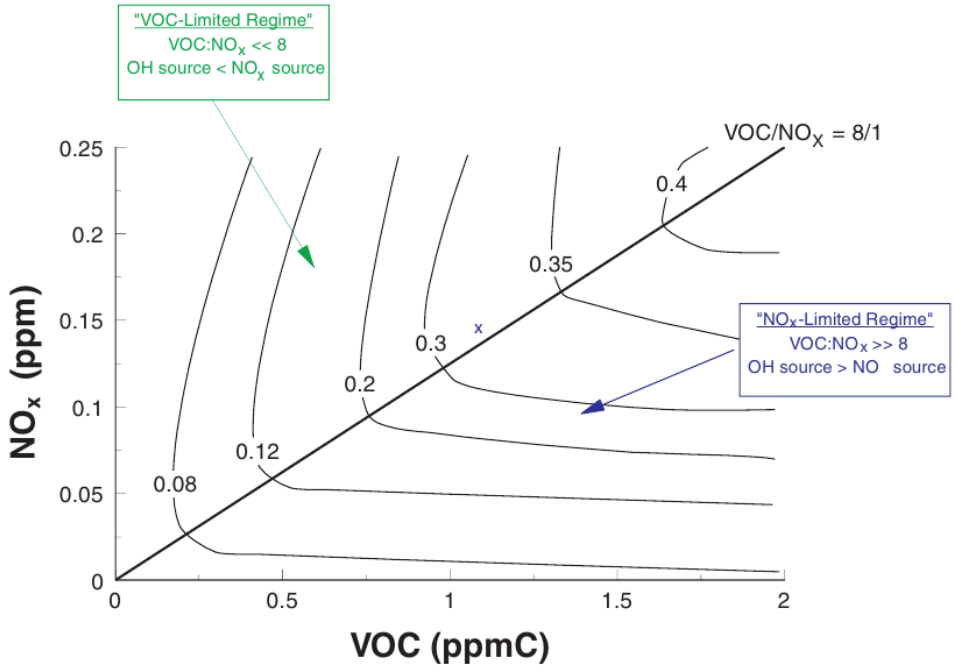

Figure 2.8: Isopleths of 1-hour maximum O_3 concentrations (in ppm) calulated as a function of initial VOC and NO_x concentrations, from NARSTO (2000).

Figure 2.8 shows the ozone concentration isopleths as a function of the initial concentrations of equivalent carbon due to VOC and NO_x. It shows a complex relationship between these three variables with a NO_x-limited regime, where an increase in VOC does not lead to an increase in ozone, and a carbon-limited regime where the situation is nearly symmetric. An important consequence of the isopleths' shapes is that in the VOC-limited regime, a reduction of NO_x may yield an enhancement in ozone production. The VOC-limited regime is often encountered inside cities. Brussels often experiences such an increase in ozone

during weekends, when the traffic, the main source of NO_x, is reduced (IBGE, 2009). Note that authorities do not limit the traffic during the ozone alerts in summer, contrary to the winter pollution episodes, associated with high NO_x and aerosols.

2.2.3 Sources and sinks of NO_x

Table 2.2 lists the sources of NO_x in teragrammes of nitrogen (1 teragramme = 10^{12} g) for the year 2000. This is the result of two top-down studies comparing satellite data with a chemical transport model. The main chemical production originates from several processes occurring during combustion. At high temperature, N_2 and O_2 are decomposed and recombine, directly or indirectly in NO_x. This process occurs also during thunderstorms close to the lightning channel. In addition, some fuels contain nitrogen that is oxidized and released during combustion. Nitrogen is also emitted by soils, all the more so as they have been fertilized. The transport from the stratosphere exists but, as with ozone, it represents a very limited source in the troposphere. The table points out that the NO_x present close to the ground is mostly anthropogenic.

Table 2.2: Global emissions of NO_x in 2000, adapted from (Vlemmix, 2011).

Source	Emission rate (Tg N/year)
Fossil fuel combustion	25.6
Lightning	6.2
Biomass burning	5.8
Soil	8.9
Biofuels	2.2
Aircraft	0.5
Stratosphere	0.1
Total	49.3

The main sink of NO_x is the oxidation of NO_2 to HNO_3, which takes different paths during day and night depending on the presence of the hydroxyl radical. During day time, ozone can be photodissociated and the free oxygen atoms combine with H_2O to produce OH, leading to reaction 2.13.

As seen in figure 2.6, the lifetime of the OH radical is very short, and it is thus absent during the night. The oxidation of NO_2 is in this case less direct and involves ozone:

$$NO_2 + O_3 \longrightarrow NO_3 + O_2 \tag{2.15}$$

$$NO_3 + NO_2 + M \longrightarrow N_2O_5 + M \tag{2.16}$$

$$N_2O_5 + H_2O \longrightarrow 2\,HNO_3 \tag{2.17}$$

An alternate NO_x sink is its conversion to an organic form, namely peroxyacetyl nitrate (PAN, $C_2H_3NO_5$). This happens in the presence of carbonyl (R′CHO in reaction 2.10). This sink is less important than the conversion to nitric acid, but it enables the long-range transport of NO_x, since PAN is not as soluble in water as nitric acid. In fact, PAN decomposition increases with temperature, releasing NO_x further away than expected from its natural lifetime of a few hours (figure 2.6).

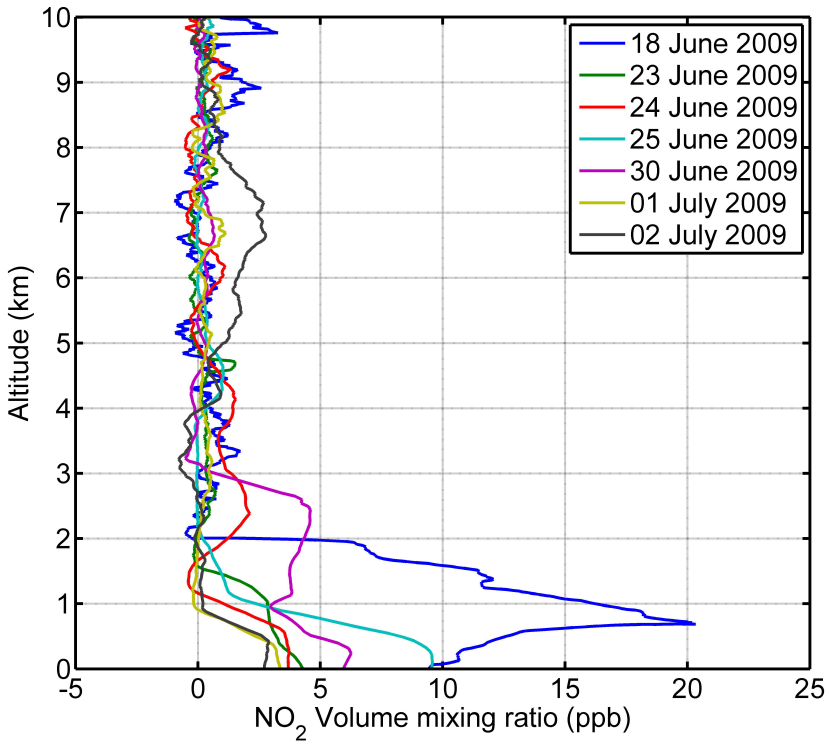

Figure 2.9: In-situ tropospheric NO_2 profiles during CINDI campaign.

2.2.4 Time and space patterns in the NO_2 field

With its short lifetime, NO_2 mostly stays close to its sources and inside the boundary layer. Considering also that the sources described in the previous section are

mostly anthropogenic, it is not surprising to find the highest NO_2 loadings close to populated and industrial places. To illustrate that, figure 2.7 presents the average global NO_2 field derived from satellite data of June 2010. It should be noted that the NO_2 distribution largely varies with time, but the most populated places are always visible: e.g. Eastern China, Europe, and East coast of the United States. Smaller spots also correspond to populated places like the Nile Valley or Sydney. In Europe, the highest concentrations are observed in Benelux and in the Ruhr basin, around London and in the Po Valley. In India, Africa and South America, biomass burning contributes significantly to the observed levels. On the contrary, the oceans and deserts appear relatively free of NO_2.

Regarding the vertical distributions, figure 2.9 presents in-situ measurements from balloons around Cabauw during the CINDI campaign (see chapter 7 and Sluis et al. (2010) for a description of the instrument, which is still under development). The shapes and volume mixing ratios vary with the soundings but the bulk of NO_2 is always close to the ground, except for the last one (2 July 2009) which shows the lowest NO_2 levels.

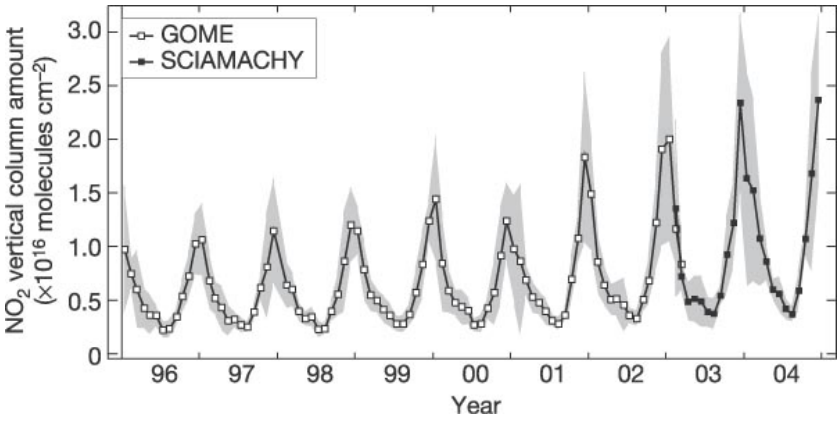

Figure 2.10: Time series of NO_2 column as seen from the satellite instruments GOME and SCIAMACHY above China (Richter et al., 2005).

The NO_2 concentration at a given place depends on the types of sources and local meteorological conditions, but several cycles are often observed. For an industrialized location like Europe, the daily maximum occurs at rush hours. A weekly cycle is also visible due to the traffic reduction during weekends (Kramer et al., 2008; Boersma et al., 2009). Finally, as discussed in section 2.2.2, the seasonal variation of available sunlight also leads to a yearly cycle with a winter maximum (Hayn et al., 2009; Lamsal et al., 2010). This last cycle is visible for China in figure 2.10, which also illustrates the increasing trend in this region from

the 90s to 2004. This tendency is directly linked with the industrialization and economic growth. During the economic crisis in 2008-2009, a reduction of NO_2 over China was also detected from space (Lin and McElroy, 2011). In Europe and North America, NO_2 trends are overall weakly negative (van der A et al., 2008; Konovalov et al., 2008; Stavrakou et al., 2008).

These trends, as the columns shown in figures 2.10 and 2.7, were derived from satellite measurements of the spectral radiance in the ultraviolet-visible, using Differential Optical Absorption Spectroscopy, the same technique used for our lower altitude instruments. The next chapter details the principles of this method.

Chapter 3

Scattered-light DOAS

This chapter presents the methods used in this thesis to retrieve geophysical quantities from the spectral analysis of scattered light. The first section describes physical concepts of the interaction of light with gas molecules and presents the principle of Differential Optical Absorption Spectroscopy (DOAS). The second section details how the DOAS algorithm disentangles in practice the various contributions to the light spectrum recorded in the atmosphere. These contributions are interpreted in term of gas and aerosols loadings, in the third section, by modeling the atmospheric radiative transfer.

3.1 Differential Optical Absorption spectroscopy

3.1.1 Light absorption by molecules

Light was described in the previous chapter to induce chemical reactions in the atmosphere through photodissociations of molecules such as NO_2 and O_3. At longer wavelengths, the radiative field interacts non-destructively with matter through scattering and absorptions of photons. The latter phenomenon is the physical principle of our measurement: molecules absorb photons around specific energies, which depend on their molecular orbitals and the symmetries in atomic arrangement. Studying the light after this interaction enables thus to discriminate absorbing molecules and quantify their abundances. We introduce here the origin of the specific absorption energies and their repartition in the spectral range. Our description only summarizes important ideas. For an exhaustive treatment of the relation between the shape of spectra, the reader is referred to Bernath (1995). An overview of the applications of spectroscopy from the radio waves to the gamma rays is given by Svanberg (2004).

The absorption of light by a molecule corresponds to allowed transitions in

its internal energy, whose amplitudes are determined by the photon wavelengths. Starting from the low energies of the radio waves to the mid-infrared, a photon may induce a transition between two rotational states[1]. This is possible if the molecule has a permanent electric dipole, which depends on its symmetries. From the mid-infrared to the visible, the vibration state may change as well, if a dipole can be induced on the molecule. This is not possible if the molecule is completely symmetric like N_2 and O_2[2]. In this case, the charges stay equally distributed around the nuclei, which prevents not only the existence of a permanent dipole, but the possibility for a dipole to be induced on the molecule by an external field. This impossibility explains why these two major atmospheric constituents are not greenhouse gases: they can not absorb light in the infrared. Decreasing again the wavelength down to the ultraviolet, the photon can change the electronic orbital configurations of the molecule, which happens with free atoms as well. The possible transitions cumulate: in the ultraviolet and visible part of the spectrum (uv-visible), which is the range of our DOAS instruments, most of the transitions correspond to a mix between the three processes. Such transitions are referred to as ro-vibronic.

The distribution of absorption around the transition energies is not infinitely narrow. The most fundamental limit arises from the Heisenberg principle, relating the spontaneous lifetime of an excited state with its energy width. This natural width happens to be negligible in the earth's atmosphere due to pressure and temperature broadenings. The pressure effect originates at the microscopic level from collisions leading to phase discontinuities in the dipole state. The resulting line shape is given by a Lorentzian. The distribution of molecule velocities, which depends on the temperature, yields Doppler shifts. The associated line profile is in this case a Gaussian distribution. In the uv-visible range and at atmospheric temperature, the temperature and pressure broadening are of the same order of magnitude. The resulting line shape for a single transition appears thus analytically as the convolution of a Gaussian and a Lorentzian, namely a Voigt profile. However, the rotational transitions are usually too close compared to their widths to be isolated, at least at the resolution of the spectrometers. This results in the uv-visible absorption spectra in systems of relatively broad vibration bands, which are composed of mixed rotation lines, centered around specific electronic transitions.

So far, we have only described the interaction processes between light and matter qualitatively and at microscopic level. Theoretical spectroscopy can be used to interpret spectra as was done on Venus atmosphere to discover a new CO_2 band

[1] At room temperature, the rotation transitions and thermal kinetic energy of a molecule have the of same order of magnitude, so the molecules are already rotationally excited.

[2] Note that this description neglects other effects such as collision-induced absorptions, which appears for instance to N_2 in the infrared.

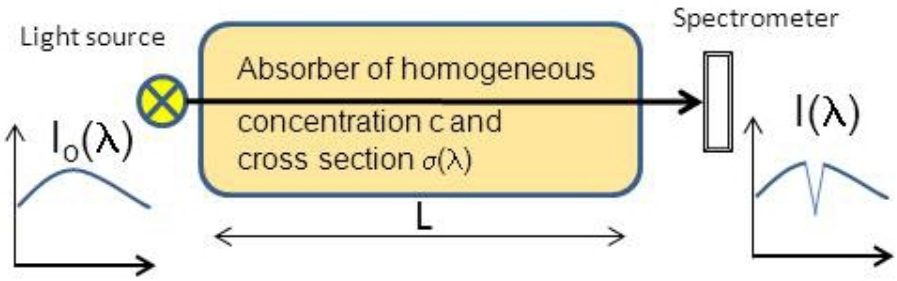

Figure 3.1: Absorption spectroscopy in the lab.

(Bertaux et al., 2008), but it does not correspond to the work presented here. A macroscopic approach to investigate the absorption spectra of the molecule is illustrated in figure 3.1. The Beer-Lambert law states that the intensity exponentially decreases while crossing a medium of length L and concentration c:

$$I(\lambda) = I_0(\lambda) \exp\left(-\sigma(\lambda) c L\right) \tag{3.1}$$

The remaining factor in the exponential is the absorption cross-section $\sigma(\lambda)$, which characterizes the ability of a molecule to absorb photon at a given wavelength λ. It depends on the molecule shape and originates from the above considerations.

From the Beer-Lambert law, the optical thickness of a medium (τ) is defined as:

$$\tau(\lambda) = \ln \frac{I_0(\lambda)}{I(\lambda)} = \sigma(\lambda) c L \tag{3.2}$$

The optical thickness is the interesting measured quantity to get information on the molecule. Knowing L and c leads directly to the absorption cross-section and this is the basis of laboratory spectroscopic studies. On the other hand, knowing L and σ leads to the molecular concentration. In our work, the problem arises mostly from an imperfect knowledge of the light path, as it will be discussed in the next sections.

Figure 3.2 presents the absorption cross-sections of several molecules. In the case of NO_2, the ro-vibronic system corresponds to transitions between the ground state and the first electronic level. The cross-section exhibits high frequency structures superimposed on a broadband component between 300 and 500 nm. The latter is responsible for the brown color of NO_2. All the species of figure 3.2 are detectable with the DOAS technique. Among them, we have unambiguously identified with the instruments NO_2, O_3, and H_2O. DOAS measurements of two other

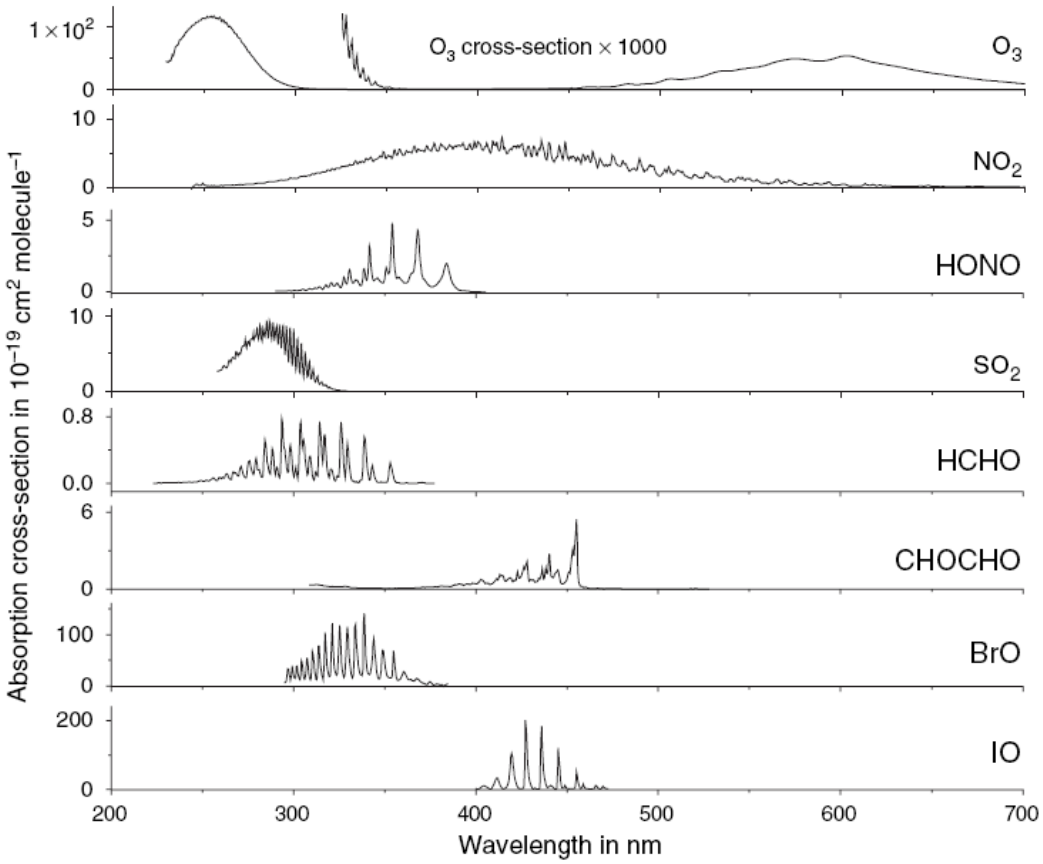

Figure 3.2: Absorption cross-sections of some atmospheric trace gases in the UV-visible, adapted from (Platt and Stutz, 2008).

species, BrO and HCHO have been the subject of two recent PhDs at BIRA-IASB, respectively by Theys (2010) and De Smedt (2011), which have inspired this writing. The absorption of the O_2-O_2 collision complex, not shown on the figure, was also measured. It was used to infer aerosol extinction profiles from the POLARCAT experiment (chapter 5) and to filter the cloud free data acquired during the Earth Challenge expedition (chapter 6). The O_2-O_2 cross section between appears in the DOAS fit of figure 5.4.

All the aforementioned molecules share two characteristics: they are simple and small compared for instance to the peroxyacetyl nitrate introduced in the previous chapter, and their absorption cross-sections are highly structured. These two properties are tightly linked, as a heavy molecule has much more possible transitions, leading to a continuous spectrum in the UV-visible range. These

structured absorptions are the basis of the DOAS method, but before entering in its detail, we will discuss how the Beer-Lambert law is transformed for scattered-sky light in the atmosphere.

3.1.2 Spectroscopy of the uv-visible scattered-light sky

Figure 3.3 presents the interaction of sun light with the atmosphere and a set-up for scattered light spectroscopy. The situation is more complicated than the one depicted in figure 3.1 in several aspects:

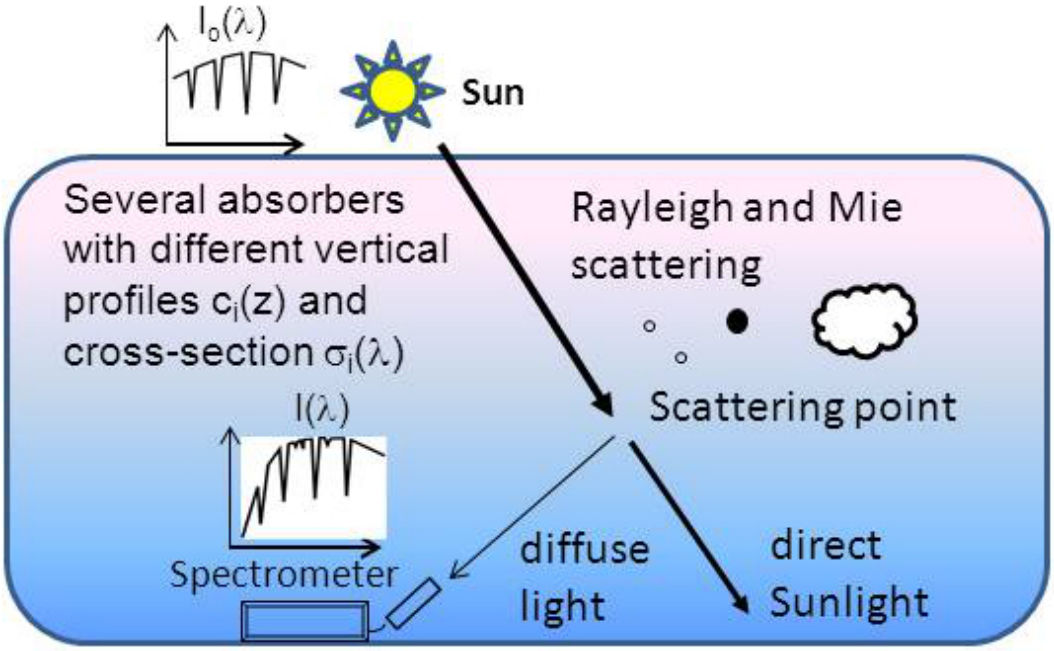

Figure 3.3: Absorption spectroscopy of the scattered-light sky in the atmosphere.

1. The light path is not straight as it would be the case if the instrument was directed toward the sun. Light recorded by the instrument has been scattered by definition at least once. The positions of the scattering points are not known a priori and depend on the observation geometry and on the atmosphere characteristics. In particular, aerosols influence the light path differently according to their size. This is illustrated in figure 3.4, showing the dependence of the scattering angular distribution (the phase function) with the particle size.

2. Several absorbers are present. Not only may their absorption spectra overlap (see figure 3.2) but their concentration is not constant in altitude.

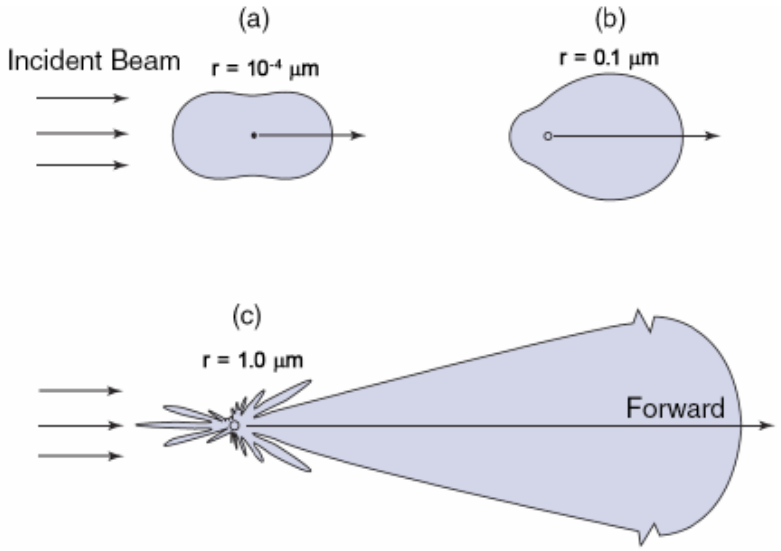

Figure 3.4: Scattering phase functions of visible light ($\lambda = 500\,\text{nm}$) on spherical particles of different size representing: (a) air molecules, (b) and (c): aerosol particles. The forward pattern of (c) is extremely large and has been scaled down for this figure (Petty, 2006).

3. The light source, i.e. the sun, presents absorption structures even before reaching the atmosphere. These so-called Fraunhofer lines originate from atomic absorptions (H, Mg, Ca, ...) in the solar atmosphere. Moreover, except for satellite-based instruments, it is not possible to measure directly $I_0(\lambda)$ since our measurements take place inside the absorbing medium.

The reduction of scattered sun light intensity in the atmosphere is thus much more complicated than in equation 3.1. A more accurate treatment of the radiative transfer in the atmosphere will be given in the next section. At this point, we can assume a single light path to reformulate the Beer-Lambert law as:

$$I(\lambda) = I_0(\lambda)A(\lambda, ...)\exp - \int [\sum_i \sigma_i(\lambda, s)c_i(s) + \epsilon_M(\lambda, s) + \epsilon_R(\lambda, s)]ds \tag{3.3}$$

$I_0(\lambda)$ and $I(\lambda)$ are respectively the intensities of the direct sun light at the top of atmosphere and the scattered fraction measured by the instrument. $A(\lambda, ...)$

represents the ratio of the scattered light in the observation geometry at the scattering point. The integral is carried along the optical path of the measured photons in the atmosphere. The extinction coefficients ϵ_M and ϵ_R represent the Mie and Rayleigh scattering. In fact, Rayleigh scattering is a limit case of Mie scattering for small particles but in atmospheric optics it is common to separate the two since the Rayleigh-only part originates from scattering on the air molecules while the scattering on aerosols has to be treated with the Mie theory. The problem lies in extracting c_i, the concentration of an individual absorber. The DOAS method enables important progress towards this objective.

3.1.3 Principle of Differential Optical Absorption Spectroscopy

For many absorbers, the uv-visible cross-section varies weakly with the temperature and pressure under atmospheric conditions. Assuming a constant cross-section, the optical depth of a given absorber τ_i in a scattered-light spectrum can thus be expressed as:

$$\tau_i(\lambda) = \int \sigma_i(\lambda, s) c_i(s)\,\mathrm{d}s = \sigma_i(\lambda) \int c_i(s)\,\mathrm{d}s \tag{3.4}$$

This leads to the definition of the slant column of an absorber as:

$$SC_i = \int c_i(s)\,\mathrm{d}s \tag{3.5}$$

This quantity has the same dimension as the vertical column previously defined (equation 2.1), but depends on the optical path of the measurement.

Integrating Rayleigh and Mie scatterings to their optical depth, equation 3.3 reduces to:

$$I(\lambda) = I_0(\lambda) A(\lambda, ...) \exp -[\sum_i \sigma_i(\lambda) SC_i(\lambda) + \tau_M(\lambda) + \tau_R(\lambda)] \tag{3.6}$$

As mentioned in the previous section, $I_0(\lambda)$ is not accessible from inside the atmosphere. We thus have to use also a scattered-light spectrum as a reference. Expressing it in the form of equation 3.6, the ratio of the measured to the reference spectrum is:

$$\ln \frac{I_{ref}}{I}(\lambda) = \ln \frac{A_{ref}}{A}(\lambda) + \sum_{i=1}^{n} \sigma_i(\lambda) \Delta SC_i + \Delta\tau_M(\lambda) + \Delta\tau_R(\lambda) \tag{3.7}$$

DOAS is based on the observation that, on the one hand, the scattering terms in the above sum vary slowly with λ. Indeed, Rayleigh scattering on molecules varies in λ^{-4}, and this wavelength dependence decreases with the particle sizes.

On aerosols, the Angström exponent α describing the dependence ($\lambda^{-\alpha}$) varies between 0 and 2. On the other hand, the cross section of some absorbers, like those of figure 3.2, presents sharp structures in the spectral domain.

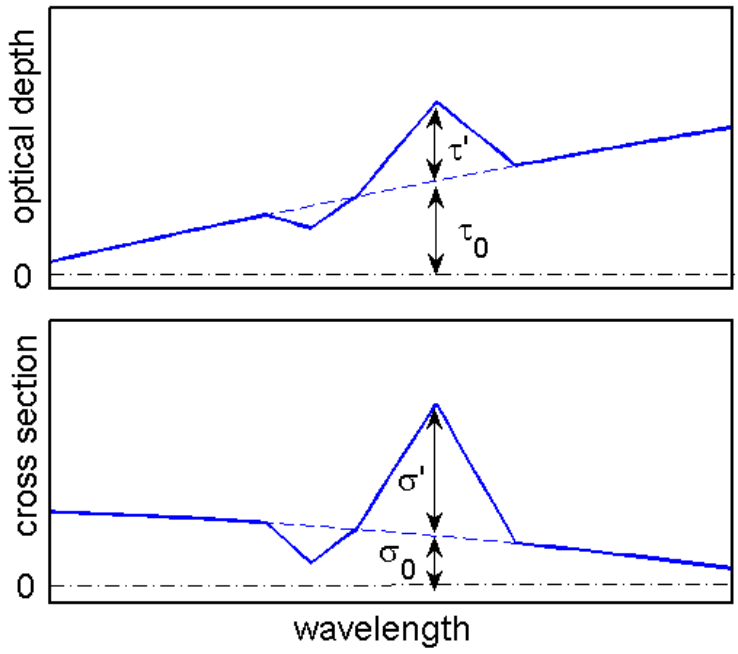

Figure 3.5: Illustration of the differential cross section and optical depth.

To disentangle these absorbers, one splits the cross-section in its continuous (σ_0) and differential (σ') contributions:

$$\sigma(\lambda) = \sigma'(\lambda) + \sigma_0(\lambda) \tag{3.8}$$

The differential part of the optical density can then be isolated from the other contributions (see figure 3.5), which can be accounted for with a low-order polynomial.

$$\ln \frac{I_{ref}(\lambda)}{I(\lambda)} = \sum_{i=1}^{n} \sigma_i'(\lambda) \Delta SC_i + \sum_{j=0}^{m} a_j \lambda^j \tag{3.9}$$

The above equation enables to retrieve the difference of slant column of an absorber between a measurement and a reference spectrum. This relative slant column is usually referred to as a differential slant column density (DSCD). Note that "differential" refers here to the reference spectrum and not to the structures in the cross section.

It is important to realize that the DOAS technique is based on the assumption that the absorber does not significantly influence the optical path. We checked this assumption for NO_2 in polluted conditions in chapter 6.

3.2 DOAS in practice

We used a dedicated software, QDOAS (Fayt et al., 2011), developed at BIRA-IASB to retrieve the different slant column densities from the spectra. This software, widely used in the DOAS community, offers many possibilities. We only detail here the algorithms used in our applications. Note that the software is also used for the spectral calibration (see next chapter).

Two effects have to be added to the description of the problem given above when analyzing real spectra of scattered sky light: the filling-in of Fraunhofer lines commonly referred to as the Ring effect and the occurrence of non-linear terms in equation 3.9, originating from stray light and wavelength shift in the measured and cross-section spectra. We detail here these two problems and the algorithmic recipes used by QDOAS to deal with them.

3.2.1 Ring Effect

In 1962, Grainger and Ring observed that the Fraunhofer lines do not look the same in the direct moon light and in the scattered sky light (Grainger and Ring, 1962b). They assumed that this could be explained by "a day-light airglow". This phenomenon was later interpreted as an effect of rotational Raman scattering (Brinkmann, 1968). A small part of the Rayleigh scattering is non-elastic and redistributes the frequencies of the light source, leading to a filling-in of the Fraunhofer lines. As expected, the so-called Ring effect increases with the scattering events, toward the short wavelengths and in limb geometry. The associated optical depths are typically a few percent, which is the same order of magnitude as the absorption of the investigated trace gases.

The Ring effect is corrected in our case by introducing a source term based on the convolution of a Fraunhofer spectrum with O_2 and N_2 rotational Raman spectra (Chance and Spurr, 1997a). This source is divided by the Fraunhofer spectrum to produce a ring cross section as described by Van Roozendael et al. (2002), which is reproduced below. Note that Raman scattering from trace gases, as well as vibrational Raman scattering, are neglected.

A measured spectrum contains an elastic and a non-elastic part, the latter originating from rotational Raman scattering (RRS):

$$I_{meas} = I_{elastic} + I_{RRS} \tag{3.10}$$

The rotational Raman scattering (I_{RRS}) represents only a few percent of the total intensity I_{meas}. Thus, the logarithm of the sum 3.10, which is the fitted quantity, may be approximated by its Taylor development:

$$\ln I_{meas} = \ln \left(I_{elastic}(1 + \frac{I_{RRS}}{I_{elastic}}) \right) = \ln I_{elastic} + \frac{I_{RRS}}{I_{elastic}} \tag{3.11}$$

The differential structures of the Ring optical depth can be calculated by convoluting the solar spectrum I_0 and a rotational Raman cross section of air based on N_2 and O_2 Raman spectra, and dividing the result by the solar spectrum. The exact contribution of the Ring effect in the differential optical depth will depend linearly on this pseudo cross section as:

$$\frac{I_{RRS}}{I_{elastic}} = \frac{I_0 * \sigma_{RRS_{air}}}{I_0} C_{Ring} \tag{3.12}$$

This contribution, C_{Ring}, can then be fitted together with the other absorbers.

The Ring effect can be observed in figure 5.4. Note that in this case, the differential optical depth of the Ring (6e-3) is much larger than NO_2 (1e-3). This illustrates the necessity of an accurate correction of the Ring effect.

3.2.2 Resolution of the linear problem

As the equation 3.9 is linear, it may be written in matrix form:

$$\boldsymbol{\tau} = \mathbf{A}\mathbf{x} \tag{3.13}$$

Where $\boldsymbol{\tau}$ is a column vector of optical depths in the wavelength range of the fitting window, $\mathbf{A}$ is a $m \times n$ matrix whose columns are the differential cross-sections $\sigma'_i(\lambda)$ and the powers of lambda taken into account in the polynomial $P(\lambda)$, and $\mathbf{x}$ a vector composed of the Differential Slant Column Density (DSCD) of each absorber and of the polynomial coefficients.

$$\mathbf{A} = \begin{bmatrix} \sigma'_1(\lambda_1) & \dots & \sigma'_n(\lambda_1) & 1 & \lambda & \dots & \lambda_1^m \\ \sigma'_1(\lambda_2) & \dots & \sigma'_n(\lambda_2) & 1 & \lambda & \dots & \lambda_2^m \\ \vdots & \vdots & \vdots & \vdots & \vdots & \vdots & \vdots \\ \sigma'_1(\lambda_l) & \dots & \sigma'_1(\lambda_l) & 1 & \lambda & \dots & \lambda_l^m \end{bmatrix} \tag{3.14}$$

In practice, the number of lines of $\mathbf{A}$ is much larger than the number of columns. The system is thus overdetermined, which implies the definition of a criterion to choose a solution. A common criterion is the minimization of the quadratic cost function $[\boldsymbol{\tau} - \mathbf{A}\mathbf{x}][\boldsymbol{\tau} - \mathbf{A}\mathbf{x}]^T$. This least-square solution, $\mathbf{x_{ls}}$, corresponds to the maximum likelihood solution if the errors on the measured $\boldsymbol{\tau}$ are normally distributed, which is a reasonable assumption for physical measurements. In QDOAS,

the solution $\mathbf{x_{ls}}$ is found computing the Singular Value Decomposition (SVD) of $\mathbf{A}$. This means expressing $\mathbf{A}$ as the matrix product $\mathbf{UWV^T}$, where in particular $\mathbf{W}$ is a rectangular diagonal matrix. This method is robust compared to inverting $\mathbf{A^TA}$ which may be ill-conditioned. Moreover, the uncertainties on the solution are also expressed from the SVD (Press et al., 1992).

The SVD allows to write a pseudo-inverse of $\mathbf{A}$ and thus $\mathbf{x_{ls}}$ as:

$$\mathbf{x_{ls}} = \mathbf{V} \cdot \mathbf{diag}(\frac{\mathbf{1}}{\mathbf{w_j}}) \cdot \mathbf{U^T} \cdot \boldsymbol{\tau} \tag{3.15}$$

The value of the cost-function at $\mathbf{x_{ls}}$, divided by the degree of freedom of the problem $(m-n)$, can be used to estimate the mean error σ on the elements of $\boldsymbol{\tau}$, since their normal distribution is assumed:

$$\sigma^2 = \frac{[\boldsymbol{\tau} - \mathbf{Ax_{ls}}][\boldsymbol{\tau} - \mathbf{Ax_{ls}}]^T}{m-n} \tag{3.16}$$

This error is propagated on the slant column space using the SVD:

$$\boldsymbol{\Sigma} = \sigma^{\mathbf{2}} \cdot [\mathbf{V^T} \cdot \mathbf{diag}(\frac{\mathbf{1}}{\mathbf{w_j}}) \cdot \mathbf{V}] \tag{3.17}$$

The above equation defines the covariance matrix of $\mathbf{x_{ls}}$. In QDOAS, the error on the slant columns corresponds to the respective diagonal element of Σ:

$$\sigma_{\Delta SCi} = \sqrt{\Sigma_{ii}} \tag{3.18}$$

3.2.3 Treatment of the nonlinearities due to offset and shift

The above formulas are used to fit the slant columns and estimate the associated uncertainties. However, the equation 3.9 does not describe the problem well enough for small absorbers. It is first necessary to fit an offset, which may originate from stray light inside the spectrometer (the so called spectral stray light, see next chapter) or from an imperfect Ring correction. Secondly, a small spectral shift may be introduced by instrument instabilities between the reference and the measured spectrum.

Adding these two parameters leads to a new form of the Beer-Lambert law:

$$\ln \frac{I_{ref}(\lambda)}{I(\lambda + shift) - offset(\lambda)} = \sum_{i=1}^{n} \sigma_i'(\lambda) \Delta SC_i + \sum_{j=0}^{m} a_j \lambda^j \tag{3.19}$$

The offset and shift can not be determined at once by SVD since the equation is not linear regarding these parameters. Keeping the least-square criterion, the associated cost-function is $\boldsymbol{rr^T}$ where

$$r(\lambda, shift, offset, \Delta SC_i, a_j) =$$
$$\ln I(\lambda + shift) - offset(\lambda) + \sum_{i=1}^{n} \sigma_i'(\lambda)\Delta SC_i + \sum_{j=0}^{m} a_j \lambda^j - \ln I_{ref}(\lambda) \qquad (3.20)$$

Among the various algorithms to deal with non-linear least-square problems, QDOAS uses the Levenberg-Marqardt algorithm (Madsen et al., 2004) to fit the shift and offset[3] Note that the effects of offset and shift are not taken into account in the slant column uncertainties, derived from the SVD. The error introduced is however negligible for small values of offset and shift (Stutz and Platt, 1996).

3.3 Interpretation of DOAS measurements by modeling the radiative transfer

The results of the DOAS analysis are the integrated concentrations of the absorbers along the photon paths of the measured spectrum, relative to the same quantity in a reference spectrum. These relative slant columns depend on the observation geometry, sun position, and atmospheric state. This can be seen on figure 3.6, which presents the effect of the absorber altitude relative to the scattering point for a ground-based MAX-DOAS measurement. To retrieve more interesting geophysical quantities, it is thus necessary to model the radiative transfer in the atmosphere. We first introduce theoretical notions on the transport of scattered sky-light then describe how they are applied numerically to interpret the slant columns.

[3]The Levenberg-Marqardt iteration is a weighted mean of the steps given by two algorithms: the steepest descent and the Gauss-Newton methods. The former uses the gradient of the cost function and always converges, at least to a local minimum, but is slow. The latter approximates the Hessian of the cost function and is less robust but converges faster. The weight coefficient is adjusted at each iteration according to the value of the cost function.

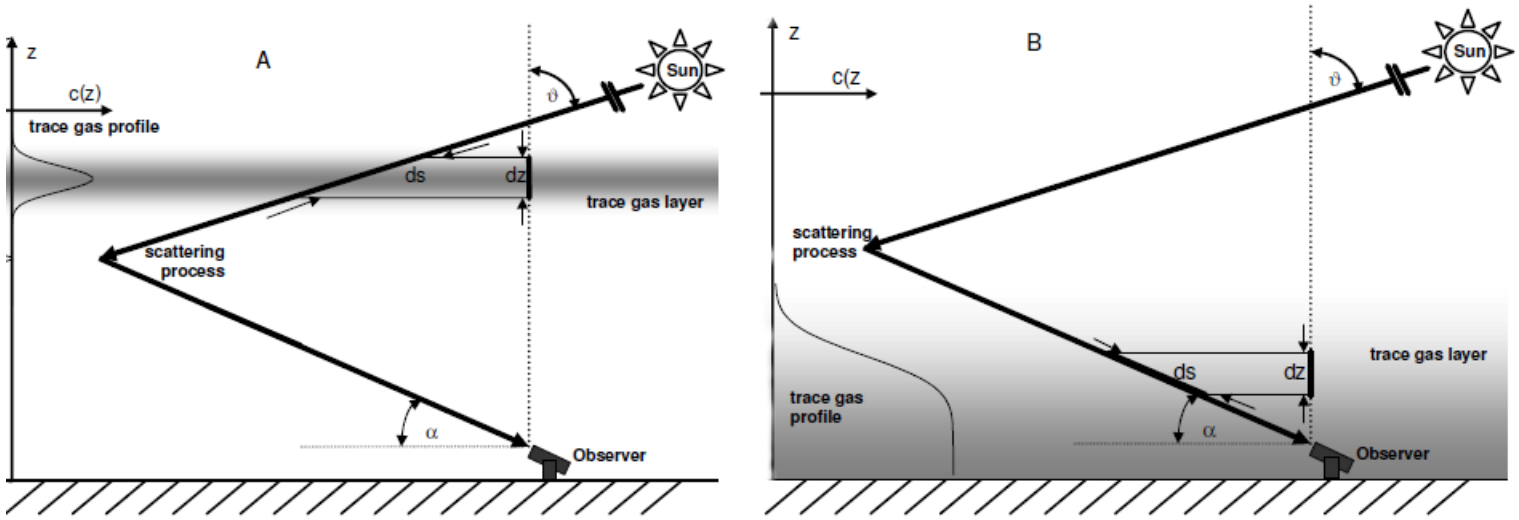

Figure 3.6: Illustration of the profile dependence of the slant columns (Hönninger et al., 2004). If the absorber is above the scattering point, the slant column decreases with the solar elevation but is independent of the telescope elevation, if the absorber is below the scattering point, the opposite is true. Of course the reality is more complex than this geometrical approximation due to multiple scatterings and the fact that several light paths contribute to the measurements.

3.3.1 The radiative transfer equation in a plane-parallel atmosphere

We consider first the transport of uv-visible radiation inside a thin layer of an atmosphere where the optical properties are constant. The primary source is sun light hitting the top of atmosphere at zenith angle θ_0 and azimuth ϕ_0. This sun light is scattered across the atmosphere in all directions. The light extinction originates from absorption and scattering processes, defined by their respective coefficients k_{abs} and k_{sca}. The scattering is furthermore described by a phase function p representing the angular distribution after the scattering.

It is convenient to change the variables for the altitude inside the atmosphere and for the zenith angle. The altitude is expressed with the vertical depth from the top of the atmosphere, τ, integrating the extinction upward from the layer altitude. The zenith angle is replaced by its cosine $\mu = \cos\theta$. It is also convenient to introduce the ratio of the scattering over the total extinction, referred to as the single scattering albedo ω:

$$\omega = \frac{k_{sca}}{k_{abs} + k_{sca}} \tag{3.21}$$

The above description is illustrated in figure 3.7. Neglecting the thermal emissions and the polarization effects, the variation of the intensity across the layer in a given direction is written as (Liou, 2002):

$$\begin{aligned} \mu \frac{dI(\tau,\mu,\phi)}{d\tau} =& I(\tau,\mu,\phi) \\ &- \frac{\omega}{4\pi} p(\mu,\mu_0,\phi-\phi_0) e^{\frac{-\tau}{\mu_0}} F_0 \\ &- \frac{\omega}{4\pi} \int_0^{2\pi} \int_{-1}^{1} p(\mu,\mu',\phi-\phi') I(\tau,\mu',\phi') \mathrm{d}\mu' \mathrm{d}\phi' \end{aligned} \tag{3.22}$$

This is the equation of radiative transfer for the scattered light radiative field in the uv-visible. The first line corresponds to the Beer-Lambert law and describes the attenuation of light in a medium of given extinction. The two others are source terms that originate from single and multiple scattering, respectively. It is an integrodifferential equation, reflecting the fact that the light at a given point depends both on local and remote conditions. As such, it is not easy to solve analytically.

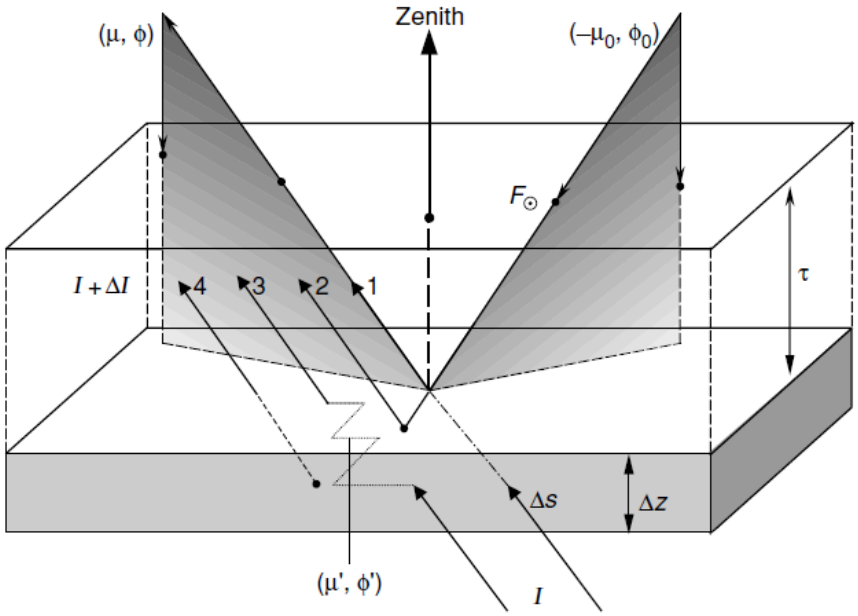

Figure 3.7: Transfer of scattered light in a plane-parallel layer: (1) attenuation by extinction, (2) single scattering of the solar flux, (3) multiple scattering, (4) represents thermal emissions from the layer, neglectable in the uv-visible (Liou, 2002).

3.3.2 The discrete ordinates method for anisotropic scattering in an inhomogeneous plane-parallel atmosphere

The discrete ordinates method originates from the seminal work of Chandrasekhar (1960), who was originally interested in stellar atmospheres. It consists in replacing the integral by sums, to obtain a system of differential equations. We only give the main ideas for anisotropic scattering here, the complete solution leads to many difficulties and does not correspond to the main work presented here. The interested reader should consult Chandra's book or the technical report by Stamnes et al. (2000) which digs into the technical details.

The atmosphere is described as plane-parallel but inhomogeneous: this means that several layers are defined in the vertical dimension, in which the scattering and absorption properties are constant. We first consider a single layer, which is afterward extended to the full atmosphere.

The phase function is first expanded in its Legendre polynomials expansion relative to the scattering angle, Θ_s, expressed as:

$$\Theta_s = \mu\mu' + \sqrt{(1-\mu^2)(1-\mu'^2)}\cos(\phi - \phi') \tag{3.23}$$

This is particularly convenient for pure Rayleigh scattering ($p(\Theta_s) = \frac{3}{4}(1 + \cos^2\Theta_s)$) for which only two Legendre polynomials are enough. Considering the more complicated patterns of figure 3.4, a useful analytical description is the Henyey-Greenstein function, which also leads to a simple expression for the Legendre coefficients:

$$P_{HG}(\cos\Theta_s) = \frac{(1-g^2)}{(1+g^2-2g\cos\Theta_s)} = \sum (2l+1)g^l P_l(\cos\Theta_s) \tag{3.24}$$

In the above equation, the parameter g, referred to as the asymmetry factor, varies between -1 (pure backward scattering) to 1 (pure forward).

The analytical expression of the intensity is not known, after all that is what we try to get. Nevertheless, the symmetry of the problem naturally yields to expand it in its Fourier cosine series:

$$I(\tau,\mu,\phi) = \sum I(\tau,\mu)\cos(\phi - \phi_0) \tag{3.25}$$

Substituting these equations in equation 3.22 and using the orthogonality properties of the Legendre and Fourier decomposition, the problem takes the form of a system of independent equations, one for each Fourier component. This Fourier component is itself expanded replacing the integral on μ by a quadrature sum. The new system of linear differential equations is solved in the different layers with the

boundary conditions that the intensities are continuous at the layer interfaces and determined at the top of the atmosphere by the given solar radiation and at the bottom by the given ground albedo or the more accurate bidirectional reflectance distribution function.

3.3.3 The radiative transfer model used: UVSPEC-DISORT

The radiative transfer model we use is based on the LibRadtran package (Mayer and Kylling, 2005) which itself implements the DISORT program (Stamnes et al., 1988, 2000) to solve the radiative transfer equation. The code has been validated in an intercomparison exercise involving six different radiative transfer models (Hendrick et al., 2006a). The user defines the solar position, a geometry of observation including the altitude, and an atmosphere, including the temperature and pressure profiles and the optically relevant trace gases abundances (O_3, NO_2 in the stratosphere). It is then possible to introduce a given absorber, its profile and cross-section and study its absorption at a given wavelength (see the two next sections).

One important difference with the description given above is the correction for the spherical shape of the atmosphere. For zenith observations, discrepancies from the plane parallel approximation can be neglected at small solar zenith angles but as some of our measurements use a limb geometry, this aspect is important. Treating the radiative transfer in full spherical geometry is possible but implies heavy computational costs. The calculations were performed instead with a common trade-off, the so-called pseudo-spherical approximation, in which the direct-light attenuation ($e^{\frac{-\tau}{\mu_0}} F_0$) is replaced by its spherical counterpart, while the other terms are treated in the plane-parallel approximation.

Beside this pseudo-spherical approximation, the assumptions in the radiative transfer are the horizontal homogeneity and the perfect coherence of the scattering (which neglects in particular the Ring effect). The model used does not take into account the polarization either. The influence of polarization on the measurements will be detailed in the next chapter.

3.3.4 Air mass factors and weighting functions

Given the possibility to reproduce numerically the radiative transfer in the atmosphere, it is easy to isolate the effect of one specific absorber, by including and removing it from the computation of the intensity. These two calculations give two corresponding intensities, I_{abs} ans I_{noabs}, which define the optical depth of the absorber. Writing the Beer-Lambert law of the scattered light enables to calculate

the slant column corresponding to the simulated atmosphere and observation:

$$SC = \frac{1}{\sigma} \ln \frac{I_{noabs}}{I_{abs}} \tag{3.26}$$

Dividing this simulated slant column by the model vertical column (VC) gives the enhancement factor due to the slant path of light in the atmosphere, commonly referred to as the Air Mass Factor (AMF):

$$AMF = \frac{SC}{VC} \tag{3.27}$$

The vertical columns from our DOAS measurements can now be retrieved, dividing the measured slant columns by their simulated air mass factors. As noted in section 3.1.3, this implies that the absorber does not significantly modify the radiative transfer because the AMF must be independent of the absorber loading. For weak absorbers like NO_2, this assumption is usually realistic. This assumption is checked for polluted conditions and limb geometry in chapter 6. It is important to realize that if the absorber absolute abundance should not matter, the shape of its vertical distribution has, on the contrary, a huge impact on the AMF, as can be seen on figure 3.6. Note that modeling the radiative transfer also enables to study the influence of other geophysical quantities on the AMF like the albedo and the visibility. Uncertainties on these parameters can thus be propagated in the error budget through their effect on the AMF. Air mass factors calculations varying several parameters are shown for the ULM-DOAS instrument on figure 6.7 and for the Mobile-DOAS on figure 7.4, where we compare it to the geometrical approximation of figure 3.6.

The AMF is useful to get a vertical column from a single measurement. However, the vertical distribution of an absorber - or of another geophysical parameter - may also be retrieved if multiple measurements are performed in different geometries. This can be done from the ground with a zenith-sky instrument using the variation of the solar zenith angles at twilight (e.g. Hendrick et al. (2004)), or varying the elevation of the telescope (e.g. Hönninger et al. (2004)). Note that these two configurations are not sensitive to the same layer of the atmosphere (respectively, to the stratosphere and the lower troposphere). The amount of information in the measurements depends then on the different sensitivity of the measurements to the altitude of the absorber. These sensitivities are expressed by the so-called weighting functions. For a vertical distribution $\mathbf{x} = x_{i=1...n}$ and given an observation geometry and an atmospheric state, the weighting function WF is expressed as:

$$WF_{i=1...n} = \frac{\partial SCD}{\partial x_{i=1...n}} \tag{3.28}$$

Weighting functions are calculated with UVSPEC-DISORT by successive perturbations on x_i in the layers of the altitude grid. In chapter 5, We retrieve profiles of extinction and NO_2 using the limb DOAS measurements during the sounding, i.e. varying the altitude of observation. Figure 5.5 presents some of the weighting functions for this kind of measurements.

A careful reader may have noticed that the above discussion missed an important point: in practice, a fitted DSCD is relative to a reference spectrum which may itself contain absorption from the measured species. Therefore, a reference column must in general be estimated and added to the result of the DOAS fit. Dealing with this reference column is done in different ways for our different experiments, using or not radiative transfer modeling. These methods are detailed in the respective chapters.

Chapter 4

Instrumental aspects in DOAS measurements

This chapter presents common aspects of the DOAS apparatus developed in this work, each instrument being presented more in detail in its respective chapter. The first section follows the light path from the input optics to the spectrometer and the detector. We give the geometrical relations along the optical axis characterizing the set-up and describe more specifically the spectrometers used. The second section characterizes the relevant properties of our instruments. This leads, in the last section, to discuss the detection threshold and how it can be optimized.

4.1 Components of DOAS instruments

4.1.1 Input optics

In most scattered-light DOAS instruments, light is collected by an optical fiber mounted behind a lens. The lens role is to reduce the field of view of the fiber. This set-up was used for all the instruments developed in this work, except the ULM-DOAS instrument presented in chapter 6, for which the fiber was directly collecting the light. A black baffle was common to all the instruments to reduce stray light. Commercial optics were used for all the instruments, so the choice in materials and size were limited to the catalogs. Nevertheless, we give some theoretical background here, useful to understand the different parts. The schematic 4.1 describes the geometry of the baffle-lens-fiber set-up.

The optical fibers of our instruments are multi-mode, step index silica. The core is made of pure silica (SiO_2) while the cladding is made of fluorine-doped silica and a polymide protective buffer. The acceptance[1] cone angle originates from Snell's

[1]Here and in what follows, we consider the full cone angles, not the half angles, which are

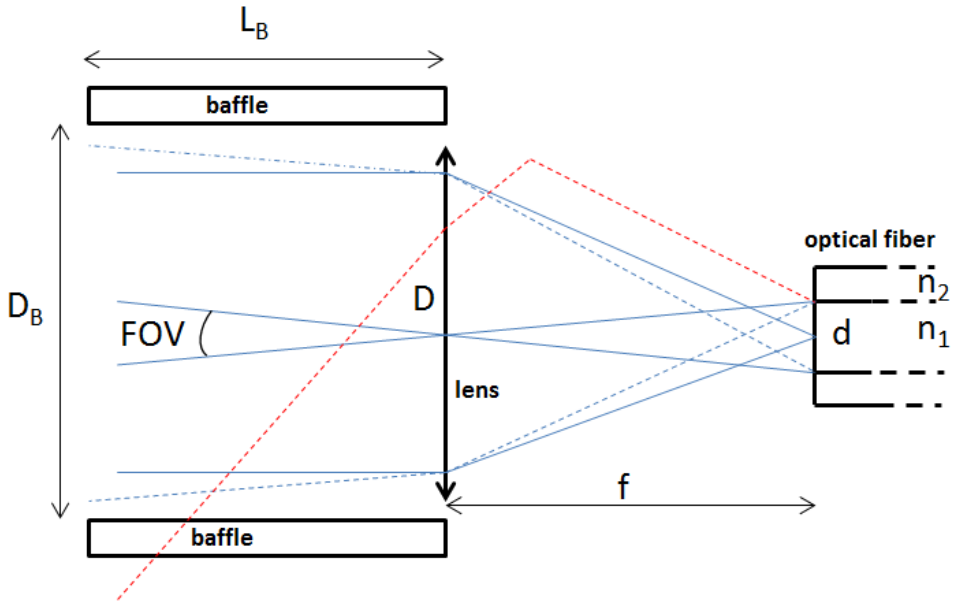

Figure 4.1: Input optics of scattered light DOAS instrument: lens, fiber, and baffle, with the relevant dimensions (see text for details). The signal light is in blue while the red line represents possible spatial stray light scattered in the housing (not shown) if no baffle is present.

law at the limit of total internal reflection, derived from the two refractive indices n_1 and n_2 of the fiber core and cladding, respectively. These numbers are not given accurately by the manufacturers. Instead, they give the numerical aperture (NA) to characterize the acceptance cone:

$$NA = n \sin \frac{\theta_{fmax}}{2} = \sqrt{n_1^2 - n_2^2} \tag{4.1}$$

In this formula, n represents the refractive index of the medium (taken as unity for air) and θ_{fmax} the acceptance cone angle. In practice, all the fibers used in our instruments have a standard numerical aperture of 0.22 ± 0.02, leading to a cone angle of 25.4°.

In scattered-light applications, the sensitivity increases with the optical path length in the atmosphere, so the lens, if present, is put at its focal length (f) in front of the fiber to collect a parallel beam of its diameter (D). The cone angle (θ_{lmax}) of light behind the lens is thus:

also often used.

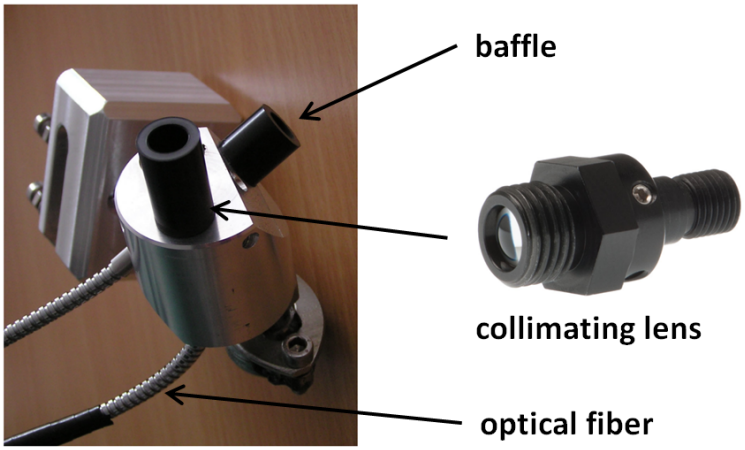

Figure 4.2: Optical head of the Mobile-DOAS instrument (left) and Avantes collimating lens (right).

$$\theta_{lmax} = 2 \arctan \frac{D}{2f} \tag{4.2}$$

This cone angle should be at least as large as the acceptance cone angle of the fiber to optimize the signal.

The field of view (FOV) of a naked fiber is simply its acceptance cone angle. With a lens, it is considerably reduced and given by the focal length (f) and the fiber diameter (d):

$$FOV = 2 \arctan \frac{d}{2f} \approx \frac{d}{f} \tag{4.3}$$

As illustrated in figure 4.2, light originating from outside the theoretical field of view can be scattered in the collimating optics, e.g. through reflections on metallic parts. This light is dispersed with the signal light by the grating. We refer to this as spatial stray light, contrasting with the spectral stray light due to the spectrometer (Gottwald and Bovensmann, 2011). Spatial stray light modifies the expected light path, leading to problems in the interpretation of the slant columns densities. Moreover, if the spectral characteristics of the sources of signal and stray light are different, the measured spectrum is distorted. Black baffles, either in plastic or in paperboard, were added in front of the lens or directly on the fiber for the ULM-DOAS. The field of view (θ_B) limited by the baffle is:

$$\theta_B = 2 \arctan \left(\frac{D_B - D}{2L_B}\right) \tag{4.4}$$

where D_B is the baffle diameter, L_B its length, and D the lens diameter. The baffle should not hide part of the beam ($\theta_B > FOV$). In practice, most of the spatial stray light is removed with a small baffle.

Figure 4.2 illustrates the different elements of the input optics with the optical head of the Mobile-DOAS (chapter 7). The lens used in both channels is shown on the right with its housing: it is a commercial collimating silica lens from Avantes, with a 6 mm diameter and a 8.7 mm focal length. Black baffles (internal diameter: 9 mm, length: 2 cm) are screwed on one end of the lens housing, while the 400 μm optical fibers are attached on the other end through the SMA connectors. These dimensions lead to instrument and baffle fields of view of respectively 2.6° and 8.5°. The housing are held by a custom aluminium structure manufactured in our workshop, enabling to attach itself to a car window and align the channels accurately with the ball-joint. Figure 5.2 shows the baffle and fiber of the ALS-DOAS instrument.

4.1.2 Grating spectrometer

The acceptance angle of a spectrometer can be quite different from the one of the fiber, as is the case for the ALS-DOAS instrument. It is usually expressed as a f-number. For a lens of focal length f and diameter D, the f-number($f/\sharp$) is simply the ratio f/D. From equations 4.1 and 4.2 and taking unity for the refractive index of air, the f-number can be related to the numerical aperture and the acceptance cone as:

$$NA = \sin \arctan \frac{1}{2f/\sharp} = \sin \frac{\theta_{fmax}}{2} \tag{4.5}$$

For a spectrometer, the entrance f-number is calculated from the focal length of the first mirror (f_1) and an equivalent diameter as seen from the entrance slit. This equivalent diameter, D', is expressed from the width (W_g) and height (H_g) of the grating and from the incidence angle of the incoming light (α) as (Lerner and Thevenon, 1998):

$$D' = 2\sqrt{\frac{W_g H_g \cos\alpha}{\pi}} \tag{4.6}$$

Note that the angle of diffraction is different from the angle of incidence and that the second focusing mirror in the spectrometer may have another focal length. This leads to a different f-number for the spectrometer as seen from the detector.

In the ALS-DOAS instrument used during POLARCAT (chapter 5), the f-number of the spectrometer is $f/4$, corresponding to an acceptance angle of 14.3°, much smaller than the fiber divergence of 25.4°($f/2$). The loss of brightness is

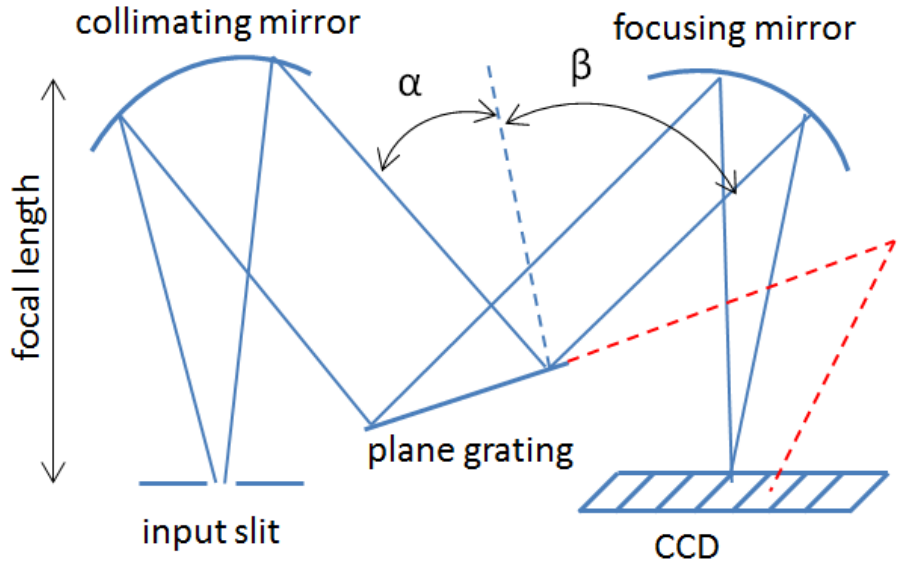

Figure 4.3: Czerny-Turner set-up. The dashed red line represents spectral stray light originating for instance from the second order of diffraction and scattered in the (not shown) housing.

proportional to the square of the ratio of the f-numbers (Platt and Stutz, 2008), which implies that 75% of the fiber light would not reach the grating and could be source of stray light inside the spectrometer. Such stray light is referred to a spectral and its effects are different than the spatial stray light discussed above. Spectral stray light corresponds to light of a given wavelength scattered to a detector pixel corresponding to another wavelength (see figure 4.3). It deteriorates the spectra leading to problems in the DOAS analysis. Therefore a f-number matcher was added between the input optics and the spectrometer, seen in figure 4.4.

The matcher set-up looks like the inside of a Newtonian telescope working backwards. The fiber light is reflected by a small off-axis 45° plane mirror toward a concave mirror which reduces the cone of light to match the f-number of the spectrometer.

From the mirror equation, we can express the angles of input (θ_f) and output (θ_s) of the f-number matcher as a function of the illuminated part of the mirror (D_m) and its focal length (f_m):

$$\frac{D_m}{2f_m} = \tan\frac{\theta_f}{2} + \tan\frac{\theta_s}{2} \tag{4.7}$$

The grating spectrometers used in all our instruments are based on the popular

Czerny-Turner set-up, shown in figure 4.3. This configuration uses two concave mirrors and a plane reflective diffraction grating. The first mirror collimates the light coming from the input slit towards the grating. The grating disperses the light according to the wavelengths and the second mirror focuses this spectrum on the detector.

The fundamental equation of gratings is:

$$\sin\alpha + \sin\beta = kn\lambda \tag{4.8}$$

where λ is the wavelength of the light, α and β are respectively the incidence and diffraction angles, which are illustrated in figure 4.3, k is the order of diffraction and n is the groove density of the grating.

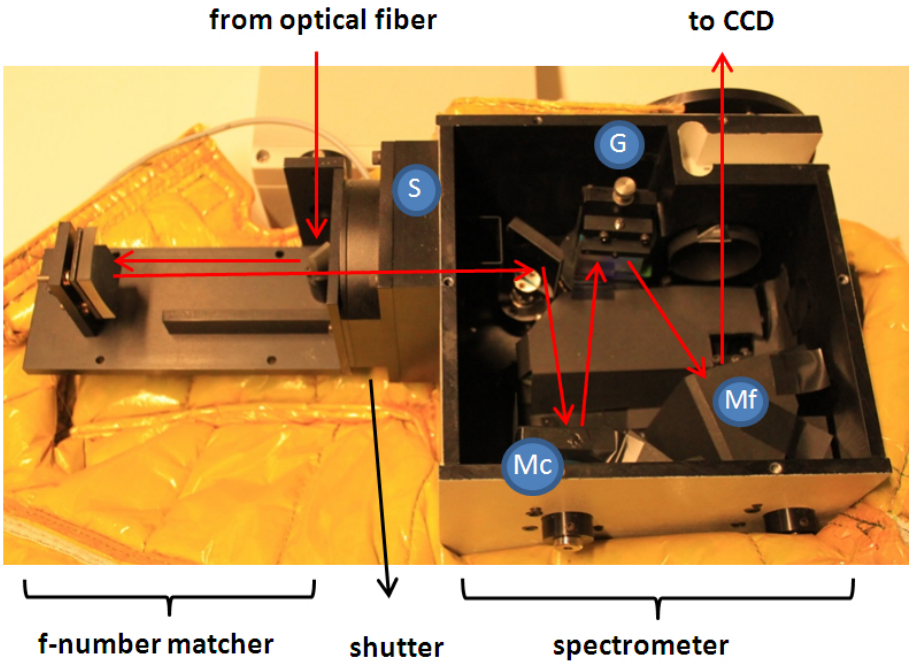

Figure 4.4: ARC spectrometer and matcher used for the POLARCAT campaign. The red lines represent the optical path inside the instrument. The complete instrument onboard the plane is shown in figure 5.2.

From equation 4.8, the angular dispersion $(d\beta/d\lambda)$ may be calculated. It is converted with the focal length of the second mirror (f_2) to a linear dispersion $(dx/d\lambda)$ where x is the position on the focal plane of the second mirror. Its inverse, the reciprocal linear dispersion $(d\lambda/dx)$ is more useful in practice:

$$\frac{\mathrm{d}\lambda}{\mathrm{d}x} = \frac{\cos\beta}{knf_2} \tag{4.9}$$

The spectral resolution of the spectrometer, defined by its bandpass, is the product of the linear dispersion and the image of the entrance slit width (Lerner and Thevenon, 1998). The image of the entrance slit width (W') is, given its object width (W) and the previously defined parameters:

$$W' = W\frac{\cos\alpha}{\cos\beta}\frac{f_2}{f_1} \tag{4.10}$$

This leads to the following expression for the bandpass (BP):

$$BP = \frac{W\cos\alpha}{f_1 kn} \tag{4.11}$$

This equation expresses that the bandpass increases with the slit width. The latter being directly related to the amount of light received at the detector, the optimal slit width is a trade-off between the resolution and light requirements. Equation 4.11 also indicates that it is difficult to achieve a high spectral resolution with compact grating spectrometers, whose size is determined by their mirror focal lengths.

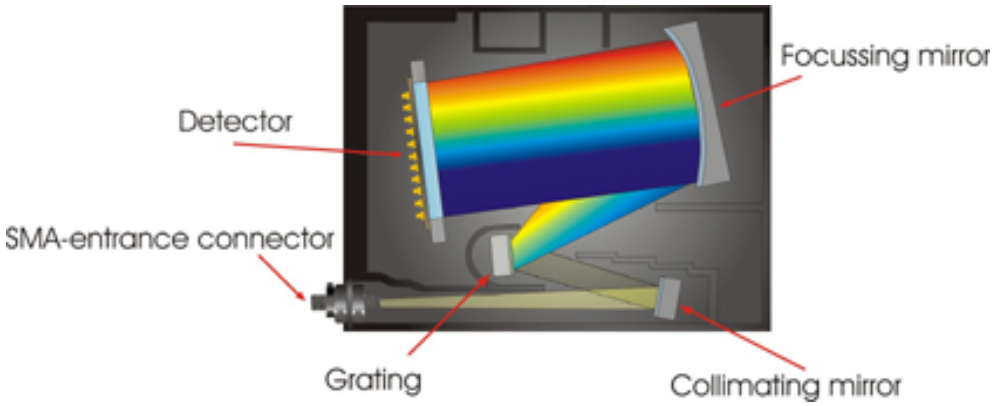

Figure 4.5: Schematic of the Avantes spectrometer used for ULM-DOAS, Mobile-DOAS, and SWING, from `www.avantes.com`.

Figures 4.4 and 4.5 show the two different Czerny-Turner spectrometers used respectively in the ALS-DOAS instrument (chapter 5) and in the three more compact instruments developed later on (chapters 6, 7, and 8). They illustrate in particular the flexibility of the Czerny-Turner configuration, due to the use of two separate mirrors. Note that for the ALS-DOAS, the theoretical bandpass from

equation 4.11 corresponds to 0.5 nm, which is confirmed by measurements with a Hg-Cd lamp (figure 4.8).

4.1.3 CCD and CMOS detectors

Two kinds of digital detectors are currently used in digital imaging: Charge Coupled Device (CCD) and Complementary Metal Oxide Semiconductor (CMOS). Both of them are based on linear or matrix arrays of metal oxide semiconductors (MOS). These MOS pixels convert individually incoming photons into electric charges through the photoelectric effect. The process is characterized by its quantum efficiency, defined as the percentage of photons that create charges. The difference between CCD and CMOS lies is the way the charges are read, as illustrated in figure 4.6. In a CCD, the charges are sequentially transferred across the pixels to a unique charge-to-voltage converter, while in a CMOS, this conversion is achieved for each pixel separately.

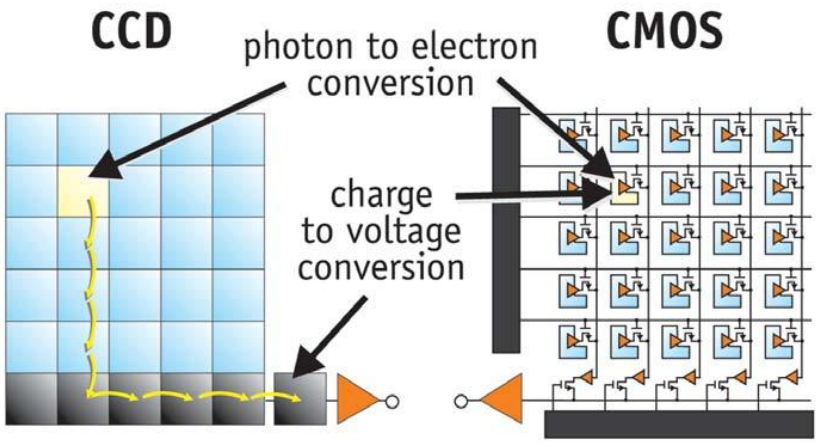

Figure 4.6: CCD and CMOS principles, from Litwiller (2005).

In addition, CCD and CMOS sensors can either be front or back-illuminated. The two configurations are shown for a single pixel on figure 4.7, which also shows the MOS set-up. In the front-illuminated design, light enters the CCD through the 'M' part of the MOS (Aikens et al., 1989), usually made of polycrystalline silicon. This material is relatively transparent in the visible but opaque under 400 nm. Therefore, a better set-up for UV applications is to receive light directly from the 'S' part of the MOS, where the charges are kept. This back-illuminated configuration has a better quantum efficiency, especially in the UV.

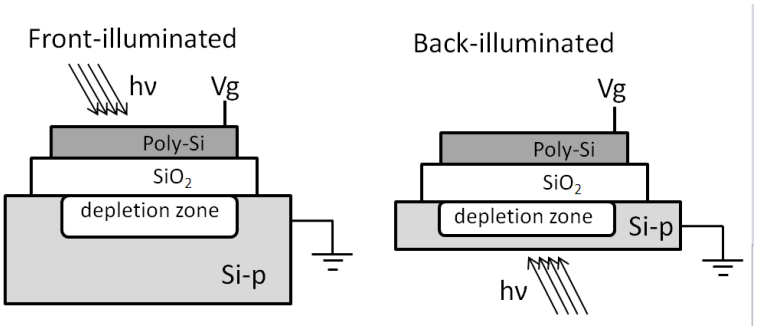

Figure 4.7: CCD: front and back-illuminated configurations.

The detectors in our instruments are all CCDs. An ultra-compact spectrometer using a CMOS, the Ocean Optics STS (f = 28 mm), was tested for the UAV experiment. Its sensitivity is not compatible with this application, which requires very short integration time. The CCD used in the ALS-DOAS instrument (chapter 5) is a back-illuminated matrix (2048×512) while in the Avantes spectrometer it is a linear array of 2048 pixels.

An important characteristics of a detector is its signal-to-noise ratio. The most fundamental source of noise in counting photons originates from the quantum nature of light and is thus independent of the quality of the detector. This shot noise is analytically described by a Poisson distribution on the number of detected photons (N), leading to a standard deviation of $\sqrt{N}$. Considering a perfect detector measuring N photons, its signal-to-noise-ratio (SNR_{shot}) is thus:

$$SNR_{shot} = \frac{N}{\sqrt{N}} = \sqrt{N} \tag{4.12}$$

Working with a CCD, two other sources of noise can be important. First, the dark noise arises from electrons thermally generated inside the CCD. Their number also follows a Poisson distribution and this source can be reduced by cooling the detector, as is done for the PIXIS of the ALS-DOAS. Secondly, the read noise arises from the charge-to-voltage and analog-to-digital conversions. This sources depends on the quality of the electronics, in particular the pre-amplifier. The signal-to-noise ratio for a CCD (SNR_{CCD}) is expressed as:

$$SNR_{CCD} = \frac{IQ_E t}{\sqrt{IQ_E t + Dt + N_r^2}} \tag{4.13}$$

where I is the incident photon flux (photons/pixel/second), Q_E is the quantum efficiency, t is the integration time(seconds), D is the dark current value

(electrons/pixel/second), and N_r is the read noise (electrons rms/pixel) (`http://learn.hamamatsu.com/articles/ccdsnr.html`).

In practice, if the signal is high enough, the shot-noise often dominates the two other sources. In this case, the measurement is said photon-noise limited. This assumption is used for the simulations shown in figure 8.3.

Table 4.1: Characteristics of the different spectrometers

	ARC+Pixis	Avantes	STS
Czerny turner design	Astigmatism-Corrected	Symmetrical	Asymmetric crossed
Focal length (mm)	150	75	28
Slit (μm)	100	50	25
Lines/mm	1200	600	600
Blaze(nm)	300	300	n/a
Size (mm^3)	320x160x160	175x110x44	40x42x24
Weight (g)	4500+2270	716	68
Wavelength range (nm)	330-450	200-750	350-800
Resolution (FWHM in nm)	0.5	1.3	2.3
f-number	f/4	n/a	n/a
Detector type	Back thinned 2D CCD	Linear CCD	Linear CMOS
Number of pixels	2048x512	2048	1024
Sampling ratio (pixels)	6	4.9	5.2
Pixel size (μm)	13.5x13.5	14x56	7.8x125
A/D resolution (bits)	16	16	14
Cooling	Thermoelectric, up to -75°	no	no

4.2 Characterization

4.2.1 Calibration, instrument function, and sampling ratio

The calibration means here the relationship between the detector pixels and the wavelength. For commercial spectrometers like the Avantes, it is usually given rather accurately by the manufacturer. It was nevertheless characterized for the different spectrometers using the emission lines of a Hg-Cd lamp. This first calibration is refined during the spectral analysis with QDOAS using the Fraunhofer lines. The software aligns the spectrum with respect to a calibrated solar spectrum (Kurucz, 1995) convoluted at the resolution of the instrument. The process is similar to the slant column fitting described in the previous chapter. It uses a Levenberg-Marqardt iteration in which the shift between the solar and measured spectrum is fitted as a non linear parameter. It is possible to fit at the same time the spectral resolution using a predefined instrument function, e.g. a Gaussian profile. Note also that in QDOAS, several sub-windows are defined inside the spectrum. A value of the shift is fitted in each sub-window and these values are fitted a second time as a polynomial to reconstruct an accurate wavelength calibration(Fayt et al., 2011).

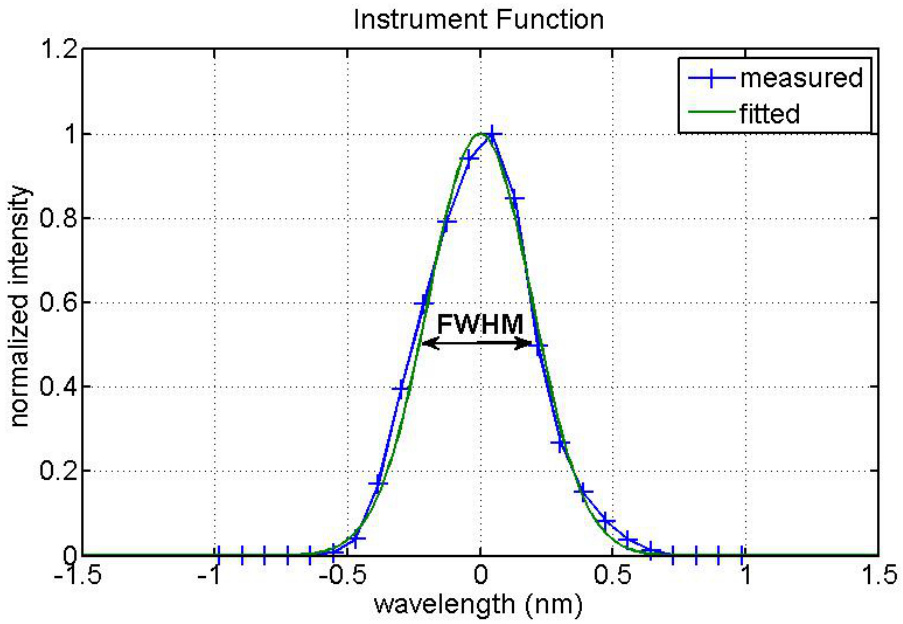

Figure 4.8: Instrument function of the ALS-DOAS instrument measured with an Hg-Cd lamp at 404.7 nm and fitted as a Gaussian using QDOAS. The crosses in the measured function indicate the pixel centers.

Figure 4.8 shows the instrument function of the ALS-DOAS instrument measured with the 404.7 nm line of a Hg-Cd lamp and fitted as a Gaussian with QDOAS. This second solution was used for the DOAS analysis because the bandpass increased towards the UV (from 0.5 nm to 0.7 nm FWHM), probably due to a small misalignment. The instrument function of an Avantes spectrometer (1.3 nm FWHM) may be seen in figure 6.5 of chapter 6.

The sampling ratio is also visible on figure 4.8. It is defined as the number of pixels inside the bandpass of the instrument, 5.8 in this case. The sampling ratio originates from the sampling theorem and determines the ability of the discrete pixels of the CCD to reproduce the spectral information. For a Gaussian instrument function, the minimum sampling ratio should be 4.5 to avoid undersampling and associated problems in the spectral analysis (Chance et al., 2005). It is obvious that the sampling ratio (S) may be roughly estimated with a typical bandpass (BP), the number of pixels of the detectors (nb_{pix}), and the total spectral range (R) as:

$$S = BP\frac{nb_{pix}}{R} \tag{4.14}$$

Using this equation and the values of table 4.1, the sampling ratio of the Avantes and STS spectrometers are respectively 4.9 and 5.2.

4.2.2 Dark current, offset, and spectral stray light

To optimize the DOAS analysis, it is necessary to subtract from the recorded spectrum a component, which is not part of the signal. This bias includes several contributions: a fixed offset tuned by the CCD manufacturer to avoid negative value for pixels, the dark current originating from thermal creations of electron-hole pairs (see section 4.1.3), and possible spectral stray light (see section 4.1.2).

In theory, the first two sources of bias are easily determined from the datasheet and the temperature. In some applications, the dark-current for a given measurement is estimated by a CCD acquisition of the same integration time with the shutter closed. For the third source of bias, an accurate characterization and correction method was proposed by Zong et al. (2006). It consists first in recording at successive wavelengths the so-called spectral line-spread function, i.e., the response across the pixel to a monochromatic excitation, which is a tunable laser in Zong et al. (2006). The second step involves the building of a correction matrix from the line-spread functions measurements.

We have implemented the method of Zong et al. with a Bentham double monochromator and a broadband source. Figure 4.9 is an example of line-spread function (LSF) measured with this set-up. In particular, our work has consisted in the automation of the LSF measurements, which take a lot of time. Indeed, each

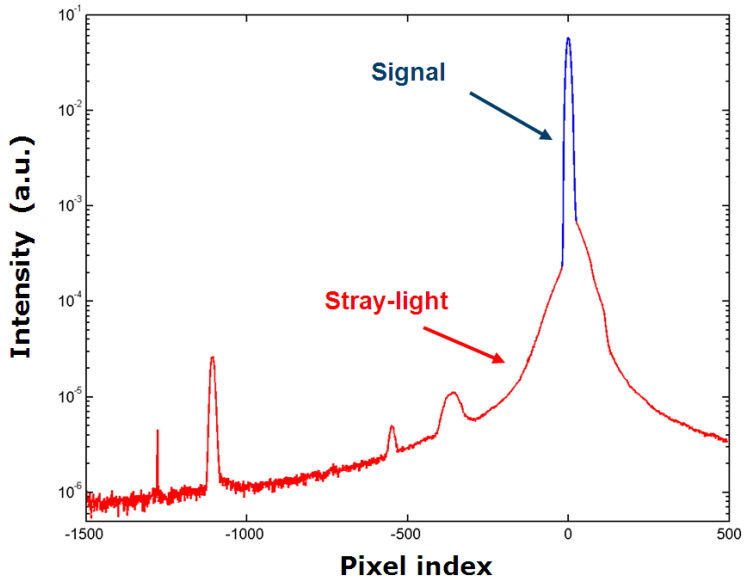

Figure 4.9: Spectral stray light measurements in the lab with a double monochromator: example of line-spread function.

LSF is reconstructed from four measurements, including a saturated version to increase the signal away from the nominal wavelength and the dark currents. Unfortunately, the offset on the ALS-DOAS CCD was found to be too much unstable and the stray-light matrix did not improve the DOAS fits.

The biases in the spectra were thus pragmatically corrected using an average CCD values in the most UV section of the spectra and assuming it constant across the spectral range. For the Avantes spectrometer, assuming no signal in the region below 250 nm (see figure 4.10) is justified from the oxygen and ozone absorption. For the ALS-DOAS, the bias was estimated from the signal between 332 and 335 nm where the BK7 port (see figure 5.2) is almost opaque.

4.2.3 Polarization response

The instrument polarization sensitivity can be a source of problems in DOAS instrument. The scattered sky light is polarized differently with respect to the position of the sun. Inside the instrument, the grating efficiency is highly sensitive to the polarization state. If the resulting structure is smooth, it is filtered out by the polynomial in the DOAS fit. But any grating presents Wood's anomalies, which are sharp polarization dependent discontinuities in the grating efficiency (Stewart and Gallaway, 1962). If a Wood's anomaly falls within a fitting window,

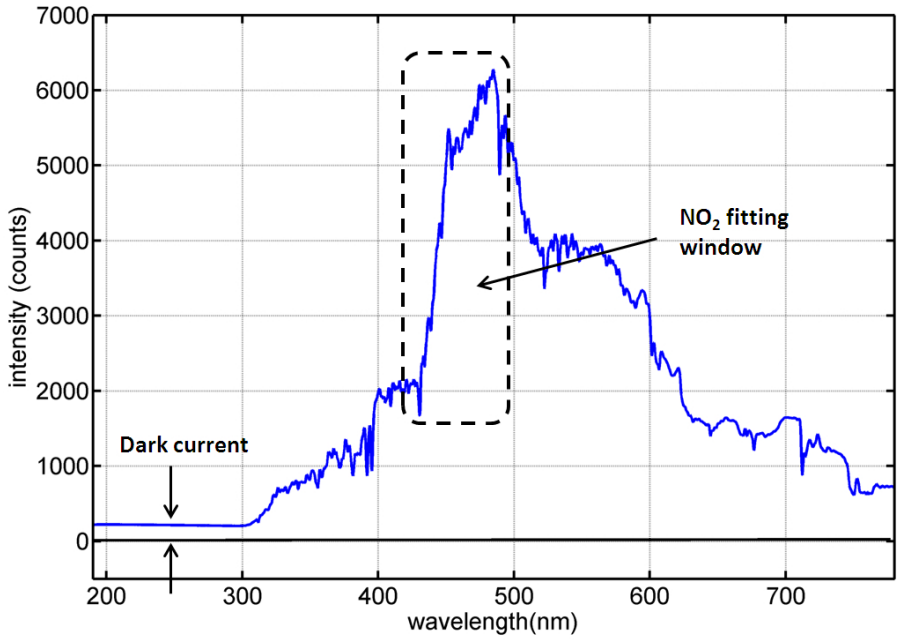

Figure 4.10: Typical spectrum of scattered sky light as recorded by the Avantes spectrometer. The signal between 200 and 250 nm is used to estimate the bias.

it must be properly taken into account (see McLinden et al. (2002) for a discussion about the effect of polarization on the OSIRIS instrument).

Regarding the instruments used in this thesis, the polarization sensitivity is reduced by the use of the optical fibers, which act as polarization scramblers. Figure 4.11 shows the spectrum of a halogen lamp recorded with the Avantes spectrometer. There seems to be a Wood's anomaly between 600 and 630 nm, but it is well outside the NO_2 fitting window (see figure 4.10). Nevertheless, to ensure that no polarization effect would affect the measurements, we have investigated the sensitivity to polarization in the lab with a Wollaston prism. For the ULM-DOAS, this characterization is shown in our reply to the referee comments (`www.atmos-meas-tech-discuss.net/5/C1445/2012/`). It indicates that the differential structures introduced by the polarization sensitivity are inferior to 4 per mil with the 5 m fiber. For the SWING instrument however, the fiber is only 25 cm long so the polarization problem is worth considering. Preliminary tests seem to indicate that the polarization sensitivity remains acceptable but further investigations are necessary to quantify it accurately. Note that if the polarization structures are not correlated with the NO_2 cross section, they can be accounted for as the Ring effect, by treating them as a pseudoasbober.

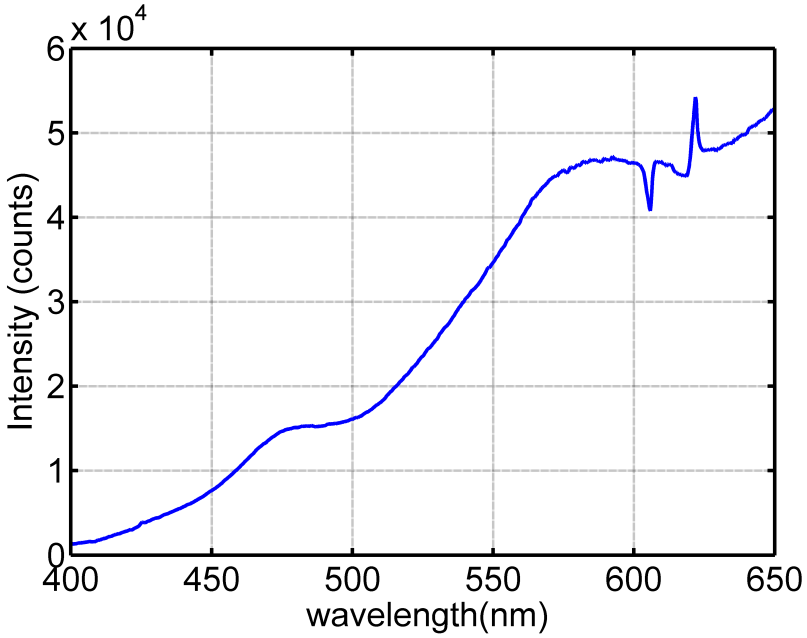

Figure 4.11: Spectrum of a halogen lamp as recorded by the Avantes spectrometer. The structures between 600 and 630 nm are probably Wood's anomalies but they are outside the fitting window of NO_2.

4.3 Detection limit and optimal spectral resolution

In a DOAS measurement, the detection threshold is determined by the root mean square deviation of the residual (RMS). If no systematic structure appears in the residual, the RMS indicates the standard deviation (σ) of a Poisson distribution corresponding to the photons measured in the fitting window. For an absorber to be clearly identified, its fitted differential optical depth (the signal) must therefore be larger than the RMS (the noise). Depending upon the used definition used for the detection threshold (1-σ, 2-σ), a multiple of the RMS is propagated to a differential slant column density by dividing it with the value of a differential cross section. The corresponding minimum vertical column can then be estimated with the air mass factor. This is done in chapter 5 for the NO_2 inside the maritime boundary layer measured by the ALS-DOAS instrument.

A related problem consists in choosing the optimal spectral resolution to detect an absorber. As explained in section 4.1.2, there is a trade-off between the resolution and the amount of light collected, because they both depend on the slit width but in opposite way. This trade-off is important for DOAS measurements. On the

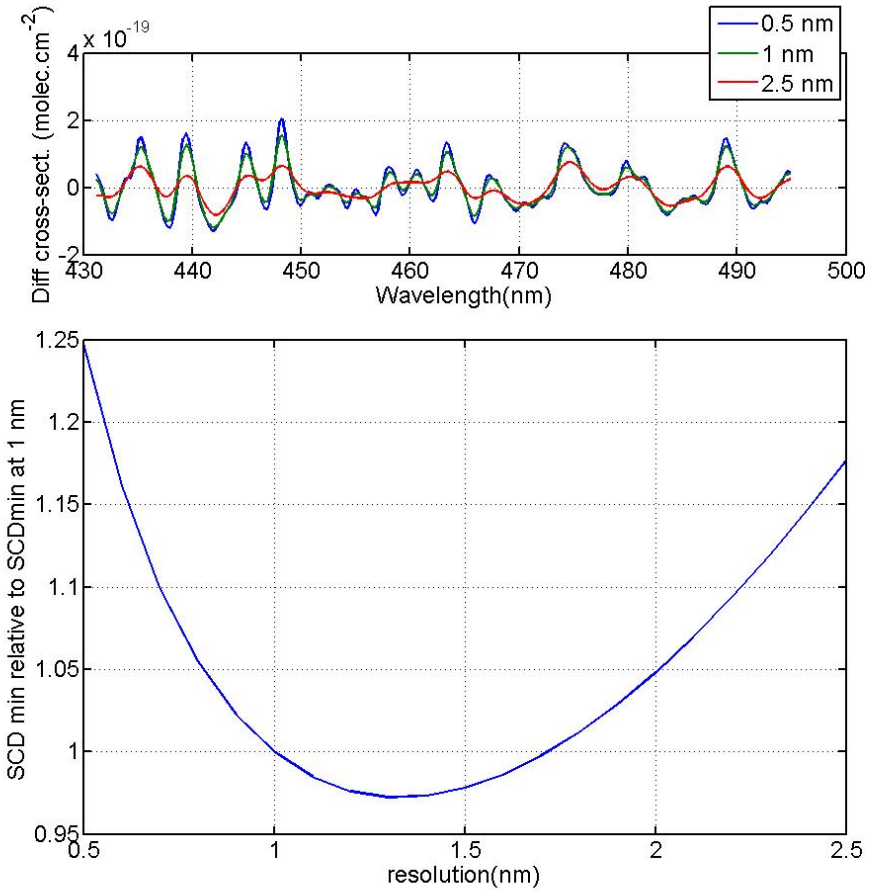

Figure 4.12: Investigations on the optimal spectral resolution to detect NO_2.

one hand, a wider slit enables to measure more photons and thus to improve the signal-to-noise ratio (equation 4.12). On the other hand, the associated broadening of the bandpass (equation 4.11) reduces the differential structures in the spectra and thus the signal-to-noise ratio, as discussed in the previous paragraph.

Let us consider how the NO_2 detection threshold varies with the slit width relatively to a bandpass base value of 1 nm. Multiplying the slit width by α leads to the same factor α for the number of detected photons. Assuming a photon noise limited situation[2], the signal-to-noise ratio is thus increased by $\sqrt{\alpha}$. The effect of α is analytically more complicated for the cross section. To estimate it, the NO_2 cross section is convoluted at various resolutions around 1 nm. Secondly,

[2]In practice, the signal on each pixel follows a different Poisson distribution

the values of the convoluted cross section are plotted against the reference 1 nm cross section. It is then possible to fit a slope which represents the change in the amplitude of the differential structures. This method has the advantage that all the points inside the fitting window are taken into account. Ordering the slopes against α gives thus the variation of the signal-to-noise ratio due to the differential structures, $F(\alpha)$. The resulting equation of the detection threshold (D_t) is thus:

$$D_t = \frac{1}{F(\alpha)\sqrt{\alpha}} \tag{4.15}$$

Figure 4.12 presents the results with three versions of the NO_2 cross section at different spectral resolution. The minimum is at 1.3 nm which is fortunately the resolution of the Avantes spectrometer. Note that Peng et al. (2008) did a similar exercise for DOAS measurements of monoaromatic hydrocarbons. They use a different approach based on the assumption that the throughput varies with the square of the spectral resolution. It seems to us, following Lerner and Thevenon (1998), that this assumption is only valid in the cases when the slit is circular or the CCD pixels are binned.

Chapter 5

Airborne DOAS measurements in Arctic: vertical distributions of aerosol extinction coefficient and NO_2 concentration

Writing about the future of technology, von Neumann (1955) described, together with the greenhouse effect of CO_2, a method to control the climate: by spreading "microscopic layers of colored matter" on the icy surfaces of the poles, the albedo would be reduced and hence more solar energy would be available to warm the ground. In fact, the process was already ongoing in the 1950s, but unintentionally through the transport of pollution. This was understood later on from the early observations of Arctic haze in Alaska (Mitchell, 1957).

This chapter presents the Airborne Limb Scanning-DOAS and its contribution to the Polar Study using Aircraft, Remote Sensing, Surface Measurements and Models, of Climate, Chemistry, Aerosols, and Transport (POLARCAT) international field campaign in April 2008. It is based on a study published in the POLARCAT special issue of the Atmospheric Chemistry and Physics.

5.1 Geophysical context and previous airborne DOAS experiments

Despite its remoteness, the Arctic troposphere is affected by trace gases and aerosols emissions from mid-latitude regions. The Arctic Haze phenomenon is a visible manifestation of this long-range transport (Shaw, 1995). The effects of this pollution are specific to the area and may explain part of the enhanced warming observed there. Indeed, the dry arctic air makes the area more sensitive to

non-water-vapor greenhouse gases' increase. Furthermore, above the high-albedo snow and ice surfaces, aerosols - even if only weakly absorbing - can lead to a warming, contrary to their global cooling effect (Law and Stohl, 2007, and references therein). Climate change may further modify the arctic tropospheric composition. For instance, if the summer sea ice continues its decline, ship traffic through the Northern passages will become an important source of aerosols and NO_x, the latter also driving an increase in tropospheric ozone (Granier et al., 2006). Quantifying such phenomena requires an accurate knowledge of the Arctic troposphere, which motivates dedicated airborne missions.

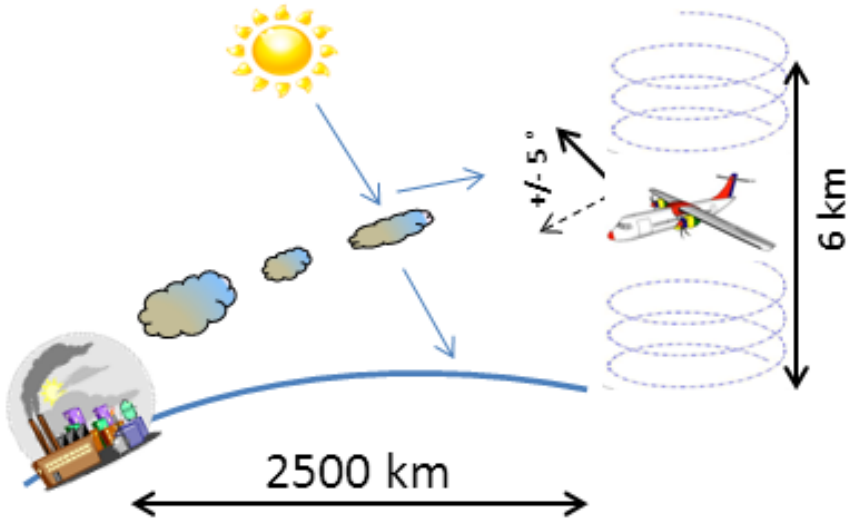

Figure 5.1: Principle of the ALS-DOAS measurements during the POLARCAT campaign.

Differential Optical Absorption Spectroscopy (DOAS) has been widely used for atmospheric research (Platt and Stutz, 2008). First applied to the retrieval of stratospheric gas columns using zenith-sky observations of solar scattered light, the technique has been recently extended to the detection of tropospheric gases by means of observations along multiple viewing directions (Multi-Axis DOAS; Hönninger et al. (2004)). Such measurements also yield information on the vertical distribution of the gases (Wittrock et al., 2004). The possibility to extend this profiling technique to aerosol extinction was demonstrated (Wagner et al., 2004; Frieß et al., 2006) and implemented by several groups (Irie et al., 2008; Clémer et al., 2010a). The approach uses the $(O_2)_2$ collision complex, referred to hereafter

as O_4, which has strong absorption bands in the UV-Visible range. Aerosols affect DOAS measurements of any absorber by modifying the light path but the effect can be isolated for O_4 since its vertical distribution is well-known. The vertical resolution retrieved from the ground-based measurements remains poor however; typically two independent layers can be retrieved close to the surface and only little information in the free troposphere. On the other hand, satellite-borne instruments using UV-visible limb radiance measurements date back to the Solar Mesosphere Explorer (SME, Mount et al. (1984)). This geometry provides a good vertical resolution in the stratosphere, but for tropospheric studies from satellites, nadir-looking instruments have to be used, such as the Ozone Monitoring Instrument (OMI, Levelt et al. (2006)), which are only sensitive to the total tropospheric column. A way to overcome this limitation relies on operating a DOAS instrument from aircraft, combining the multi-axis measurements at different altitudes. The Airborne Multi-Axis DOAS (AMAXDOAS) instrument, recording simultaneously scattered-light spectra at different angles from an airplane, has already measured NO_2 vertical distributions (Bruns et al., 2006) in a polluted region. Prados-Roman et al. (2011) have used another airborne set-up with a single line-of-sight, parallel to the ground, and derived BrO Arctic profiles from the ascent of the aircraft. The instrument developed in this work, namely the Airborne Limb Scanning DOAS (ALS-DOAS), combines the two set-ups with a single line-of-sight scanning the horizon continuously. Its observation geometry is illustrated in figure 5.1.

The next section describes the technical aspects of the ALS-DOAS instrument and its operation on the Safire ATR-42 during the POLARCAT-France spring campaign. The methods used for the data analysis, i.e. the DOAS settings, radiative transfer modeling, inversion schemes and error budget are presented in section 5.3. These methods are applied in section 5.4 to two soundings performed during the flights on 8 and 9 April 2008. Retrieved extinctions are compared with Mie-scattering calculations performed on aerosol size distributions measured in situ. In section 5.5, these results are interpreted using ancillary measurements of CO and ozone mixing ratios, as well as backward trajectories calculations.

5.2 The ALS-DOAS instrument and its operation during a POLARCAT campaign

5.2.1 Instrumental description

The Airborne Limb Scanning DOAS (ALS-DOAS) was developed at BIRA-IASB in the framework of this thesis and first used during the POLARCAT campaign. Based on a grating spectrometer, it records limb-scattered sky light spectra at several angles around the horizon, following the Multi-Axis DOAS (MAX-DOAS)

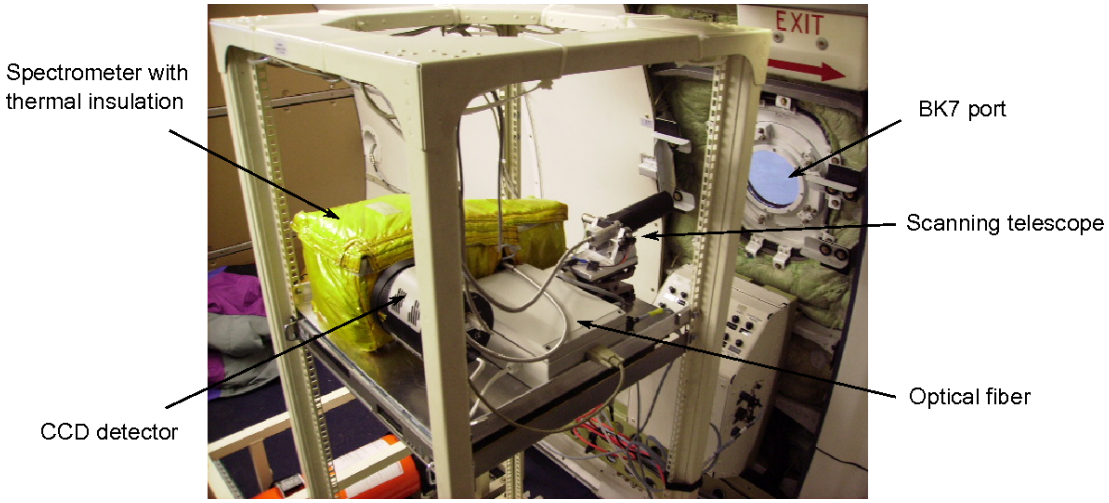

Figure 5.2: The Airborne Limb Scanning Differential Optical Absorption Spectrometer (ALS-DOAS) onboard the Safire ATR-42 aircraft. A scanning telescope collects scattered sky-light at different angles near the horizon, this light being transmitted through an optical fiber to a grating spectrometer. A CCD detector is used to record the spectra. See text for technical details.

principle (Hönninger et al., 2004).

Figure 5.2 shows the ALS-DOAS installed in the SAFIRE ATR-42 aircraft. The entrance optic is composed of a 1° field-of-view telescope focusing the light into an optical fiber. A 5-cm black paperboard baffle limits the stray light at the entrance of the telescope. This telescope, standing behind a BK-7 glass port, is mounted on a stepper-motor axis and scans continuously between -5° and 5° by steps of 1°. Between the fiber and the spectrometer, a Jobin Yvon optical interface matches the fiber and spectrometer numerical apertures. The spectrometer is a SpectraPro-150 (imaging Czerny-Turner set-up, 150 mm focal length) from Acton Research Corporation, with a 100 μm entrance slit. The spectral range is 330-450 nm, with a resolution of 0.4 nm full width at half maximum (UV) to 0.6 nm (visible). A custom Terimide 7 thermal insulation limits the thermal effects on the spectrometer and the matching interface. The detector, a back-illuminated Pixis CCD 2048*512 pixels^2 from Princeton Instruments, is cooled to -50 °C to increase the signal-to-noise ratio on the spectra. The whole set-up including the computer is mounted on a 19-inch (482.6 mm) rack. While measuring, the CCD integration time is automatically adjusted to optimize the signal, typically between 0.4 and 1.3 seconds. Each measurement represents a 30 s average at a certain telescope angle. The acquisition is controlled automatically and the instrument does not need an operator onboard.

Several tropospheric molecules absorb light in the spectral range of our instrument and thus are potentially detectable: O_3, NO_2, HCHO, CHOCHO, O_4, IO and BrO. During the campaign, O_4 and NO_2 were most clearly identified. In addition, O_3 was visible in the DOAS analysis, but attempts to isolate its tropospheric contribution were unsucessful. Similarly, the presence of IO in the low altitude spectra was investigated but no clear conclusions could be drawn.

5.2.2 The POLARCAT-France spring campaign

The POLARCAT-France spring campaign was part of the POLARCAT international research activity (Polar Study using Aircraft, Remote Sensing, Surface Measurements and Models, of Climate, Chemistry, Aerosols, and Transport), in the framework of the International Polar Year (IPY). Based in Kiruna, Sweden (68°N, 20°E), the Safire ATR-42 aircraft performed twelve scientific flights between continental Norway and Svalbard between 30 March and 11 April 2008. Scientific objectives of the campaign included the study of pollution transport, aerosol/cloud interactions and satellite validation. Various flight patterns were achieved in different weather conditions to fulfill these different research requirements. The aircraft's payload included remote sensing (e.g. Lidar, Radar) and in situ instruments (e.g. aerosol sampler, cloud particle imager). In section 5.4, the aerosol size distributions measured by the Scanning Mobility Particle Sizer (SMPS, (Villani et al., 2008)) and by the Passive Cavity Aerosol Spectrometer Probe (PCASP 100-X DMT) aboard the Safire ATR-42 are used to calculate aerosol extinctions and compared with our retrievals. Together the instruments cover the size range between 0.02 and 3 μm. Section 5.5 also presents ozone and CO profiles from the MOZART instrument (Nédélec et al. (2003), Ancellet et al. (2009)) and attenuated backscatter ratio profiles at 532 nm and 1064 nm measured with the Lidar as described in de Villiers et al. (2010).

The ALS-DOAS instrument recorded spectra continuously during the campaign, except during the flight as0829 (7 April 2008) due to a computer problem. This study focuses on the data collected during two soundings on 8 (flight as0831) and 9 April 2008 (flight as0833), respectively at 71°N, 22°E and 70°N, 17.8°E. Figure 5.3 displays these flight tracks and the position of the soundings. During the first sounding, the plane was first flying at 6 km then started a spiral descent (between 9h35 and 9h59 UTC), and reached the marine boundary layer where it continued with a level flight at 300m. The sky was then cloud-free around the plane, which simplifies the radiative transfer calculations and reduces considerably the uncertainties in the results. During the second sounding, the plane, flying at 5 km altitude, started its descent at 9h44 UTC and reached its lowest altitude (250 m) at 10h04. Some clouds were present close to the sea surface.

Figure 5.3: Tracks of the flights as0831 (8 April 2008) and as0833 (9 April 2008) of the POLARCAT-FRANCE Spring campaign. Two soundings are studied in this work, respectively at 71°N, 22°E and 70°N, 17.8°E.

Table 5.1: DOAS analysis settings for the ALS-DOAS.

	O_4	NO_2
Fitting window	340-370 nm	415- 446 nm
O_4	Hermans (see text)	Ibid.
NO_2	Bogumil et al. (2003)	Ibid.
O_3	Bogumil et al. (2003)	Ibid.
H_2O	-	Harder and Brault (1997)
Ring	Chance and Spurr (1997b)	Ibid.
Polynomial order	3	5

5.3 Spectral analysis and profiling method

The data analysis consists of three steps: 1) quantification of O_4 and NO_2 molecular absorptions in the spectra, 2) retrieval of the vertical distributions of aerosol extinction and NO_2 concentration from these measured absorptions and 3) error budget.

The first step is achieved with the DOAS technique using the setttings presented in section 5.3.1. The second step involves a modeling of the atmospheric radiative transfer to study the sensitivity of the measurements to aerosol extinction and NO_2 concentration and a regularization method to solve the inverse problem of retrieving those quantities. This study uses the maximum a posteriori solution as described in Rodgers (2000), which also provides a rigorous error analysis.

5.3.1 DOAS analysis

Table 5.1 lists the DOAS analysis settings used for the retrievals of O_4 and NO_2 DSCDs. These settings were implemented in the QDOAS software, developed at Belgian Institute for Space Aeronomy (BIRA-IASB) (Fayt et al., 2011). The molecular cross-sections references are in the table except for O_4 for which the Hermans version is used (`http://www.aeronomie.be/spectrolab/o2.htm`). The Ring effect (Grainger and Ring, 1962a) originates from rotational Raman scattering by O_2 and N_2 and produces a filling-in of solar Fraunhofer lines in scattered light. We fit a Ring pseudo-absorption as described in Chance and Spurr (1997b) to take it into account.

Figure 5.4 presents a typical NO_2 DOAS result. The spectrum was recorded at 9h57 UTC when the aircraft was flying at 0.43 km altitude inside the marine boundary layer during the flight as0831 (8 April 2008). The solar zenith and relative azimuth angles were then respectively 64° and 223°. The telescope angle was -1° which corresponded to a range between -10° and +20° around the horizon,

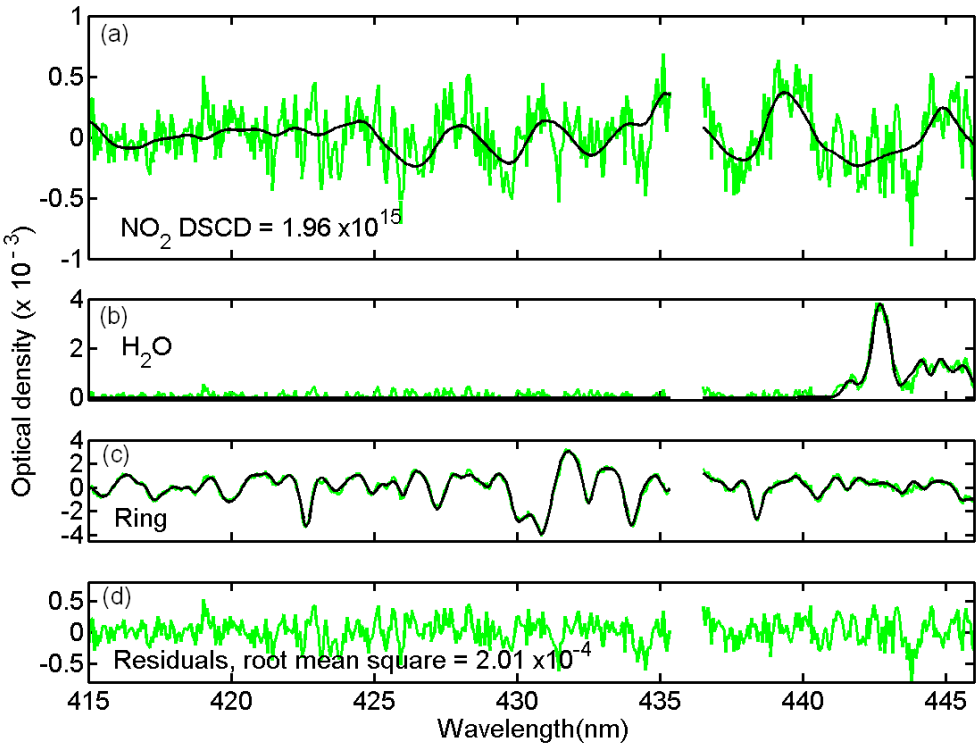

Figure 5.4: Example of a DOAS fit of a spectrum recorded on 8 April 2008, when the plane was in the marine boundary layer. Black lines correspond to molecular and Ring cross-sections scaled to the detected absorptions in the measured spectrum (green lines). Note that the pixels between 435.4 and 436.5 nm are damaged.

due to the plane's roll variations during the 30s of the measurement. The reference spectrum was recorded on the same flight at high altitude (see Sect.4.1). The figure shows the NO_2 fit (panel a), the water vapor optical density (panel b) which contributes significantly to the signal at the end of the analysis spectral window, the Ring effect (panel c) and the fit residuals (panel d). Note that the pixels between 435.4 and 436.5 nm are damaged and therefore not considered in the DOAS fit.

5.3.2 Radiative transfer modeling

The Differential Slant Column Density (DSCD) obtained with the DOAS analysis depends on the light path, which is different for every single observation due to the telescope scanning and the variations in azimuth and altitude when the planes performs a vertical sounding. Moreover, for scattered sky-light as in our experiment, multiple unknown photon paths contribute to the signal simultaneously. Modeling the radiative transfer in the atmosphere is thus necessary to define an effective light path and interpret the measurements.

The radiative transfer model used here is UVspec/DISORT (Mayer and Kylling, 2005), presented in chapter 3. Considering the DOAS fitting windows, the calculations were done at 360 and 440 nm respectively for O_4 and NO_2. To calculate the true Slant Column Density (SCD) from the DOAS DSCDs measurements, the SCD in the reference spectrum (SCDref) must be estimated (cf section 5.4.1).

Some of the atmospheric state parameters, usually sources of uncertainties in the retrieval of a particular geophysical quantity, were measured in-situ onboard the plane, such as the temperature, pressure and ozone concentration. Their measured profiles are included in our model, completed higher up in the troposphere and in the stratosphere with values extracted from the TOMSV8 climatology (McPeters et al., 2007). The latter depends on the ozone total column, estimated at 390 Dobson units in our case from the AURA AVDC values at Ny-Ålesund and Tromsø (http://avdc.gsfc.nasa.gov/). The NO_2 profile is built from the TM4 model (Boersma et al., 2007), the stratospheric part being scaled to reproduce the stratospheric vertical column measured by the Ozone Monitoring Instrument (OMI) instrument. The albedo of open-water can be calculated accurately assuming a Fresnel reflection (Brandt et al., 2005) which leads to an albedo value of 0.1 for 65° solar zenith angle. This value depends on the refractive index of water which is almost constant between 350 and 450 nm so the same albedo value was used for the two wavelengths. The aerosol optical properties (extinction, absorption and asymmetry parameter) are estimated using the Optical Properties of Aerosols and Clouds (OPAC) software package (see next section).

The observation geometry is not constant during a measurement due to the circular flight pattern and the 30s accumulation time. In particular the relative

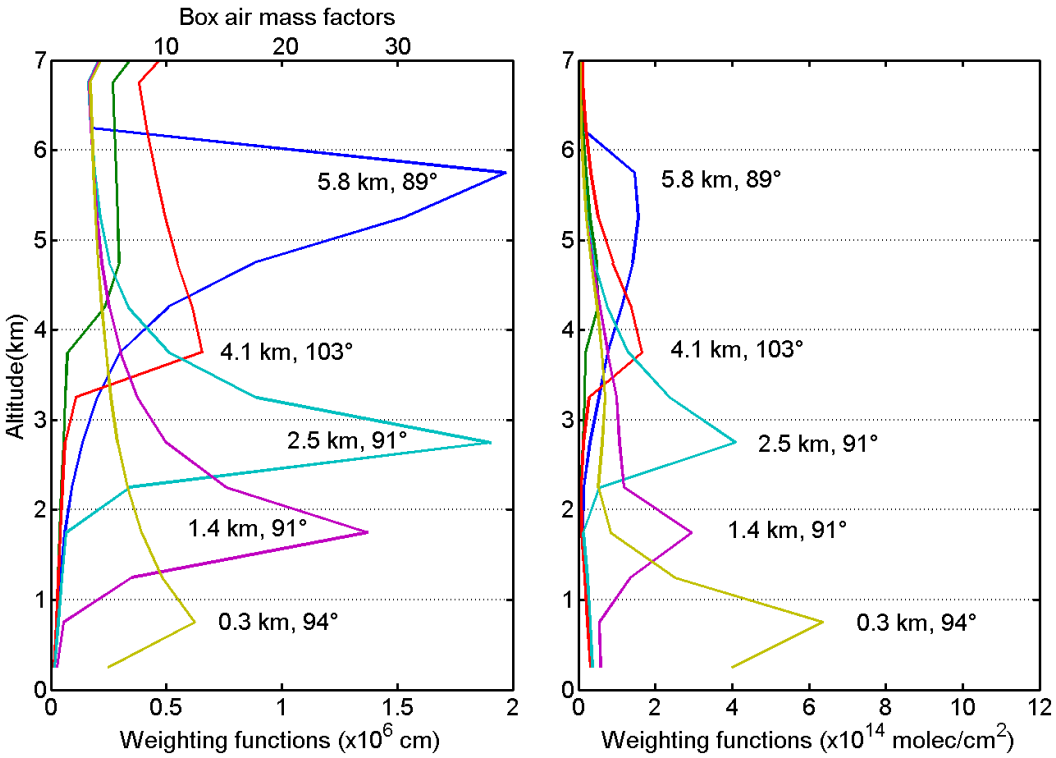

Figure 5.5: Some of the weighting functions relative to the NO_2 slant column measurements of the 8 April 2008 in linear (left panel) and logarithmic (right panel) scale. Beside the altitudes of observations are indicated the telescope line-of-sight angles (0° is nadir, 90° horizontal).

azimuth angle varies by up to 30°. To overcome this problem, each simulated SCD at a single telescope angle corresponds to a weighted mean of 9 intermediary SCDs equally distributed in the 30s measurement interval. The weights correspond to the different relative radiances calculated in the respective intermediate SCD geometries, defined by the orientations and altitudes of the aircraft, telescope angles and solar positions.

As described in chapter 3, weighting functions are required to retrieve vertical distributions. They are calculated here by perturbations on the predefined profiles of extinction and NO_2. In addition to the linear weighting functions ($\frac{\partial SCD_{O_4}}{\partial ext_i}$, $\frac{\partial SCD_{NO_2}}{\partial [NO_2]_i}$), we also calculate logarithmic weighting functions ($\frac{\partial SCD_{O_4}}{\partial \ln ext_i}$, $\frac{\partial SCD_{NO_2}}{\partial \ln [NO_2]_i}$). This enables to constrain the retrievals to positive values (see next section).

Figure 5.5 shows typical NO_2 weighting functions for the sounding of the flight as0831 (8 April 2008). While the shapes are different for the linear and logarithmic

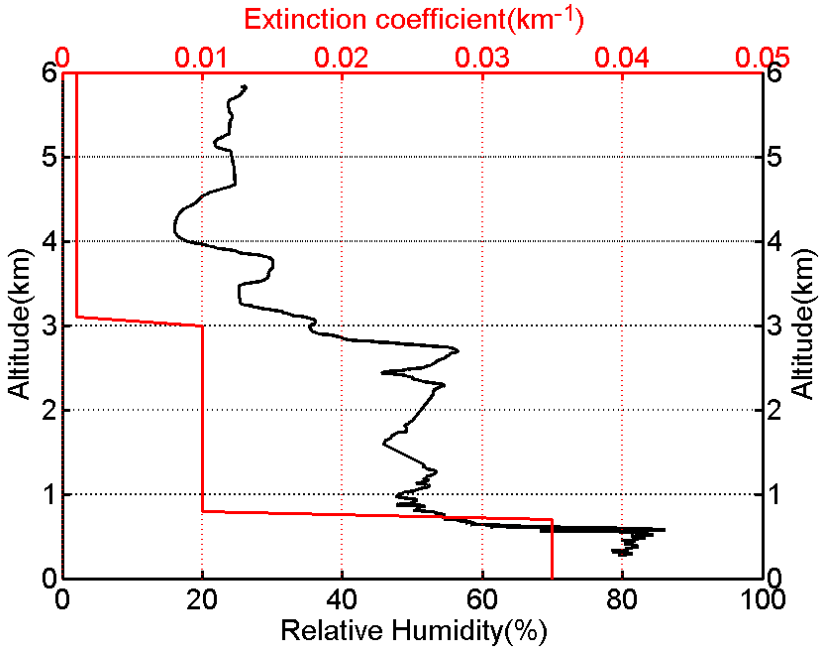

Figure 5.6: Construction of the a priori aerosol extinction coefficient profile (red) from the measured relative humidity (black). The extinction values are derived for 350 nm from the software package OPAC, using the Arctic Spring predefined aerosol type.

approaches, both indicate a sensitivity across the whole sounding altitude range. The maximum sensitivity is achieved for viewing angles close to the horizon (90°) at the altitude of observations. This happens when the telescope angle compensates the plane's roll and is due to the enhanced light path in this layer. This indicates that the optimal geometry for profiling applications is obtained during the ascents or descents of the plane while maintaining the telescope parallel to the horizon. The maximum absolute values vary in opposite way with the observation altitude: they tend to increase for the linear case whereas they decrease for the logarithmic one. In the first case, this is due to the reduced scattering at high altitude: as aerosol and Rayleigh scattering decrease the light path increases. In the second case, this effect, still present, is dominated by the decrease of sensitivity to the logarithm for smaller concentrations, as most of the NO_2 in the predefined profile is assumed to be in the boundary layer. Indeed, for small $[NO_2]$ values, $\partial \ln [NO_2]$ gets large and reduces thus the derivative $\frac{\partial SCD_{NO_2}}{\partial \ln [NO_2]_i}$.

Dividing the linear weighting functions by the layers' thickness defines the box air mass factors (box AMF, (Wagner et al., 2007)). The box Air Mass Factor

(AMF) scale is also displayed on figure 5.5 and can be compared with the same quantity calculated for nadir looking satellites (e.g. by Zhou et al. (2009, Fig. 1)) and ground-based MAX-DOAS instruments (e.g. by Wittrock et al. (2004, Fig. 4)). In the OMI case, Zhou et al. indicates a box air mass ranging from unity near the ground to two in the high troposphere. Ground-based MAX-DOAS measurements are most sensitive close to the ground, corresponding to quasi horizontal pointing, when the light path enhancement is maximum. The box AMF, around 20, is then comparable to airborne limb measurements. But this sensitivity decreases rapidly with altitude contrary to our airborne set-up which enables to look at the horizon from any altitude reachable by the plane. As a result, the airborne approach is particularly well suited for the study of the free troposphere.

5.3.3 Retrieval of the geophysical quantities with a maximum a posteriori evaluation

The weighting functions express the sensitivity of a measurement to a vertical distribution $\mathbf{x}$. For a set of measurements $\mathbf{y}$ $y_{j=1...m}$, defining the weighting functions matrix $\mathbf{K}$ as $\frac{\partial SCD_j}{\partial x_i}$ enables to write, if $\mathbf{x}$ is close to the linearization point $\mathbf{x_0}$:

$$\mathbf{y} - \mathbf{y_0} = \mathbf{K}(\mathbf{x} - \mathbf{x_0}) + \epsilon \tag{5.1}$$

where $\mathbf{y_0}$ represents a measurement series at the linearization point $\mathbf{x_0}$, which can be calculated with the radiative transfer model.

Due to the error ϵ, which represents instrument noise and model uncertainties, the solution $\hat{\mathbf{x}}$ is a statistical estimate of the true state. The problem is generally ill-posed and some regularization is required to retrieve $\hat{\mathbf{x}}$. This regularization is achieved here with the maximum a posteriori solution as presented in Rodgers (2000), often referred as "the optimal estimation" (for a semantic discussion, see apendix B). It requires a priori knowledge of the quantity to retrieve and assumes Gaussian statistics for this a priori and the error. The solution with maximum probability after the measurements (a posteriori), due to the non-linearity of the problem, must be reached by iterations, in our case with the Gauss-Newton algorithm:

$$\begin{aligned}\mathbf{x_{i+1}} =& \mathbf{x_i} + \\ & (\mathbf{S_a^{-1}} + \mathbf{K_i^T S_\epsilon^{-1} K_i})^{-1}[\mathbf{K_i^T S_\epsilon^{-1}}(\mathbf{y} - \mathbf{F}(\mathbf{x_i})) - \mathbf{S_a^{-1}}(\mathbf{x_i} - \mathbf{x_a})]\end{aligned} \tag{5.2}$$

where $\mathbf{S_a}$ and $\mathbf{S}_\epsilon$ are respectively the a priori and error covariance matrix, and $\mathbf{K_i}$ the weighting functions matrix calculated with the vertical distribution $\mathbf{x_i}$.

After convergence, the solution is a weighted mean of the a priori knowledge and the information coming from the measurement. The averaging kernels matrix

$\mathbf{A}$ measures this weight, its trace being the number of independent information retrieved, namely the Degrees Of Freedom of Signal (DOFS):

$$\mathbf{A} = (\mathbf{K_i}^{\mathbf{T}}\mathbf{S}_{\epsilon}^{-\mathbf{1}}\mathbf{K_i} + \mathbf{S_a^{-1}})^{-\mathbf{1}}\mathbf{K_i}^{\mathbf{T}}\mathbf{S}_{\epsilon}^{-\mathbf{1}}\mathbf{K_i} \tag{5.3}$$

The averaging kernels matrix also contains information about the vertical resolution of the retrieval: for a given level, it is estimated from the Full Width at Half Maximum (FWHM) of the main peak of the corresponding averaging kernel.

To save computing time, the weighting function matrices K_i are not recalculated after each iteration, as suggested in Rodgers (2000). With this approximation, which seems reasonable since the real state is close to the linearization point, the retrieval takes around one hour to converge. Moreover $\mathbf{S_a}$ is used here as a tuning parameter. In practice, $\mathbf{S_a}$ is a diagonal matrix with coefficients S_a(i,i) constructed respectively as $\beta x_a^2(i,i)$ or $\beta \ln {x_a}^2(i,i)$ in the linear or logarithmic retrieval, and β is adjusted to optimize the DOFS while preventing non-physical values and oscillations in the retrieved profiles.

For both extinction and NO_2 retrievals, vertical distributions corresponding to a priori, linearization point and starting point of the Gauss-Newton iterations are the same. Both soundings are retrieved independently. For the first sounding (8 April 2008), the chosen altitude grid extends from 0 up to 8 km in steps of 0.5 km each, except for the lowest step which is 1 km thick. For the second sounding (9 April 2008), clouds prevent modelling of the radiative transfer in the lower part of the atmosphere and, therefore, the grid starts at 3 km and the layers are 1 km thick up to 8 km.

The a priori on aerosol extinction profiles are constructed with the software package OPAC (Optical Properties of Aerosol and Clouds, Hess et al. (1998)). OPAC assumes ten types of spherical particles that can be mixed to reproduce typical aerosol conditions and provides their optical properties in the solar and terrestrial spectral range as a function of relative humidity. Conveniently, one of these predefined mixtures corresponds to the Arctic spring, and the relative humidity was measured in situ during the flight. Figure 5.6 shows an a priori extinction profile built from the OPAC output at 350 nm, the closest wavelength in OPAC to the O_4 360 nm absorption band, together with measured relative humidity.

For the NO_2 retrieval, the extinction profile at 360 nm retrieved from O_4 DSCDs is corrected to take into account the scattering reduction in the visible with the Angström coefficients given by OPAC. The a priori NO_2 vertical distribution is extracted from the corresponding TM4 vertical distributions available with the DOMINO (Dutch OMI NO_2) product (`http://www.temis.nl/airpollution/no2col/no2regioomi_v2.php`).

The assumption of Gaussian statistics, needed to establish equation 5.2 is realistic for the instrument noise but less obvious for the quantity to retrieve. For

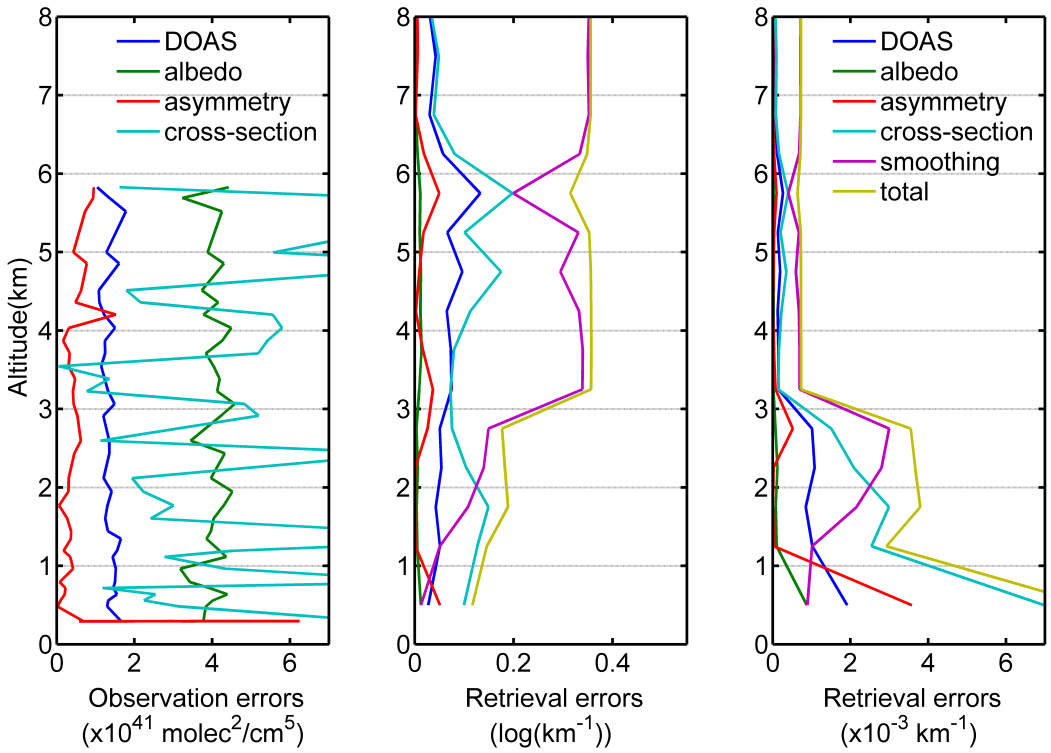

Figure 5.7: Error contributions for the extinction profile of the 8 April 2008 retrieved in logarithmic scale, estimated from the diagonal elements of the error covariance matrices.

positive geophysical quantities with large variability around a small mean, a significant part of the probability density lies in the negative range which is unphysical. Retrieving the logarithm of the quantity, i.e. assuming a lognormal probability distribution, can overcome the problem. It implies calculating logarithmic weighting functions, as described in the previous section. This has been done already, e.g. for water vapor (Schneider et al., 2006), and CO (Deeter et al., 2007). For these two species, the authors further indicate that in situ measured statistics are closer to lognormal distributions. The results of both methods are compared in section 5.4.

5.3.4 Error analysis

The uncertainties in the retrieval originate from three sources: the instrument noise, the uncertainties in the model parameters which are not retrieved (e.g. albedo) and the finite vertical resolution of the retrieval. The error from the

model itself is neglected, which seems reasonable from previous intercomparison exercises (Hendrick et al., 2006b).

The two first sources limit the accuracy in relating a profile $\mathbf{x}$ to a set of measurements $\mathbf{y}$ and correspond to the measurement error ϵ in Eq. (5.1). The associated error covariance matrix is calculated from the noise covariance ($\mathbf{S_N}$) and the model parameters covariance ($\mathbf{S_b}$) according to:

$$\mathbf{S}_\epsilon = \mathbf{S_N} + \mathbf{K_b}\mathbf{S_b}\mathbf{K_b^T} \tag{5.4}$$

where $\mathbf{K_b}$ is the matrix of sensitivities to the model parameters, constructed by perturbations on these parameters. The interest of including the uncertainties on the forward model parameters is discussed in apendix B.

The noise covariance $\mathbf{S_N}$ is built with the square of the error in the slant columns, which is an output of the DOAS analysis depending on the fit residuals. Note that the off-diagonal elements are set to zero.

Retrieving O_4 profiles in a similar experiment, Prados-Roman et al. (2011) identified the albedo and the asymmetry parameter as major sources of model parameter errors. Therefore, uncertainties on these parameters are introduced with respective standard deviations of 0.02 and 0.01. To take into account the O_4 cross-section uncertainties (see Sect. 5.4.1), another error source was introduced corresponding to 2 % of the measured DSCD. For the NO_2 retrieval, the considered uncertainties are on the albedo ($\sigma = 0.02$) and on the aerosol extinction, with standard deviations estimated from our extinction retrieval.

The measurement error, with its covariance $\mathbf{S}_\epsilon$ is propagated in the retrieval with the gain matrix $\mathbf{G}$ defined as $(\mathbf{K^T S_\epsilon^{-1} K} + \mathbf{S_a^{-1}})^{-1}\mathbf{K^T S_\epsilon^{-1}}$, representing the relationship between the retrieval and the signal. The corresponding retrieval error covariance is thus expressed as:

$$\mathbf{S_R} = \mathbf{G}\mathbf{S}_\epsilon\mathbf{G^T} \tag{5.5}$$

The retrieval is a smoothed version of the true profile. This finite vertical resolution is the third error source and is calculated as:

$$\mathbf{S}_S = (\mathbf{A} - \mathbf{I})\mathbf{S}_{var}(\mathbf{A} - \mathbf{I}) \tag{5.6}$$

where $\mathbf{S_{var}}$ is the natural variability covariance and $\mathbf{I}$ the identity matrix. Natural variability is often difficult to quantify. For the extinction, it is estimated from aerosol optical thickness (AOT) measurements between 1995 and 1999 at Ny-Ålesund (Herber et al., 2002). This study presents statistics for measurements at 532 nm for different seasons and conditions. The background (no Arctic Haze) spring value is 0.067 ± 0.017. Considering this, the variability covariance matrix is built assuming standard deviations of 0.005 in all the layers with relative humidity

larger than 50%, no correlation is considered between the layers. For NO_2, natural variability in the free troposphere is derived from the TOPSE aircraft campaign. Stroud et al. (2003) give statistics for the NO_x measurement during the campaign: a mean and standard deviation of 17±13 ppt. Interestingly the median is also calculated and its value, 15 ppt, is smaller than the mean, which is typical of a lognormal distribution. We use the standard deviation of these NO_x measurements. Again, no off-diagonal elements are added to the variability covariance matrix. Figure 5.7 displays the different error sources and their propagation in the aerosol extinction retrieval on 8 April 2008. The error profiles for each parameter represent the square root of the diagonal elements of its covariance matrix. It is noteworthy that the main error source on the measurements, the albedo, is insignificant after the retrieval. The total uncertainty appears dominated by the smoothing error.

5.4 Results for the soundings on 8 and 9 April 2008

This section presents the O_4 and NO_2 DSCD measured during the flights as0831 (8 April 2008) and as0833 (9 April 2008) and the corresponding retrieved aerosol extinction and NO_2 concentration profiles, for which are compared the linear and logarithmic approach. Between these two steps, we make sure the measurements are qualitatively reproduced by the radiative transfer model and use the latter to infer in particular the residual columns in the reference spectrum and a detection limit for NO_2.

5.4.1 Residual columns and O_4 DSCD scaling factor

DSCD measurements are relative to the slant column in a reference spectrum. Determination of this reference column is thus necessary for any further quantitative discussion on geophysical quantities. O_4 and NO_2 DSCDs presented in the following are relative to their respective columns in the same spectrum, selected at the top of the as0831 sounding, near 6 km altitude. The telescope angle was then 0°. For both species the reference slant column is estimated comparing high altitude DSCD measurements with calculated SCDs. We make the assumption that the geophysical quantities to be retrieved do not affect significantly the slant column calculation at high altitude, which we believe is a reasonable hypothesis based on sensitivity tests using the radiative transfer model.

O_4 DSCD measurements are commonly corrected with ad hoc scaling factors to retrieve extinction. During an intercomparison exercise involving four MAX-DOAS instruments, Zieger et al. (2010) reported scaling factors from 0.75 to 0.83.

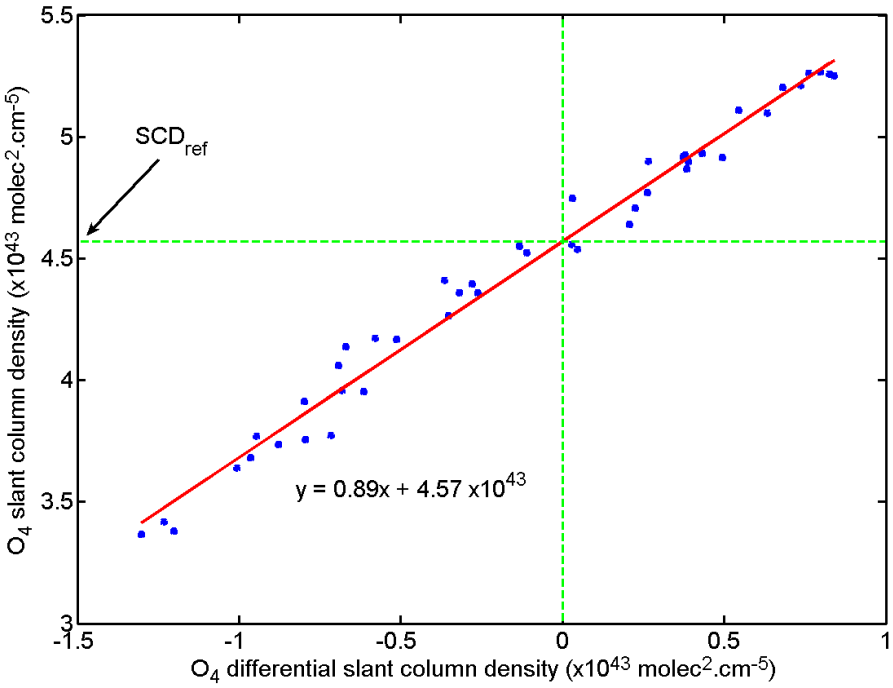

Figure 5.8: Determination of the residual column density and of the O_4 DSCD scaling factor. DSCD measurements at high altitude, where aerosols scattering can be neglected, are plotted versus simulated absolute SCD. The linear regression fits simultaneously the residual slant column density in the reference spectrum (the intercept, SCD_{ref}) and the DSCD correcting factor (the slope).

Spectra obtained at high altitudes give an opportunity to estimate accurately such a scaling factor. Indeed, the O_4 vertical distribution depends only on the air density, which can be calculated from pressure and temperature measured onboard the plane. Moreover, aerosol scattering, the major uncertainty source in O_4 SCD calculations, can be neglected above 6 km and this is confirmed by comparing measurements and simulations.

To quantify the O_4 residual slant column in the reference spectrum (SCD_{ref}) and the DSCD correction factor(α), we apply a linear regression between measured $DSCD$ and calculated SCD in the same geometries:

$$SCD = \alpha \cdot DSCD + SCD_{ref} \tag{5.7}$$

Figure 5.8 shows the fit results for two O_4 DSCD series measured when the aircraft was flying above 5.5 km. The modeled atmosphere neglects aerosol scattering but uses the in situ measurements (pressure, temperature, ozone) during the sounding. The O_4 vertical distribution is calculated from the observed pressure and temperature. This leads to a scaling factor α of 0.89. DSCD measurements used to retrieve the aerosol extinction coefficient were therefore scaled by this value, which is higher than the values reported by Zieger et al., but closer to the direct-sun measurements of Spinei[1].

For NO_2 measurements, the same high-altitude series is used to estimate a reference SCD, without fitting a correction factor on the cross-section. This leads to a NO_2 reference column of 7.81×10^{15} molec/cm^2. Aerosol optical effects are also neglected and the NO_2 profile used is taken from the TM4 model (see Sect. 5.3.2).

5.4.2 Measured versus simulated slant columns

In Fig. 5.9, O_4 and NO_2 measured DSCDs are compared with simulations for the spectra recorded between 9h16 and 10h01 UTC during the as0831 flight. The upper panel shows the aircraft altitude and the telescope line-of-sight angle. During the period considered, the aircraft was flying at high altitude (6 km) before descending to the marine boundary layer and continuing with a level flight at 300m. The two lowest panels display the measured and simulated O_4 and NO_2 DSCD series. The telescope kept scanning during the whole period, which explains the variations in the DSCDs. These oscillations are qualitatively reproduced by the simulations, which indicates the radiative transfer in the model atmosphere approximates the measurements correctly. The O_4 slant column series are closer to the simulations

[1] `http://www.knmi.nl/omi/documents/presentations/2010/ostm15/OSTM15_AIS_Spinei_O2-O2_Cross_Sections.pdf`

than the NO_2, especially at high altitude, due to the weak aerosol extinction there and the known vertical distribution of O_4

The oscillations are anticorrelated for the two species during the high altitude part. This is due to the fact that the NO_2 signal at that altitude is dominated by the stratospheric contribution (see Sect. 5.4.3), and thus maximum when the telescope points upward, while the O_4 concentration is largest at the ground, and so DSCD is highest when the telescope looks downward. The altitude dependence is also different for the two species. The O_4 DSCD, beside the oscillations, systematically increases during the descent, which is expected from the increase of air density. In the boundary layer where the aerosol extinction limits the optical path, the DSCD decreases again. In contrast, the NO_2 is stable during the descent but increases only in the boundary layer, indicating a very low NO_2 concentration in the free troposphere and higher values close to the sea surface.

Deviations between measured and simulated DSCDs indicate differences between the true state of the atmosphere and the radiative transfer parameters used. This is visible at the end of the two DSCD series, corresponding to the boundary layer. In this region, aerosol extinction is no longer negligible and the NO_2 concentration is higher than the one in the model atmosphere.

5.4.3 NO_2: Influence of the stratosphere and detection limit

For NO_2, the SCD simulations reveal a substantial influence of stratospheric NO_2 overhead although the measurements were performed in the troposphere. This effect can be clearly identified in Fig. 5.10, which compares measured NO_2 DSCDs during the sounding and simulations with and without taking into account the stratospheric part. The effect is particularly visible at higher altitudes where discrepancies between the measurements and simulations without the stratospheric part are larger than discrepancies when taking into account the stratosphere. Since the NO_2 concentration is low in the free troposphere, the signal originates mostly from the stratosphere and the boundary layer, where a NO_2 layer is detected (see previous section). The stratospheric influence is largest when the telescope points upward, towards the stratosphere, whereas the opposite is valid for the boundary layer.

To constrain the stratospheric NO_2 content in the simulations, we have used measurements of stratospheric NO_2 columns obtained from the OMI satellite instrument, which was flying above the sounding area, precisely at 9h42m on the orbit 19850. Assimilated vertical stratospheric column (2.91×10^{15} molec/cm^2) from the DOMINO data product (see Sect. 5.3.3) have been used to scale to the TM4 vertical distribution in the stratosphere.

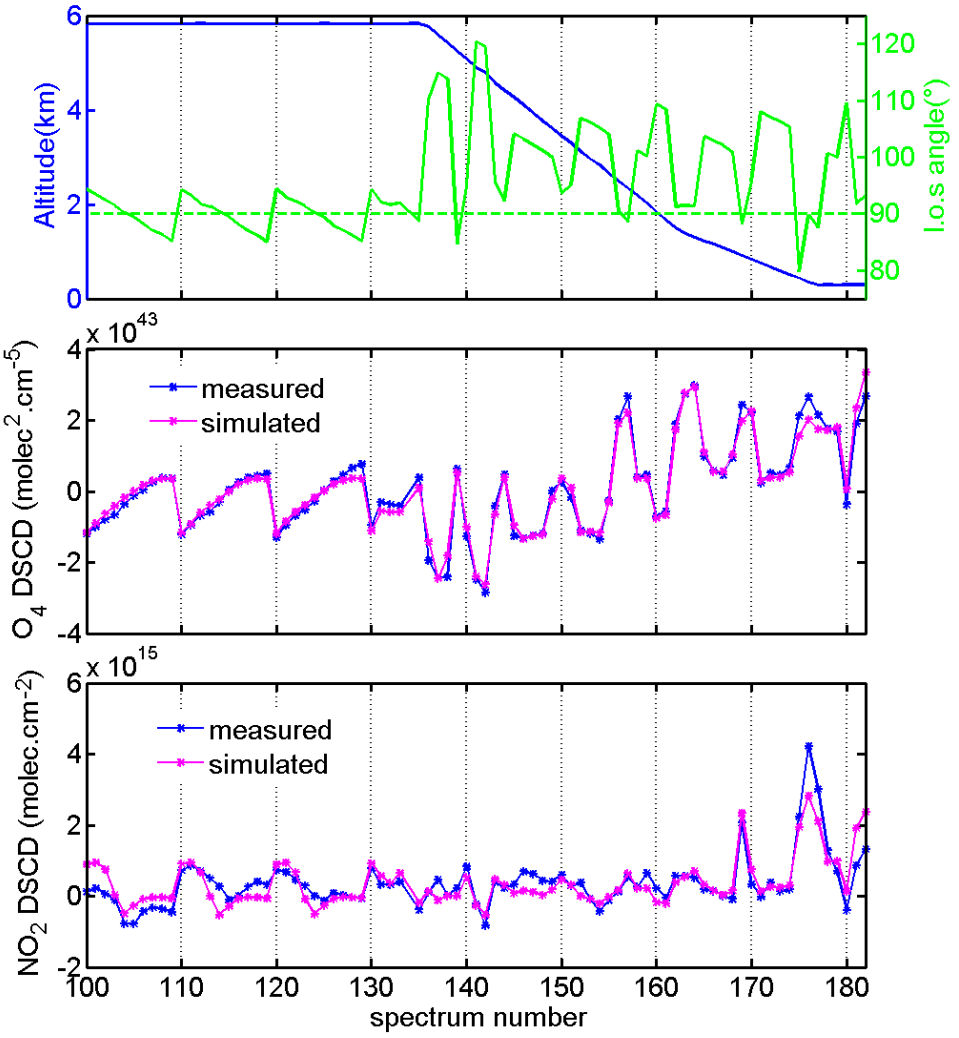

Figure 5.9: DSCD measurements during the as0831 flight (8 April 2008). The upper panel shows the plane altitude (blue) and the telescope line-of-sight angle (green, 0° is nadir, 90° horizontal). On the middle and bottom panels, measured DSCD, respectively of O_4 and NO_2, are compared with simulations. Oscillations on the DSCD series are caused by the telescope scanning. Discrepancies between measured and simulated DSCD are larger in the boundary layer, where true aerosol extinction and NO_2 concentration are different from the model.

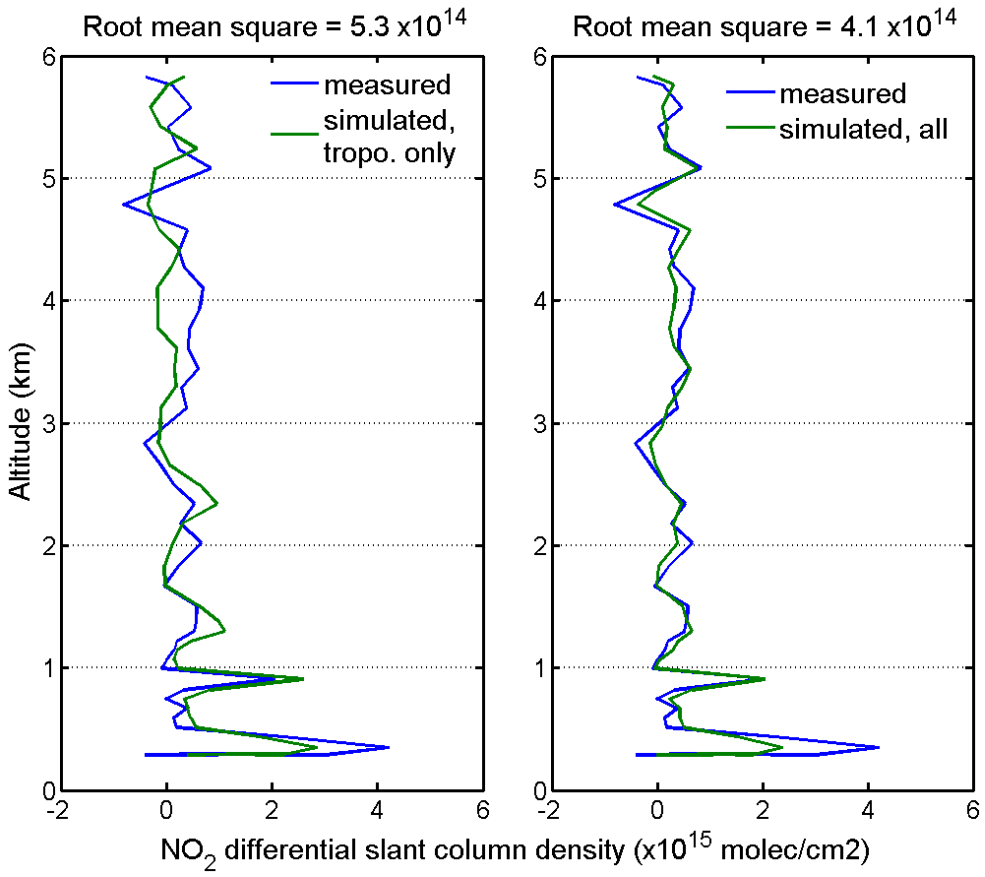

Figure 5.10: Influence of the stratosphere on NO_2 tropospheric observations. Measured NO_2 DSCD during the sounding (blue) are compared with simulations (green) neglecting the stratosphere (left) or not (right). The latter agrees better with the observations.

The minimum detectable DSCD corresponds to an optical density of two times the DOAS fit residual root mean square deviation (RMSD). Converting this minimum DSCD to a vertical column density requires knowledge of the enhancement factor between the Vertical Column Density (VCD) and the DSCD, namely the AMF, which can be derived from simulations. The detection limit is thus $\frac{2RMSD}{AMF\sigma}$ where σ is the NO_2 cross-section value. With a RMSD of around 2.1×10^{-4} (Fig. 5.4) and an AMF in the boundary layer of around 10, the minimum detectable vertical column is 7.3×10^{13} molec/cm^2. Assuming a homogeneous layer 1 km thick, this corresponds to a concentration of 6.6×10^8 molec/cm^3 and a volume mixing ratio of 27 ppt. Taking the NO/NO_2 ratio of 0.5 given by Ridley et al. (2000) in similar conditions, this leads to a total NO_x mixing ratio of 40 ppt. These detection limits are below the 50 ppt achieved with commercial airborne chemiluminescent analyzers (Ancellet et al., 2009), but above the 2 ppt mentionned by Ridley et al. (2000) for a custom-made instrument using also the chemiluminescence technique.

5.4.4 Retrievals of aerosol extinction coefficient and NO_2 concentration

Preliminary retrievals demonstrated the difficulty to reproduce quantitatively the measurements corresponding to the telescope pointing slantwise downward when the aircraft is at low altitude. A similar problem has been mentioned for DOAS ground-based measurements in the same region (Wittrock et al., 2004). Increasing the albedo improves the situation for these points but deteriorates it for the others. Wittrock et al. suggested that the presence of thin clouds might explain the problem. Such clouds were not noticed during this part of the flight so the problem could arise from another cause, e.g. a small BRDF effect on the albedo. The measurements below the horizon were not considered for the retrievals.

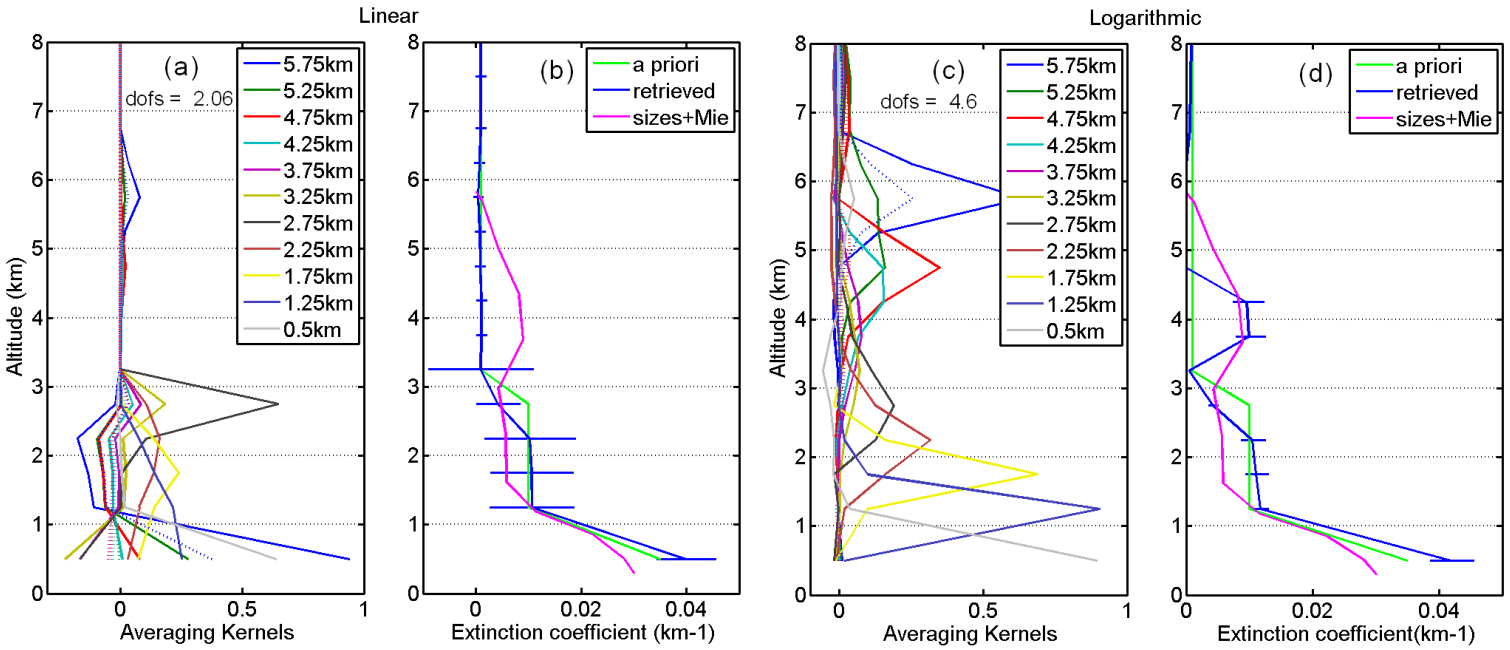

Figure 5.11: Comparison of the aerosol extinction profile retrieval using linear (left) and logarithmic (right) weighting functions for the sounding of the as0831 flight (8 April 2008). For the same a priori, the logarithmic retrieval agrees better with an extinction profile calculated from in situ size distribution. Averaging kernels indicate also a higher sensitivity of the retrieval to the true state in the logarithmic case.

Figure 5.11 shows the retrievals of the vertical distribution of aerosol extinction coefficient for the sounding at 71°N, 22°E on 8 April 2008. The panels a and b correspond to the linear retrieval, i.e., assuming Gaussian statistics on the a priori, the panels c and d to the logarithmic retrieval and the lognormal a priori (see Sect. 5.3.3). Averaging kernels (panels a and c) are different for the two methods. They do not represent the same quantity in linear and logarithmic scale but indicate that the logarithmic retrieval is more strongly constrained by the measurements than the linear one, the DOFS being respectively 4.6 and 2.06. For the linear case, the averaging kernels get very close to zero above 3 km altitude, where the a priori extinction is 0.001. The retrieved profiles are similar below 3 km altitude, with an extinction in the boundary layer of 0.04 ± 0.005 km^{-1}. Above 3 km altitude the linear retrieval, due to the averaging kernels, remains close to the a priori profile, whereas the logarithmic retrieval exhibits a layer with enhanced extinction (0.01 ± 0.003 km^{-1}) around 4 km altitude.

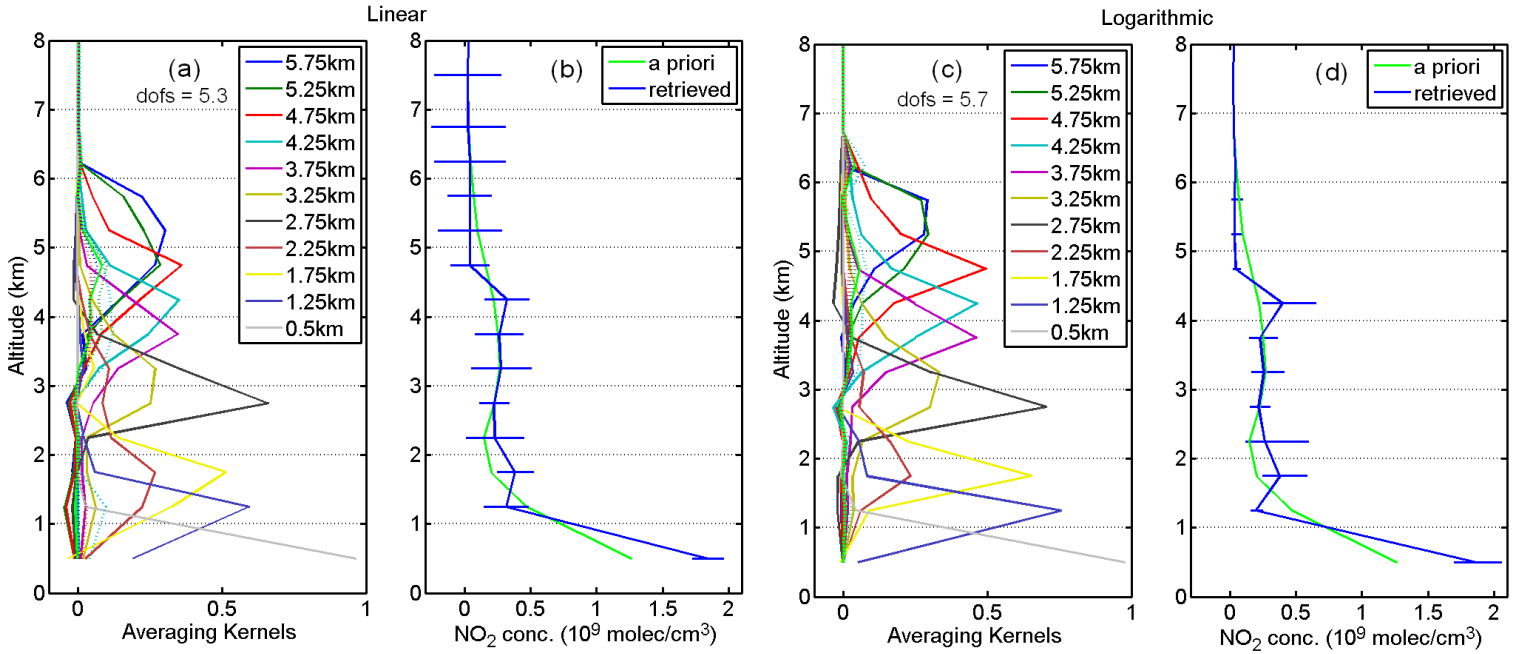

Figure 5.12: Comparison of the NO_2 profile retrieval using linear (left) and logarithmic (right) weighting functions for the sounding of the as0831 flight (8 April 2008). The two panels show the respective averaging kernels and retrieved profiles. The results are very close, contrary to the aerosol extinction retrieval.

For the linear case, the loss of sensitivity to the measurements above 3 km is explained by the low a priori extinction in these layers. As mentioned in Sect. 5.3.3, the a priori covariance matrix (S_a) used is diagonal, each element being the variance of the aerosol extinction in the considered layer. Tuning these variances to optimize the retrieval is a trade-off: large variances lead to small constraints of the a priori compared to the measurements and thus higher DOFS. On the other hand large variances imply consideration of negative values of the probability density function as non-negligible if their square roots (the standard deviation) gets close to the mean, i.e the a priori extinction in $\mathbf{x_a}$. This is the case for small a priori extinction values, i.e. the ones above 3 km altitude. Negative aerosol extinction values are non-physical and not supported by the model. It was thus necessary when building the $\mathbf{S_a}$ matrix to set variances small enough to avoid negative values, especially above 3 km altitude, reducing the sensitivity in these layers.

Figure 5.11 also presents the extinction profile calculated from the measured aerosol size distribution (see section 5.2.2) using a Mie scattering model (Mätzler, 2002; Bond et al., 2006). The complex refractive index is assumed constant for the calculation. The value, 1.5+0.01i, is taken from Tomasi et al. (2007). One of the aerosol samplers, the PCASP which measures the aerosol size distribution between 0.1 and 3 μm, could not be completely calibrated during the campaign. The missing calibration mainly affects aerosol extinction calculated for the marine boundary layer, where large sea-salt aerosols may be present. Nevertheless, the Mie calculation provides information about the shape of the true profile. The enhanced extinction layer at 4 km altitude in the Mie calculated profile is obtained only with the logarithmic retrieval. The same holds true for the second flight, indicating that an assumed lognormal probability density function (pdf) for the distribution of extinctions is well suited.

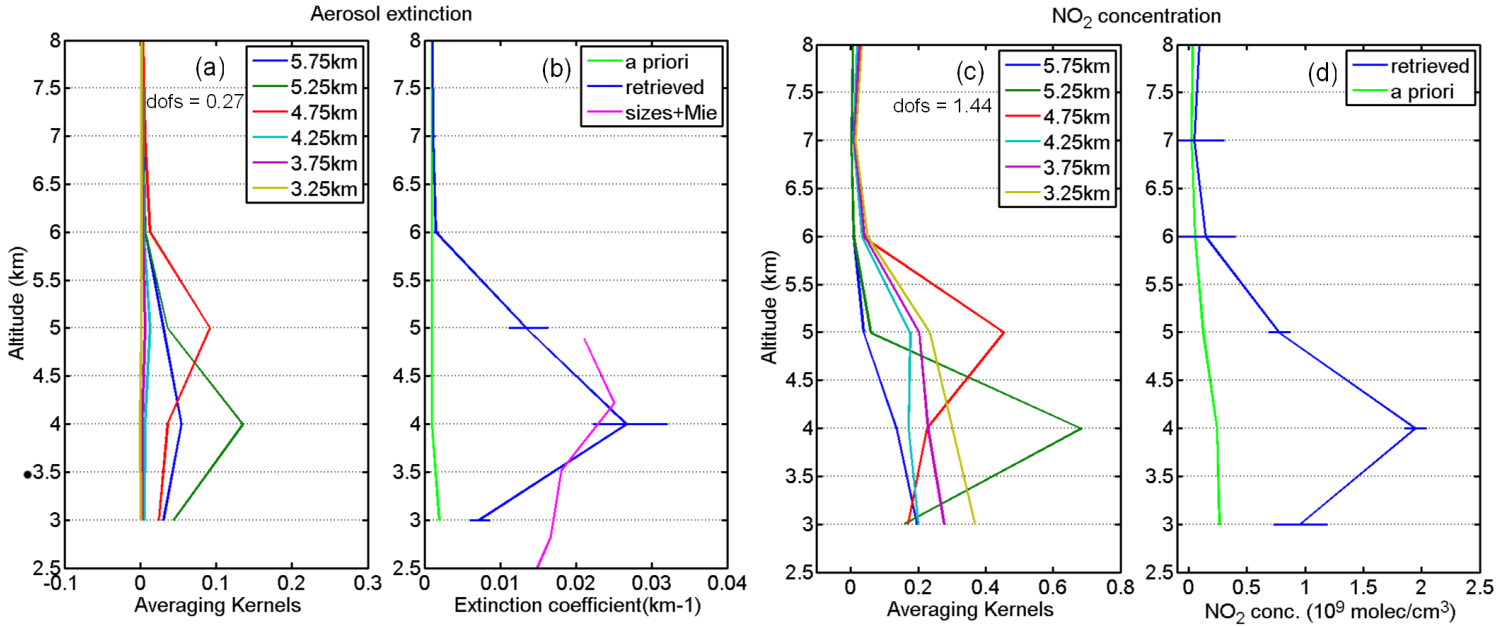

Figure 5.13: Retrieved extinction and NO_2 profiles for the sounding of the as0833 flight (9 April 2008). Under 3 km high, the radiative transfer is too strongly affected by clouds to enable quantitative retrievals. Around 4 km high, an enhanced layer is measured for both extinction and NO_2.

A drawback of the logarithmic retrieval scheme with respect to the linear one is a slower convergence, it generally takes five iterations for the former as compared to two for the latter. This may come from a smaller degree of linearity in the logarithmic statement of equation (5.1) as mentioned by Schneider et al. (2006) for water vapor retrievals from ground-based infrared spectra. A second limitation comes with a likely underestimation of the errors, when the retrieved extinction is low, e.g., for altitude above 5 km (see Fig. 10). This is due to the logarithmic behavior toward small values (see Sect. 5.3.2). Indeed, in figures 5.11, 5.12 and 5.13, error bars correspond to the square root of the diagonal elements of the total error covariance matrix. Converting a logarithmic error covariance ($\mathbf{S_{lnx}}$) to a linear one ($\mathbf{S_x}$) often implies a Taylor expansion leading to the simple expression $\mathbf{S_{lnx}} = \mathbf{x}\mathbf{S_x}\mathbf{x}$, as detailed in (Dubovik et al., 1995). It is clear from this expression that for small values the associated covariance is small. For this retrievals, we do not apply the Taylor expansion and use the exponential of the logarithmic error, but the problem is the same. These problems and a more detailed analysis of what the lognormal assumption can bring to the extinction retrieval from DOAS measurements deserve further attention, but this is outside the scope of this study.

Figure 5.12 shows the retrievals of the vertical distribution of the NO_2 concentration during the same sounding on 8 April 2008. In this case, the linear and logarithmic approaches yield similar results. The averaging kernels indicate a fairly constant sensitivity for the whole sounding with typical DOFS of 5.3 and 5.7 for the linear/logarithmic case. Three zones are distinguishable: (a) the boundary layer with a NO_2 concentration of $1.9\pm0.3 \times 10^9$ molec/cm^3, (b) the lower free troposphere with around $3\pm1 \times 10^8$ molec/cm3 between 1 and 4 km altitude and (c) the higher troposphere with negligible concentrations. In the boundary layer the corresponding NO_2 volume mixing ratio is 66 ± 19 parts per trillion (ppt), well above the detection limit of 40 ppt calculated in the previous section. No in situ measurements are available for comparison but integrating the profile leads to a tropospheric column of 1.99×10^{14} molec/cm^2. The OMI tropospheric column extracted from the DOMINO product at the sounding time above the area is $1.705\pm6.146 \times 10^{14}$ molec/cm^2. This value is close to the ALS-DOAS measurement but it lies inside its own error bars, which indicates that such low NO_2 concentrations can barely be detected by OMI.

Figure 5.13 presents the extinction and NO_2 retrievals for the sounding at 70°N 17.8°E on 9 April 2008. The radiative transfer was complicated by clouds close to the surface, so the retrieved profiles start at 3 km altitude. The logarithmic approach is used for the extinction retrieval. The DOFS value is low (0.27) nevertheless the retrieved profile is distinctly different from the a priori and exhibits an extinction maximum, 0.025 ± 0.005 km^{-1} at 4 km altitude, which is also visible in the extinction calculated from the size distribution. A maximum in the NO_2

concentration of 1.95±0.2 × 10^9 molec/cm^3 is also observed at the same altitude. For this NO_2 retrieval, the DOFS value is 1.44.

5.5 Interpretation of the retrieved profiles

Figure 5.14 shows in situ measurements of ozone and CO during the two soundings studied here, together with total attenuated backscatter ratio (R) measured with the lidar at 532 and 1064 nm. This quantity, described in de Villiers et al. (2010, Appendix. A), tends to unity when aerosol loading decreases. For the second sounding, the lidar profile was measured above 69.6°N, 19°E around 11h40 UTC i.e. two hours and 60 km off the sounding mainly since later the cloud cover mentioned in the previous section prevented a co-located measurement. CO can serve as a pollution tracer due to its long life time (around 20 days in the free troposphere (Forster et al., 2001)) and has both anthropogenic and natural sources, many of them correlated to the sources of NO_2 and aerosols. The first sounding (8 April 2008) exhibits anticorrelated variations of ozone and CO volume mixing ratio (vmr) around the altitude where is visible the extinction enhancement in the free troposphere. The layer around 3.7 km altitude shows an increase of 15 ppb CO over the level at 3 km altitude (150 ppb); this corresponds to a reduction of ozone of the same order of magnitude. At 4.2 km altitude, the situation is opposite: a layer with higher ozone vmr (40 parts per billion (ppb) over the level of 3 km altitude) corresponds to a 25 ppb reduction of CO vmr. Above 4.5 km altitude, weaker structures are still visible in the ozone profile. The lidar profile clearly shows the boundary layer, with R values for 1064 nm of 2.8 at 0.8 km altitude, and other layers in the free troposphere, in particular at 4.3 km altitude, where R is around 1.8. During the second sounding (9 April 2008), ozone is increasing smoothly from 50 to 60 ppb with height, but CO presents two layers with enhanced vmr, around 2.7 km (+35 ppb) and from 3.5 km to 5 km (+50 ppb). These layers are correlated with enhancement of the R values (respectively 2.3 and 1.8)

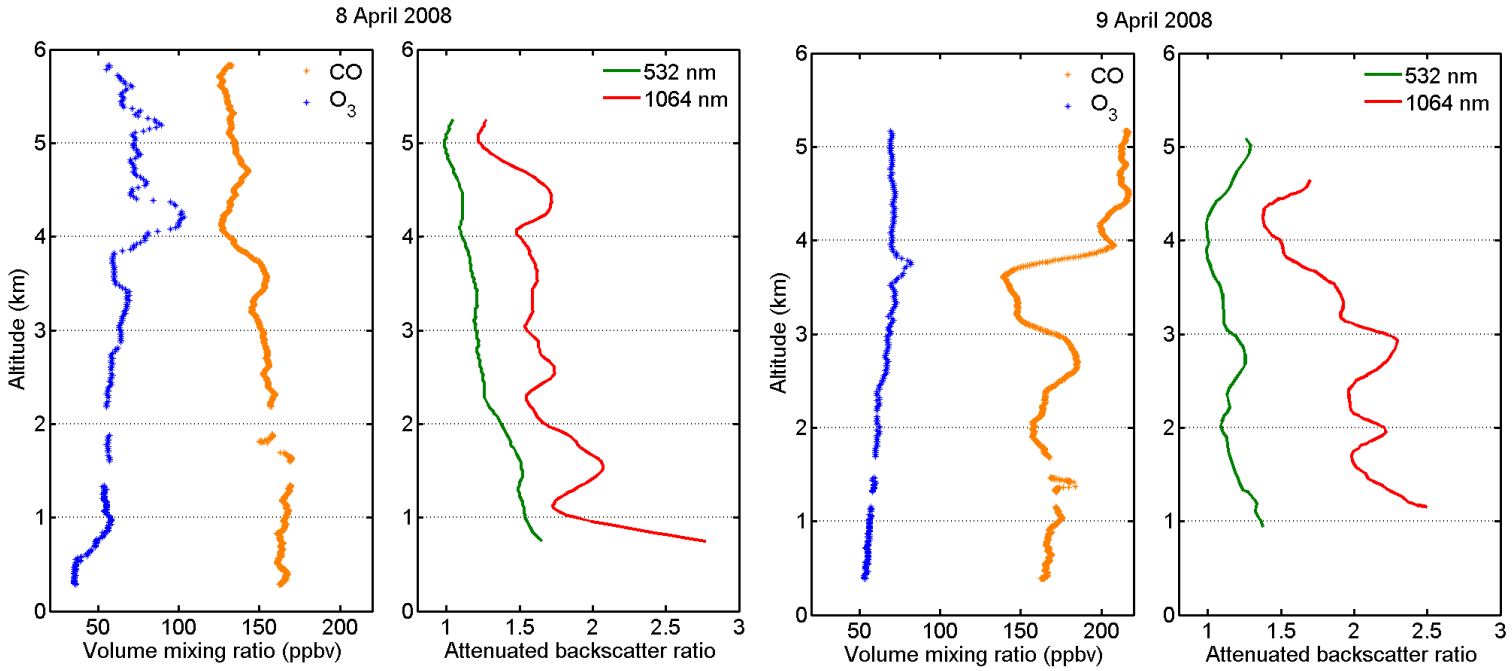

Figure 5.14: Ozone and CO in situ measurements together with lidar total attenuated backscatter ratio during the two soundings. On the second one (9 April 2008) a layer with enhanced CO above 3.7km indicates pollution transport.

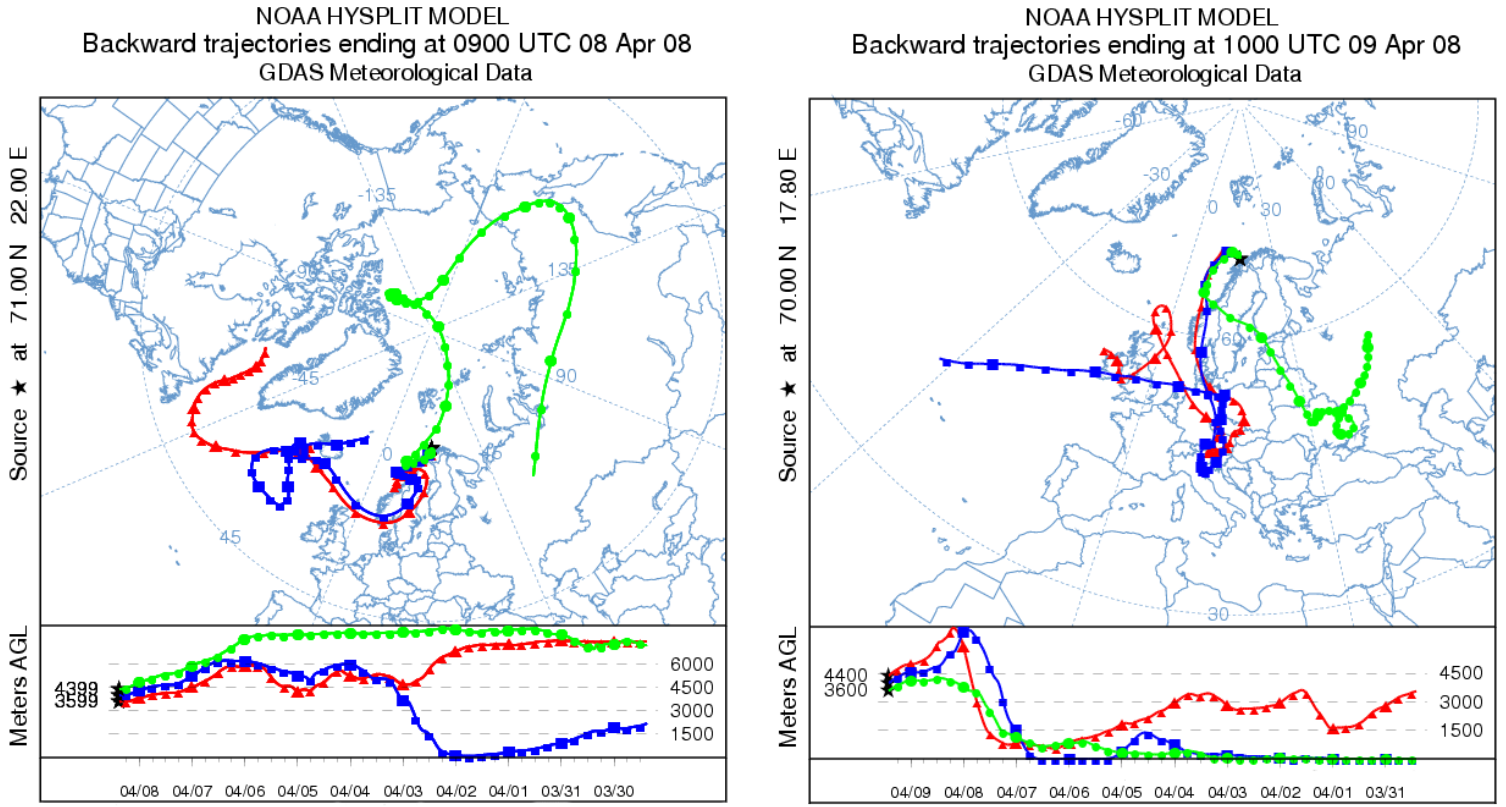

Figure 5.15: Back-trajectories for the two soundings' positions calculated for altitudes of 3.6, 4 and 4.4 km. During flight as0833 (9 April 2008), the air masses are clearly influenced by polluted zones, i.e. the boundary layer in central Europe.

Anticorrelations between higher ozone concentration and CO have been observed in previous aircraft measurements (Koike et al. (1997), Zahn et al. (2000), Stohl et al. (2007)). They have been explained by a stratospheric origin of the observed air or mixing with stratospheric air. The extinction layer around 4 km detected by the ALS-DOAS during the first sounding is unlikely to come from the stratosphere since the background extinction observed is one order of magnitude smaller (Vanhellemont et al., 2010) and no major volcanic eruptions were reported before the period of the campaign. From the lidar profile, it is not obvious if the structure at 3.7 km altitude with higher CO corresponds to the ALS-DOAS extinction maximum. Indeed, this is probably at the altitude of the R maximum, 4.3 km, even if it appears lower with the low vertical resolution of the ALS-DOAS retrieval achieved at this altitude, seen from the width of the averaging kernels in Fig. 5.11. On the second flight, the situation is clearer: a layer with high CO vmr and backscatter ratio occurs where the retrieved profiles of extinction and NO_2 are maximum.

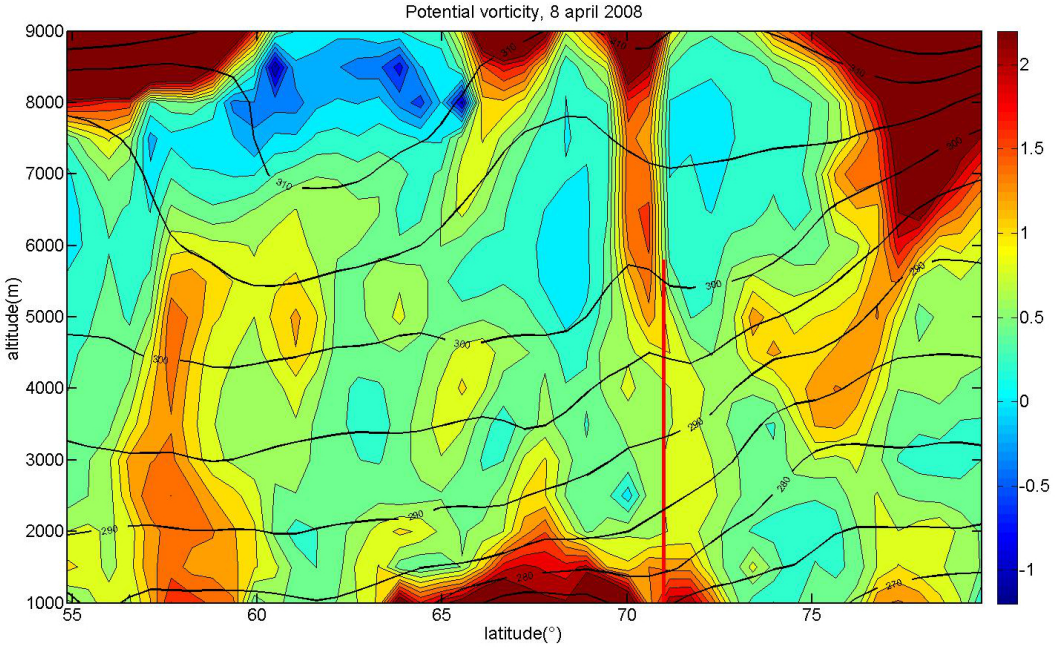

Figure 5.16: Potential vorticity on 8 April 2008

Figure 5.15 presents backward air mass trajectories for both flights calculated using the HYSPLIT (HYbrid Single-Particle Lagrangian Integrated Trajectory) model (Draxler and Hess, 1998) with the GDAS meteorological data serving as input. To understand the vertical variability around 4 km altitude in the two

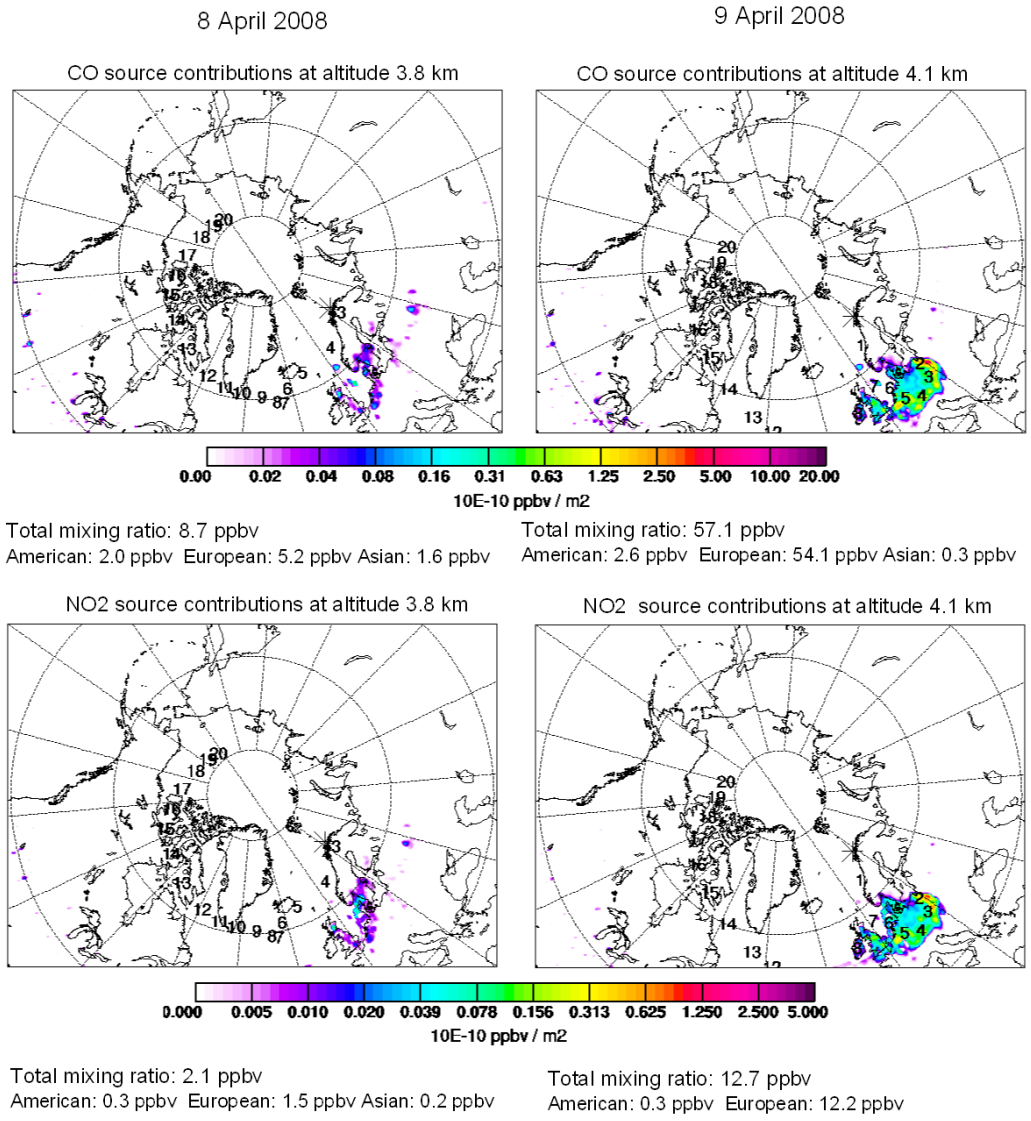

Figure 5.17: CO and NO_2 source contributions for the altitude with maximum CO concentration in the two soundings. Europe appears the dominant source and its influence is much larger on the second sounding (9 April 2008).

cases, the calculations start at 3.6, 4 and 4.4 km altitude for both soundings and consider a period of 10 days. HYSPLIT back trajectories calculated for the first sounding suggest a potential mixing of high and low altitude air masses: the air at 4 km appears to come from the boundary layer close to Iceland and is sandwiched between two air masses originating from higher up in the atmosphere.

At 4.4 km height, the air originates from above the North pole and stayed mainly above 7 km altitude during the last 10 days, which agrees with the high measured ozone mixing ratios. A stratospheric intrusion is also consistent with the ECMWF potential vorticity[2] and potential temperatures visible on figure 5.16. Indeed, two vorticity filaments are visible at 70 and 75°N, which both may well be associated with a stratospheric intrusion. The measurements of the first sounding can thus be explained by a mixing of stratospheric and boundary layer air masses. HYSPLIT results for the second sounding are again easier to interpret: the air mass at 4 km altitude originate from the central European boundary layer, where it has been lifted two days before the measurements. This back-trajectory explains the more polluted air mass of the second flight in the free troposphere, with higher CO and aerosol extinction, compared to the corresponding air mass in the first sounding.

The presence of the short-lived NO_x in the Arctic is usually explained by peroxyacetic nitric anhydride (PAN) decomposition (Stroud et al., 2003), from local sources like ships (Wittrock et al., 2004) or snow photochemistry (Honrath et al., 1999). The back-trajectories of Fig.14 tend to eliminate the last two options for the free tropospheric NO_2 observed during the second flight. The air does not come from a close marine or snow-covered boundary layer. Considering PAN decomposition, which occurs mostly in summer (Beine and Krognes, 2000), the temperature at the altitude of the detected layer, 255 K is too low for it to be significant (Stroud et al., 2003). These considerations and the correlations between the CO, aerosol extinction and NO_2 layer suggest that this NO_2 was directly transported from pollution source regions in Europe. The lifetime of NO_2 depends on the meteorological conditions, its main diurnal sink being the reaction with OH, and at night, the hydrolysis of N_2O_5 on aerosols (Evans and Jacob, 2005). This lifetime can however be approximated by a decreasing exponential depending on the surrounding air mass temperature. According to the study of Dils (2008), this lifetime is 2.14 days with an in situ temperature of 255 K. This result is close to the lifetime of NO_x presented in Stroud et al. (2003), which is above 2.5 days. The back-trajectory of the second flight indicates that the air mass was in a polluted boundary layer 2 days before the measurement, which supports the idea of transported NO_2.

We also ran the Lagrangian Particle Dispersion Model FLEXPART version 8 (Stohl et al., 2005) 20 days backward from short segments along all campaign flights. The output of these calculations are emission sensitivities (Stohl et al., 2003), which can be used to interpret transport processes and to identify potential pollution source regions. When ignoring removal processes and multiplying the emission sensitivities with emission flux densities of CO and NO_x, we obtain maps

[2]Potential vorticity (PV) is a fluid analogy for solid body angular momentum. PV increases with altitude and the tropopause can be defined as the height of 2 PV-units. Higher PV values in the troposphere may indicate a stratospheric intrusion.

of source contributions, identifying the areas where pollution sources contributed to the sampled air mass. The emission data was taken from the EDGAR v32 database (Olivier et al., 2005) globally but EMEP emissions were used for Europe. Browsing the source contributions along the soundings, local maxima are found for the CO source contributions close to the altitude where the in situ sounding vmr are the largest. For the second flight, the NO_2 source contribution is maximal at 4 km altitude. According to Fig. 15, NO_2 is released in the same regions as CO, namely over Europe, especially over Poland. The total simulated CO mixing ratio of 57 ppb accumulated for 20 days prior to the sounding is close to the measured CO enhancement over the background. During the first flight, the simulated CO tracer enhancement is less than 9 ppb, in agreement with the small measured CO enhancements. In this case, CO sources located in Northwestern Europe are responsible for the detected CO enhancement. Notice that the simulated total NO_2 tracer measurements are much larger than the measured NO_2, because the model accumulates emissions over 20 days without considering removal processes. In reality, only a fraction of the NO_x emitted over the last 20 days is transported to the measurement location and only a fraction of it is present as NO_2.

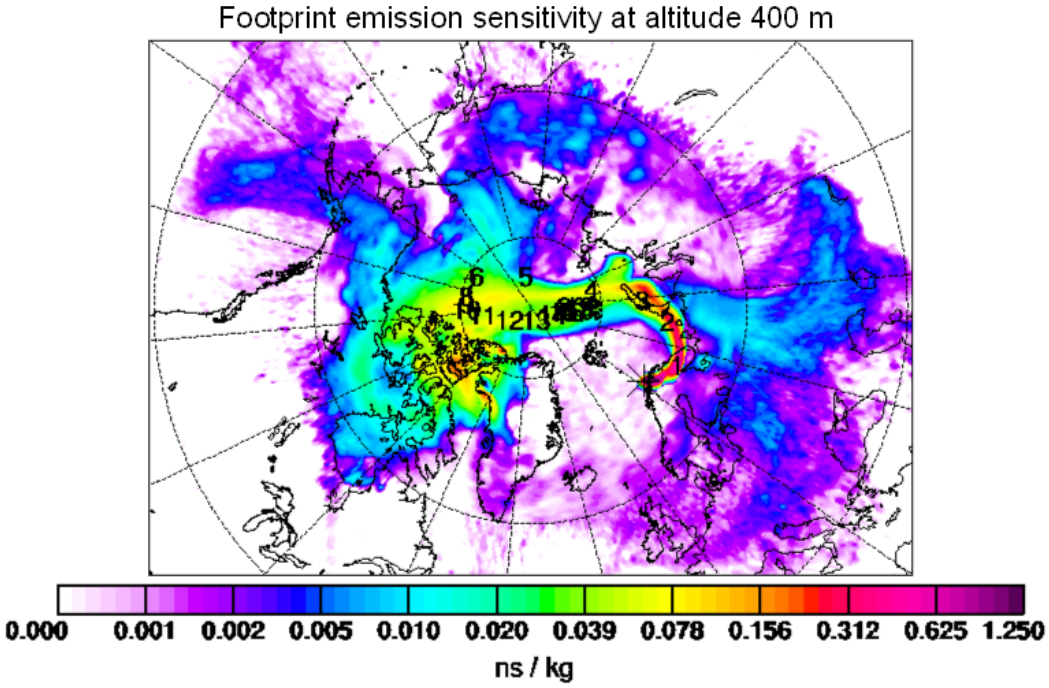

Figure 5.18: Footprint emission sensitivity for the air in the boundary layer of the 8 April 2008 sounding, where enhanced NO_2 is measured.

Considering the boundary layer NO_2 observed during the first flight, footprint emission sensitivities shown in Fig. 5.18 indicate that the surface areas influencing the air mass are Northern Lapland, parts of the Kola peninsula and Barents Sea. While FLEXPART does not indicate a large CO or NO_2 source contribution from these areas, transport times from the Kola Peninsula were less than 1 day and even the small (1 ppb) simulated NO_2 tracer mixing ratio (originating mostly from the Kola Peninsula) is much larger than the measured NO_2 mixing ratio. Furthermore, emissions on the Kola Peninsula are notably uncertain, with known errors in the emission inventories. In particular, NOx emissions transported from Nikel which is located on the western Kola Peninsula are apparently too low and appear erroneously attributed in the inventories to emissions of Murmansk (Prank et al., 2010). Emissions from the smelters are sulfur-rich, so that it is likely that the observed aerosols are mainly sulfate. The smelter emissions are relatively poor in CO, so the small measured CO enhancements are not contradictory to this source.

5.6 Conclusions on our participation to POLARCAT

We have retrieved vertical distributions of the aerosol extinction coefficient and NO_2 concentration using a recently developed airborne DOAS instrument flown on board the ATR-42 during the POLARCAT-France campaign in spring 2008 between continental Norway and Svalbard. The instrument recorded scattered skylight spectra at the horizon, in which NO_2 and O_4 absorption structures were identified. The latter were used to infer aerosol extinction profiles at 360 nm, which were included in the NO_2 profile retrievals. The results were then interpreted using ancillary in situ chemical measurements and transport models back-trajectories.

For a sounding performed on 8 April 2008, the retrieved extinction is 0.04 ± 0.005 km^{-1} in the boundary layer and a smaller extinction layer (0.01 ± 0.003 km^{-1}) appears at 4 km altitude. NO_2 is also present in the boundary layer, its retrieved concentration being $1.9\pm0.3 \times 10^9$ molec/cm^3. For a sounding performed on the 9 April 2008, a layer with enhanced extinction and NO_2 was detected at 4 km altitude, with respective values of 0.025 ± 0.005 km^{-1} and $1.95\pm0.2 \times 10^9$ molec/cm^3.

For both soundings, the extinctions inferred for the free troposphere match layers of enhanced CO which indicates pollution transport. The magnitudes are however very different. The small extinction detected in the first sounding is explained from back-trajectories indicating a mixture of stratospheric air and polluted air transported from Northwestern Europe, whereas for the second sounding the air masses originated mostly from central Europe. The aerosols and NO_2 seen

in the boundary layer during the first flight seem to originate from metal smelters and industry near Nikel on the Kola peninsula. The NO_2 layer at 4 km altitude observed during the second flight seems to have been directly transported from central Europe with the CO and aerosols.

The instrument and the inversion method successfully fulfilled the scientific objectives of the study, yielding quantitative insights into the chemical composition and aerosol content of the Arctic troposphere, with a vertical resolution unachievable from ground or satellite, especially in the free troposphere. The logarithmic approach used for the aerosol extinction, which yielded better agreement with ancillary data in the two studied cases, should be further investigated as it could also improve ground-based retrievals. The experiment could be repeated in other areas to measure profiles of potentially all species detectable with the DOAS technique in the spectrometer spectral range. The high sensitivity could be further increased by adding a feedback on the scanning telescope[3] to maintain it parallel to the horizon. We believe interesting future applications could concern molecules for which fewer observations are available, such as IO which deserves further investigations due to its importance in ozone chemistry.

[3]Such a configuration has since then been implemented by Baidar et al. (2012), the results are indeed promising.

Chapter 6

DOAS measurements of NO_2 from an ultralight aircraft

From the experience gained from the Airborne Limb Scanning DOAS (ALS-DOAS), we have developed a more compact instrument, the Ultralight Motorized-DOAS (ULM-DOAS), primarily targeted to measure tropospheric NO_2 from an ultralight aircraft. This chapter describes this instrument and its operation during the Earth Challenge expedition in November and December 2009. It is based on a study published in Atmospheric Measurement Techniques.

6.1 Motivation

Nitrogen dioxide (NO_2) is a key species both in atmospheric chemistry, through its role in the ozone cycle, and as an indicator of air quality. In the troposphere, its main sources are anthropogenic and related to fossil fuel combustion in car engines, thermal power stations and industries (Jacob, 1999). NO_2 contributes to the photochemical smog seen above many cities and its effects on health have motivated the definition of acceptable exposure thresholds. The World Health Organization (WHO, 2003) recommends a maximum 1-h exposure concentration of $200\,\mu g/m^3$ and an annual average of $40\,\mu g/m^3$.

The tropospheric NO_2 loading can be remotely retrieved using its absorption bands in the ultraviolet-visible and the Differential Optical Absorption Spectroscopy (DOAS) technique (Platt and Stutz, 2008). This is achieved from space by nadir-looking satellite-borne sensors like Ozone Monitoring Instrument (OMI) (Levelt et al., 2006) or Global Ozone Monitoring Experiment 2 (GOME-2) (Munro et al., 2006). These measurements are particularly valuable since they offer a global picture of the NO_2 field. However, their spatial resolution is limited by the pixel size ($13 \times 24\,km^2$ for OMI, $80 \times 40\,km^2$ for GOME-2), which does not resolve

fine-scale patterns. Satellite data also suffer from instrument drifts and require validation involving mostly ground-based DOAS instruments (e.g. Kramer et al., 2008; Herman et al., 2009; Pinardi et al., 2010; Shaiganfar et al., 2011), airborne in-situ measurements (Bucsela et al., 2008; Boersma et al., 2008) or, less frequently, airborne DOAS instruments (Heue et al., 2005). An aircraft is able to cover the spatial extent of a pixel in a short time, but such an experiment is expensive and requires dedicated aircraft.

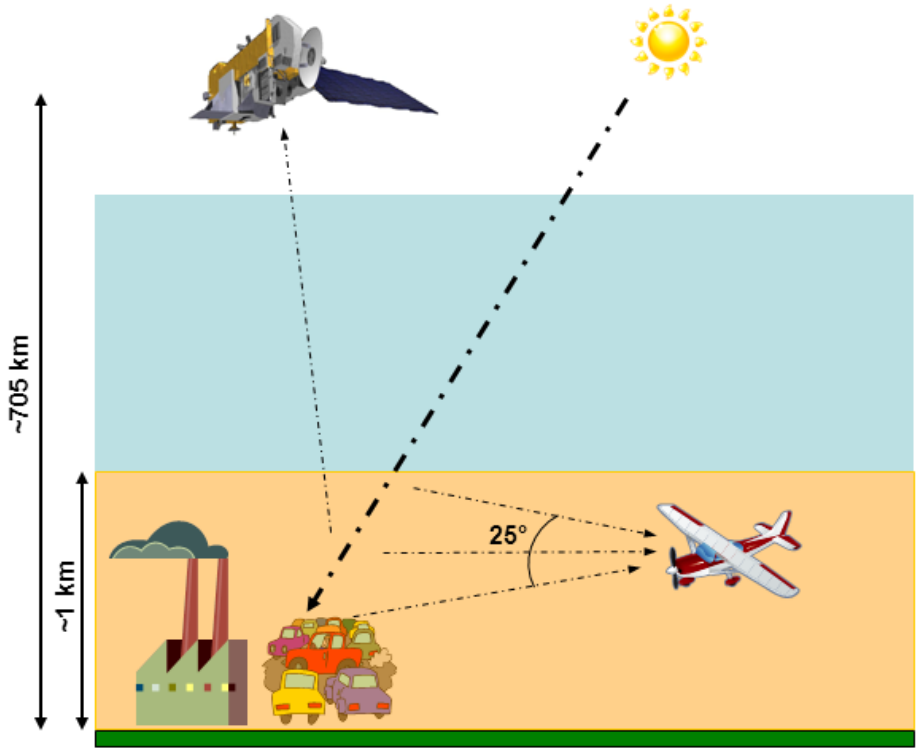

Figure 6.1: Geometry of our ULM-DOAS measurements compared to a nadir-looking satellite instrument like OMI.

Ultra-light aircraft are well suited for NO_2 studies. Their ceiling is relatively low, but, at least in polluted zones, most of the NO_2 is close to the surface. Aircraft modifications are much easier than on normal planes since they do not require certifications from the aeronautics authorities. Ultra-light aircraft have so far been used to study the actinic flux (Junkermann, 2001), the aerosol profiles (Chazette et al., 2007; Raut and Chazette, 2008) and formaldehyde distribution (Junkermann, 2009).

The Earth Challenge expedition (De Maegd, 2010), which took place in 2009, involved four ultralight aircraft flying from Australia to Belgium. It provided an opportunity to develop and test a new compact DOAS instrument, namely the ULM-DOAS. In comparison with previous airborne DOAS experiments (e.g. Bruns et al., 2006; Prados-Roman et al., 2011; Merlaud et al., 2011), the optical set-up is very simple. The instrument records the scattered light intensity at the horizon within a large field of view without any telescope or scanner. However, this measurement geometry optimizes the sensitivity to boundary layer NO_2 while it limits the errors due to aircraft attitude (pitch, roll, and yaw) instabilities.

In the next section, we describe the technical aspects of the ULM-DOAS instrument and the Earth Challenge expedition. The methods used for the data analysis, i.e. the DOAS settings, radiative transfer modeling, and inversion schemes, are presented in section 6.3. Section 6.4 investigates the sensitivity of the measurements to geometrical and geophysical parameters and how uncertainties on these parameters are propagated in an error budget. The methods and error analysis are applied in section 6.5 to derive tropospheric NO_2 above interesting areas for which few local measurements have been reported. The measurements are compared with OMI and GOME-2 data for the days where it is possible. In addition to NO_2 tropospheric columns, the ULM-DOAS also confirm the presence of a soil signature recently reported in GOME-2 spectra.

6.2 The ULM-DOAS instrument and the Earth Challenge expedition

6.2.1 Instrument description

Figure 6.2 shows the ULM-DOAS, which was developed at the Belgian Institute for Space Aeronomy (BIRA-IASB) in the framework of this thesis and first used during the Earth Challenge expedition. The light is collected by a 400 μm-diameter optical fiber, which, during operation, is attached under a wing of the aircraft, pointing forward to the horizon. There is no focusing element at the entrance of the fiber, hence the field of view is directly related to the numerical aperture of the fiber, which corresponds to 25° (figure 6.1). This choice is motivated in section 6.4. A black plastic baffle (figure 6.3) is added to limit the stray light. The other extremity of the fiber is screwed to the spectrometer, which lies inside a $27 \times 27\,cm^2$ aluminum box together with a PC-104 that controls it. The spectrometer is an AvaSpec-2048 with a 50 μm entrance slit and a 600 l/mm grating, blazed at 300 nm. It covers the spectral range from 200 to 750 nm at a resolution of approximately 1.2 nm Full Width at Half Maximum (FWHM) at 460 nm. Figure 6.5 shows the slit function in the NO_2 fitting window. The instrument sensitivity to polarization is

under 4 per mil. The detector is not temperature-stabilized and the typical shift variation during a flight is 0.2 nm. Both the spectral resolution and the shift are characterized in the DOAS analysis (section 6.3.1). A GPS antenna is connected to the PC-104 for georeferencing the measurements. The whole set-up is powered by the aircraft's 12 V.

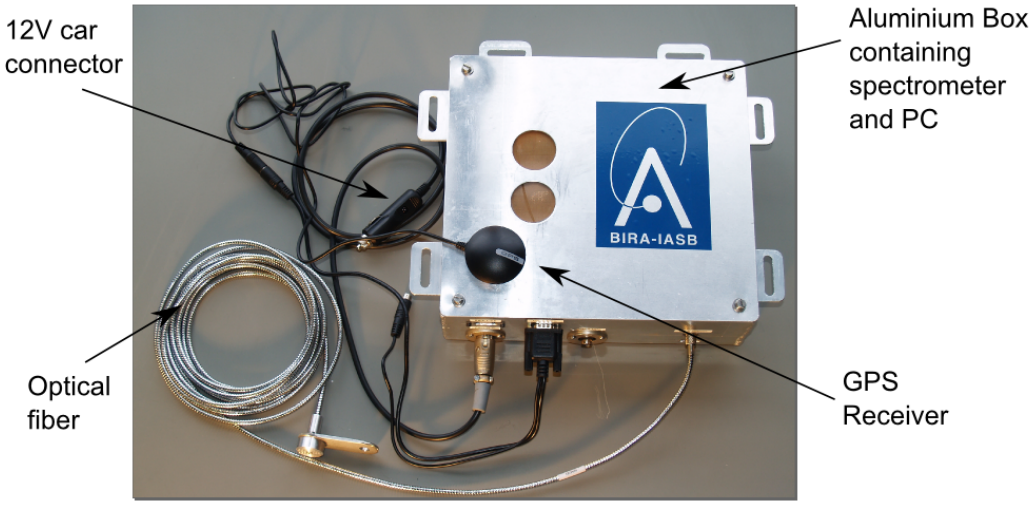

Figure 6.2: The ULM-DOAS instrument. Inside the box are a compact UV-Vis spectrometer and a PC-104. Light is collected directly by the optical fiber and a GPS is used to geolocalize the measurements. The whole system is powered with 12 V.

While measuring, the instrument is recording spectra continuously at an integration time of 5 ms. The noise is reduced by averaging a series of 10 accumulations on the Charge Coupled Device (CCD) to produce a spectrum. These spectra are transferred to the computer and filtered by the acquisition program, removing those with too low or saturated signal. A second averaging is then applied to a spectra series of 5 s to produce a final measurement point, the process being repeated continuously. The dark current is estimated from the mean of the signal in the range of 280–300 nm, where the atmosphere is opaque due to ozone absorption. Preliminary DOAS analyses (see section 6.3.1) with preconvoluted cross-sections are done in real time and saved on a USB key attached to the aluminum box. This allows for easy monitoring of the behavior of the instrument, especially when no scientists are present, as was the case during the Earth Challenge expedition.

Figure 6.3: Input optics of the ULM-DOAS instrument installed under the wing of the ultralight aircraft. The fiber collects directly the scattered light without any focusing element. The black plastic baffle limits the spatial stray light.

6.2.2 The Earth Challenge expedition

Earth Challenge was a 27 000 km expedition between Australia and Belgium onboard four ultralight aircraft, which took place in April and November 2009 (De Maegd, 2010). The team left from Sydney (Australia) on 5 April 2009 and reached Bangkok (Thailand) on 30 April 2009 with 37 flights. The second stage started from Bangkok, after the monsoon season, on 30 October 2009 and ended after 21 flights in Charleroi (Belgium) on 5 December 2009. The objective of the 7 pilots team, beside reaching Belgium, was to draw the public's attention to major environmental problems, such as sea level rising, pollution and climate change, in cooperation with the World Wildlife Fund (WWF). The project was supported by BIRA-IASB, which used this opportunity to develop and test the new instrument described in the previous section.

The aircraft used were four Coyote RANS-S6. Their cruise speed is 180 km/h and they can reach an altitude of 4.8 km with a payload (including pilots) of 300 kg. The range is around 700 km, but additional 50 l oil tanks were added for the longest flights of the expedition, e.g. the 874 km crossing of the Gulf of Oman between Gwadar (Pakistan) and Dubaï (United Arab Emirates).

Figure 6.4 shows the second part of the expedition superimposed on a monthly-averaged map of GOME-2 NO_2 tropospheric measurements during November 2009. The circled numbers correspond to the areas further studied in this work. Except for India and the Po Valley, they correspond to places where few local NO_x mea-

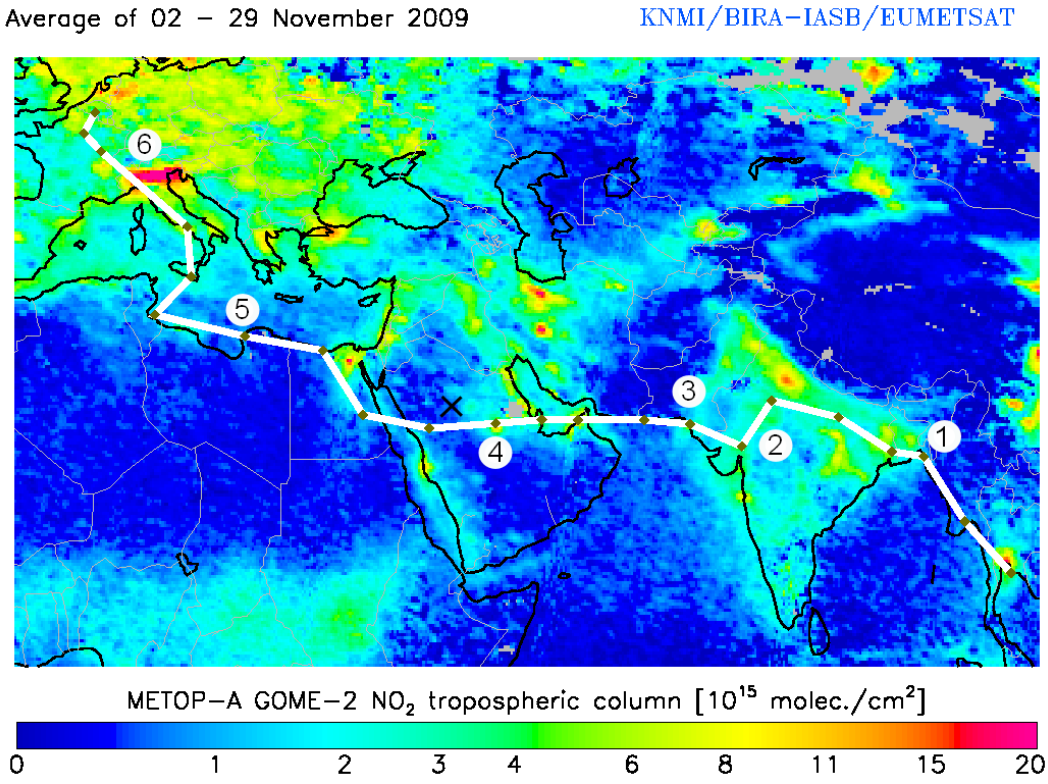

Figure 6.4: Flight tracks of the Earth Challenge expedition on a NO_2 GOME-2 map. The numbers correspond to the measurements presented in this paper: (1) Chittagong (Bangladesh, 4 November 2009), (2) Rajasthan (India, 15 November 2009), (3) Karachi (Pakistan, 16 November 2009), (4) Riyadh (Saudi Arabia, 24 November 2009), (5) Benghazi (Libya, 27 November 2009), (6) Po Valley (Italy, 2 December 2009). The cross west of Riyadh indicates a sand storm (see section 6.5.3).

surements have been reported in the literature. For some of them, e.g. megacities like Karachi and Riyadh, high pollution levels are expected to be found. During the first part, instrument problems prevented the making of measurements after Brisbane (Australia).

6.3 Spectral analysis and NO_2 column retrieval

This section describes the three steps of the data analysis: the DOAS fit, which retrieves integrated concentration along the photon path, the air mass factor cal-

culation used to derive a geophysical interpretation from the DOAS fit, and finally the propagation of the different uncertainties in the error budget.

6.3.1 DOAS analysis

Molecular absorption of NO_2 is commonly retrieved in UV-visible atmospheric spectra using the DOAS technique (Platt and Stutz, 2008). This method relies on the fact that, for certain molecules including NO_2, the absorption cross-sections vary much more rapidly with wavelength than the scattering effects (Rayleigh and Mie). In practice, a measured spectrum ($I(\lambda)$) is divided by a reference ($I_{\text{ref}}(\lambda)$) to remove solar Fraunhofer structures and reduce instrument effects. The slow variations in the logarithm of this ratio are filtered out with a low-order polynomial ($P(\lambda)$), and the remaining absorption structures are fitted in a least-square sense with high-pass filtered laboratory cross-sections ($\sigma'_i(\lambda)$). The equation of DOAS, originating from the Beer–Lambert law, can thus be written as:

$$\ln \frac{I(\lambda)}{I_{\text{ref}}(\lambda)} = -\sum_i \sigma'_i(\lambda) \cdot \text{DSCD}_i + P(\lambda) \tag{6.1}$$

In the above equation the index i represents one particular absorber. DOAS analysis results are, for each considered absorber, in the form of Differential Slant Column Density (DSCD), i.e. the differences between the concentration integrated along the optical path of the measurement (SCD, slant column density) and the corresponding quantity in the reference spectrum (SCD_{ref}):

$$DSCD = SCD - SCD_{\text{ref}} \tag{6.2}$$

Table 6.1 lists the DOAS analysis settings used for the retrieval of NO_2 DSCDs. These settings were implemented in the QDOAS software, developed at BIRA-IASB (Fayt et al., 2011). The Ring effect is fitted as a pseudo-absorption as described in Chance and Spurr (1997b).

Figure 6.6 presents a typical NO_2 DOAS result. The corresponding analyzed and reference spectra originate from the same flight on 2 December 2009, but the former was recorded in the Po Valley while the latter above a clean zone at higher altitude. The first four panels show the simultaneously fitted absorptions of NO_2 (panel a), water vapor (panel b), the $(O_2)_2$ collision complex referred to as O_4 (panel c), and ozone (panel d) in the form of optical densities relative to the reference spectrum. The lowest panel displays the fit residuals. The four absorbers are clearly detected, and NO_2 optical density is particularly high (1 % peak-to-peak), which is expected in the Po Valley, one of the most polluted areas in Europe regarding NO_2 (see figure 6.4).

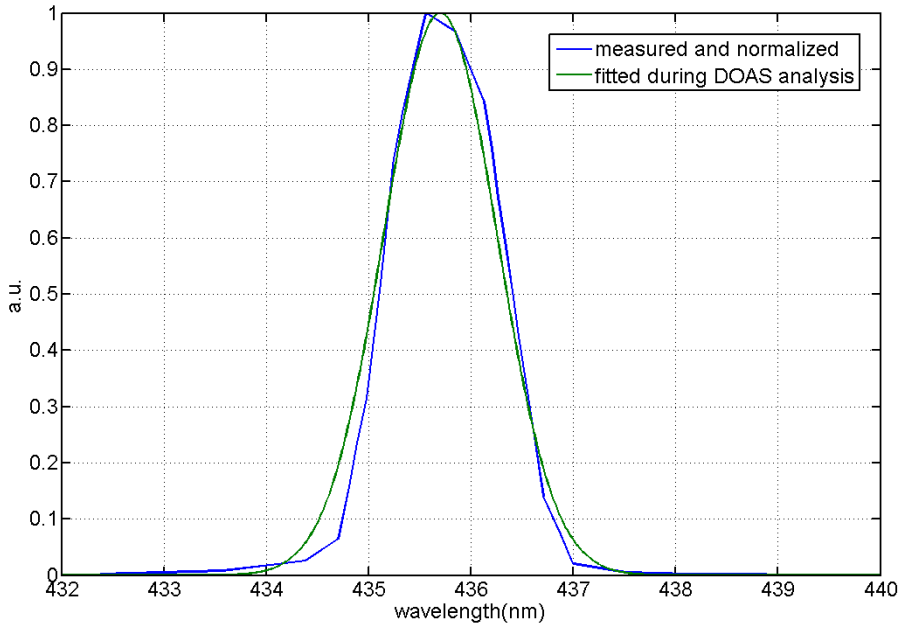

Figure 6.5: Slit function measured in the lab using a Hg lamp and fitted from the spectra.

6.3.2 Air mass factors calculation

The DOAS analysis per se provides only a qualitative insight into the NO_2 field. Indeed, beside being relative to a reference column, a DSCD depends on the light path through the atmosphere. A more relevant geophysical quantity is the NO_2 concentration integrated vertically along the atmosphere, i.e. the NO_2 Vertical Column Density (VCD). The Air Mass Factor (AMF) is defined as the ratio between the slant and vertical column densities:

$$AMF = SCD/VCD \tag{6.3}$$

In the following, we describe our assumptions to derive the tropospheric VCD from Eq. (6.3) and the practical calculations of a tropospheric AMF.

6.3.2.1 Assumptions for the tropospheric column retrieval

The slant column is first splitted in its tropospheric and stratospheric components:

$$SCD = AMF_{\text{tropo}} VCD_{\text{tropo}} + AMF_{\text{strato}} VCD_{\text{strato}} \tag{6.4}$$

Using the above expression for the slant column density in equation 6.2 leads to the following formula for the measured DSCD:

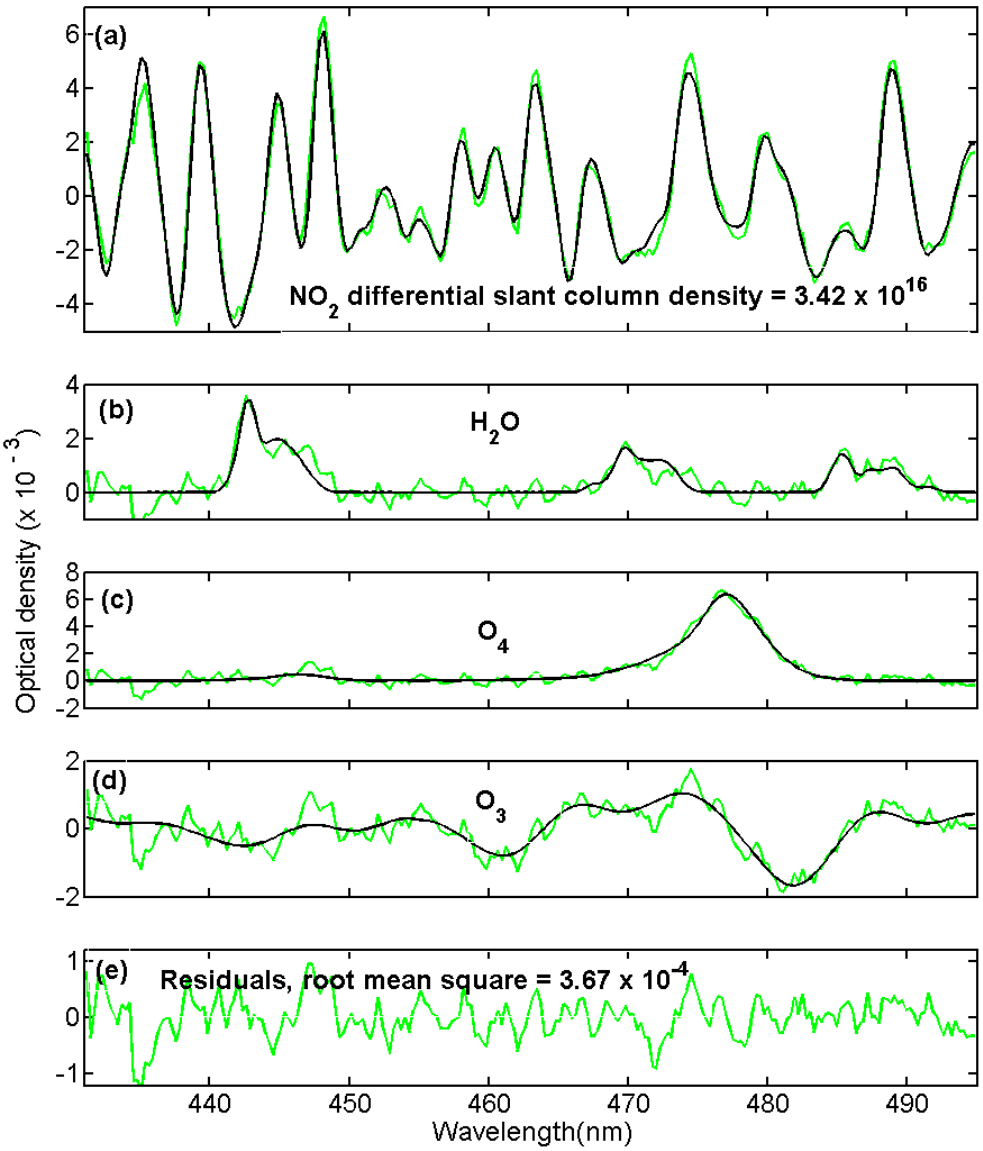

Figure 6.6: Example of a DOAS fit; the spectrum was recorded in the Po Valley. Black lines correspond to molecular cross-sections scaled to the detected absorptions in the measured spectrum (green lines).

$$\begin{aligned} DSCD =& AMF_{\text{tropo}} \cdot VCD_{\text{tropo}} + AMF_{\text{strato}} \cdot VCD_{\text{strato}} \\ & -(AMF_{\text{tropo}_{\text{ref}}} \cdot VCD_{\text{tropo}_{\text{ref}}} + AMF_{\text{strato}_{\text{ref}}} \cdot VCD_{\text{strato}_{\text{ref}}}) \end{aligned} \tag{6.5}$$

Table 6.1: DOAS analysis settings for the ULM-DOAS.

Fitting window	431–495 nm
NO_2	Vandaele et al. (1998)
O_4	Hermans
	`http://www.aeronomie.be/spectrolab/o2.htm`
H_2O	Harder and Brault (1997)
O_3	Burrows et al. (1999)
Ring	Chance and Spurr (1997b)
Polynomial order	3

Equation 6.5 may be simplified if the reference spectrum is well chosen. Due to its short lifetime in the troposphere, $\mathrm{VCD}_{\mathrm{tropo}_{\mathrm{ref}}}$ column can be assumed to be null far enough from the NO_2 emission sources, e.g. above the deserts or the oceans. If on the other hand the reference spectrum is taken the same day when the Sun is high enough, stratospheric contributions cancel each other, since the stratospheric NO_2 is slowly varying during the day and the stratospheric AMF is constant. Equation 6.5 can be thus approximated as:

$$DSCD = AMF_{\mathrm{tropo}} \cdot VCD_{\mathrm{tropo}} \tag{6.6}$$

From Eq. (6.6) it is possible to retrieve $\mathrm{VCD}_{\mathrm{tropo}}$, assuming independence between a given $\mathrm{AMF}_{\mathrm{tropo}}$ and $\mathrm{VCD}_{\mathrm{tropo}}$. This is usually done and implies that the NO_2 loading is optically thin enough that it does not influence the radiative transfer. The resulting AMF still depends then on the NO_2 profile but not on its absolute value. This hypothesis is used in the following after having checked its validity (see next section).

6.3.2.2 Radiative transfer: assumptions on NO_2 and aerosol extinction profiles

The radiative transfer model used in this study is UVspec/DISORT (Mayer and Kylling, 2005). Setting a grid 10 km high, the stratospheric contribution is neglected, as discussed in the previous section.

Considering the DOAS fitting window (see section 6.3.1), calculations are done at 460 nm. The GPS data recorded with the spectra allow for an accurate calculation of the Sun's position and the aircraft's heading. To take into account the numerical aperture of the optical fiber, each SCD is the weighted mean of 13 SCDs at uniformly distributed angles between -12 and 12 degrees around the horizon. The weights correspond to the different radiances calculated in the respective intermediate Slant Column Density (SCD) geometries.

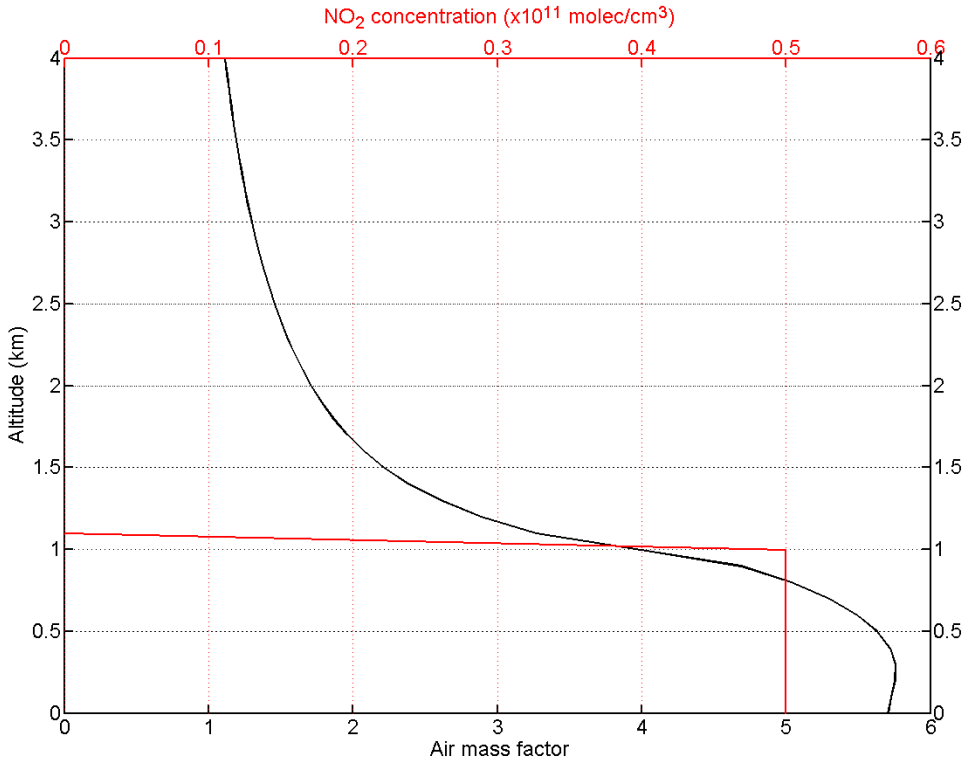

Figure 6.7: Air mass factor versus altitude (black) for an idealized NO_2 tropospheric profile (red) well mixed in the boundary layer and of negligible concentration in the free troposphere. The calculations were done at 460 nm, setting an albedo of 0.1, a relative azimuth and solar zenith angle of 90° and 45°, respectively, and a surface visibility of 20 km.

The NO_2 and aerosol profiles in the model both correspond to a well-mixed boundary layer and negligible concentrations and extinction in the free troposphere (for the NO_2, see figure 6.7). The boundary layer heights are interpolated from European Centre for Medium-Range Weather Forecasts (ECMWF) forecasts at the time and heights of the measurements, except for Riyadh (see section 6.5.1). In clean areas, these assumptions may not be realistic enough, as was showed by the ALS-DOAS measurements during Polar Study using Aircraft, Remote Sensing, Surface Measurements and Models, of Climate, Chemistry, Aerosols, and Transport (POLARCAT), where we detected a NO_2 layer in the free troposphere. On the other hand, in urban areas, larger concentrations are found close to the ground than higher up in the boundary layer (Dieudonné, 2012). The measurements presented in this study were recorded in polluted zones but not directly above cities, where turbulent dispersion lead to homogeneous vertical distribution

(Vinuesa and Galmarini, 2009). Considering NO_2, Heland et al. (2002) studied the effect of the profile's shape comparing aircraft in-situ and OMI data, concluding that it was relatively weak. Boersma et al. (2009) also assumed a homogeneous boundary layer to compare in-situ surface NO_2 concentrations with SCIAMACHY (SCanning Imaging Absorption SpectroMeter for Atmospheric CartograpHY) and OMI columns. This is also confirmed by the few tropospheric NO_2 lidar measurements available (Volten et al., 2009). Considering aerosol extinction, the many lidar profiles available in polluted zones (e.g. Landulfo et al., 2003; Guibert et al., 2005) indicate a maximum extinction in the boundary layer, even if the shape is less step-like. In practice, we derive aerosol optical thickness at 550 nm from Moderate Resolution Imaging Spectroradiometer (MODIS) retrieved from Giovanni (GES-DISC Interactive Online Visualization ANd aNalysis Infrastructure), Acker and Leptoukh, 2007) and divide it by the Boundary Layer Height (BLH) to get the extinction coefficient. This extinction coefficient is then scaled at 460 nm using the Angstrom coefficient as described in Nebuloni (2005), and derive visibility at this wavelength from the Koschmieder law (Koschmieder, 1926). The same approach to estimate the visibility will be used for the GEOS-R satellite (NOAA-NESDIS, 2010).

Figure 6.7 shows the variation of the AMF with the observation's altitude for the idealized profile considered in the model. In the calculations, the solar zenith angle was 45°, the visibility 20 km, and the albedo 0.1. These numbers are representative of the conditions of the campaign. The AMF and thus the sensitivity are maximum when the aircraft flies at 500 m altitude, where the AMF is around 5.6. The AMF then decreases sharply when the plane crosses the boundary layer. This indicates that this parameter is important for the accuracy of our measurements.

Figure 6.7 also indicates the typical horizontal resolution of our measurements, directly related to the product of the AMF and the boundary layer height with our assumptions on the profile. Flying inside the NO_2 layer, the horizontal resolution is close to 5 km. This rather large number arises from the limb geometry.

For the retrievals, air mass factors are interpolated in look-up tables calculated for each flight around the places of interest (see figure 6.4). The parameters in the look-up tables are aircraft's altitude, relative azimuth, solar zenith angle, boundary layer height, visibility, and albedo. For a given flight, the first three parameters vary according to the GPS data, while the last three are set constant.

6.4 Sensitivity studies and error analysis

Figure 6.8 shows the variation of the air mass factor for the visibility, pitch angle and albedo in the typical ranges of the flights. Surface visibility plays the largest

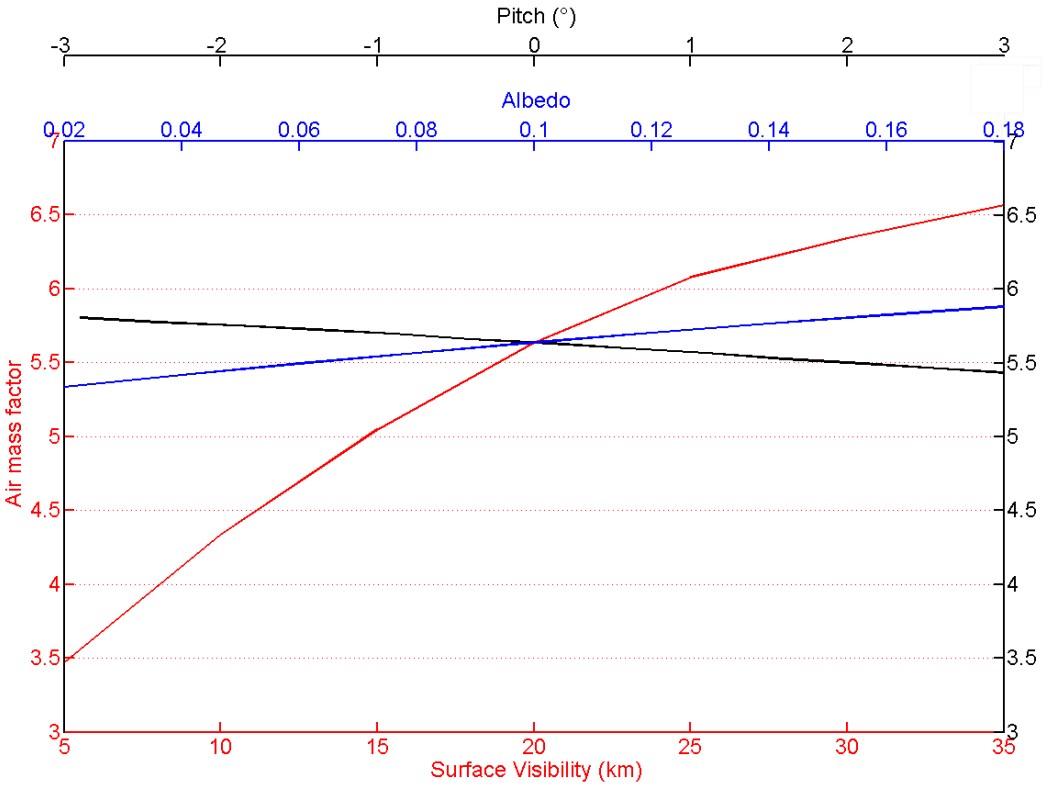

Figure 6.8: Air mass factor versus surface visibility (red), albedo (blue) and pitch angle (black). The last two parameters only have small effects due to the limb observation geometry and the large field of view, respectively. The calculations were done at 460 nm for an altitude of 0.5 km, setting a relative azimuth and solar zenith angle of 90 ° and 45°, respectively, and with a 1 km thick homogeneous boundary layer.

role in the AMF variation, which is understandable from the limb geometry of our measurements. For the same reason, albedo very weakly affects the air mass factor. Indeed, most of the detected photons are scattered before reaching the ground, as illustrated in figure 6.1, and thus not affected by its reflectivity. This is very different from nadir-looking satellites, for which the albedo uncertainty matters much more in the final error budget, as can be seen in Boersma et al. (2004). Finally, the small effect of the pitch angle is due to the large field of view: the multiple lines of sight smooth the variation in aircraft attitude.

Figure 6.9 displays an effect that is often neglected in DOAS studies, i.e. the influence of the studied absorber on the radiative transfer and thus the AMF itself. When the absorber's column, in our case NO_2, is high enough, it can not

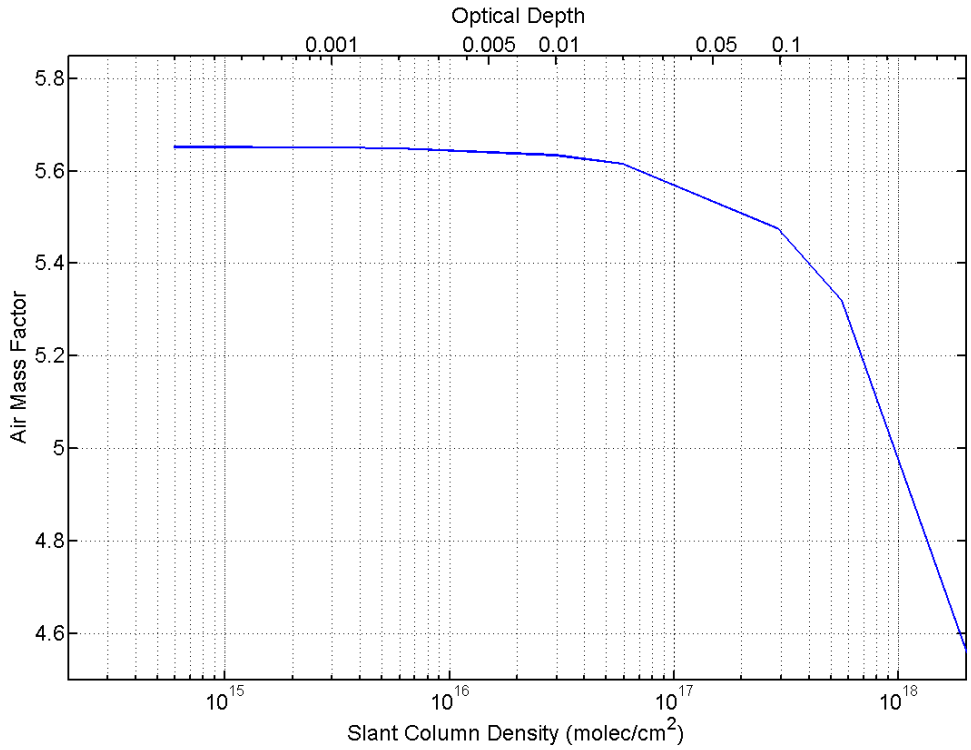

Figure 6.9: Air mass factor versus slant column density. NO_2 loading starts to influence significantly the radiative transfer above 5×10^{16} molec/cm^2. The calculations were done at 460 nm for an altitude of 0.5 km, setting a relative azimuth and solar zenith angle of 90° and 45°, respectively, and with a 1 km thick homogeneous boundary layer.

be considered as optically thin and reduces the air mass factor. The effect is visible from 5×10^{16} molec/cm^2, corresponding to an optical density of 0.02. We believe this error should be considered when accurate error budgets are necessary, since it could play a larger role than the cross-section uncertainties, for instance, which are often taken into account. In particular, low-elevation Multi-Axis DOAS (MAX-DOAS) measurements in polluted regions are likely to be affected by this error.

Table 6.2 indicates the uncertainties considered in this study and their effect on the relative air mass factor. The accuracy of the ECMWF boundary layer heights was investigated by Palm et al. (2005), who concluded that the BLH were 200–400 m underestimated. We thus consider an error of 300 m for this parameter. This is the major source of error in our measurements, leading to 15 % uncertainty on the AMF. Considering the albedo, Kleipool et al. (2008) derived an absolute

uncertainty of 0.01 to 0.02 for the OMI albedo used in our AMF calculation. We use 0.05, as this parameter's role is not critical anyway (1 % on AMF). The uncertainty in the visibility is set to 6 km. This value originates from the propagation in Koschmieder's law of the 300 m uncertainty for the BLH already mentioned and a typical uncertainty of 0.1 for the aerosol optical thickness (AOT), which was derived from a comparison between MODIS Aqua and CALIPSO (Cloud-Aerosol Lidar and Infrared Pathfinder Satellite Observations) (Kittaka et al., 2011). Finally, the error due to the effect of NO_2 on the radiative transfer leads to 1 % uncertainty on the AMF, a small effect, but comparable to the errors due to the pitch and the albedo.

Table 6.2: Error contributions to the air mass factor (AMF).

	Δ parameters	$\frac{\Delta \mathrm{AMF}}{\mathrm{AMF}}$
Boundary layer height	300 m	15 %
Visibility	6 km	12 %
Correlation between BLH and visibility	0.95	14 %
Pitch	2°	2 %
SCD	5×10^{14} molec/cm^2	1 %
Albedo	0.05	1 %

In practice, the error on the tropospheric column is derived from Eq. (6.6) as:

$$\sigma_{\mathrm{VCD_{tropo}}} = \sqrt{\left(\frac{\sigma_{\mathrm{DSCD}}}{\mathrm{AMF}}\right)^2 + \sigma^2_{\mathrm{AMF}} \left(\frac{\mathrm{DSCD}}{\mathrm{AMF}^2}\right)^2} \tag{6.7}$$

In this equation, the error on the DSCD (σ_{DSCD}) is an output of the DOAS analysis (Fayt et al., 2011). The error on the AMF is the quadratic sum of the different errors discussed previously. Note that the correlation between the boundary layer height and the visibility is taken into account, introducing an adequate term in Table 6.2. The correlation coefficient is estimated from the values of the BLH and visibility in Table 6.3.

6.5 Results

This section presents the results for the flights of figure 6.4. First, our measurements are compared with satellite data (OMI and GOME-2) for the flights when these are available at the locations of our flights, and indicate the NO_2 loading above other interesting hot spots. Then, the measurements are used to estimate a flux for an isolated point source, Riyadh. Finally, we confirm a soil signature

in the spectra that closely matches results from a previous study on satellite data (Richter et al., 2011).

6.5.1 Comparisons with satellites

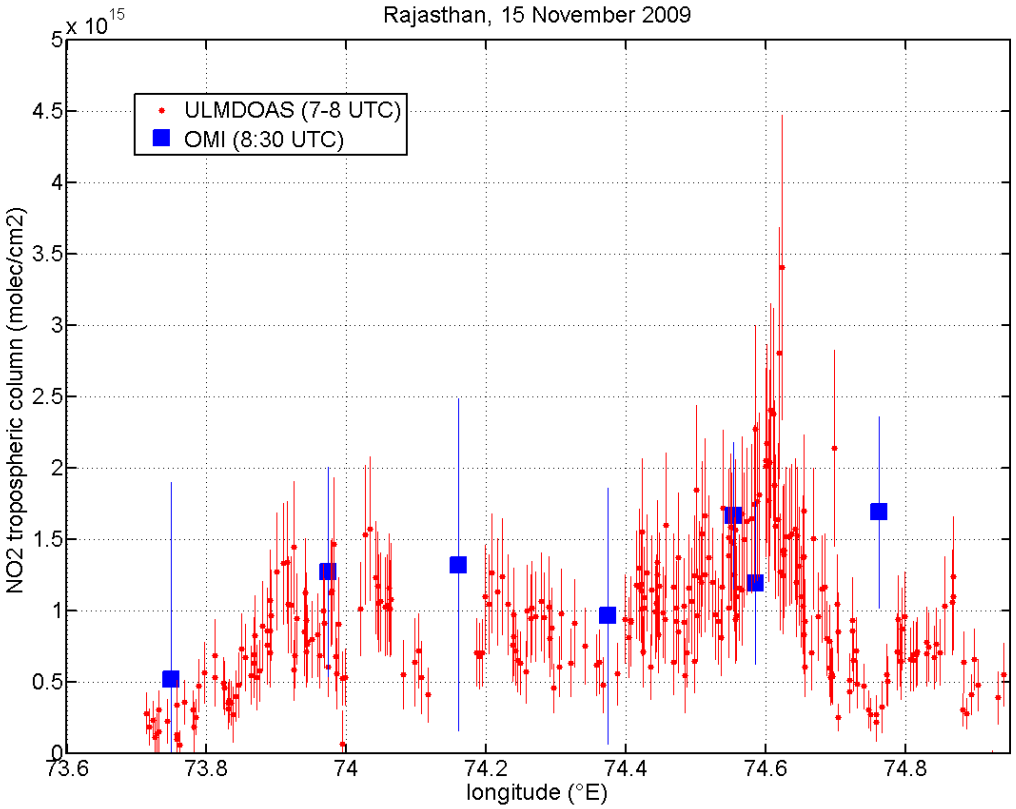

Figure 6.10: ULM-DOAS (red) and OMI (blue) measurements over Rajasthan, India (15 November 2009). ULM-DOAS data were recorded between 07:26 and 08:47 UTC and cover the latitude range from 25.79° to 24.39°. The NO_2 field is rather uniform.

Figures 6.10, 6.11, and 6.12 compare OMI (DOMINO (Dutch OMI NO_2) version 2.0, Boersma et al., 2011) and GOME-2 (TM4NO2A version 2.1, Boersma et al., 2004) data with our ULM-DOAS measurements, above Rajasthan (15 November 2009), the Po Valley (2 December 2009), and Saudi Arabia (24 November 2009). The flight conditions are detailed in lines 2, 6, and 4 of Table 6.3, respectively. These three areas represent an interesting sample of the global tropospheric NO_2

field above land. Indeed, the first two areas indicate rather homogeneous tropospheric NO_2 loadings, but absolute values are one order of magnitude higher in the Po Valley than in Rajasthan. In Saudi Arabia, the situation is very different, since one megacity, Riyadh, is surrounded by desert with very few NO_2 sources. This yields high columns close to the city, rapidly decreasing to reach negligible values further away above the desert.

The agreement between ULM-DOAS and satellite data is qualitatively good for the three days, but better quantitatively above Rajasthan and Italy than above Saudi Arabia. Above Rajasthan (figure 6.10), the tropospheric NO_2 columns seen from the aircraft span from 0.1 ± 0.1 to $3 \pm 1 \times 10^{15}$ molec/cm^2, whereas from OMI 0.5 ± 0.6 to $1.7 \pm 1 \times 10^{15}$molec/cm^2. This discrepancy might be explained by a dilution effect; indeed OMI is not able to resolve spatial structures at scales smaller than 20 km. Most of the points are, however, inside the error bars. Considering the Po Valley (figure 6.11), OMI data are unfortunately affected by the row anomaly (Boersma et al., 2011), but the GOME-2 measurement and our airborne measurements are very close, around $2.6 \pm 0.6 \times 10^{16}$ molec/cm^2. Note that the two peaks at longitude 10.1° and 10.4° E are coincident to O_4 DSCD higher values and are thus probably due to enhancement in the light path owing to scattering in clouds.

Figure 6.12 indicates a positive bias between ULM-DOAS measurements and satellite data in the region where the NO_2 columns are highest. In the case of GOME-2, this can be explained by the dilution effect considering the size of the pixels, and partly by the 3 h time difference. Considering OMI data, these effects are expected to be much smaller, since the two measurements are almost simultaneous and the spatial resolution of OMI is much better than GOME-2. For this area, standard MODIS Aqua data are not available and we had to use the MODIS Deep blue product AOT, i.e. 0.2, to estimate the visibility. There is an Aeronet station close to Riyadh (Sabbah and Hasan, 2008), but the data set is discontinuous for the period of the flight, and the only AOT measurement point, 0.45, leads to a reduced AMF and thus an even higher bias between our measurements and OMI. Note that offsets could also originate from an error in the boundary layer height, which is close to the observation altitude (see Table 6.3), or from a non-negligible part of the AOT in the free troposphere. The latter would increase the AMF for the ULM-DOAS measurements, while simultaneously reducing the satellite AMF, thus partly reducing the observed bias. For this area only, we use the GDAS (Global Data Assimilation System) archived boundary layer height instead of the ECMWF, which is surprisingly low for this day and leads to even larger discrepancies between OMI data and our measurements. This persistent bias and the fact that no validation has been achieved, to our knowledge, over deserts leads us to point out the necessity of other measurements to check for a

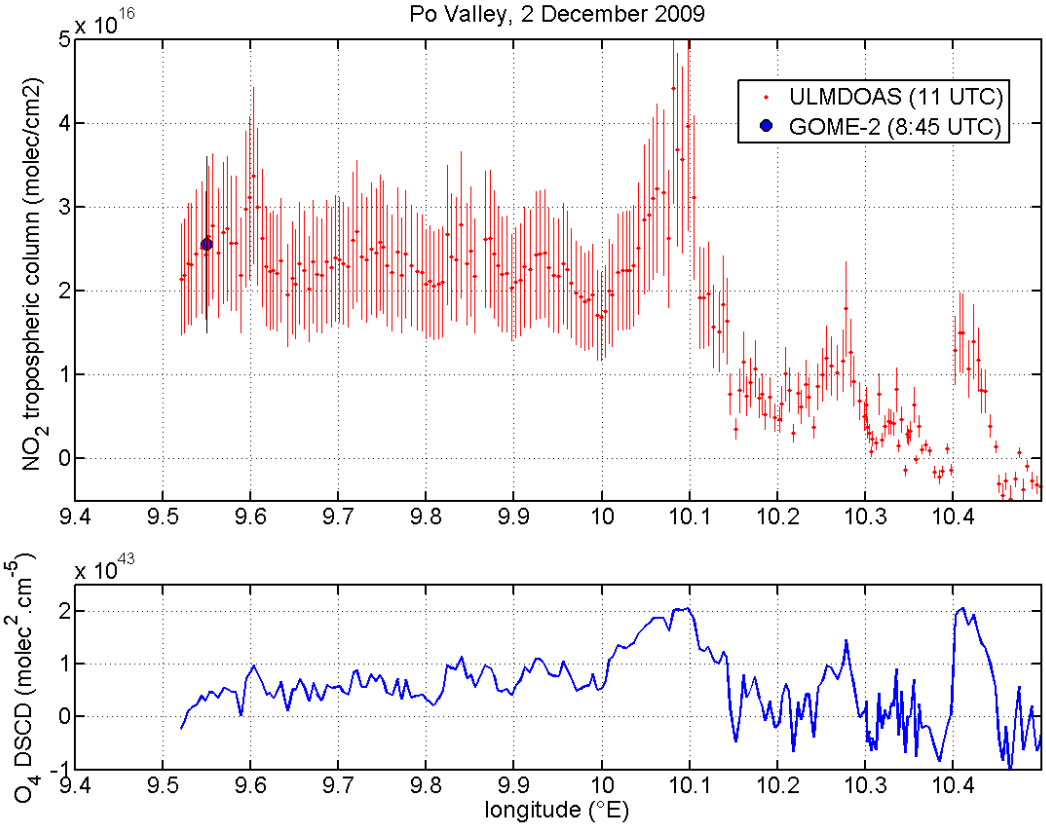

Figure 6.11: ULM-DOAS (red) and GOME-2 (blue) measurements over Italy (2 December 2009). ULM-DOAS data were recorded between 10:29 and 12:14 UTC and cover the latitude range from 44.58° to 45.54°. The zone west of 10° E is the Po Valley.

possible underestimation of OMI data in similar areas.

Table 6.3: Conditions and results of the campaign. See figure 6.4 for the places and dates of the measurements. We give the main parameters for calculating the air mass factor (AMF), i.e. the surface visibility (Vis.), the solar zenithal angles (SZA) and relative azimuth (rel Az.), the boundary layer height (BLH), the albedo (Alb.) and the altitude of the aircraft (Alt.). The tropospheric column (VCD_{tropo}) is the typical value found while overflying the areas.

Meas.	Vis. (km)	SZA (°)	rel Az. (°)	BLH (km)	Alb. (%)	Alt. (km)	AMF	VCD_{tropo} (molec/cm^{-2})	Conc. (μg/m^3)
1	n/a	38	140	1.3	6	0.3	n/a	n/a	n/a
2	24	45–51	16	2.1	10	0.6	4.4	$0.25 \pm 0.8 \times 10^{16}$	1
3	20	59	25	1.6	11	0.15	4.9	$2.4 \pm 0.8 \times 10^{16}$	10
4	15	46–64	70	1.1	14	1.25	2.1	$2 \pm 0.6 \times 10^{16}$	15
5	23	57	125	1.5	8	0.5	5.8	$2.3 \pm 0.8 \times 10^{16}$	10
6	10	67	145	0.4	6	0.65	2.1	$2.2 \pm 0.8 \times 10^{16}$	40

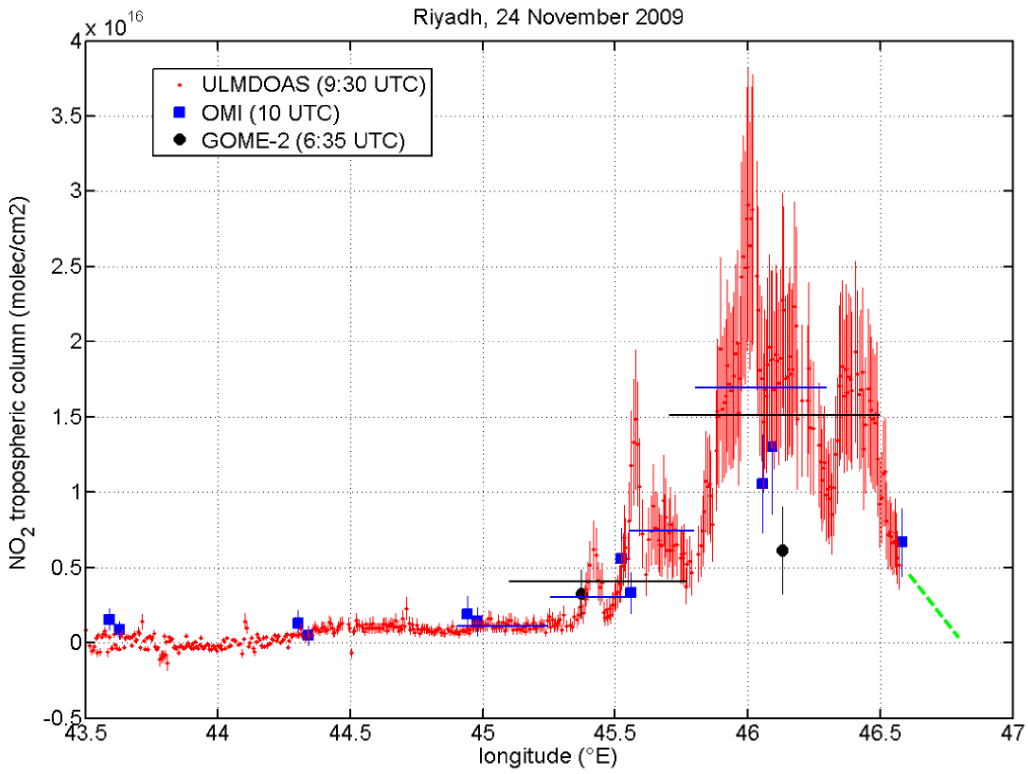

Figure 6.12: ULM-DOAS (red), OMI (blue), and GOME-2 (black) measurements over Saudi Arabia (24 November 2009). ULM-DOAS data were recorded between 09:07 and 12:03 UTC and cover the latitude range from 25.18° to 24.79°. Horizontal blue and black lines correspond to ULM-DOAS data averaged over OMI and GOME-2 pixel extensions, respectively. ULM-DOAS tropospheric NO_2 measurements are larger in this case than the ones seen by both satellites.

Figure 6.13 helps to interpret the patterns seen in the pink box of figure 6.12. It presents the OMI pixels around Riyadh, superimposed on a map with Riyadh extent, the main wind direction retrieved from GDAS and the ULM-DOAS flight track. The color code is the same for OMI and ULM-DOAS data. The megacity occupies an area slightly smaller than three OMI pixels, and the aircraft was flying 70 km northwest of it when it detected the highest NO_2 columns. ULM-DOAS and OMI data are both understandable from the wind direction as a pollution plume of the city, which would have, compared to this source, a relatively similar horizontal extent. It is thus possible to calculate the NO_2 flux, integrating horizontally the column and then multiplying by the projection of the wind vector on the normal to the flight track. Such a calculation leads to a flux of around 140 mol/s. Note

that to obtain this value, we added the ghost part of the plume west of 46.7° E, depicted in green in figure 6.12. Due to that and the wind uncertainties, we find it difficult to estimate the associated error. Nethertheless, the value is relatively close to the one derived by Beirle et al. (2011) from satellite, i.e. 187 ± 14mol/s. This points out that, providing accurate wind data, our instrument would be useful to estimate flux from megacities. This has been done from cars (e.g. Johansson et al., 2009a), but an aircraft covers an exhaust plume in a much shorter time and is thus less sensitive to temporal variations of the NO_2 field.

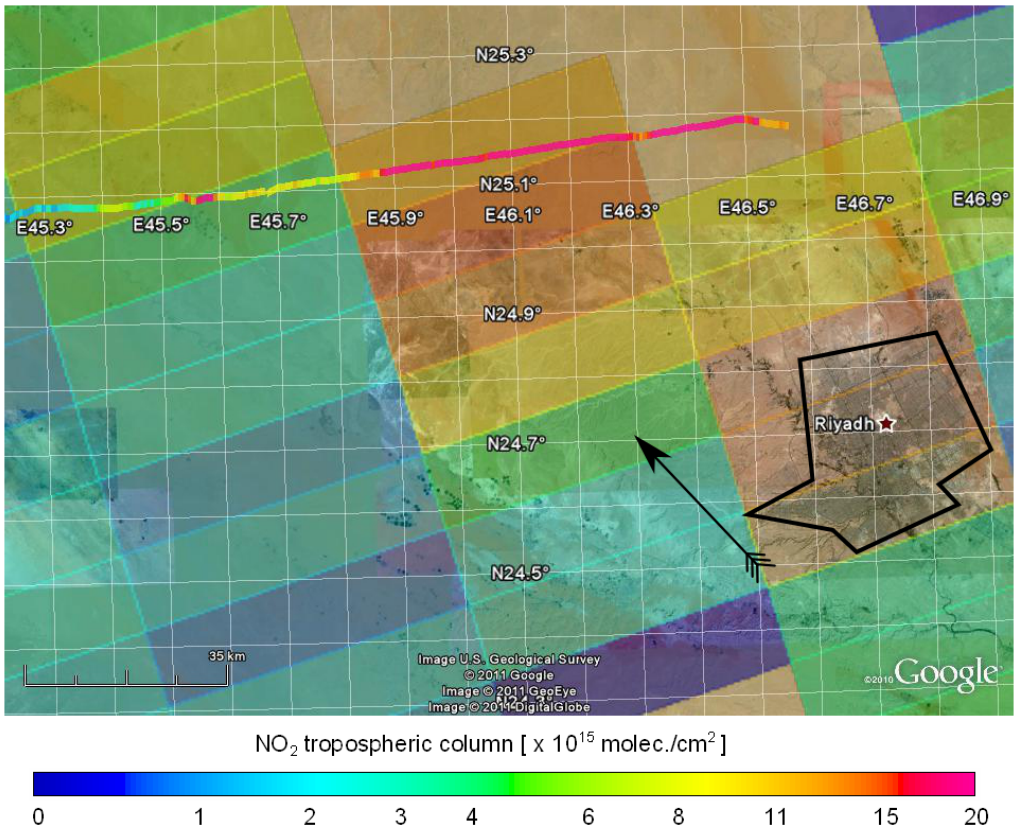

Figure 6.13: Map of Riyadh surrounding, with ULM-DOAS and OMI NO_2 data superimposed. Riyadh agglomeration is delimited by the black polygon. The arrow indicates the wind direction according to the GDAS archive.

6.5.2 Other interesting measurements

Table 6.3 summarizes the main results of the campaign and the conditions of the measurements. The numbers representing the measurements are related to figure 6.4. We do not estimate the uncertainty on the mass concentration, which would be correlated to the uncertainty on the boundary layer height, because even if our measurements have a finer spatial resolution than satellites, the real NO_2 field can be much more heterogeneous than seen by our instrument. These considerations also apply to our measured vertical columns, but they are less relevant in the context of comparing with satellite data.

Figure 6.14: Picture of Chittagong ship cemetery taken during the expedition. The visibility is obviously low. Courtesy of Michel de Maegd.

In addition to the measurements described in the previous section, we report the measured NO_2 tropospheric column close to three large cities, Chittagong (1), Karachi (3) and Benghazi (5). The latter two are usually visible from OMI and the corresponding MODIS Aqua AOT is available for both. Karachi is one of the largest cities in the world regarding population (15 million inhabitants). We estimate the tropospheric NO_2 column during the landing on an airport 15 km east of the city center to be $2.4 \pm 1 \times 10^{16}$ molec/cm^2. Benghazi is a comparatively much smaller city. Nevertheless we also detected high NO_2 loadings there, around $2.3 \pm 0.8 \times 10^{16}$ molec/cm^2. Such high columns are certainly linked to the industries of the city and particularly to its refineries.

Figure 6.14 is a picture taken by the pilots during the campaign, while flying above Chittagong. It shows one of the city's main industries, i.e. one of the largest ship cemeteries in the world. The picture coincided with high measured slant columns, around 4×10^{16} molec/cm^2. However, we did not convert these values to vertical columns, since no AOT data were available for the day of the flight. It is, however, obvious from the picture that the visibility is quite small, probably under 5 km. This probably results from a combination of a heat fog and of aerosols from the city. Therefore we can expect the AMF to be very small, which suggests that the NO_2 pollution was probably very high in this region.

6.5.3 Soil signature above desert

Richter et al. (2011), while improving GOME-2 NO_2 retrieval, empirically derived a soil signature visible in the spectra corresponding to desert areas. The inclusion of this signature yielded an improvement in the DOAS fit, mostly visible in regions with bare soils, e.g. the Sahara and the Arabic peninsula. Richter et al. (2011) also found a similar spectral shape in a lab experiment using sand. They nevertheless pointed out that more measurements were necessary to solidly confirm the attribution to a soil effect, particularly due to possible correlations with O_4.

Figure 6.15 shows the fit of the soil signature (A. Richter, personal communication, 2011) together with O_4 in a spectrum recorded above Saudi Arabia on 24 November 2009. The DOAS settings, except for the fitting window, are given in Table 6.1. The reference spectrum was recorded in Italy on 2 December 2009, which leads to a larger signal of the soil signature than using a reference spectrum from Saudi Arabia. This is understandable if the signature really originates from bare soil, which is present all along the flight on 24 November 2009, and thus in all the spectra, but not in Italy.

Figure 6.16 displays the time series of the DOAS fit results for the soil signature (upper panel) and the RMS (root mean square) fit with and without the soil signature (lower panel). Several episodes of enhanced soil signal are visible, the largest one just before 11:30 UTC. In the lower panel we see that these episodes appear as increased RMS time series if the DOAS fit does not include the soil signature (green curve). If the soil signature is taken into account (blue curve), the RMS is relatively constant over the flight.

The episodes just discussed are coincident with a sand storm that was reported by the pilots while approaching Medina. This reinforces our confidence that the soil signature identified by Richter et al. (2011) has indeed a geophysical origin, and that it can be detected on suspended sand particles. Using a reference spectrum recorded over the Gulf of Oman to analyze other flight spectra, we detected smaller low visibility episodes associated with soil signature in Rajasthan, Egypt

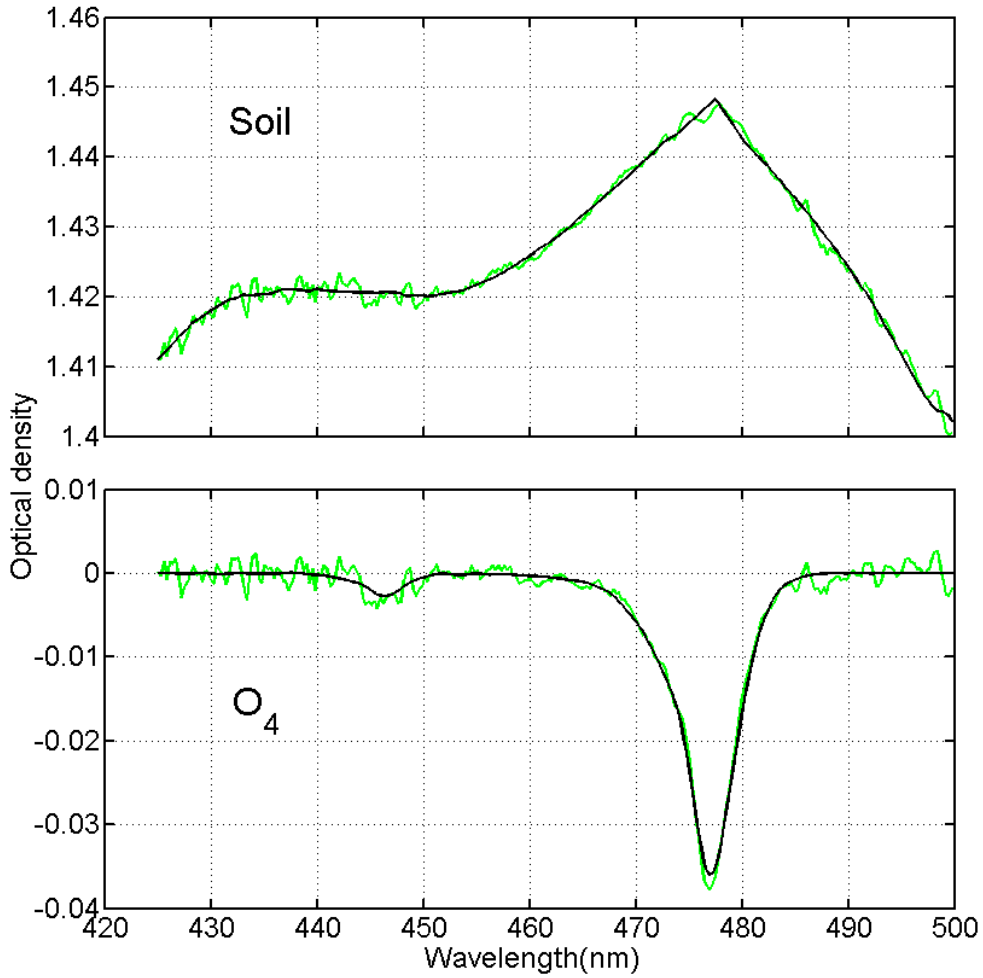

Figure 6.15: Soil signature in the spectra over the Arabian desert (upper panel). For comparison, the O_4 signature is displayed in the lower panel.

and Pakistan, but not over Italy. Note that the soil signature, due to its broad-band structure, is partly hidden in the DOAS fit using a higher order polynomial.

6.6 Conclusions on our participation to Earth Challenge

We presented a new airborne instrument designed for tropospheric NO_2 column measurement, the ULM-DOAS. It was operated during the Earth Challenge expe-

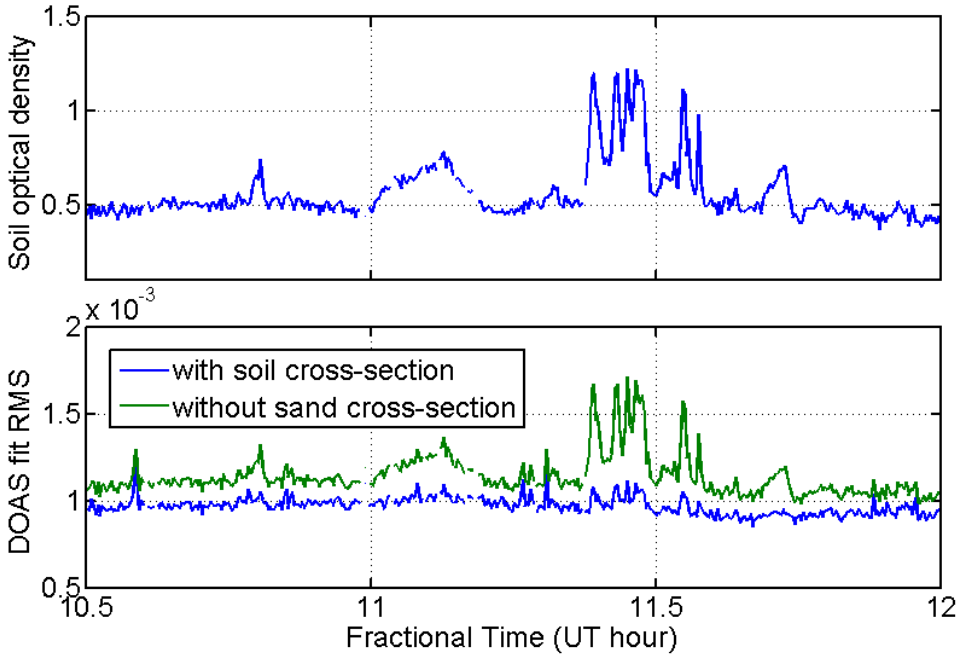

Figure 6.16: Time series of the soil signature signal (upper panel) and root mean square of the DOAS fit (lower panel), with (blue curve) and without (green curve) the soil signature in the fit. The spectra were recorded above Saudi Arabia when the pilots reported their crossing of a sand storm.

dition, which took place in 2009 between Australia and Belgium. The ULM-DOAS was designed to fit onboard the ultralight aircraft of the expedition and to be fully automatic. The set-up is simple without any attitude stabilization, and related uncertainties are minimized by the use of a large field of view. The limb geometry of the instrument makes it suitable for low-flying aircraft and maximizes the sensitivity to boundary layer NO_2.

Measurements during the Earth Challenge expedition are consistent with OMI and GOME-2 data and are interesting on their own, since very few validation campaigns were performed in the countries overflown. Highest NO_2 loadings were detected above megacities such as Karachi ($2.4 \pm 0.8 \times 10^{16}$ molec/cm^2) or Benghazi ($2.3 \pm 0.8 \times 10^{16}$ molec/cm^2). Our measurements also confirm the recent finding of a soil signature above desert.

Compared to satellite data, our instrument is able to detect higher spatial frequency patterns in the NO_2 field (around 5 km compared with an OMI pixel width of 13 km). We believe it is well suited for tropospheric NO_2 column validation, offering a low-cost alternative to larger aircraft measurements. Such measurements

are also well suited for flux measurements from extended sources, providing accurate wind data. The measurement accuracy would benefit from the addition of a compact PTU (pressure, temperature, relative humidity) sensor, indicating the aircraft position relative to the boundary layer, and of a small lidar to accurately measure simultaneously the extinction profile.

Chapter 7

Mobile-DOAS measurements

The Cabauw Intercomparison Campaign of Nitrogen Dioxide measuring Instruments (CINDI) took place in the Netherlands during summer 2009, between the two stages of the Earth Challenge expedition. CINDI provided another opportunity to develop an instrument for measurements of NO_2. The new instrument is operated from a car and we refer to it as a mobile DOAS system, to respect the terminology of previous studies.

This chapter is based on an article in preparation for the special issue on the CINDI campaign in Atmospheric Measurement Techniques. Two other mobile instruments have been of particular importance for the origin of this PhD: a LIDAR used, e.g. to detect SO_2 from the volcanic plume of Mount Etna (Weibring et al., 2003) and a FTIR which, in particular, quantifies alkenes from oil refineries (Mellqvist et al., 2010).

7.1 State-of-the-art of mobile trace gases measurements

Two kinds of DOAS instruments are now used from cars, defined by their observation geometry: zenith-only and multi-axis (MAX) systems. Both of them quantify trace gases absorption in scattered sky-light and they both have, for instance, enabled estimations of flux from given sources by driving around them in stable wind conditions. Zenith mobile DOAS system are simple and robust apparatus, which enables estimation of large sources like megacities (e.g. NO_2 and H_2CO from Mexico (Johansson et al., 2009b)) or extended industrial complexes (e.g. NO_2 and SO_2 around Texas refineries (Rivera et al., 2010)). Multi-axis mobile system reported so far use a compact motorized scanner. Looking closer to the horizon enhances the sensitivity to the lowest layers of the troposphere, where lies the bulk of short-lived pollutants (Hönninger et al., 2004). Such mobile MAX-DOAS measurements

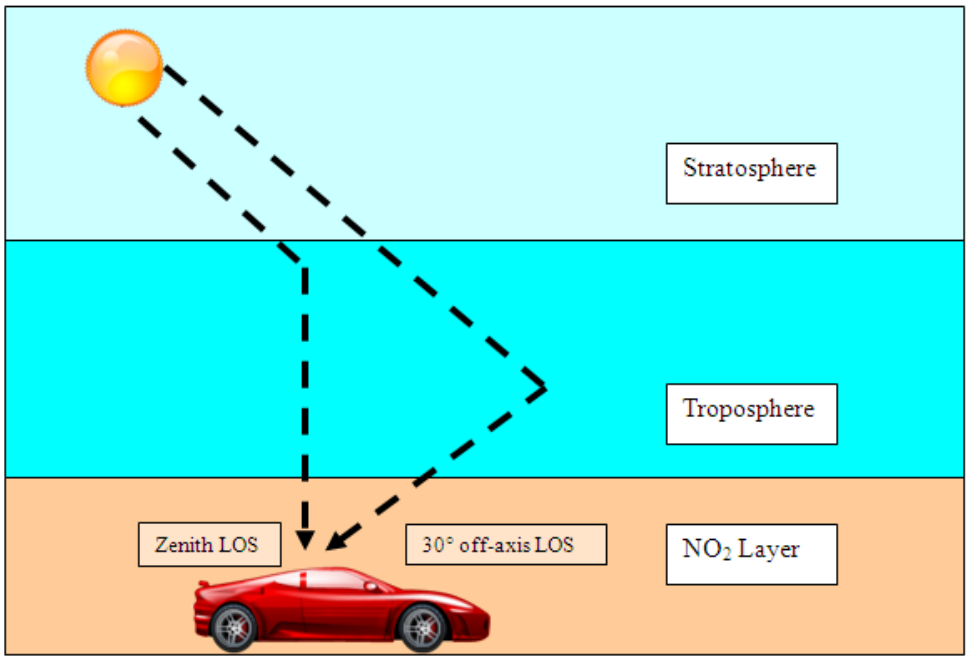

Figure 7.1: Geometry of the Mobile-DOAS measurements.

are reported in Europe (Wagner et al., 2010), (Ibrahim et al., 2010), and around Dehli, India (Shaiganfar et al., 2011).

The originality of the work presented here consists, first, in the newly developed instrument, secondly, in the data analysis strategy, and thirdly and most importantly, in the large measurements database. The instrument follows the MAX-DOAS principle, but using two spectrometers measuring scattered light spectra in parallel at different elevation angles. This reduces the problem of inhomogeneities in the trace gases field observed from mobile MAX-DOAS instruments (Wagner et al., 2010). To retrieve the vertical tropospheric columns, previous mobile MAX-DOAS studies (Wagner et al., 2010; Ibrahim et al., 2010; Shaiganfar et al., 2011) assume that the light path can be approximated from the observation geometry - the so called geometrical approximation- leading to an error of 15%. We show with radiative transfer calculations that this uncertainty may be underestimated. As a consequence, we do not use the geometrical approximation. Regarding the measurements database, a common characteristics of all the aforementioned studies is their short timespan. Measurements are typically performed during expensive field campaigns of a few weeks at most, in which the number of interesting days is even further reduced by meteorological conditions. In contrast, we took advantage of the business travels of a maintenance engineer across Belgium in 2010 and 2011

Figure 7.2: The Mobile-DOAS in Hoek Van Holland during CINDI.

to perform Mobile-DOAS observations whenever the weather enabled it.

We describe in the next section the Mobile-DOAS instrument and its data analysis scheme, primarily targeted to boundary layer NO_2. In section 3, we report the first operation of the new instrument during the CINDI campaign in summer 2009. In section 4, we present the routine measurements of 2010-2011. The scientific interest of the dataset is first illustrated by comparing them with a chemical transport model.

7.2 Description of the Mobile-DOAS

Figure 7.1 presents the observation geometry of the BIRA-IASB Mobile-DOAS instrument. The scattered light spectra are recorded simultaneously in the zenith direction and 30° above the horizon, following the MAX-DOAS approach. The system originates from the ULM-DOAS instrument (see chapter 6) and its technical details are described in (Piters et al., 2012). It is based on two similar compact Avantes spectrometers. The entry slit of each spectrometers is 50 μm, the focal length 75 mm and the grating is a 600 l.mm^{-1}, blazed at 300 nm. The CCD detector is a Sony 2048 linear array. An optical head (see figure 4.2), mounted on the car window, holds the two telescopes with fused silica collimating lenses of

focal length 8.7 mm, leading to a field of view of 2.6°(see chapter 4). Two 400 μm optical fibers, protected with chrome plated brass, connect the telescopes to the spectrometers. The spectrometers are controlled by a laptop and a GPS antenna is used for georeferencing the measurements. The whole set-up is powered by the 12V car battery through an inverter. The optical head, fibers, and GPS antenna can be seen on figure 7.2 taken in Hoek Van Holland during the CINDI campaign.

While measuring, the instrument is recording spectra continuously from the two directions. The integration time is fixed during a measurement sequence and is typically around 5 ms. The signal-to-noise ratio is increased by averaging a series of 10 accumulations on the CCD to produce an intermediate spectrum. These intermediate spectra are transferred to the computer and filtered by the acquisition program, removing those with too low or saturated signal. A second averaging is then applied to a spectra series of 8s to produce a final spectrum, the process being repeated continuously. The spatial resolution of the measurements depends on the car speed. At 60 km.h^{-1}, each measurement represents an horizontal integration on 133 m. The DOAS settings are similar to the one used for the ULM-DOAS spectra (see table 6.1 in chapter 6).

7.3 Retrieval scheme for NO_2 vertical columns

This section presents the methods used to estimate the tropospheric vertical columns of NO_2 from the DOAS fits corresponding to the spectra recorded in the two directions. We establish first the relationships holding between the DOAS measurements and the vertical columns if the NO_2 field is the same for the two channels. The commonly used geometrical approximation is then ruled out from considerations on the NO_2 profile and radiative transfer simulations. Finally, a method to take into account the NO_2 field inhomogeneities is proposed together with its error budget.

7.3.1 Case of a homogeneous NO_2 field

The DOAS analysis extracts from the spectra of the two channels the integrated absorption of NO_2 along the light path, relative to a reference spectrum, namely the differential slant column densities ($DSCDs$). This quantity is related to the tropospheric vertical column (VCD_{tropo}) through the tropospheric air mass factor (AMF_{tropo}), the reference column (SC_{res}), and the stratospheric slant column (SC_{strato}). The reference spectra are specific to each spectrometer but they are recorded at the same time in the same geometry so SC_{res} is the same in the two channels. Moreover, for ground-based Max-DOAS observations, the light path in the stratosphere, and thus SC_{strato} can be considered constant with respect to the

viewing angle (Hönninger et al., 2004). Neglecting the horizontal variation of the NO_2 field, the DSCDs can thus be expressed as:

$$DSCD(zen) = AMF_{tropo}(zen)VCD_{tropo} + SCD_{strato} - SCD_{res} \tag{7.1}$$

and

$$DSCD(30°) = AMF_{tropo}(30°)VCD_{tropo} + SCD_{strato} - SCD_{res} \tag{7.2}$$

VCD_{tropo} is directly extracted, combining these two equations, as:

$$VCD_{tropo} = \frac{DSCD(30°) - DSCD(zen)}{AMF_{tropo}(30°) - AMF_{tropo}(zen)} \tag{7.3}$$

7.3.2 Realism of the geometrical approximation?

A convenient way to derive the tropospheric column from equation 7.3 is the so-called Geometrical Approximation (GA), described by Hönninger et al. (2004). It consists in expressing AMF_{tropo} as $\frac{1}{\sin\alpha}$, where α is the viewing angle relative to the ground. This method assumes that the last scattering event occurs above the absorber layer. It leads, in our case, to a very convenient equation:

$$VCD_{tropo} = DSCD(30°) - DSCD(zen) \tag{7.4}$$

The GA is widely used due to its simplicity, both for static MAX-DOAS instruments (e.g. Brinksma et al. (2008), Celarier et al. (2008)) and Mobile-DOAS studies (all the aforementioned mobile DOAS studies, Shaiganfar et al. (2011) introducing however an azimuth dependent correction for large NO_2 VCDs.) Several studies (e.g. Pinardi et al. (2008), Vlemmix et al. (2010)) have compared the GA with radiative transfer calculations, varying parameters such as the sun position, NO_2 and aerosol layer height, or visibility. They indicate that the GA can lead to biases up to 50% compared to calculated AMFs in some configurations. For zenith-only, the reader is referred to Chen et al. (2009), who shows that the real AMF may exceed 2, corresponding to a bias larger than 100%. The larger difference for the zenith-sky is understandable by the high albedo (0.18) used by Chen et al. (2009), but also by the fact that in MAX-DOAS, the investigated quantity is the differential AMF. This quantity (in our case: $AMF_{tropo}(30°) - AMF_{tropo}(zen)$) is more stable since the two AMFs are correlated. Considering only mobile Max-Doas measurements (Wagner et al. (2010), Ibrahim et al. (2010), Shaiganfar et al. (2011)), the error due to the GA is assumed to lie between 15 and 20%. The 15% also originates from radiative transfer simulations (Ibrahim et al., 2010), assuming in particular a NO_2 layer under 200 m altitude.

Table 7.1: Parameters and ranges used in the air mass factors calculations.

Wavelength(nm)	460
Direction	Zenith,30°
Surface visibility(km)	5, 10, 15, 20, 25, 30
NO_2 mixing height(m)	100, 300, 500, 700, 900
Relative azimuth(°)	0, 30, 60, 90, 120, 150, 180
Solar zenith angle(°)	20,30, 40, 50, 60, 70, 80, 90
Albedo	0.01, 0.03, 0.05, 0.07, 0.09, 0.11, 0.13, 0.15

This last assumption of a surface-near NO_2 loading is hardly trustable outside cities. In semi-rural areas, NO_2 tends to be well mixed in the boundary layer as is shown by LIDAR and sonde measurements in Cabauw (Volten et al. (2009); Sluis et al. (2010), see also figure 2.9, and as is predicted by diffusion models (Vinuesa and Galmarini, 2009)). Note that using a scanning DOAS system, it is possible to identify the points where the GA is the most unrealistic. This is done adding a third off-axis measurement to equations 7.1 and 7.2, as described in Brinksma et al. (2008) and Wagner et al. (2010). On the contrary, only two angles are accessible with our Mobile-DOAS instrument. Given these different arguments, we used calculated AMFs instead of the GA.

Table 7.1 presents the parameters used in the radiative transfer model UVspec-/DISORT to calculate the tropospheric air mass factors. Contrary to what we did for Earth Challenge, we do not study the sensitivity of the AMF to a given parameter fixing the other ones. Instead, we calculate the AMFs for each possible configuration of parameters and study their resulting distributions. This choice is motivated by the difficulty to know these parameters accurately. In particular, very close to the sources, the height of the NO_2 layer may well be very low as suggested by Dieudonné (2012). If so, using the boundary layer height as was done for Earth Challenge data could be largely inaccurate.

Figure 7.3 shows the general distributions of zenith, 30°AMFs, and differential AMFs. According to the GA, the latter should be close to one, its mean value is 1.18 on the figure. Moreover, the standard deviation of the distribution around this mean is 0.28, indicating that biases of 50% may easily occur using the GA, and that the assumed 20% of the previous studies is quite optimistic. The left panel also indicates that scattering inside the NO_2 layer should not be taken into account even for zenith-only instrument. Indeed, the mean of the zenith AMF is 1.33 and should also be 1 according to the GA. Note that the larger standard deviation of the 30°AMF is due to its dependency on the relative azimuth, contrary to the zenith AMF.

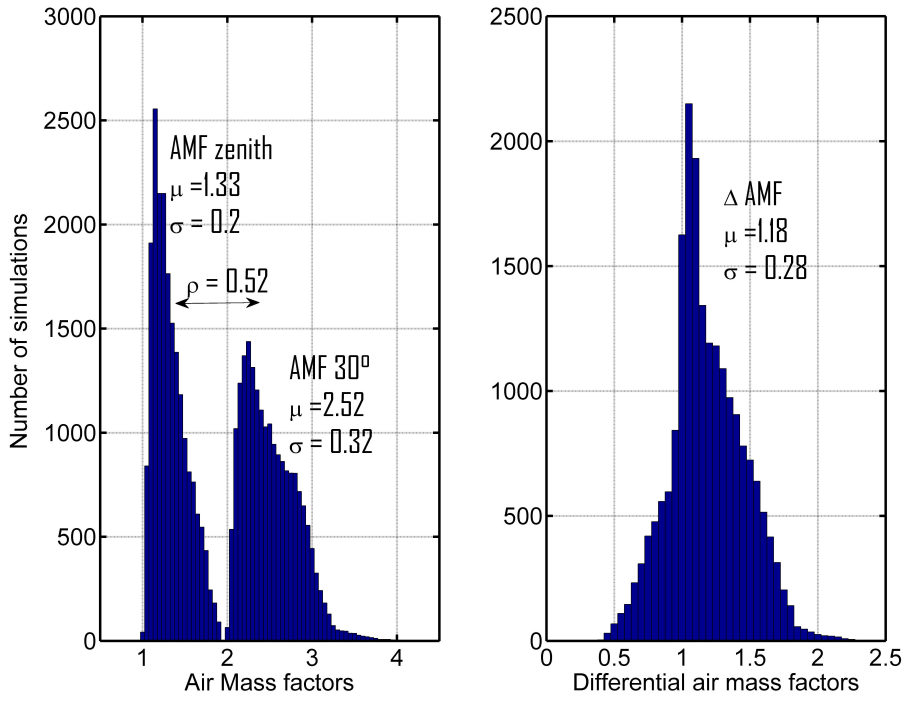

Figure 7.3: Distribution of air mass factors calculated with the parameters of table 7.1(left) and of the resulting differential air mass factor (right).

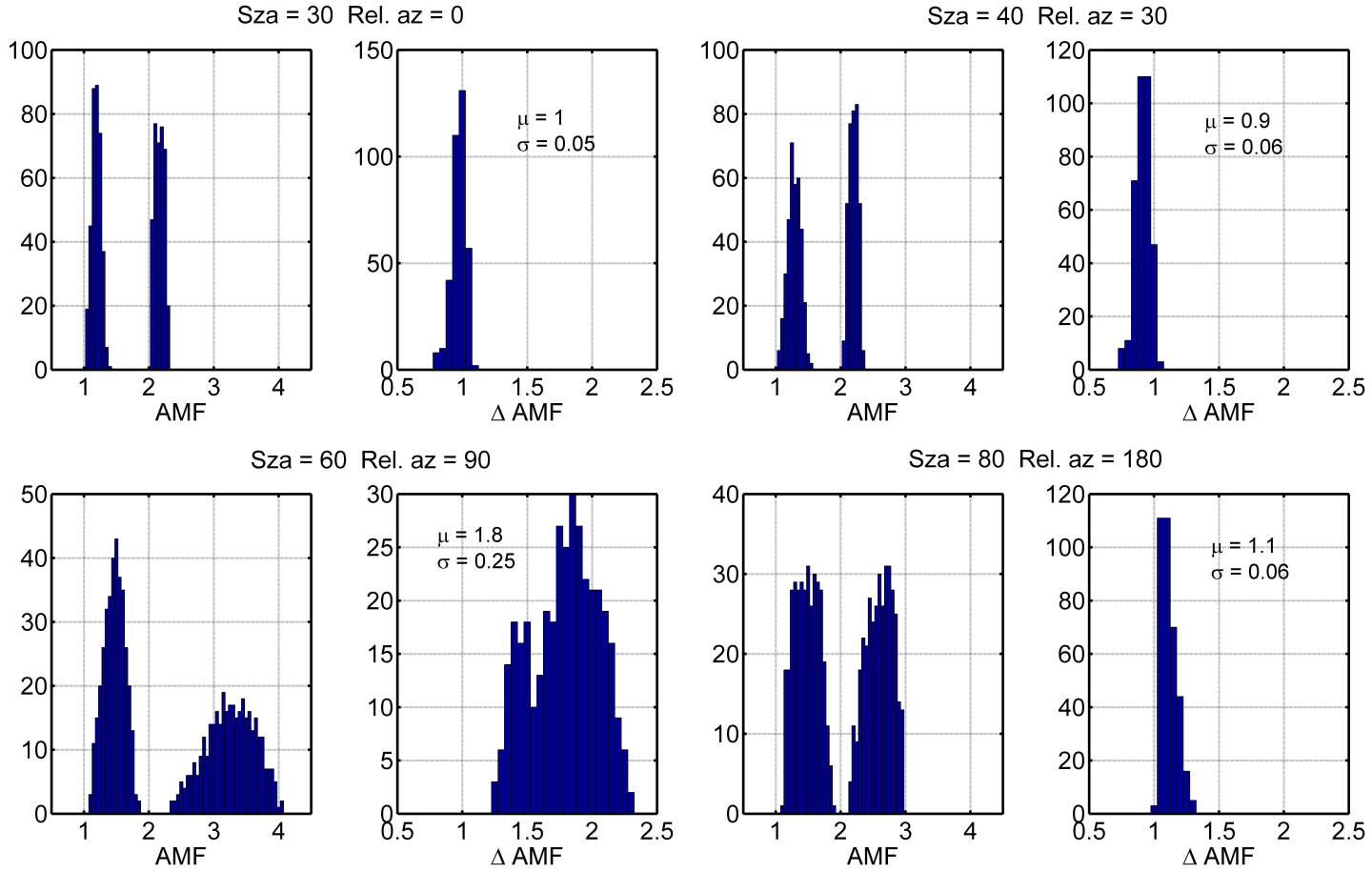

Figure 7.4: Distribution of Mobile-DOAS air mass factors for four different positions of the sun, calculated with the parameters given in table 7.1.

Figure 7.4 also shows AMF distributions, but around given sun positions. It indicates in particular that the GA is unrealistic for the differential AMF (1.8 instead of 1) for a relative azimuth of 90°and a solar zenith angle of 60°. Such a sun position can not be disregarded from astronomical considerations at Europe's latitudes.

The calculated air mass factors were used to create a look-up table, depending only on the sun position compared with the instrument. The look-up table contains in addition to the AMFs, the standard deviation as shown in figure 7.4. This solution is expected to reduce the biases in our measurements.

7.3.3 Solution for the NO_2 field inhomogeneities

The two channels of the instrument point to different elevations, thus to different air masses. This is not problematic in areas where the NO_2 is constant. However, since a major objective of these Mobile-DOAS experiments is the study of horizontal gradients, the problem must be addressed as accurately as possible.

Wagner et al. (2010) proposed a method based on the idea that equation 7.3 could be considered true if a large number of points were averaged. Combining then equation 7.3 with equation 7.1, the offset $SC_{res} - SC_{strato}$ can be expressed from $DSCD(zen)$ and $DSCD(off)$. Only SC_{strato} varies in this offset, and only smoothly with time if the measurements are not close to twilight. $SC_{res} - SC_{strato}$ can thus be fitted as a low order polynomial, and used in equation 7.1 to derive the vertical column. The method has been applied to following mobile MAX-DOAS studies (Ibrahim et al., 2010; Shaiganfar et al., 2011).

Figure 7.5 illustrates a problem which can arise with the method when dealing with a small number of measurements. It presents NO_2 vertical columns derived from Mobile-DOAS measurements performed inside Brussels on 2 April 2011. In this case, the quantity $SC_{res} - SC_{strato}$ is not well enough represented by the fit (lower panel) due to the short timespan of the measurements. This leads to an unphysical result: the stratospheric contribution appears maximum in the middle of the day, around 12.6 UT. This problem propagates in the VCD (blue curve, upper panel). It becomes important at the edge of the fitting window when the fit is less constrained. This is visible in the offset with the green curve, probably more realistic, which was calculated as described below.

The method we propose to take into account the field inhomogeneities uses another approach. It is based on the idea that compared to a scanning system with one single channel, our measurements are simultaneous in two directions. The sampled air masses, if not exactly the same, are thus closer than for a scanning system. This implies that equation 7.3 applies more often and that fewer points are necessary to make a correct average for equation 7.3, again compared to a scanning system. Instead of fitting $SC_{res} - SC_{strato}$ as a polynomial, we decompose VCD_{tropo}

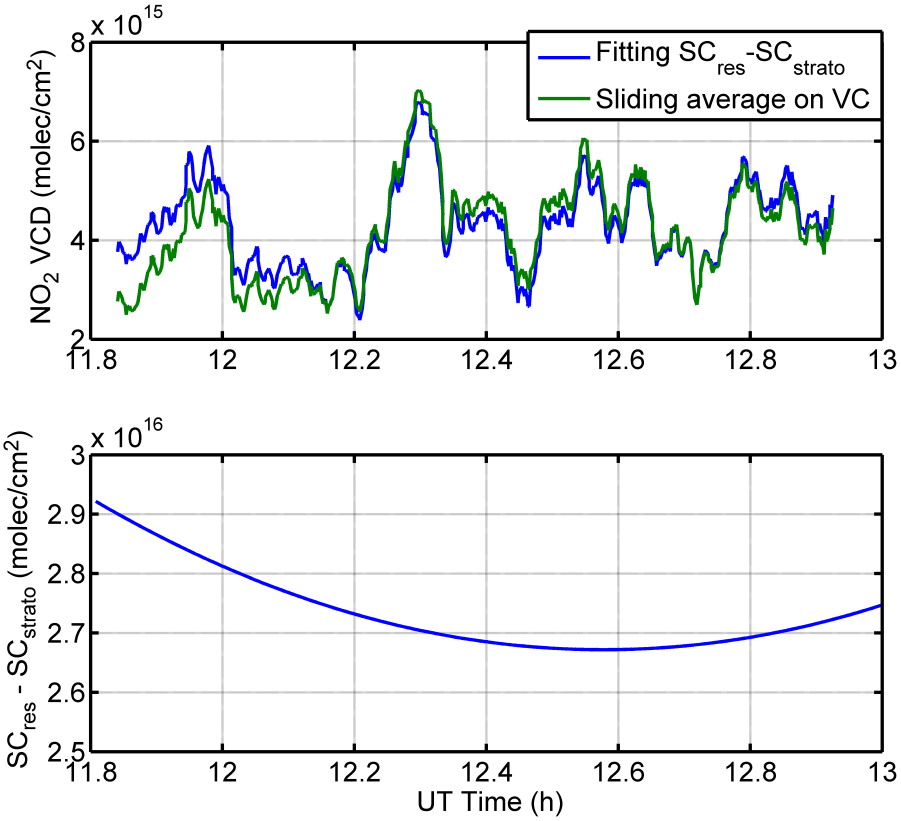

Figure 7.5: Comparisons of two methods for correcting inhomogeneities: (blue) fitting the stratospheric contribution as a polynomial (Wagner et al., 2010) and (green) reconstructing the VCD as described in the text.

in two components according to their spatial gradients:

$$VCD_{tropo} = VCD^0_{tropo} + VCD'_{tropo} \tag{7.5}$$

In equation 7.5, VCD^0_{tropo} is the smooth component of VCD_{tropo} whereas VCD'_{tropo} is the structured one. We use a sliding average as a filtering method. Noting $\langle\rangle_n$ the sliding average on n points, VCD^0_{tropo} is calculated as:

$$VCD^0_{tropo} = \left\langle \frac{DSCD(30°) - DSCD(zen)}{AMF_{tropo}(30°) - AMF_{tropo}(zen)} \right\rangle_n \tag{7.6}$$

The structured component of VCD_{tropo} can be estimated from:

$$VCD'_{tropo} = \frac{DSCD_{zen} - \langle DSCD_{zen}\rangle_n}{AMF_{zen}} \tag{7.7}$$

The number of points to consider in the sliding average is not critical: above 100, our method gives very similar results as the one proposed by Wagner et al. (2010). This can be seen on figure 7.5, except at the beginning of the measurements series, for the reason given above. Leaving aside the technical aspects, the difference of our method compared to fitting $SC_{res} - SC_{strato}$ is that we do not assume a relationship between all points of a measurement, but only on the n points of the sliding average.

7.3.4 Error budget

The errors originate from the DSCDs and the AMFs. The DSCDs errors are random and reduce in the sliding average with the square root of the number of measurements. Considering typical fit residuals and the uncertainties in AMF previously described, we thus neglect the DSCD error in equation 7.6. The randomness argument can not be applied to the air mass factor, since its uncertainty depends on parameters which are expected to be correlated, for instance the visibility of the height of the layer of NO_2. This leads to the following error for the smooth part of the column:

$$\sigma_{VCD^0_{tropo}} = \frac{VCD^0_{tropo}}{\Delta AMF}\sigma_{\Delta AMF} \tag{7.8}$$

Considering equation 7.7, the DSCD error matters since it is an individual measurement. The propagation of uncertainties leads to:

$$\sigma_{VCD'_{tropo}} = \sqrt{\frac{\sigma^2_{DSCD}}{AMF_{Zen}} + \frac{VCD'_{tropo}}{AMFzen}\sigma^2_{AMF_{zen}}} \tag{7.9}$$

There is a correlation between AMF_{zen} and ΔAMF but its either positive or negative according to the relative azimuth so we do not take it into account and sum the two error components in quadrature.

7.4 Participation to the CINDI campaign

The CINDI Campaign (Piters et al., 2012) took place in June-July 2009 at the Cabauw Experimental Site for Atmospheric Research (CESAR, 51.97°N, 4.93°E, at sea level). Its main scientific purpose was an intercomparison of MAX-DOAS instruments for tropospheric NO_2 (Roscoe et al., 2010), which was achieved from 15 to 30 June 2009. In addition to DOAS systems, NO_2 was also measured by the LIDAR described by Volten et al. (2009) and in-situ, by chemiluminescence, both from ground by a commercial system and by the newly developed sondes described by Sluis et al. (2010). The sondes profiles can be seen in figure 2.9.

The BIRA-IASB Mobile-DOAS was operated after the intercomparison on the local roads around Cabauw and on the highways between Utrecht and Rotterdam. The motivation, beside testing the newly developed instrument, was to study the variability of the NO_2 field inside one OMI pixel ($13 \times 24\,km^2$). Unfortunately, for the best measurements days, when the Mobile-DOAS and OMI measurements are coincident, the latter are affected by the row anomaly (see `http://www.knmi.nl/omi/research/product/rowanomaly-background.php`). The Mobile-DOAS dataset collected during CINDI is thus not optimal for such a comparison, nevertheless it reveals accurately the NO_2 horizontal gradients around the CESAR site.

As an example, figures 7.6 and 7.7 present NO_2 tropospheric columns measured in the afternoon of 14 July 2009, between CESAR and Utrecht. Figure 7.7 also shows the vertical column derived from the static MAX-DOAS at 13H04, when the Mobile-DOAS was still at the CESAR site. A description of the MAX-DOAS instrument is given by Clémer et al. (2010b). Note in particular that the radiative transfer is based on LIDORT (Spurr, 2008) instead of DISORT in our case, and uses an optimal estimation scheme to retrieve the NO_2 profile. The two measurements are very close, around $3 \pm 1 \times 10^{15}\,molec/cm^2$. This gives confidence in the NO_2 loading derived from the Mobile-DOAS instrument.

7.5 Routine measurements in Belgium

After the CINDI campaign, Mobile-DOAS measurements were performed on a routine basis between March 2010 and August 2011. The instrument was installed on the car of a maintenance engineer traveling mostly across Belgium, but also to Germany, Luxembourg and France. This was possible thanks to the highly automated acquisition program and the ease of installation, on any car with a window and a 12V socket. Combining this with the measurements performed during CINDI yielded a large database.

Table 7.2 details the number of measurements collected with the MobileDOAS during CINDI and the routine measurements. Altogether, this represents a total of over 460 h, covering 18700 km. An advantage of the routine measurements compared to a campaign is that the instrument can be started only in good meteorological conditions. The data from 2011 are in particular almost completely cloud free.

Table 7.2: Mobile-DOAS measurements between 2009 and 2011.

	CINDI 2009	2010	2011	Total
Date range	07/01-08/06	04/03-10/21	02/17-07/01	-
Number of days	13	64	63	140
Distance (km)	2353	8920	7498	18771
Time (h)	47	199	217	463

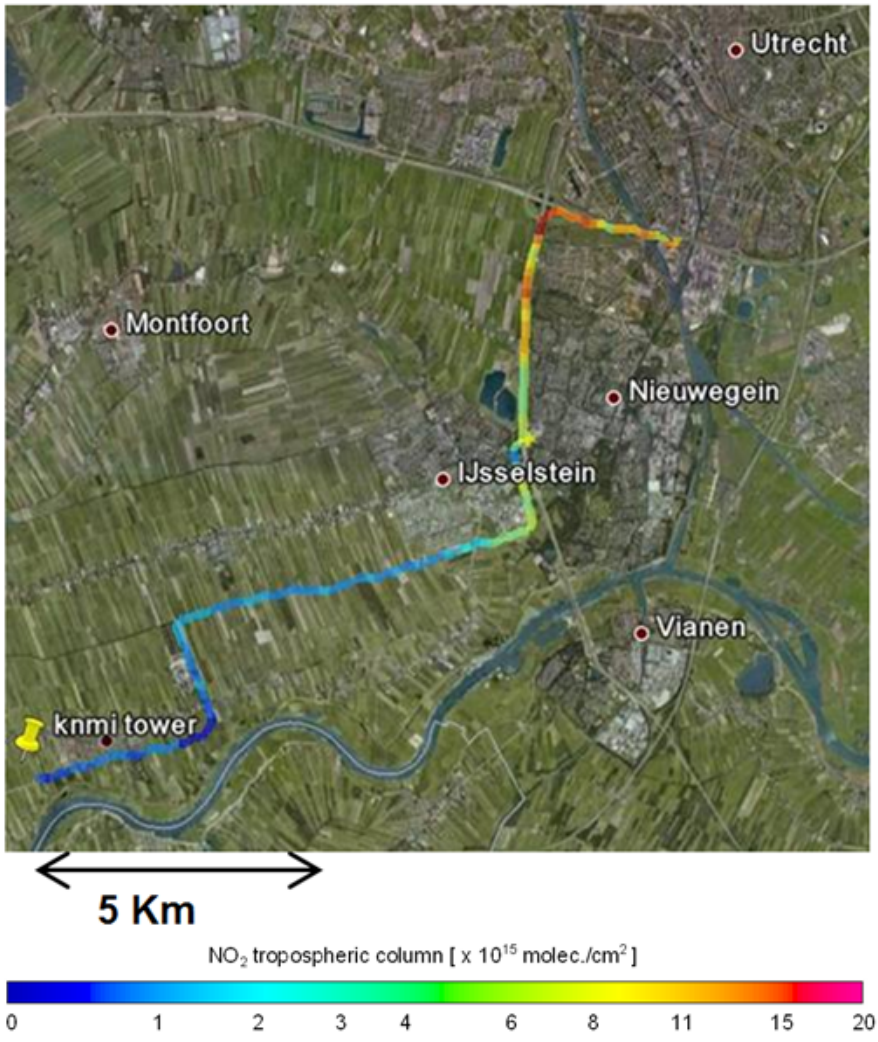

Figure 7.6: Mobile-DOAS measurements on 14 July 2009 from Cabauw to Utrecht: map.

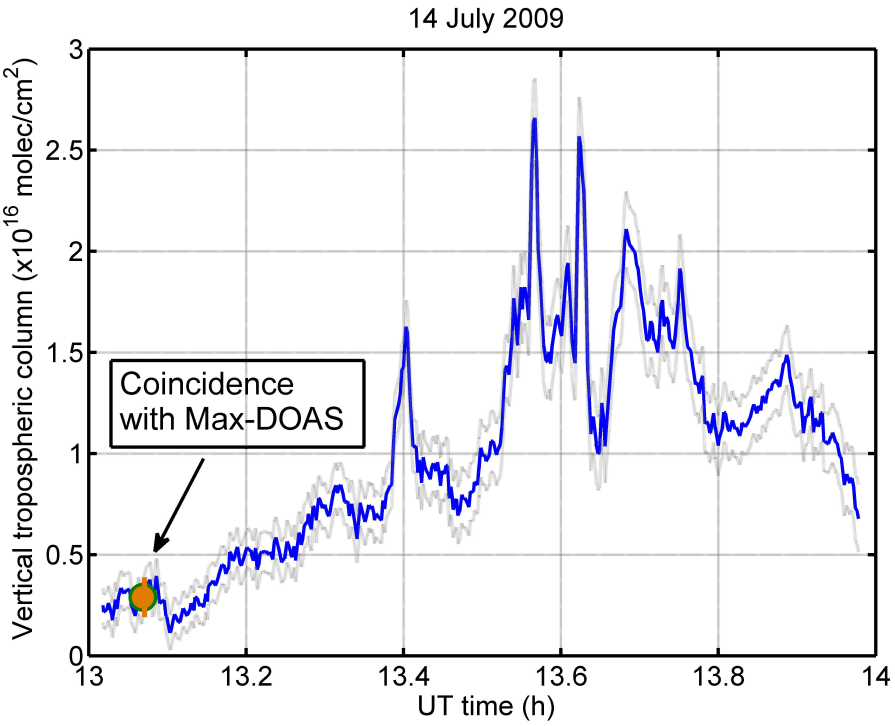

Figure 7.7: Mobile-DOAS measurements on 14 July 2009 from Cabauw to Utrecht: time series.

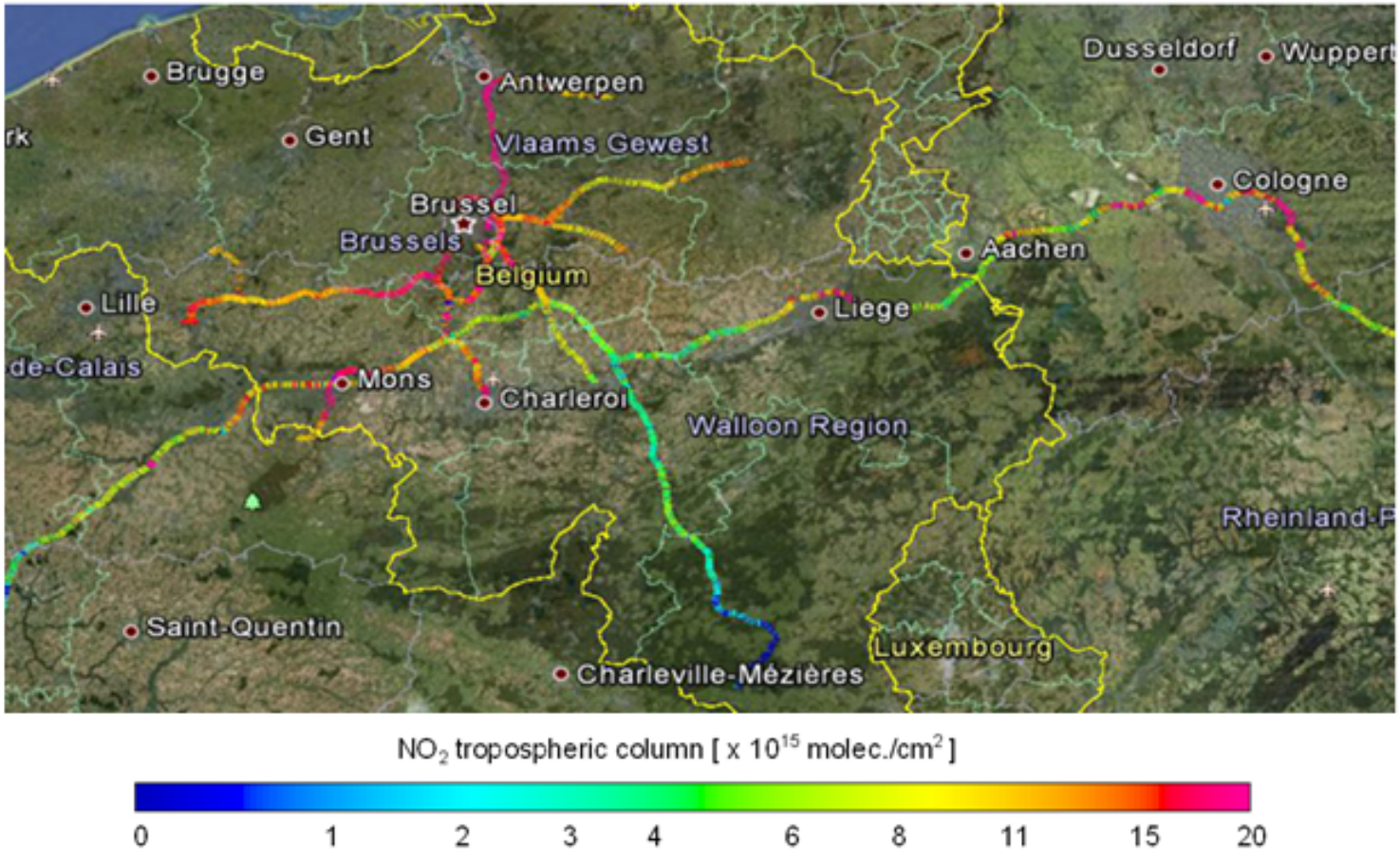

Figure 7.8: Some of the 2011 Mobile-DOAS measurements taken into account in the comparison with CHIMERE.

7.6 Comparison with Chimere Model

CHIMERE (Vautard et al., 2001) is a European scale Eulerian chemistry transport model. The full settings are described by Lambert et al. (2011). Note in particular that the emission inventory originates from EMEP (2002). The ground resolution in latitude and longitude is 0.5°x 0.5°, which corresponds roughly to 55x35 km^2 in Belgium.

We selected a subset of 2011 cloud-free measurements to study their relationship with CHIMERE model output. They correspond to 29 days between 22 February 2011 and 2 June 2011. The measurements cover mostly Belgium, but also highways in Germany and particularly Aachen and Cologne, and in France up to Nantes and the Atlantic coast. Figure 7.8 shows some representative days. The populated areas in Northern Belgium appear much more heavily NO_2 polluted than the much less dense southern part of the country. Many local high spots correspond to large cities such as Liege and Cologne.

Figure 7.9 shows the scatter plot of CHIMERE model output and Mobile-DOAS measurements of tropospheric NO_2. The latter were calculated as a mean of the measurements crossing a 4-D CHIMERE pixel. The three panels correspond to three different criteria on the minimum of Mobile-DOAS measurements inside a CHIMERE pixel. These panels indicate that the comparison is rather stable regarding the number of points taken into account. From the figure, the criterion of 100 points seems to be a good trade-off. The correlation coefficient is 0.71, while the slope is 0.63, which may indicate a positive bias of the model. This correlation can be compared with the correlation of 0.88 reported for in-situ measurements in Belgium (Lambert et al., 2011). The investigated period was 01/03/2007 to 9/02/2008. Note that the instrument is static and installed in Houtem (51.016°, 2.581°), which is a background station for air quality monitoring. This last aspect may explain the better correlation of these in-situ measurements with CHIMERE. On the other hand, it is well established that the NO_2 trends are negative in Western Europe (see Castellanos and Boersma (2012) and section 2.2 for further references). This is in agreement with the observed bias between the Mobile-DOAS and CHIMERE. However, the Mobile-DOAS errors (see section 7.3.4) still have to be propagated in the scatter plot before drawing conclusions.

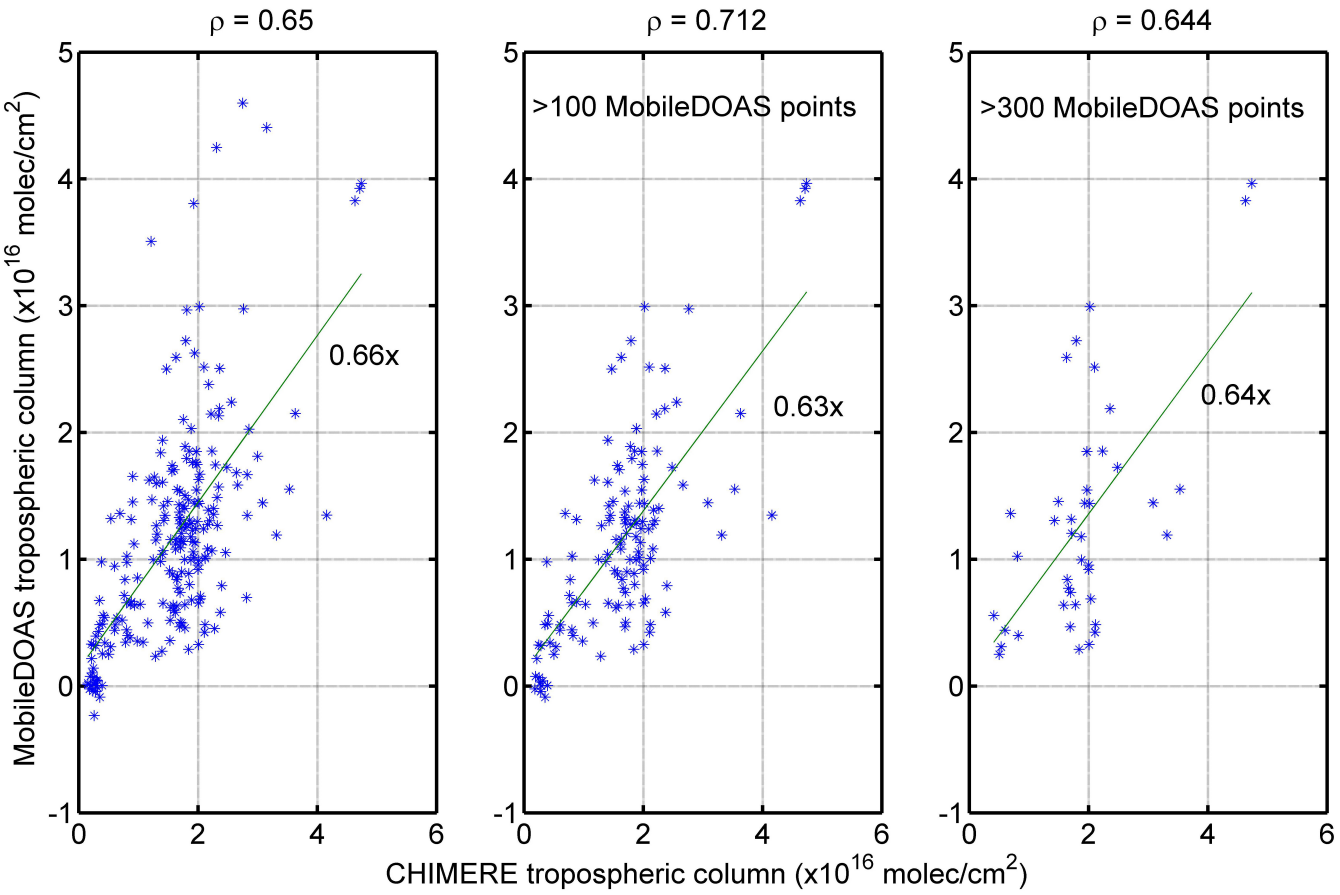

Figure 7.9: Comparison of tropospheric NO_2 columns derived from the Mobile-DOAS data and from the Chimere model. The three panels correspond to three different criteria on the minimum of Mobile-DOAS measurements inside a CHIMERE pixel. These Mobile-DOAS points are averaged for the comparison.

7.7 Conclusion on the Mobile-DOAS measurements

A large database of Mobile-DOAS observations was built during the CINDI campaign in July 2009 and routine measurements in 2010 and 2011. The measurements were interpreted in term of vertical columns with a new analysis strategy. In particular, we did not use the geometrical approximation on the air mass factor. During CINDI, tropospheric NO_2 columns derived from this experiment show good agreement with a more sensitive MAX-DOAS instrument. Considering the measurements which were collected in spring 2011, preliminary comparisons with the CHIMERE model indicate a negative bias compared to CHIMERE which, if confirmed, may be explained by the decreasing trends of NO_2 in Western Europe. The progress with respect to the geometric approximation should be evaluated against other datasets like OMI data or IRCEL-CELINE[1] in-situ air quality samplings.

[1] http://www.irceline.be/

Chapter 8

Development of a compact payload for trace gases imaging from unmanned aerial vehicles

This chapter presents the development and first tests of a UAV payload dedicated to atmospheric research. Such a project was actually the original motivation of this thesis (De Mazière et al., 2006) but delayed for technical reasons.

8.1 Interest of UAV measurements

Unmanned Aerial Vehicles (UAVs) are useful platforms for atmospheric research. The most obvious applications involve measurements in dangerous environments, e.g. inside a typhoon (Lin, 2006) or a volcanic plume (McGonigle et al., 2008). Compared to traditional aircraft, UAVs can probe the troposphere at lower altitudes, which makes them particularly interesting for profiling applications (Martin et al., 2011; Corrigan et al., 2008). Their relative low cost also enables to use several aircraft together (Ramana et al., 2007).

Regarding air quality, a trace gases mapping system operating from an UAV would be useful to quantify emissions from moving point sources, for instance, NO_2 and SO_2 exhausts by ships, as is already done from traditional planes (Berg et al., 2012), but at a lower cost. Other useful applications could involve satellite and model validation studies. From the ground it is not possible to cover the full extent of a satellite pixel in a reasonnable time, and horizontal gradients can only be measured along roads, as was done with the Mobile-DOAS (see chapter 7). On the other hand, the spatial scale of state-of-the-art local chemistry and transport models can reach down to 100 m (Cosemans and Mensink, 2005). Space based instruments are not able to validate such models, nor will they be in the near

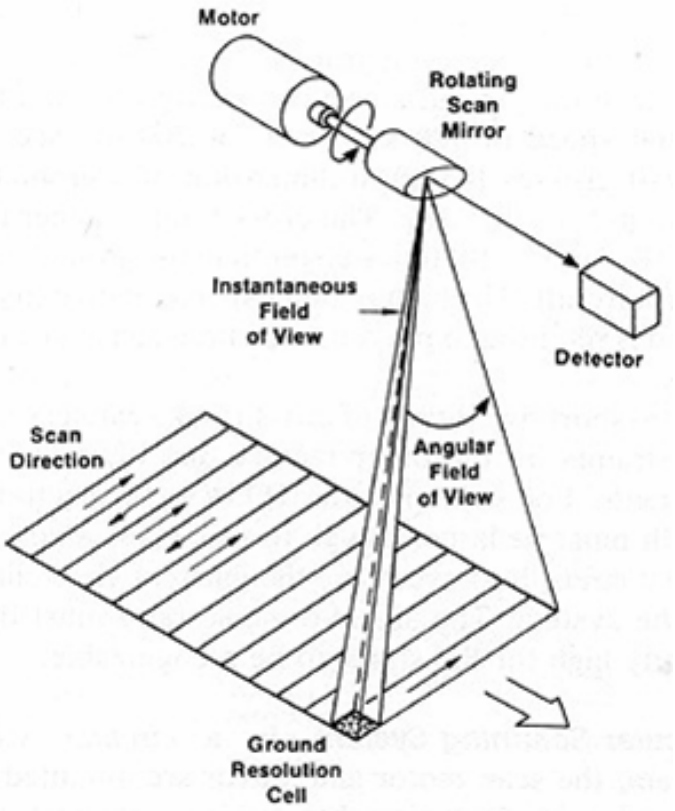

Figure 8.1: Principle of whiskbroom imaging (Sabins, 1997).

future. Again, this is possible from traditional planes. Popp et al. (2012) have recently presented high resolution (50x120 m^2) maps of tropospheric NO_2 columns derived over Zurich with the APEX instrument. But the same cost argument applies in favor of trying similar experiments from a UAV.

The above considerations, and the opportunity of a dedicated platform through a collaboration with the University of Galati, Romania (see figure 8.7), led us to develop a new instrument, compact enough for a UAV, but with imaging capabilities. Once again the primary target is NO_2 but application to SO_2 is foreseen as well. The instrument, namely the Small Whiskbroom Imager for trace gases monitoriNG (SWING), has been tested in Belgium from an ultralight aircraft and the first flights from UAV are expected in early 2013. Another whiskbroom instrument has recently been operated from a UAV for DOAS measurements, the Airborne Compact Atmospheric Mapper (ACAM, Kowalewski and Janz (2009)). It has already measured NO_2, formaldehyde, and even tropospheric ozone above Houston. However, the platform used is much larger and the payload is over 20

kg, compared to the 900 g allowed in our case.

The next section introduces the principle of whiskbroom imaging and what kind of resolution is achievable from a UAV platform flying at 4 km with a spectrometer fitting the requirements. Section 3 details the technical aspects of the payload. Finally, we present the first SWING measurements from an ultralight aircraft in section 4.

8.2 Whiskbroom imaging from a UAV

8.2.1 Geometry of whiskbroom imaging

Whiskbroom scanning is a common set-up for remote sensing from aircraft, e.g. for the AVIRIS instrument (Green et al., 1998), or from satellite, e.g. GOME-2 (Munro et al., 2006) and IASI (Clerbaux et al., 2009)). It consists in collecting the light reflected by a mirror scanning across the flight direction. A single detector is thus needed to produce images of the ground.

Figure 8.1 illustrates the geometry of whiskbroom scanning. The most important dimensions are the platform altitude (h), the angular field of view (A), defined as the full angle the scanner can perform, and the instantaneous field of view (ω), defined as the field of view of the instrument when all motion is stopped.

The angular field of view and the altitude define the swath (S), i.e. the width of the imaged line perpendicular to the platform movement:

$$S = 2h \tan \frac{A + \omega}{2} \tag{8.1}$$

Within the swath, the pixels size depends on the instantaneous field of view, the altitude, and the angle of the scanner (Θ). In the direction of the platform movement, the pixel size depends furthermore on the speed of the aircraft (v) and the integration time (τ_D). The respective expression are the along-track pixel size (P_{along_track}) and the cross-track pixel size (P_{cross_track})

$$P_{cross\_track} = h \tan (\Theta + \frac{\omega}{2}) - h \tan (\Theta - \frac{\omega}{2}) \tag{8.2}$$

and

$$P_{along\_track} = 2h \tan \frac{\omega}{2} \sec \Theta + v\tau_D \tag{8.3}$$

This change in pixel extent along the swath is referred to as the panoramic distortion (Breuer and Albertz, 2000).

In our case, the altitude reachable with the platform is 4 km at a speed of 60 km/h. Assuming respectively 120° and 2° for the angular and instantaneous fields

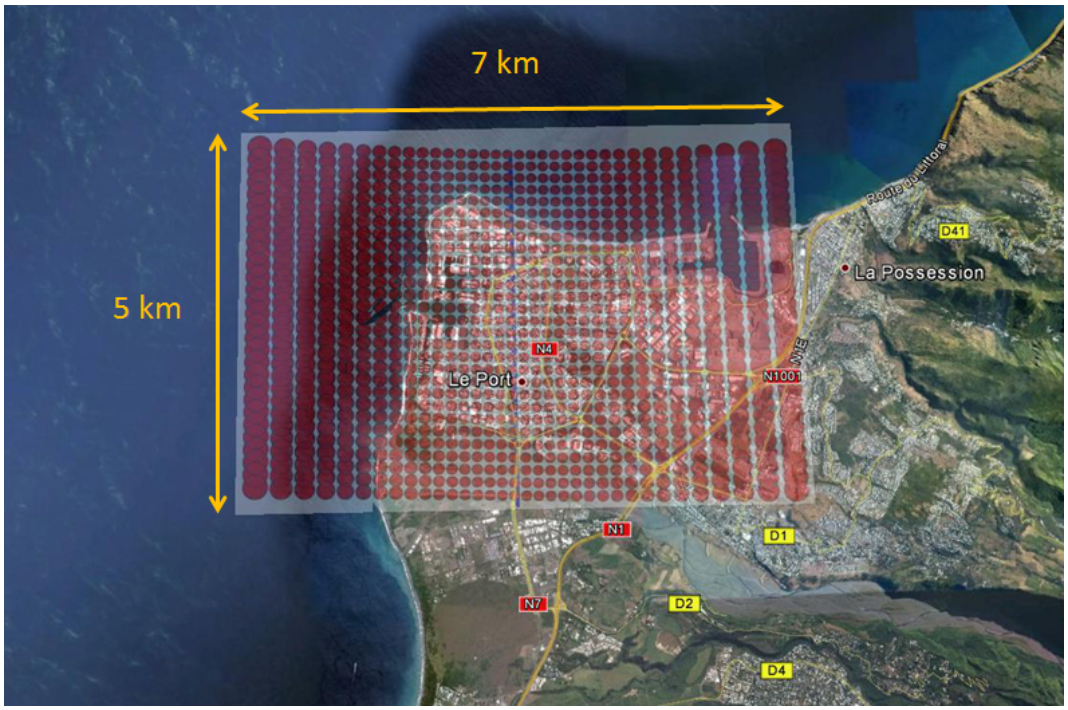

Figure 8.2: Ground cover for a flight altitude of 3 km and an angular field of view of 100°.

of view leads thus to a swath of 14,4 km and a nadir pixel of approximately 150 m at one second of integration time. These parameters would not be optimal for the ground cover but it is intended to give the orders of magnitude. Figure 8.2 presents another possible configuration, in which the aircraft is flying at 3 km altitude. The angular and instantaneous fields of view are respectively 100° and 2.6°, and the time per pixel is 0.3 s.

8.2.2 Choice of the spectrometer and simulations of observations

A major feature of whiskbroom imaging is its inherent short integration time. Two spectrometers were tested for possible use in SWING: the Avantes AvaSpec-2048 already used in the ULM-DOAS and an Ocean Optics STS. The latter is very compact, with a focal length of 28 mm (see table 4.1 for its main characteristics). The tests were performed from the roof of our observatory pointing nadir to be closer to airborne measurements. It turned out that the STS spectrometer was not sensitive enough for our application. In addition, its spectral resolution (2.3 nm) was not optimal for NO_2 retrieval (see chapter 3) so the Avantes spectrometer was selected.

To estimate the ground resolution achievable with the Avantes, we performed simulations of measurements above a polluted zone, namely the Antwerp agglomeration in Belgium. High resolution NO_2 field forecasted around this area were taken from the PROMOTE air quality forecast service (`http://promote.vito.be/webtool/`) which is based on the IFDM model (Cosemans and Mensink, 2005). Only surface concentrations were available so the columns were roughly built assuming an homogeneous boundary layer of 500 m.

The relationship between the pixel size (P_s) and the integration time (τ_D) used in these simulations is as follow:

$$\tau_D = \frac{P_s^2}{vS} \tag{8.4}$$

where v and S are again respectively the speed of the aircraft and the swath. This does not take into account the panoramic distortion for instance. The objective of the simulations is to estimate the level of horizontal details due to the trade-off between spatial resolution and signal-to-noise ratio.

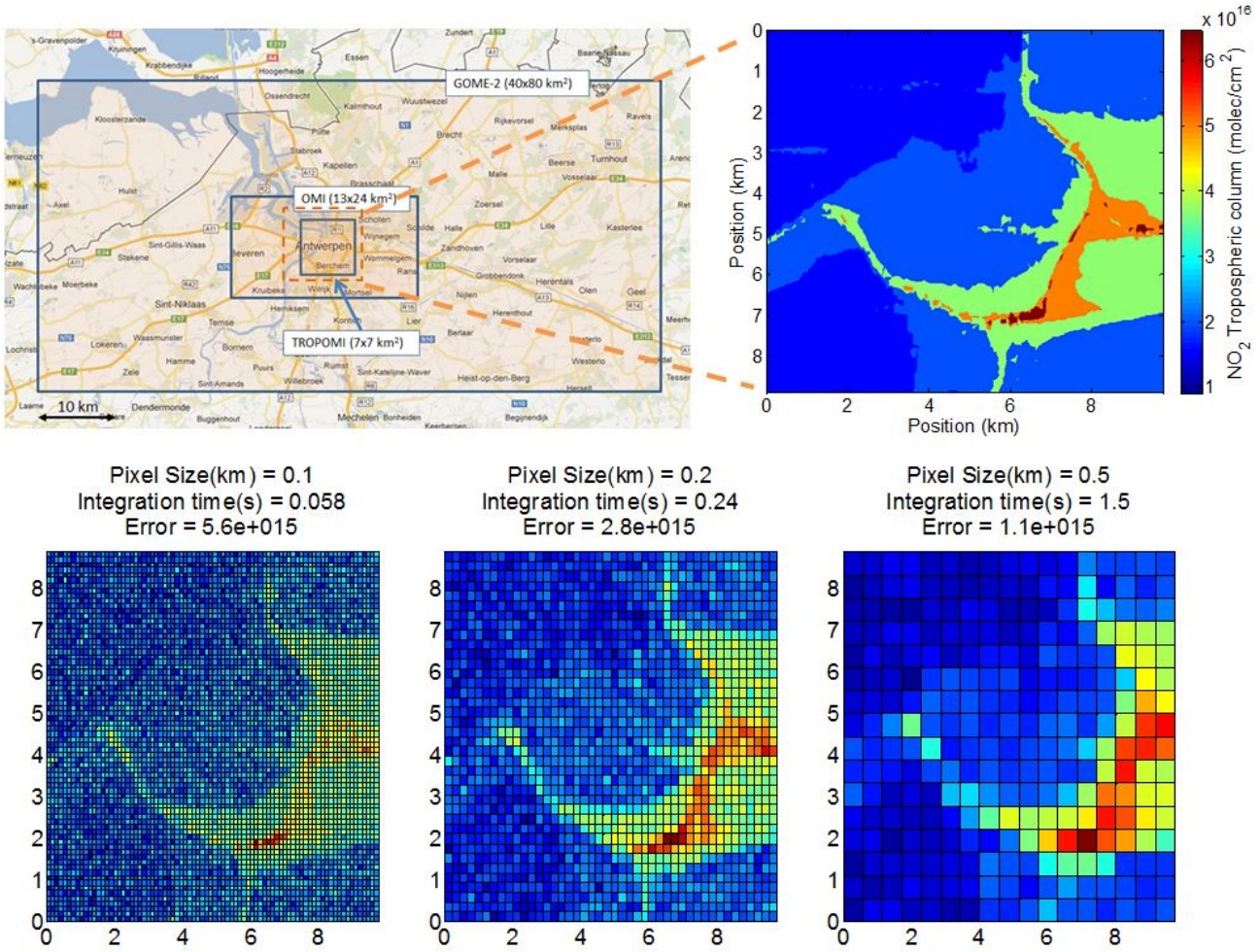

Figure 8.3: Simulations of NO_2 measurements from an UAV at different pixel size. The figure illustrates the trade-off between the ground resolution and the signal-to-noise ratio. Also shown are the pixel extents from current (GOME-2, OMI) and near-future (TROPOMI) satellite instruments, and the model field used as an input in the simulations.

The baseline for the noise level of the Avantes spectrometer was estimated from the Earth Challenge data, which is more representative of the UAV conditions than the measurements from the roof previously described. The typical error on the fitted NO_2 DSCD was scaled for the shorter integration times and for the different geometry assuming photon-noise limited conditions and using relative intensities calculated with UV-Spec.

Figure 8.3 presents the NO_2 model field used as an input and corresponding simulated observations for three different ground resolutions: 100 m, 200 m, and 500 m. The figure also shows, for a comparison, the pixel size of the current and near-future satellites GOME-2 ($80 \times 40\,km^2$), OMI ($80 \times 40\,km^2$), and TROPOMI ($7 \times 7\,km^2$). An interesting pattern for its horizontal gradients is the South West part of the Antwerp ring-road. It appears in the model field highly polluted and it is surrounded by cleaner areas due to the wind direction. According to the simulations, the noise level for a 100 m pixel still enables to distinguish the road from the background. In comparison, for a 500 m pixel, the image is much less noisy but the small scale of the road is almost completely diluted in the broader pixels. In real conditions, flying directly above such a perfect NO_2 source may be difficult in the near-future due to clearances reasons. The intermediate value of 200 m for the ground resolution below the aircraft represents thus, from these simulations, a good compromise.

8.3 Instrument and platform description

The Small Whiskbroom Imager for trace gases monitoriNG (SWING) was developed at BIRA-IASB in the framework of this thesis. This section presents the instrument in more technical details than the previous chapters did because of the miniaturization effort that was necessary to respect the size and weight constraints. We start by describing the overall instrument principle, then its different components and their implementation. Finally we show the UAV platform and discuss the payload integration.

Figure 8.4 illustrates the principle and different parts of the instrument. Light is collected by an optical fiber and a lens facing a mirror installed on a motor shaft. The motor scans in the nadir direction ($\pm$ 60° max. from the vertical direction). It is also possible to record spectra in the zenith direction by rotating the scanning mirror at 90° relatively to nadir, pointing to a zenith mirror. This possibility is useful to estimate the contribution of the total column of NO_2 which lies above the platform. The PC controls the spectrometer and the motor, via a driving circuit based on a microcontroller. A GPS antenna is also connected to the PC. The whole system is powered by 5V.

In practice, the spectrometer is an AvaSpec-2048 Avantes, like the ULM-DOAS

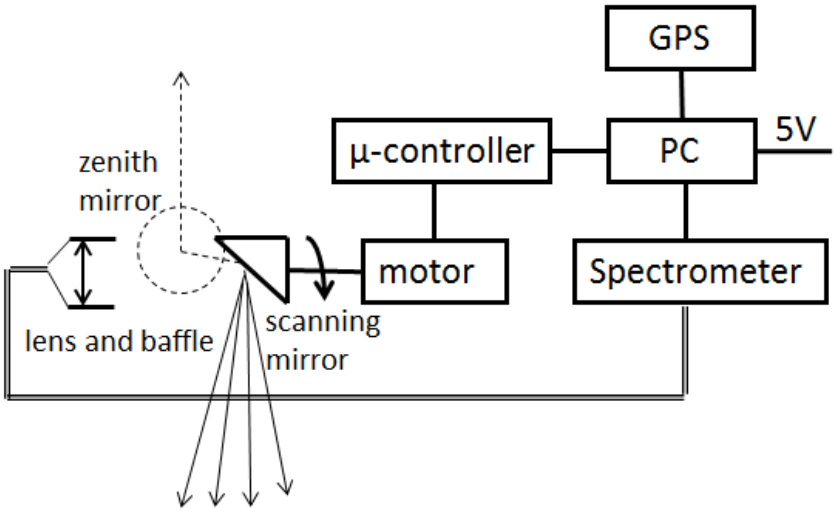

Figure 8.4: Scheme of the SWING payload.

instrument (see chapter6). The computer is also a PC-104 but it is powered by 5V to use the same input voltage as the scanning driver, avoiding thus the need of a power converter inside the payload. The other useful characteristic of this PC-104 for our application is the integrated 2 GB solid sate drive, which is enough for a minimal operating system (Debian Squeeze in text mode), the acquisition program, and the data storage. This solution was chosen to save the space of a hard drive and reduce the risk of disk failures experienced with the ULM-DOAS. The lens is the collimating set-up from Avantes already used in the Mobile-DOAS and shown on figure 4.2. This choice was motivated by the compact housing of the lens, which made it easily integrable. The fiber is a 400 μm-diameter leading to an instantaneous field of view of 2.5°. Compared to the ULM-DOAS fiber, there is no chrome plated brass outer tubing around this fiber and its length is 26 cm.

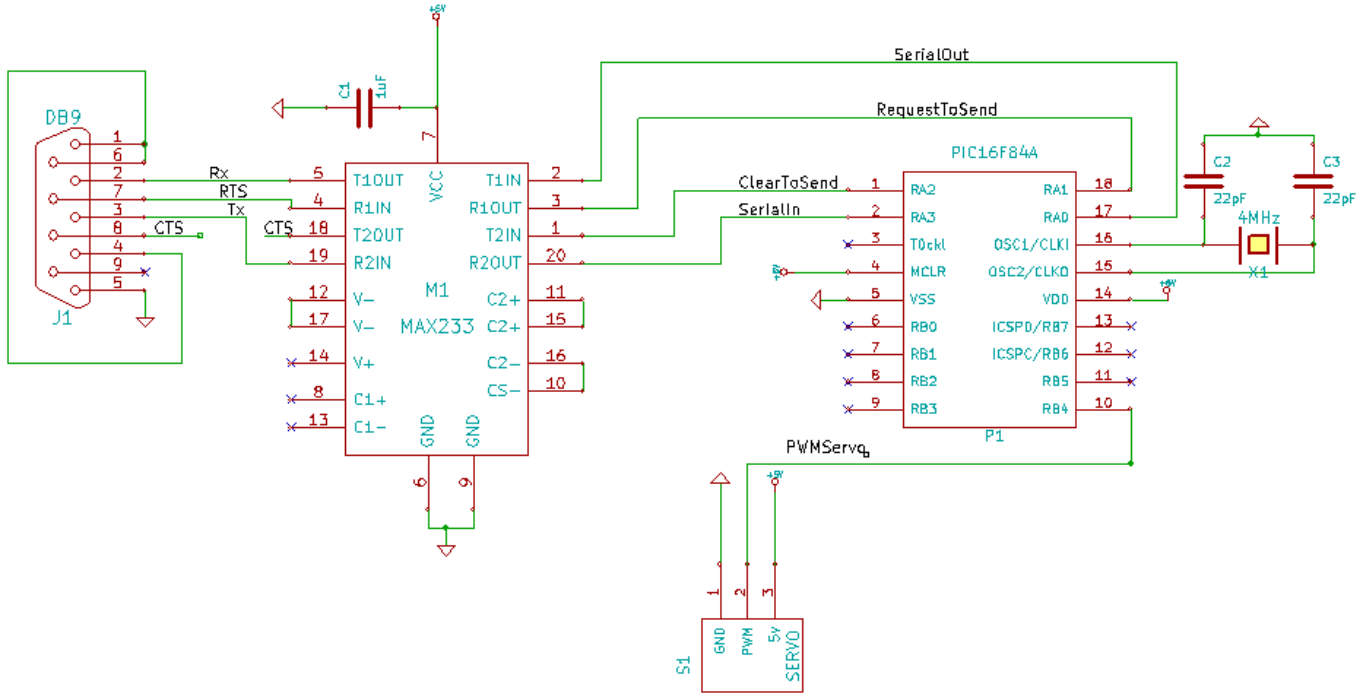

Figure 8.5: Electronic scheme of the scanning mechanism.

A Hitec servomotor was selected for the scanning system, contrary to the stepper motor used for the ULM-DOAS instrument. Compact servomotors are widely used in leisure radio-controlled aircraft, which makes them both worth considering for a UAV application and affordable. Such a motor is characterized by an integrated position feedback mechanism controlled by Pulse Width Modulation (PWM). The angular position of the shaft is tuned by varying the width of a periodic (50 Hz) pulse between roughly 0.8 and 2 msec. Contrary to a stepper motor, the angular resolution of a servomotor is not limited by its hardware.

Figure 8.5 presents the electronic circuit of the scanning system. It is inspired from a device designed to control several servomotors individually (Roll, 2000). The communication with the PC is achieved via RS-232 through a serial port and the DB9 connector. A MAX-233 converts the RS-232 signals to TTL ones, which are then suitable for the PIC microcontroller. This converter was a MAX-232 in the original scheme of Roll (2000). Using a MAX-233 reduces the number of external capacitors needed outside the integrated circuit compared to a MAX-232, and thus the total size of the electronic board. In operation, the PC sends three ASCII bytes coding a position. This information is converted to a pulse width by the microcontroller which continuously sends the pulse to the servomotor at a frequency of 50 Hz. The PIC also returns the received bytes to the PC, which enables to detect communication problem, and thus pointing errors.

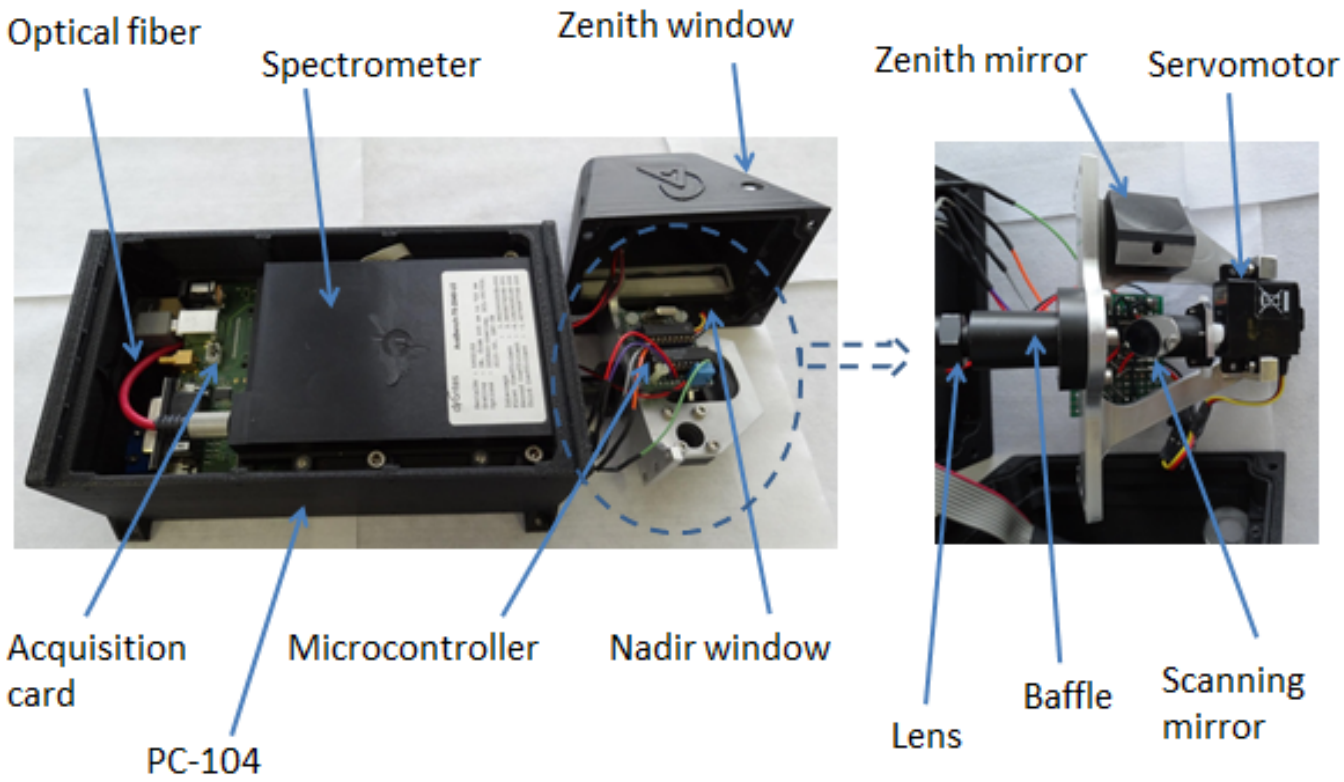

Figure 8.6: The SWING instrument. The size is 27x12x12 cm^3 for 920 g, the power consumption is 6 W at 5 V. The right panel shows the scanning system in more details.

Figure 8.7: The Unmanned Aerial Vehicle built by Reev River Aerospace and dedicated to the SWING payload. It is electrically-propelled and can reach 3 km altitude with its 2.5 m wingspan. The typical speed is 60 km/h.

Figure 8.6 shows the instrument with its open housing. To fit the total size and weight, the cover of the AvaSpec spectrometer was removed and the optical bench uncoupled from the acquisition card. This was also done for the GPS antenna, whose chip is fixed above the scanning system. The spectrometer is connected to the PC with a dedicated right-angle USB cable. Considering the application, the windows are not in BK7 or fused silica but in a plastic material suitable for optical applications (Zeonex). Except the scanner support which is aluminium made, the structural parts and the housing are in plastic material. They were manufactured by 3d printing, which optimized their weight and shape.

Everything included, the weight, size and power consumption of SWING are respectively 920g, 27x12x12 cm^3, and 6W.

Figure 8.7 shows the UAV dedicated to the SWING payload in a lab of the university of Galati, Romania. The latter is fixed on the back of the aircraft, in measurement position. This UAV was customly-built for the experiment by Reev River Aerospace. It is electrically powered, with a wingspan of 2.5 m and it can reach an altitude of 3 km during 2 hours. The typical speed is 60 km/h and tracks can be preprogrammed. At the time of writing (January 2013), the aircraft was in test phase in Romania. We expect the first flights with SWING to take place in Spring 2013.

8.4 Test flights from an ultralight aircraft in Belgium

To test the instrument overall stability, several test flights were performed in Belgium from an ultralight aircraft, in July and October 2012. The platform was a motorized deltaplane, contrary to the 3-axis ultralight used during Earth Challenge (chapter 6). This platform was selected for the ease of installation of a nadir-looking instrument underneath the aircraft.

Figure 8.8 includes two pictures taken on 28 October 2012, in the Avernas aerodrome (50.71°N, 5.07°E), where the aircraft is based. The SWING payload is fitted under the seat of the pilot and is visible on the ground and in flight. The left picture also shows the network cable (red) used to communicate with the instrument and download the data, and the 5V power supply cable (blue), which was connected to a motorcycle battery (not visible in the picture).

Figure 8.9 presents a NO_2 map derived from the flight performed on 28 October 2012 between 13h05 and 13h25 UT. The pilot flew from the aerodrome to the city of Landen (50.75°N, 5.07°E) and back. The wind was blowing from the west. Note that the NO_2 tracks do not represent the spatial extent corresponding to the instantaneous field of view. No information was available on the aircraft attitude so the georeferencing is highly inaccurate. The tracks are thus drawn with a constant width, assuming that the platform remains horizontal. They only provide some insight about the NO_2 field below the aircraft. The amount of noise in the measurements can be estimated from the right panel of the figure, which shows the NO_2 DSCDs (blue) and their errors (red) during the beginning of the flight, when the aircraft was flying in straight direction (blue dashed ellipse). It is obvious that the integration time should be longer in this configuration. However, the higher NO_2 loadings visible on the east of Landen may well be explained by the city exhaust carried along the wind direction.

Figure 8.8: Installation of SWING on an ultralight and illustration of the test flight on 28 October 2012.

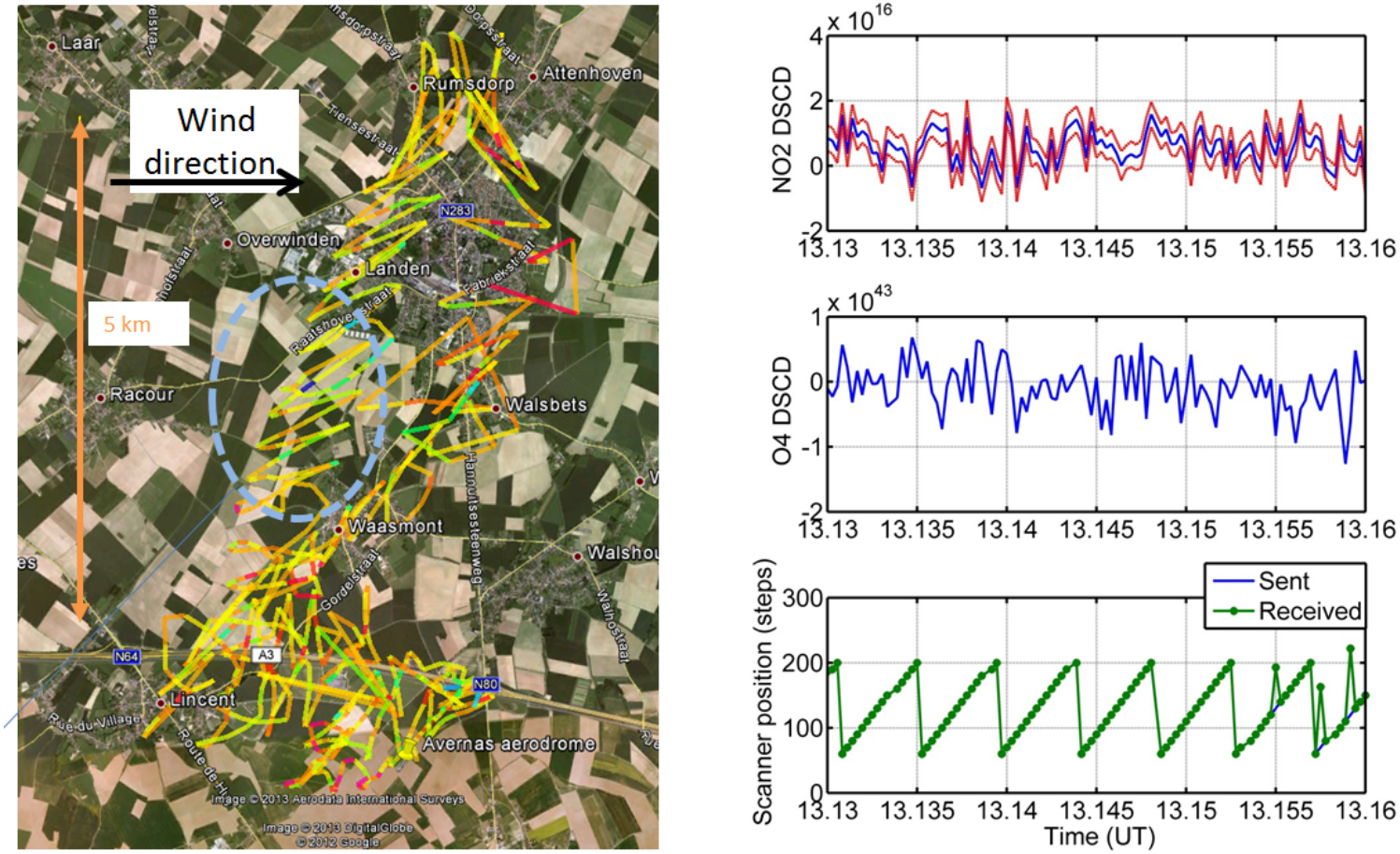

Figure 8.9: First SWING measurements from an ultralight aircraft on 28 October 2012.

8.5 Conclusions and perspectives

In this thesis, we concentrated on developing the payload and testing it using several flights of an ultralight aircraft. Although first results are encouraging and consistent with expected performances, several improvements are necessary. The scanning loop can be improved. Currently, the PC sends the position command in ASCII at each step. Less time would be lost in serial communication if the scanning loop was moved to the microcontroller. The PC would then only read the angular position sent by the PIC to record it with the spectra. This would eliminate at least some of the missed steps. The RS-232 baud rate could also be increased. Concerning the data analysis, a full processing chain has to be developed to generate quality assessed NO_2 columns. This includes the DOAS analysis, the georeferencing, and the air mass factor estimation for each individual pixel. We expect the first test flights in Romania in spring 2013.

8.6 Acknowledgments

The development of SWING has taken place in the framework of a collaboration between BIRA-IASB, the University of Galati, and Reev River Aerospace. We wish to particularly thank our Romanian colleagues from the University: Daniel-Eduard Constantin, Lucian P. Georgescu, Gabriel Murariu, and M. Voiculescu. From Reev River, we thank Florin Mingireanu and Ionut Mocanu. We also wish to thank colleagues at BIRA-IASB and particularly: Jeroen Maes and Caroline Fayt, and the ultralight aircraft pilot, Hugo Maes.

Chapter 9

Conclusions and perspectives

This thesis has consisted in the development and use of four innovative instruments dedicated to atmospheric research, namely the Airborne Limb Scanning DOAS (ALS-DOAS), Ultralight Motorized-DOAS (ULM-DOAS), Mobile-DOAS, and Small Whiskbroom Imager for trace gases monitoriNG (SWING). These instruments are all based on uv-visible spectrometers installed on mobile platforms. They all measure the absorption of trace gases in the scattered skylight using the Differential Optical Absorption Spectroscopy (DOAS) technique, but with different observation geometries. Their characteristics and uses are summarized in table 9.1.

Three of these instruments (ALS-DOAS, ULM-DOAS, and Mobile-DOAS) have already demonstrated their capacity to provide original contributions to atmospheric research, leading to two publications in the peer-reviewed literature. The findings of these three instruments are, moreover, complementary. The ALS-DOAS, which operates from a traditional aircraft dedicated to scientific research (the Safire ATR-42), measures profiles of trace gases and aerosol extinction with a high sensitivity. It is particularly valuable for investigations in the clean free troposphere. The ULM-DOAS, installed on an ultralight, measures NO_2 tropospheric columns at a relatively low spatial resolution but with the flexibility of movement and speed of an ultralight. This makes the instrument a good tool to study the average columns in semi-rural areas or the exhaust plumes of cities. The Mobile-DOAS, installed on a car, also measures columns but at a finer resolution and along roads, which reveals accurately the sharp horizontal gradients inside a city.

The SWING payload, developed for a dedicated UAV, will produce high spatial resolution maps of tropospheric NO_2 columns, combining thus the advantages of the ULM-DOAS and Mobile-DOAS.

Geophysical findings

Low levels of aerosol extinction and NO_2 were detected off the North coast of Norway in April 2008 (Merlaud et al., 2011). Back-trajectories and in-situ CO indicate that the aerosols are probably of anthropogenic origin. On 8 April 2008, the free troposphere appeared to be affected both by pollution transport from Northwestern Europe, responsible for extinction values around 0.01 km^{-1} and by a stratospheric intrusion. In the boundary layer, the observed aerosol extinction (0.04 km^{-1}) and NO_2 (1.9×10^9 molec/cm^3) seem to originate from metal smelters and industry near Nikel on the Kola peninsula. On 9 April 2008, long-range transport from central Europe is more clearly visible with a polluted layer in the free troposphere, with respective values for NO_2 and aerosol extinction of 0.025 km^{-1} and 1.95×10^9 molec/cm^3.

During the Earth Challenge expedition in November and December 2009, tropospheric columns of NO_2 were measured between Thailand and Belgium, above areas were local measurements have been reported (Merlaud et al., 2012). The highest NO_2 loading was detected above Karachi (2.4×10^{16} molec/cm^2. Measurements agreed relatively well with the satellite data (Ozone Monitoring Instrument (OMI) and Global Ozone Monitoring Experiment 2 (GOME-2)) except in the exhaust plume of Riyadh were our NO_2 columns were 40% larger than those seen by OMI. The spectra recorded while crossing a sand storm also confirm the recent finding of a soil signature above desert.

A large database of Mobile-DOAS measurements was built from the Cabauw Intercomparison Campaign of Nitrogen Dioxide measuring Instruments (CINDI) campaign in July 2009 to July 2011. These measurements, performed in Benelux, Germany, and France, are primarily intended to estimate the NO_2 tropospheric columns. During CINDI, they show a good agreement with a more sensitive Multi-Axis DOAS (MAX-DOAS) instrument. The database is valuable for instance to study the horizontal gradients at several scales: from the clean forestry regions of the Ardennes to the cities of Brussels and Antwerp, and from the Sonian Forest to the Uccle observatory. Preliminary comparisons with the CHIMERE model indicate a negative bias compared to CHIMERE which, if confirmed, may be explained by the decreasing trends of NO_2 in Western Europe. A paper on these results in preparation.

Lessons learned on instrumental aspects

Passive DOAS instruments based on compact spectrometers are good candidates for miniaturization compared to other spectroscopic techniques used in atmospheric research, such as Fourier Transform Infrared Spectroscopy (FTIR) or Light Detection And Ranging (LIDAR) systems. Compared specifically to

compact devices like acousto-optic tunable filters or Fabry-Perot interferometers, research-grade grating spectrometers are available off-the-shelf, which simplifies the instrument development and reduces the overall price.

For the ALS-DOAS instrument, the Terimide 7 thermal isolation was a very cost-effective choice. The baffle for spatial stray light on the input optics was found to be very important. There was no baffle on the ALS-DOAS telescope during the first flights of the campaign and that led to problems in the DOAS analyses. Vibrations were found to be a source of problems from an ultralight aircraft, as was experienced with the ULM-DOAS and SWING instruments. A solid state drive improves the reliability of the instrument, but only to a limited extent. Considering the operating system, Linux is a good choice for compact applications because it enables to get rid of most of the unnecessary pieces of software and particularly the Graphical User interface (GUI).

The development of these instruments would not have been possible without the workshops of Belgian Institute for Space Aeronomy (BIRA-IASB). The possibility to interact with skilled people at all stages of the manufacturing process was fundamental for this work. This aspect was important for the miniaturization effort, but also due to the sharp deadlines that were always respected. Similarly, the acquisition software is a crucial part of the instruments. It required experienced and motivated computer scientists more than the last fancy programming languages. None of the measurements ever failed because of a software deficiency.

Lessons learned on data analysis

The logarithmic approach used to analyze the Polar Study using Aircraft, Remote Sensing, Surface Measurements and Models, of Climate, Chemistry, Aerosols, and Transport (POLARCAT) data yielded aerosol extinction profiles more consistent with independently measured size distributions. Regarding the NO_2 profile, the logarithmic and linear approaches led to similar results. It should be noticed that, for retrievals based on DOAS measurements, the forward model is linear with respect to the concentration. Retrieving the logarithm of the concentration breaks this linearity and may do more harm than good, even if the distribution is closer to a lognormal. In these retrievals, the forward model parameters errors were included in the measurement uncertainty. This is not always done but it could be important in several applications. It was also shown from the POLARCAT data that the stratosphere must be accounted for when retrieving tropospheric profiles of NO_2 in pristine areas. The method we proposed to estimate a scaling factor for the O_4 cross section was applied by Baidar et al. (2012) in a similar airborne DOAS experiment.

The data analysis strategy used for Earth Challenge was very simple, following the simplicity of the instrument itself. Nevertheless, it led to reasonable results

when compared to satellite measurements. The spatial resolution of the measurements is, like in the ALS-DOAS case, limited by the limb geometry of the ULM-DOAS. However, the instrument is able to detect higher spatial frequency patterns in the NO_2 field than the the OMI satellite (around 5 km compared with an OMI pixel width of 13 km). A common assumption of scattered-light DOAS studies is the independence of the radiative transfer with respect to the absorber loading. It was shown that this assumption should be checked for NO_2 in polluted regions, since it could lead to larger errors than other sources usually taken into account in the error budget. This is important in particular for ground-based MAX-DOAS application in urban areas.

Regarding the Mobile-DOAS experiment, we showed that the commonly used geometrical approximation led to larger errors than what is assumed in other similar experiments, but that these errors were significantly reduced by taking into account the solar position. We also proposed a new method to reconstruct the high-frequency parts of the tropospheric NO_2 field from MAX-DOAS data. This method yields in general similar results compared to the solution of Wagner et al. (2010), but it does not imply the fit of an unphysical parameter in the cases when the duration of measurements of a given day is reduced.

Table 9.1: Main characteristics and use of the instruments developed in the framework of the thesis. The dectection limit (2σ) is calculated with a typical air mass factor for the given instrument and a 1 km thick boundary layer.

	ALS-DOAS	ULM-DOAS	Mobile-DOAS	SWING
Platforms	SAFIRE ATR-42	Ultralight aircraft	Car	Ultralight, UAV
Campaigns	POLARCAT	EARTH CHALLENGE	CINDI	Test flights
Places	Arctic (Norway)	Thailand to Belgium	The Netherlands, Belgium	Belgium
Dates	April 2008	Nov-Dec 2009	July 2009, 2010-2011	July, Oct. 2012
Geophysical outputs	Profiles of extinction, NO_2	Columns of NO_2 Soil signature	Columns of NO_2	Maps of NO_2 (to be achieved)
Geometries and field of view (FOV)	Scanning around limb, FOV = 1°	Limb large FOV FOV = 25°	Zenith and 30° FOV = 2.6°	Whiskbroom FOV = 2.6°
Air Mass Factors	10 to 40	2 to 7	0.5 to 2	1.5 to 3.5
Spatial Resolutions	1 km (vertical)	5 km (horizontal)	150 m (horizontal)	200x200m^2
Weights	16 kg	2.5 kg	5 kg	920 g
Power Consumptions	85 W	12 W	20 W	6 W
Detection Limits	30 ppt	300 ppt	1 ppb	3 ppb

Perspectives

Vertical distribution of halogen oxides in the troposphere with an upgraded ALS-DOAS

Halogen oxides are key species in ozone chemistry. Specifically regarding BrO and IO in the troposphere, several elements are currently controversial. The hotspots of BrO, visible on satellite data, have been explained differently by Salawitch et al. (2010) and Theys et al. (2011), respectively from stratospheric or tropospheric origin. It has also been suggested that forest fires could be a source of BrO (Pommier et al., 2012). Considering IO, very little information is available on its vertical distribution. The first airborne DOAS profiles of IO were recently performed with the CU AMAX-DOAS instrument Dix and Volkamer, 2010; Dix et al., 2011. They are inconsistent with both satellite data and model predictions, revealing high concentrations of IO in the free troposphere. This motivates further investigation.

Both BrO and IO vertical distributions could be measured with an improved version of the ALS-DOAS. For the former, the BK-7 port should be replaced by a fused silica version to increase the signal in the UV. In fact, this port already exists but it was not used during the campaign for technical reasons. For the latter, the Charge Coupled Device (CCD) should be changed to get rid of the dead pixel, currently hiding an IO absorption band. The main improvement would however consist in adding a feedback on the telescope elevation to compensate the aircraft roll. This was done with the CU AMAX-DOAS (Baidar et al., 2012) and yielded promising results in terms of sensitivity and vertical resolution.

Probability distribution functions of aerosol extinction in the free troposphere

The idea of retrieving a positive geophysical quantity through its logarithm has been applied in several studies. Two of them have motivated this choice by investigations of the probability density functions (PDFs) of the quantity to retrieve. Working with ground-based FTIR measurements of water vapor, Schneider et al. (2006) have analyzed 4 years of daily ptu-sondes. It turned out that the lognormal assumption for the water vapor PDFs was more realistic than the normal one, except in the first 100 m above the surface. Deeter et al. (2007), who were retrieving CO from the MOPITT satellite instrument, have used 16 years of ground level CO observations all over the globe. The PDFs were again better represented by a lognormal, especially in clean areas.

To our knowledge, a similar exercise has not yet been done for the aerosol extinction in the free troposphere. This could help future airborne DOAS experiments to retrieve aerosol and trace gases profiles. It might also be applied to

ground-based DOAS observations but the possible improvement is less clear since the extinction is probably more normally distributed in the boundary layer. There exists long-term lidar observations of aerosol extinction (e.g. Cao et al. (2012)) or measurements from high-altitude observatories (Andrews et al., 2011) which could be studied but both mostly represent mid-latitude continental conditions. For the Indian Ocean, which is of particular interest for BIRA-IASB, the lidar database from the Kerguelen Aerosols Measurement from African Sources and plUmes Trajectory Reverse Analysis campaign (KAMASUTRA) campaign (Duflot et al., 2011) would be very valuable. If the extinctions PDFs are found to be better represented by a lognormal, the next step could involve simulations of measurements to compare in detail the advantages and drawbacks of the two approaches (normal and lognormal). This should be done with LIDORT, for which we have determined the logarithm inputs (see appendix A). Using LIDORT would in particular improve one aspect of the retrieval: the weighting functions could be recalculated at each iteration. From these simulations, it would in particular be possible to decide whether it is worth to apply the lognormal method to ground-based observations.

ULM-DOAS operated with other compact instruments

The main drawback of the ULM-DOAS in its current status is its high sensitivity to the altitude of the NO_2 layer. To upgrade the instrument, ancillary geophysical information are necessary. Adding the NO_2 sondes developed at KNMI (Sluis et al., 2010) would enable to derive NO_2 profiles during the same flights. These sondes also have a Vaisala PTU sensor which would be useful to derive the boundary layer height. Another candidate is a compact lidar such as the one described by Chazette et al. (2007), which has been designed to operate from an ultralight. The lidar measures the aerosol extinction coefficient which is another important source of uncertainty in the air mass factor of the ULM-DOAS. With these improvements, the ULM-DOAS would be an extremely valuable tool for atmospheric research and particularly air quality studies. Operating from an ultralight is much cheaper than from a normal plane, and the flight clearances are less tiresome than from an UAV.

Use and expansion of the Mobile-DOAS database

The database constructed from 2009 is probably the largest of its kind and offers a wide range of applications. Comparison of tropospheric NO_2 columns with the CHIMERE model are ongoing and will be the subject of a near future publication. Mobile-DOAS measurements could also be compared with satellite data or with the Belgian in-situ network IRCEL-CELINE. Besides tropospheric NO_2, no serious attempt has been made to derive other geophysical quantities. Other absorbers should be investigated in the spectra. Using similar spectrometers,

Sinreich et al. (2007) have detected glyoxal (CHOCHO) and Wagner et al. (2013) recently reported measurements of water vapor total columns. Formaldehyde could also be measured as demonstrated during the CINDI campaign (Pinardi et al., 2013).

These measurements should be continued on the same opportunistic approach, i.e. using the daily car journeys of a volunteer. One issue that should not be neglected is the rational organization of the database and the automation of scripts to check the data regularly and quickly, and to create detailed logfiles. These long-term research activities are not considered enough, as was noted by (Nisbet, 2007) about Keeling work on CO_2 measurements at Mauna Loa observatory. But they have revealed both the increase in greenhouse gases and the ozone depletion.

SWING: improvements and flights

Arguably, the most promising development in this thesis is SWING. It represents the final achievement of a miniaturization effort that started with the ALS-DOAS on the ATR-42, with its 12 kg. However, some work remains to match the performance expected from simulations. The scanning loop should be improved to increase the spatial coverage. Too much time is lost in the serial communication with the PC. Currently, the PC sends the position information in ASCII at each steps, as was done with the ALS-DOAS. This can be improved by moving the scanning loop to the PIC microcontroller. In this way, the PC will only read the angular position sent by the PIC to record it with the spectra. This will probably eliminate most of the failed steps. Some more milliseconds could be gained by increasing the RS-232 baud rate. More advanced microcontrollers have an integrated and configurable UART module (Universal Asynchronous Receiver/Transmitter) which takes care of the serial communication, and an integrated clock. Changing the PIC is thus another upgrade to consider.

We expect the first test flights in Romania this spring (2013). Once it has been demonstrated that SWING is able to detect tropospheric NO_2 from the UAV at reasonnable concentrations, more specific applications will be possible. One of the foreseen projects consists in monitoring ship exhausts around La Reunion Island, similarly to an earlier airborne DOAS experiment from a traditional plane (Berg et al., 2012). Flying above Antwerp or another Belgian like city would be very interesting but may take some time to get clearances. Monitoring SO_2 emissions from volcanoes would also be feasible, with a dedicated spectrometer. This has recently started to be done for CO_2 (McGonigle et al., 2008). One should first look at the volcanoes monitored within the NOVAC network of ground-based DOAS instruments (Galle et al., 2010), due to the possibility of intercomparisons. Initial contacts have been taken along these lines with the Popocatépetl observatory in Mexico. In a longer term, SWING-UAV measurements may become part of exist-

ing monitoring systems of volcanoes. This application would be both scientifically sound and practically useful to reduce volcanic hazards, both for volcanologists and population.

Appendix A

Logarithmic weighting functions for LIDORT

A.1 Motivation

In the radiative transfer model LIDORT (Spurr, 2008), weighting functions are calculated for a given parameter α_n using as inputs the normalized partial derivatives of the optical properties of a layer n compared to this parameter. These properties are the optical depth Δ_n, single scattering albedo ω_n and Legendre polynomial expansion coefficients of the phase functions $\beta_{l,n}$. The inputs to calculate the weighting functions are thus:

$$\frac{\alpha_n}{\Delta_n}\frac{\partial \Delta_n}{\partial \alpha_n} \tag{A.1}$$

$$\frac{\alpha_n}{\omega_n}\frac{\partial \omega_n}{\partial \alpha_n} \tag{A.2}$$

$$\frac{\alpha_n}{\beta_{l,n}}\frac{\partial \beta_{l,n}}{\partial \alpha_n} \tag{A.3}$$

When retrieving a trace gas or an aerosol extinction profile, it is natural to choose for α the concentration or the vertical column in a layer or the aerosol extinction. Using for the inversion a regularization method like the maximum a posteriori solution (MAP), unphysical negative values are sometimes retrieved, which can only be avoided by strengthening the weight of the a priori, thus losing information coming from the measurements. A way to overcome this problem is to work with weighting functions relative to the logarithm of the quantity to retrieve, either the gas loading or the aerosol extinction. With the MAP solution, this means assuming the density of probability to be lognormal instead of normal. This

has been applied for water vapor (Schneider et al., 2006) and CO (Deeter et al., 2007) retrievals from FTIR spectra. From these two studies, it was concluded that the logarithmic approach not only improved the retrievals, but also that the lognormal a priori is closer to in-situ measured distributions. In chapter 5, we use the logarithmic approach to retrieve aerosol extinction from airborne limb radiance measurements. Results obtained are in better agreement with validation data than for the linear case.

We describe in Sect. 2 the inputs needed for an absorber and in Sect. 3 for the aerosol extinction.

A.2 Jacobian inputs for an absorber

The total optical depth Δ_n of a layer n is defined as:

$$\Delta_n = G_n + R_n + \mathcal{E}_n \tag{A.4}$$

where G_n is the gas optical depth absorption, R_n the Rayleigh optical depth and E_n the aerosol optical depth.

In the linear approach, a specific gas optical depth absorption is calculated as:

$$G_n = U_n \sigma_n \tag{A.5}$$

where U_n is the partial vertical column of the considered gas in the layer n in molec/cm^2 and σ_n its molecular absorption cross-section in cm^2/molec. In reality there are usually several absorbers so Eq. A.5 is a sum over these different absorbers, but since we are interested in the derivative compared to the concentration of one specific gas this is not important here.

A.2.1 Optical depth derivative

Let $\ln U_n = V_n$ then

$$G_n = e^{V_n} \sigma_n \tag{A.6}$$

We notice that:

$$\frac{\partial \Delta_n}{\partial V_n} = \frac{\partial (e^{V_n} \sigma_n + R_n + \mathcal{E}_n)}{\partial V_n} = e^{V_n} \sigma_n = G_n \tag{A.7}$$

Substituting this into Eq. A.1 yields:

$$\boxed{\frac{V_n}{\Delta_n} \frac{\partial \Delta_n}{\partial V_n} = \frac{V_n G_n}{\Delta_n}} \tag{A.8}$$

A.2.2 Single scattering albedo derivative

The single scattering albedo is by definition the ratio of the scattering optical depth by the total optical depth:

$$\omega_n = \frac{R_n + z\mathcal{E}_n}{\Delta_n} \tag{A.9}$$

where z is the single scattering albedo for aerosols. Using the chain rule:

$$\begin{aligned}\frac{\partial \omega_n}{\partial V_n} &= -\frac{R_n + z\mathcal{E}_n}{\Delta_n^2}\frac{\partial \Delta_n}{\partial V_n} \\ &= -\frac{R_n + z\mathcal{E}_n}{\Delta_n}\frac{1}{\Delta_n}\frac{\partial \Delta_n}{\partial V_n} \\ &= -\frac{\omega_n}{\Delta_n}\frac{\partial \Delta_n}{\partial V_n}\end{aligned} \tag{A.10}$$

Thus, in Eq A.2:

$$\boxed{\frac{V_n}{\omega_n}\frac{\partial \omega_n}{\partial V_n} = -\frac{V_n}{\Delta_n}G_n} \tag{A.11}$$

A.2.3 Phase function coefficients derivative

The l^{th} coefficient in the Legendre expansion of the phase function is given by:

$$\beta_{l,n} = \frac{R_n\beta_{l,n}^{Ray} + z\mathcal{E}_n\beta_{l,n}^{Aer}}{R_n + z\mathcal{E}_n} \tag{A.12}$$

Nothing depends on the gas concentration so this derivative vanishes.

$$\boxed{\frac{V_n}{\beta_{l,n}}\frac{\partial \beta_{l,n}}{\partial V_n} = 0} \tag{A.13}$$

A.3 Jacobian inputs for the aerosol extinction

Let $f_n = \ln(\mathcal{E}_n)$ then

$$\mathcal{E}_n = e^{f_n} \tag{A.14}$$

We notice that:

$$\frac{\partial \mathcal{E}_n}{\partial f_n} = e^{f_n} = \mathcal{E}_\backslash \tag{A.15}$$

From Eq. A.4 we find:

$$\frac{\partial \Delta_n}{\partial \mathcal{E}_n} = 1 \tag{A.16}$$

A.3.1 Optical depth derivative

From the chain rule, Eq. A.15 and Eq. A.16:

$$\begin{aligned}\frac{\partial \Delta_n}{\partial f_n} &= \frac{\partial \Delta_n}{\partial \mathcal{E}_n}\frac{\partial \mathcal{E}_n}{\partial f_n} \\ &= \frac{\partial \Delta_n}{\partial \mathcal{E}_n}\mathcal{E}_n \\ &= \mathcal{E}_n\end{aligned} \tag{A.17}$$

Thus:

$$\boxed{\frac{f_n}{\Delta_n}\frac{\partial \Delta_n}{\partial f_n} = \frac{f_n}{\Delta_n}\mathcal{E}_n} \tag{A.18}$$

A.3.2 Single scattering albedo derivative

We must apply the quotient rule on Eq. A.9. We notice first that, from Eq. A.15:

$$\frac{\partial (R_n + z\mathcal{E}_n)}{\partial f_n} = z\mathcal{E}_n \tag{A.19}$$

Then:

$$\begin{aligned}\frac{\partial \omega_n}{\partial f_n} &= \frac{z\mathcal{E}_n\Delta_n - \mathcal{E}_n(R_n + z\mathcal{E}_n)}{\Delta_n^2} \\ &= \frac{1}{\Delta_n}(z\mathcal{E}_n - \omega_n)\end{aligned} \tag{A.20}$$

Thus:

$$\boxed{\frac{f_n}{\omega_n}\frac{\partial \omega_n}{\partial f_n} = \frac{f_n}{\omega_n}\frac{\mathcal{E}_n}{\Delta_n}(z - \omega_n)} \tag{A.21}$$

A.3.3 Phase function coefficients derivative

We must apply the quotient rule on Eq. A.12. We notice that, from Eq. A.15:

$$\frac{\partial(R_n\beta_{l,n}^{Ray} + z\mathcal{E}_n\beta_{l,n}^{Aer})}{\partial f_n} = z\mathcal{E}_n\beta_{l,n}^{Aer} \tag{A.22}$$

Combining with Eq. A.19, Eq. A.12 and Eq. A.9:

$$\begin{aligned}\frac{\partial(\frac{R_n\beta_{l,n}^{Ray}+z\mathcal{E}_n\beta_{l,n}^{Aer}}{R_n+z\mathcal{E}_n})}{\partial f_n} &= \frac{z\mathcal{E}_n\beta_{l,n}^{Aer}(R_n + z\mathcal{E}_n) - z\mathcal{E}_n(R_n\beta_{l,n}^{Ray} + z\mathcal{E}_n\beta_{l,n}^{Aer})}{(R_n + z\mathcal{E}_n)^2} \\ &= \frac{z\mathcal{E}_n}{R_n + z\mathcal{E}_n}(\beta_{l,n}^{Aer} - \beta_{l,n}) \\ &= \frac{z\mathcal{E}_n}{\omega_n\Delta_n}(\beta_{l,n}^{Aer} - \beta_{l,n}) \end{aligned} \tag{A.23}$$

Thus:

$$\boxed{\frac{f_n}{\beta_{l,n}}\frac{\partial\beta_{l,n}}{\partial f_n} = \frac{f_n}{\beta_{l,n}}\frac{z\mathcal{E}_n}{\omega_n\Delta_n}(\beta_{l,n}^{Aer} - \beta_{l,n})} \tag{A.24}$$

A.4 Perspectives

The logarithmic approach described above has not yet been implemented in LIDORT. A perspective of this work is the study of the added value of the logarithmic approach to the retrieval of aerosol extinction and trace gases. A first step could be the characterization of the distribution functions of aerosol extinction at different altitudes in the troposphere. This can be done for instance using lidar measurements such as those presented by Duflot et al. (2011) for the Indian Ocean. If the lognormal shape appears dominant, as can be expected at least in the free troposphere, implementing the above formulas in LIDORT would both be geophysically realistic and time-efficient.

Appendix B

Two remarks on the inverse problem

Given the state of a physical system and the physical laws involved, it is possible to predict accurately the result of a measurement[1]. The *inverse problem* of estimating some aspects of the state from measurements is more difficult, in particular because the relationship between the state and the measurements is often surjective. This implies, independently of the measurement noise, that the problem is ill-posed and that a regularization of some sort is necessary to select a solution. In practice, measurements are often represented as linear and discrete and expressed as:

$$\mathbf{y} = \mathbf{K}\mathbf{x} + \epsilon \tag{B.1}$$

This equation describes the *forward model*, which represents the physics of the measurements. The issue is to retrieve a state vector $\hat{\mathbf{x}}$ (e.g. a profile of concentration) which fits the measurements $\mathbf{y}$ (e.g. radiances) within the measurement errors ϵ, considering the physical model ($\mathbf{K}$). The inverse problem arises in many areas of science. In geophysics, Tikhonov (1963) and Backus and Gilbert (1968) proposed two different methods to deal with the inverse problem, respectively based on the stability or the norm of the results. In atmospheric sciences, (Rodgers, 1976) did pioneer work, which were at first intended to retrieve temperature profiles from satellite measurements. In chapter 5, I have used his much quoted textbook (Rodgers, 2000)[2], but differently than many previous studies did.

[1] In the cases when quantum and chaos effects can be neglected, and if the physical laws and their mathematical formulations are accurate enough.

[2] Often referred to as "the optimal estimation". This expression does not appear in the book. The solution of Tikhonov and the one of Backus-Gilbert are also optimal estimations. The (in this case 'the' seems justified) non optimal method is described by Tarantola (2006). What is meant by "the optimal estimation" is in fact the *maximum a posteriori* solution, i.e. a regularization based on *prior probabilities* on the solution.

This appendix explains this choice in the first remark. The issue is worth considering for other applications, like satellite validation. The second remark deals with a method used in geophysics which could be of interest in atmospheric retrievals as well.

B.1 Impact of the unretrieved forward model parameters

A major advantage of Rodgers (2000) compared to other textbooks on the inverse problem (e.g. Milman (2000); Tarantola (2004)) is that it deals with the different sources of error in detail. In particular, the uncertainties on the *forward model parameters* ($\mathbf{S_b}$, in the formalism of Rodgers) are taken into account. The forward model parameters are all the variables of the forward model which are not retrieved, such as the ground albedo when the experiment is targeted to retrieve NO_2 profiles. These parameters are propagated to the final error budget with their measurement sensitivity ($\mathbf{K_b}$). But if we consider again the forward model (equation B.1), it seems natural to include the forward model parameters as well in the measurement error ϵ, because they may affect the measurements $\mathbf{y}$ *by definition*. This is actually stated by Rodgers (2000) on page 61: "The perturbation in the retrieval when [the forward model parameters] are ignored ... can be significant. If it is, the proper procedure is to either include the parameters in the state vector, or to treat them as extra sources of error, and replace ... $\mathbf{S}_\epsilon$ by ...". There is then a typing error in the book for the formula. The correct equation is, with $\mathbf{S_n}$ representing the instrumental noise:

$$\mathbf{S}_\epsilon = \mathbf{S_n} + \mathbf{K_b}\mathbf{S_b}\mathbf{K_b}^\top \tag{B.2}$$

The forward model parameters are explicitly considered to estimate the final errors in many papers (e.g. Barret et al. (2002); Coheur et al. (2005); Hendrick et al. (2007); Vigouroux et al. (2009); Senten et al. (2008); Theys (2010)), but the same studies do not include them in the measurement error. This approach may be valuable, as is discussed below, but not for a single profile retrieval, as was the case during POLARCAT.

Figure B.1 presents a simulation of a NO_2 profile measurements based on a airborne DOAS instrument in limb geometry. The profile is retrieved using the sounding of the plane, as was done with the ALS-DOAS during POLARCAT (chapter 5). Errors on the visibility (10km) and on the albedo (0.1) were introduced by calculating the weighting functions and the slant columns with different values of these two forward model parameters. In the upper panel, their effect is neglected on the measurements, while they are introduced in $\mathbf{S}_\epsilon$ in the lower panel. The dofs

of the signal is reduced in the lower panel but it also shows a better agreement with the NO_2 profile in this case. It can be argued that the retrieval sensitivity to the measurement is reduced due to the larger error ($\mathbf{S}_\epsilon$). In many practical cases, the a priori covariance ($\mathbf{S_a}$) is poorly known and used as a tuning parameter to select a stable solution. It is all the more so important to use a realistic uncertainty on the measurements, i.e. including $\mathbf{S_b}$. This also appears more logical when $\mathbf{S_b}$ is used in the error budget. Using a larger uncertainty on the measurement reduces the risk of overfitting. Whereof one cannot speak...

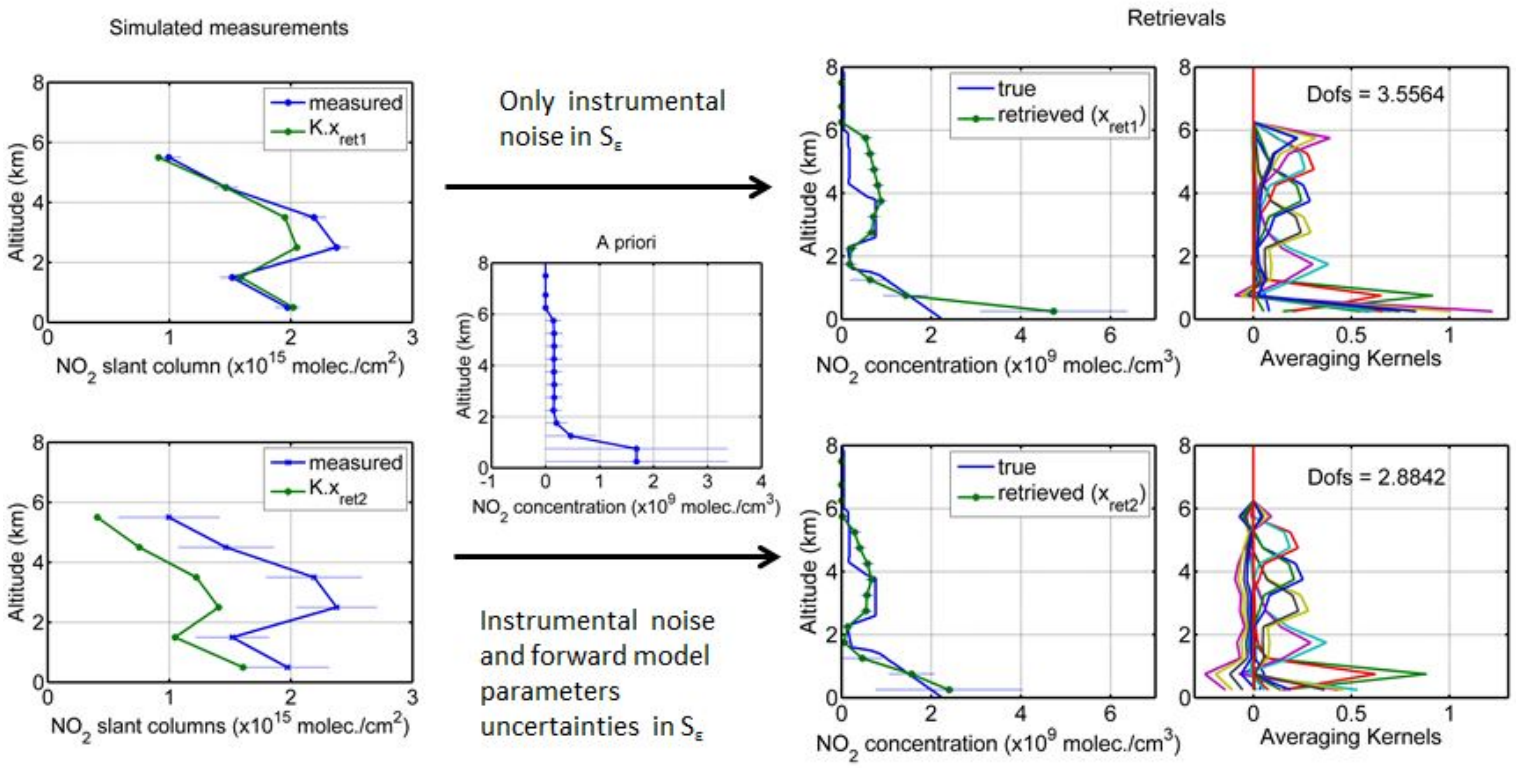

Figure B.1: Simulations of a NO_2 profile measurements illustrating the importance of the forward model parameters (here, the visibility and the albedo) for the retrieval.

The same line of reasoning should apply in particular when comparing individual measurements with space-based observation recorded during a satellite overpass. Note that leaving aside the effect of the forward model parameters in $\mathbf{S}_\epsilon$ is justified when averaging a large number of retrievals. The instrument noise is likely to be random, whereas the forward model parameters are often systematic (e.g. spectroscopic parameters). But as mentioned by Rodgers (p. 51), this dichotomy is not sharp. It could be valuable to introduce only the random forward model parameters in $\mathbf{S}_\epsilon$, if they can be identified.

B.2 Inequality-constrained maximum a posteriori solution

In some retrieval applications, e.g. when ancillary information are available, it may be interesting to limit the range of solutions to a given interval. Doicu et al. (2010) have recently proposed a retrieval method for ozone profiling from satellites which is based on an inequality constrained version of the Tikhonov regularization. The ozone vertical columns corresponding to the retrieved ozone profile is forced to a given interval $[c_{min}, c_{max}]$. Their study indicates that the method is promising.

By using the logarithm of the quantity of interest in a maximum a posteriori solution, the retrieval is constrained to positive values. It is possible to include inequality constraints in the maximum a posteriori by another change of variables, which has been proposed by Kim et al. (1999), who were primarily interested in geophysical issues. Given a quantity m (e.g. a NO_2 concentration at a given altitude) and an interval $[a, b]$ in which m is supposed to lie, the change of variable is:

$$x \leftarrow \ln \frac{m-a}{b-m} \tag{B.3}$$

This solution does not seem to be used for atmospheric retrievals. It may be worth testing. Of course, the inherent risk of this method is to overconstrain the solution. This may lead, in extreme cases, to miss a black swan (Taleb, 2008). But as for the normal case, the averaging kernels, if properly calculated, could indicate how much information originates from the measurement in the retrieval. The problems is the opposite of overfitting but it also requires an accurate error estimation.

Appendix C

Contributions to the scientific literature

Hereafter follows a list of publications I have written or co-authored in the framework of this thesis.

C.1 Peer-reviewed

- Vigouroux et al., Ground-based FTIR and MAX-DOAS observations of formaldehyde at Réunion Island and comparisons with satellite and model data, Atmos. Chem. Phys., 9, 9523-9544, doi:10.5194/acp-9-9523-2009, 2009
- Roscoe et al, Intercomparison of slant column measurements of NO_2 and O_4 by MAX-DOAS and zenith-sky UV and visible spectrometers, Atmos. Meas. Tech., 3, 1629-1646, doi:10.5194/amt-3-1629-2010, 2010
- Merlaud et al., Airborne DOAS measurements in Arctic: vertical distributions of aerosol extinction coefficient and NO_2 concentration, Atmos. Chem. Phys., 11, 9219-9236, doi:10.5194/acp-11-9219-2011, 2011
- Piters et al., The Cabauw Intercomparison campaign for Nitrogen Dioxide measuring Instruments (CINDI): design, execution, and early results, Atmos. Meas. Tech., 5, 457-485, doi:10.5194/amt-5-457-2012, 2012
- Merlaud et al., Equations for Solar Tracking, Sensors, 12, 4074-4090, doi:10.3390/s120404074, 2012
- Merlaud et al., DOAS measurements of NO_2 from an ultralight aircraft during the Earth Challenge expedition, Atmos. Meas. Tech., 5, 2057-2068, doi:10.5194/amt-5-2057-2012, 2012

- Pinardi et al., MAX-DOAS formaldehyde slant column measurements during CINDI: intercomparison and analysis improvement, Atmos. Meas. Tech., 6, 167-185, doi:10.5194/amt-6-167-2013, 2013

- Constantin et al., Measurements of tropospheric NO_2 in Romania using a zenith-sky mobile DOAS system and comparisons with satellite observations, Accepted for publication in Sensors, 2013

C.2 Proceedings and technical documents

- De Mazière et al., Regional monitoring of tropospheric NO_2 and CO using Remote Sensing from High Altitude Platforms - preliminary concepts, Second International Workshop: The Future of Remote Sensing, Antwerp, Belgium, 17-18 October 2006

- Covasnianu et al., Tropospheric exploration above Moldavia province: trace gas measurements-ATR42 flight as0729 on the 16th July 2007, Present Environment And Sustainable Development, 2, 101-110, 2008

- Constantin et al., Measurements of tropospheric NO_2 in a Romanian Region using a mobileDOAS system, 5th Workshop on Optoelectronic Techniques for Environmental Monitoring, Magurele, Romania, 28-30 September 2011

- Fayt et al., QDOAS Software User Manual, Belgian Insitute for Space Aeronomy, Brussels, Belgium, 2011

- Fussen et al., The Picasso Mission 4S ESA symposium, Portoroz, Slovenia, 4-8 June 2012

C.3 Popular science

- Merlaud et al., Earth Challenge: une aventure scientifique au service de l'environnement, Science Connection, January 2010
  (in Dutch: Earth Challenge, een menselijk en wetenschappelijk avontuur voor het milieu)

- Merlaud and Maggiolo, La scintillation des étoiles: 1. A l'oeil nu, aspects historiques et physiques, Ciel Et Terre, 127, 72-76, 2011
  (in Dutch, Fonkelende sterren met het blote oog: historische en fysische aspecten, Heelal, August 2012)

- Maggiolo and Merlaud, La scintillation des étoiles: 2. L'optique adaptative, Ciel Et Terre, 127, 104-107, 2011
  (in Dutch, Fonkelende sterren: adaptieve optica, Heelal, November 2012)

Acronyms

ALS-DOAS Airborne Limb Scanning DOAS.

AMF Air Mass Factor.

AOT aerosol optical thickness.

BIRA-IASB Belgian Institute for Space Aeronomy.

BLH Boundary Layer Height.

CCD Charge Coupled Device.

CFC chlorofluorocarbon.

CINDI Cabauw Intercomparison Campaign of Nitrogen Dioxide measuring Instruments.

CMOS Complementary Metal Oxide Semiconductor.

DOAS Differential Optical Absorption Spectroscopy.

DOFS Degrees Of Freedom of Signal.

DSCD Differential Slant Column Density.

ECMWF European Centre for Medium-Range Weather Forecasts.

FOV field of view.

FTIR Fourier Transform Infrared Spectroscopy.

FWHM Full Width at Half Maximum.

GA Geometrical Approximation.

GOME-2 Global Ozone Monitoring Experiment 2.

ITCZ Intertropical Convergence Zone.

KAMASUTRA Kerguelen Aerosols Measurement from African Sources and plUmes Trajectory Reverse Analysis campaign.

LIDAR Light Detection And Ranging.

MAX-DOAS Multi-Axis DOAS.

MODIS Moderate Resolution Imaging Spectroradiometer.

NDACC Network for the Detection of Atmospheric Composition Change.

OMI Ozone Monitoring Instrument.

OPAC Optical Properties of Aerosols and Clouds.

POLARCAT Polar Study using Aircraft, Remote Sensing, Surface Measurements and Models, of Climate, Chemistry, Aerosols, and Transport.

ppb parts per billion.

ppm parts per million.

ppt parts per trillion.

SCD Slant Column Density.

SVD Singular Value Decomposition.

SWING Small Whiskbroom Imager for trace gases monitoriNG.

TOA top of the atmosphere.

UAV Unmanned Aerial Vehicle.

ULM-DOAS Ultralight Motorized-DOAS.

VCD Vertical Column Density.

vmr volume mixing ratio.

VOC Volatile Organic Compound.

Bibliography

Acker, J. G. and Leptoukh, G.: Online analysis enhances use of NASA Earth science data, Eos Trans. AGU, 88, 14, doi:200710.1029/2007EO020003, 2007.

Aikens, R. S., Agard, D. A., and Sedat, J. W.: Solid-state imagers for microscopy, Method. Cell. Biol., 29, 291–313, PMID: 2643764, 1989.

Ancellet, G., Leclair de Bellevue, J., Mari, C., Nédélec, P., Kukui, A., Borbon, A., and Perros, P.: Effects of regional-scale and convective transports on tropospheric ozone chemistry revealed by aircraft observations during the wet season of the AMMA campaign, Atmos. Chem. Phys., 9, 383–411, doi: 10.5194/acp-9-383-2009, 2009.

Anderson, G. P., Lough, S. A., Kneizys, F. X., Chetwynd, J. H., and Shettle, E. P.: AFGL atmospheric constituent profiles (0-120km), Tech. Rep. AFGL-TR-86-0110, Air Force Geophysics Laboratory, 1986.

Andrews, E., Ogren, J., Bonasoni, P., Marinoni, A., Cuevas, E., Rodríguez, S., Sun, J., Jaffe, D., Fischer, E., Baltensperger, U., Weingartner, E., Coen, M. C., Sharma, S., Macdonald, A., Leaitch, W., Lin, N.-H., Laj, P., Arsov, T., Kalapov, I., Jefferson, A., and Sheridan, P.: Climatology of aerosol radiative properties in the free troposphere, Atmos. Res., 102, doi:10.1016/j.atmosres.2011.08.017, 2011.

Backus, G. and Gilbert, F.: The Resolving Power of Gross Earth Data, Geophys. J. Roy. Astr. S, 16, 169–205, doi:10.1111/j.1365-246X.1968.tb00216.x, 1968.

Baidar, S., Oetjen, H., Coburn, S., Dix, B., Ortega, I., Sinreich, R., and Volkamer, R.: The CU Airborne MAX-DOAS instrument: ground based validation, and vertical profiling of aerosol extinction and trace gases, Atmos. Meas. Tech. Discuss., 5, doi:10.5194/amtd-5-7243-2012, 2012.

Barck, C., Lundahl, J., Halldén, G., and Bylin, G.: Brief exposures to NO_2 augment the allergic inflammation in asthmatics, Environ. Res., 97, 58–66, doi: 10.1016/j.envres.2004.02.009, 2005.

Barret, B., De Mazière, M., and Demoulin, P.: Retrieval and characterization of ozone profiles from solar infrared spectra at the Jungfraujoch, J. Geophys. Res., 107, doi:10.1029/2001JD001298, 2002.

Beine, H. J. and Krognes, T.: The seasonal cycle of peroxyacetyl nitrate (PAN) in the European Arctic, Atmospheric Environment, 34, 933–940, doi:10.1016/S1352-2310(99)00288-5, 2000.

Beirle, S., Boersma, K. F., Platt, U., Lawrence, M. G., and Wagner, T.: Megacity Emissions and Lifetimes of Nitrogen Oxides Probed from Space, Science, 333, 1737 –1739, doi:10.1126/science.1207824, 2011.

Berg, N., Mellqvist, J., Jalkanen, J.-P., and Balzani, J.: Ship emissions of SO_2 and NO_2: DOAS measurements from airborne platforms, Atmos. Meas. Tech., 5, 1085–1098, doi:10.5194/amt-5-1085-2012, 2012.

Bernath, P. F.: Spectra of Atoms and Molecules, Oxford University Press, USA, 1995.

Bertaux, J.-L., Vandaele, A. C., Wilquet, V., Montmessin, F., Dahoo, R., Villard, E., Korablev, O., and Fedorova, A.: First observation of 628 CO_2 isotopologue band at 3.3 μm in the atmosphere of Venus by solar occultation from Venus Express, Icarus, 195, 28–33, doi:10.1016/j.icarus.2008.01.001, 2008.

Boersma, K. F., Eskes, H. J., and Brinksma, E. J.: Error analysis for tropospheric NO_2 retrieval from space, J. Geophys. Res-Atmos., 109, doi:10.1029/2003JD003962, 2004.

Boersma, K. F., Eskes, H. J., Veefkind, J. P., Brinksma, E. J., van der A, R. J., Sneep, M., van den Oord, G. H. J., Levelt, P. F., Stammes, P., Gleason, J. F., and Bucsela, E. J.: Near-real time retrieval of tropospheric NO_2 from OMI, Atmos. Chem. Phys., 7, 2103–2118, doi:10.5194/acp-7-2103-2007, 2007.

Boersma, K. F., Jacob, D. J., Bucsela, E. J., Perring, A. E., Dirksen, R., van der A, R. J., Yantosca, R. M., Park, R. J., Wenig, M. O., Bertram, T. H., and Cohen, R. C.: Validation of OMI tropospheric NO_2 observations during INTEX-B and application to constrain NO_x emissions over the eastern United States and Mexico, Atmos. Environ., 42, 4480–4497, doi:16/j.atmosenv.2008.02.004, 2008.

Boersma, K. F., Jacob, D. J., Trainic, M., Rudich, Y., De Smedt, I., Dirksen, R., and Eskes, H. J.: Validation of urban NO_2 concentrations and their diurnal and seasonal variations observed from the SCIAMACHY and OMI sensors using in situ surface measurements in Israeli cities, Atmos. Chem. Phys., 9, 3867–3879, doi:10.5194/acp-9-3867-2009, 2009.

Boersma, K. F., Eskes, H. J., Dirksen, R. J., van der A, R. J., Veefkind, J. P., Stammes, P., Huijnen, V., Kleipool, Q. L., Sneep, M., Claas, J., Leitão, J., Richter, A., Zhou, Y., and Brunner, D.: An improved tropospheric NO_2 column retrieval algorithm for the Ozone Monitoring Instrument, Atmos. Meas. Tech., 4, 1905–1928, doi:10.5194/amt-4-1905-2011, 2011.

Bogumil, K., Orphal, J., Homann, T., Voigt, S., Spietz, P., Fleischmann, O., Vogel, A., Hartmann, M., Kromminga, H., Bovensmann, H., Frerick, J., and Burrows, J.: Measurements of molecular absorption spectra with the SCIAMACHY preflight model: instrument characterization and reference data for atmospheric remote-sensing in the 230-2380 nm region, J. Photoch. Photobio. A., 157, 167–184, 2003.

Bond, T. C., Habib, G., and Bergstrom, R. W.: Limitations in the enhancement of visible light absorption due to mixing state, J. Geophys. Res., 111, doi:10.1029/2006JD007315, 2006.

Brandt, R. E., Warren, S. G., Worby, A. P., and Grenfell, T. C.: Surface Albedo of the Antarctic Sea Ice Zone, J. Climate, 18, 3606–3622, doi:10.1175/JCLI3489.1, 2005.

Breuer, M. and Albertz, J.: Geometric correction of airborne whiskbroom scanner imagery using hybrid auxiliary data, in: International Archives of Photogrammetry and Remote Sensing. Vol. XXXIII, Part B3, pp. 93–100, Amsterdam, 2000.

Brinkmann, R. T.: Rotational Raman Scattering in Planetary Atmospheres, Astrophys. J., 154, 1087, doi:10.1086/149827, 1968.

Brinksma, E. J., Pinardi, G., Volten, H., Braak, R., Richter, A., Schönhardt, A., Van Roozendael, M., Fayt, C., Hermans, C., Dirksen, R. J., Vlemmix, T., Berkhout, A. J. C., Swart, D. P. J., Oetjen, H., Wittrock, F., Wagner, T., Ibrahim, O. W., Leeuw, G. d., Moerman, M., Curier, R. L., Celarier, E. A., Cede, A., Knap, W. H., Veefkind, J. P., Eskes, H. J., Allaart, M., Rothe, R., Piters, A. J. M., and Levelt, P. F.: The 2005 and 2006 DANDELIONS NO_2 and aerosol intercomparison campaigns, J. Geophys. Res., 113, D16S46, doi:10.1029/2007JD008808, 2008.

Bruns, M., Buehler, S. A., Burrows, J. P., Richter, A., Rozanov, A., Wang, P., Heue, K. P., Platt, U., Pundt, I., and Wagner, T.: NO_2 Profile retrieval using airborne multi axis UV-visible skylight absorption measurements over central Europe, Atmos. Chem. Phys., 6, 3049–3058, doi:10.5194/acp-6-3049-2006, 2006.

Bucsela, E. J., Perring, A. E., Cohen, R. C., Boersma, K. F., Celarier, E. A., Gleason, J. F., Wenig, M. O., Bertram, T. H., Wooldridge, P. J., Dirksen, R., and Veefkind, J. P.: Comparison of tropospheric NO_2 from in situ aircraft measurements with near-real-time and standard product data from OMI, J. Geophys. Res., 113, 14 PP., doi:10.1029/2007JD008838, 2008.

Burrows, J., Richter, A., Dehn, A., Deters, B., Himmelmann, S., Voigt, S., and Orphal, J.: Atmospheric remote-sensing reference data from Gome 2. Temperature dependent absorption cross sections of O3 in the 231-794 nm range, J. Quant. Spectrosc. Ra., 61, doi:10.1016/S0022-4073(98)00037-5, 1999.

Cao, X., Wang, Z., Tian, P., Wang, J., Zhang, L., and Quan, X.: Statistics of aerosol extinction coefficient profiles and optical depth using lidar measurement over Lanzhou, China since 2005−2008, J. Quant. Spectrosc. Ra., doi:10.1016/j.jqsrt.2012.09.016, 2012.

Castellanos, P. and Boersma, K. F.: Reductions in nitrogen oxides over Europe driven by environmental policy and economic recession, Sci. Rep., 2, doi:10.1038/srep00265, 2012.

Celarier, E. A., Brinksma, E. J., Gleason, J. F., Veefkind, J. P., Cede, A., Herman, J. R., Ionov, D., Goutail, F., Pommereau, J.-P., Lambert, J.-C., Van Roozendael, M., Pinardi, G., Wittrock, F., Schönhardt, A., Richter, A., Ibrahim, O. W., Wagner, T., Bojkov, B., Mount, G., Spinei, E., Chen, C. M., Pongetti, T. J., Sander, S. P., Bucsela, E. J., Wenig, M. O., Swart, D. P. J., Volten, H., Kroon, M., and Levelt, P. F.: Validation of Ozone Monitoring Instrument nitrogen dioxide columns, J. Geophys. Res., 113, doi:10.1029/2007JD008908, 2008.

Chance, K., Kurosu, T., and Sioris, C.: Undersampling correction for array detector-based satellite spectrometers, Appl. Opt., 44, 1296–1304, doi:10.1364/AO.44.001296, 2005.

Chance, K. V. and Spurr, R. J. D.: Ring effect studies: Rayleigh scattering, including molecular parameters for rotational Raman scattering, and the Fraunhofer spectrum, Appl. Opt., 36, 5224–5230, doi:10.1364/AO.36.005224, 1997a.

Chance, K. V. and Spurr, R. J. D.: Ring effect studies: Rayleigh scattering, including molecular parameters for rotational Raman scattering, and the Fraunhofer spectrum, Appl. Opt., 36, 5224–5230, doi:10.1364/AO.36.005224, 1997b.

Chandrasekhar, S.: Radiative Transfer, Dover Publications, 1960.

Chazette, P., Sanak, J., and Dulac, F.: New Approach for Aerosol Profiling with a Lidar Onboard an Ultralight Aircraft: Application to the African Monsoon

Multidisciplinary Analysis, Environ. Sci. Technol., 41, 8335–8341, doi:10.1021/es070343y, 2007.

Chen, D., Zhou, B., Beirle, S., Chen, L. M., and Wagner, T.: Tropospheric NO_2 column densities deduced from zenith-sky DOAS measurements in Shanghai, China, and their application to satellite validation, Atmos. Chem. Phys., 9, doi:10.5194/acp-9-3641-2009, 2009.

Chiusolo, M., Cadum, E., Stafoggia, M., Galassi, C., Berti, G., Faustini, A., Bisanti, L., Vigotti, M. A., Dessì, M. P., Cernigliaro, A., Mallone, S., Pacelli, B., Minerba, S., Simonato, L., and Forastiere, F.: Short Term Effects of Nitrogen Dioxide on Mortality and Susceptibility Factors in Ten Italian Cities: the EpiAir Study, Environ. Health Persp., doi:10.1289/ehp.1002904, 2011.

Clémer, K., Van Roozendael, M., Fayt, C., Hendrick, F., Hermans, C., Pinardi, G., Spurr, R., Wang, P., and De Mazière, M.: Multiple wavelength retrieval of tropospheric aerosol optical properties from MAXDOAS measurements in Beijing, Atmos. Meas. Tech., 3, 863–878, doi:10.5194/amt-3-863-2010, 2010a.

Clémer, K., Van Roozendael, M., Fayt, C., Hendrick, F., Hermans, C., Pinardi, G., Spurr, R., Wang, P., and De Mazière, M.: Multiple wavelength retrieval of tropospheric aerosol optical properties from MAXDOAS measurements in Beijing, Atmos. Meas. Tech., 3, doi:10.5194/amt-3-863-2010, 2010b.

Clerbaux, C., Boynard, A., Clarisse, L., George, M., Hadji-Lazaro, J., Herbin, H., Hurtmans, D., Pommier, M., Razavi, A., Turquety, S., Wespes, C., and Coheur, P.-F.: Monitoring of atmospheric composition using the thermal infrared IASI/MetOp sounder, Atmos. Chem. Phys., 9, doi:10.5194/acp-9-6041-2009, 2009.

Coheur, P., Barret, B., Turquety, S., Hurtmans, D., Hadji-Lazaro, J., and Clerbaux, C.: Retrieval and characterization of ozone vertical profiles from a thermal infrared nadir sounder, J. Geophys. Res., 110, doi:10.1029/2005JD005845, 2005.

Corrigan, C. E., Roberts, G. C., Ramana, M. V., Kim, D., and Ramanathan, V.: Capturing vertical profiles of aerosols and black carbon over the Indian Ocean using autonomous unmanned aerial vehicles, Atmos. Chem. Phys., 8, 2008.

Cosemans, G. and Mensink, C.: How to determine urban background concentrations from traffic flows in neighbouring street canyons, in: Proceedings of the 10th Conference on Harmonisation within Atmospheric Dispersion Modelling for Regulatory Purposes, pp. 206–210, Heraklion, Crete, Greece, 2005.

De Maegd, M.: Earth challenge : Sydney-Bruxelles en ULM, La Renaissance du Livre, 2010.

De Mazière, M., Van Roozendael, M., and Merlaud, A.: Regional monitoring of tropospheric NO2 and CO using Remote Sensing from High Altitude Platforms - preliminary concepts, in: ISPRS Archives. Vol. XXXVI-1/W44, Second International Workshop: The Future of Remote Sensing, 2006.

De Smedt, I.: Long-Term Global Observations of Tropospheric Formaldehyde Retrieved from Spaceborne Nadir UV Sensors, Ph.D. thesis, Université Libre De Bruxelles, 2011.

De Smedt, I., Müller, J., Stavrakou, T., van der A, R., Eskes, H., and Van Roozendael, M.: Twelve years of global observations of formaldehyde in the troposphere using GOME and SCIAMACHY sensors, Atmos. Chem. Phys., 8, doi:10.5194/acp-8-4947-2008, 2008.

de Villiers, R. A., Ancellet, G., Pelon, J., Quennehen, B., Schwarzenboeck, A., Gayet, J. F., and Law, K. S.: Airborne measurements of aerosol optical properties related to early spring transport of mid-latitude sources into the Arctic, Atmos. Chem. Phys., 10, 5011–5030, doi:10.5194/acp-10-5011-2010, 2010.

Deeter, M. N., Edwards, D. P., and Gille, J. C.: Retrievals of carbon monoxide profiles from MOPITT observations using lognormal a priori statistics, J. Geophys. Res., 112, 9 PP., doi:10.1029/2006JD007999, 2007.

Dieudonné, E.: Analyse multi-instrumentale de l'influence de la variabilité de la hauteur de couche limite sur la distribution verticale des oxydes d'azote en région parisienne, Ph.D. thesis, Université Paris VI-Pierre et Marie Curie, 2012.

Dils, B.: Long Range Transport of Tropospheric NO_2 as simulated by FLEXPART, Product Specification Document TEM/LRT2/001, TEMIS, De Bilt, The Netherlands, 2008.

Dix, B. K. and Volkamer, R.: Airborne Detection of Iodine Oxide and Glyoxal in the Free Troposphere over the Remote Tropical Pacific Ocean, AGU Fall Meeting Abstracts, 53, 0288, 2010.

Dix, B. K., Bresch, J. F., Baidar, S., and Volkamer, R.: Detection of iodine oxide and glyoxal in the tropical free troposphere, AGU Fall Meeting Abstracts, -1, 07, 2011.

Dobson, G.: Forty Years' Research on Atmospheric Ozone at Oxford: a History, Appl. Optics., 7, 387–405, doi:10.1364/AO.7.000387, 1968.

Doicu, A., Schussler, O., and Loyola, D.: Constrained regularization methods for ozone profile retrieval from UV/VIS nadir spectrometers, J. Quant Spectrosc. Ra., 111, doi:10.1016/j.jqsrt.2009.11.020, 2010.

Dubovik, O. V., Lapyonok, T. V., and Oshchepkov, S. L.: Improved technique for data inversion: optical sizing of multicomponent aerosols, Appl. Optics, 34, 8422–8436, doi:10.1364/AO.34.008422, 1995.

Duflot, V., Royer, P., Chazette, P., Baray, J.-L., Courcoux, Y., and Delmas, R.: Marine and biomass burning aerosols in the southern Indian Ocean: Retrieval of aerosol optical properties from shipborne lidar and Sun photometer measurements, J. Geophys. Res., 116, doi:201110.1029/2011JD015839, 2011.

EMEP: EMEP/CORINAIR Emission Inventory Guidebook - 3rd edition October 2002 UPDATE, Technical report no 30, European Environment Agency, 2002.

Evans, M. J. and Jacob, D. J.: Impact of new laboratory studies of N_2O_5 hydrolysis on global model budgets of tropospheric nitrogen oxides, ozone, and OH, Geophys. Res. Lett., 32, doi:10.1029/2005GL022469, 2005.

Fayt, C., De Smedt, I., Letocart, V., Merlaud, A., Pinardi, G., and Van Roozendael, M.: QDOAS, Software User Manual, Belgian Insitute for Space Aeronomy, Brussels, Belgium, 2011.

Forster, C., Wandinger, U., Wotawa, G., James, P., Mattis, I., Althausen, D., Simmonds, P., O'Doherty, S., Jennings, S. G., Kleefeld, C., Schneider, J., Trickl, T., Kreipl, S., Jäger, H., and Stohl, A.: Transport of boreal forest fire emissions from Canada to Europe, J. Geophys. Res., 106, PP. 22,887–22,906, doi:10.1029/2001JD900115, 2001.

Frieß, U., Monks, P. S., Remedios, J. J., Rozanov, A., Sinreich, R., Wagner, T., and Platt, U.: MAX-DOAS O_4 measurements: A new technique to derive information on atmospheric aerosols: 2. Modeling studies, J. Geophys. Res., 111, doi:10.1029/2005JD006618, 2006.

Galle, B., Oppenheimer, C., Geyer, A., McGonigle, A. J., Edmonds, M., and Horrocks, L.: A miniaturised ultraviolet spectrometer for remote sensing of SO_2 fluxes: a new tool for volcano surveillance, J. Volcanol. Geoth. Res., 119, doi:10.1016/S0377-0273(02)00356-6, 2003.

Galle, B., Johansson, M., Rivera, C., Zhang, Y., Kihlman, M., Kern, C., Lehmann, T., Platt, U., Arellano, S., and Hidalgo, S.: Network for Observation of Volcanic

and Atmospheric Change (NOVAC) — A global network for volcanic gas monitoring: Network layout and instrument description, J. Geophys. Res., 115, doi:10.1029/2009JD011823, 2010.

Gottwald, M. and Bovensmann, H., eds.: SCIAMACHY - Exploring the Changing Earth's Atmosphere, Springer, 2011.

Grainger, J. F. and Ring, J.: Anomalous Fraunhofer Line Profiles, Nature, 193, doi:10.1038/193762a0, 1962a.

Grainger, J. F. and Ring, J.: Anomalous Fraunhofer Line Profiles, Nature, 193, doi:10.1038/193762a0, 1962b.

Granier, C., Niemeier, U., Jungclaus, J. H., Emmons, L., Hess, P., Lamarque, J.-F., Walters, S., and Brasseur, G. P.: Ozone pollution from future ship traffic in the Arctic northern passages, Geophys. Res. Lett., 33, doi:10.1029/2006GL026180, 2006.

Green, R., Eastwood, M., Sarture, C., Chrien, T., Aronsson, M., Chippendale, B., Faust, J., Pavri, B., Chovit, C., Solis, M., Olah, M., and Williams, O.: Imaging Spectroscopy and the Airborne Visible/Infrared Imaging Spectrometer (AVIRIS), Remote Sens. Environ., 65, doi:10.1016/S0034-4257(98)00064-9, 1998.

Guibert, S., Matthias, V., Schulz, M., Bosenberg, J., Eixmann, R., Mattis, I., Pappalardo, G., Ritaperrone, M., Spinelli, N., and Vaughan, G.: The vertical distribution of aerosol over Europe — synthesis of one year of EARLINET aerosol lidar measurements and aerosol transport modeling with LMDzT-INCA, Atmospheric Environment, 39, 2933–2943, doi:10.1016/j.atmosenv.2004.12.046, 2005.

Harder, J. W. and Brault, J. W.: Atmospheric measurements of water vapor in the 442-nm region, J. Geophys. Res., 102, 6245–6252, doi:10.1029/96JD01730, 1997.

Hayn, M., Beirle, S., Hamprecht, F. A., Platt, U., Menze, B. H., and Wagner, T.: Analysing spatio-temporal patterns of the global NO_2-distribution retrieved from GOME satellite observations using a generalized additive model, Atmos. Chem. Phys., 9, doi:10.5194/acp-9-6459-2009, 2009.

Heck, W. W., Adams, R. M., Cure, W. W., Heagle, A. S., Heggestad, H. E., Kohut, R. J., Kress, L. W., Rawlings, J. O., and Taylor, O. C.: A reassessment of crop loss from ozone, Environ. Sci. Technol., 17, 572A–581A, doi:10.1021/es00118a716, 1983.

Heland, J., Schlager, H., Richter, A., and Burrows, J. P.: First comparison of tropospheric NO_2 column densities retrieved from GOME measurements and in situ aircraft profile measurements, Geophys. Res. Lett., 29, 4 PP., doi:10.1029/2002GL015528, 2002.

Hendrick, F., Barret, B., Van Roozendael, M., Boesch, H., Butz, A., De Mazière, M., Goutail, F., Hermans, C., Lambert, J.-C., Pfeilsticker, K., and Pommereau, J.-P.: Retrieval of nitrogen dioxide stratospheric profiles from ground-based zenith-sky UV-visible observations: validation of the technique through correlative comparisons, Atmos. Chem. Phys., 4, 2091–2106, doi:10.5194/acp-4-2091-2004, 2004.

Hendrick, F., Van Roozendael, M., Kylling, A., Petritoli, A., Rozanov, A., Sanghavi, S., Schofield, R., von Friedeburg, C., Wagner, T., Wittrock, F., Fonteyn, D., and De Mazière, M.: Intercomparison exercise between different radiative transfer models used for the interpretation of ground-based zenith-sky and multi-axis DOAS observations, Atmos. Chem. Phys., 6, 93–108, doi:10.5194/acp-6-93-2006, 2006a.

Hendrick, F., Van Roozendael, M., Kylling, A., Petritoli, A., Rozanov, A., Sanghavi, S., Schofield, R., Von Friedeburg, C., Wagner, T., Wittrock, F., Fonteyn, D., and De Maziére, M.: Intercomparison exercise between different radiative transfer models used for the interpretation of ground-based zenith-sky and multi-axis DOAS observations, Atmos. Chem. Phys., 6, 93–108, doi:10.5194/acp-6-93-2006, 2006b.

Hendrick, F., Van Roozendael, M., Chipperfield, M. P., Dorf, M., Goutail, F., Yang, X., Fayt, C., Hermans, C., Pfeilsticker, K., Pommereau, J.-P., Pyle, J. A., Theys, N., and De Mazière, M.: Retrieval of stratospheric and tropospheric BrO profiles and columns using ground-based zenith-sky DOAS observations at Harestua, Atmos. Chem. Phys., 7, 4869–4885, doi:10.5194/acp-7-4869-2007, 2007.

Herber, A., Thomason, L. W., Gernandt, H., Leiterer, U., Nagel, D., Schulz, K.-H., Kaptur, J., Albrecht, T., and Notholt, J.: Continuous day and night aerosol optical depth observations in the Arctic between 1991 and 1999, J. Geophys. Res.-Atmos., 107, doi:10.1029/2001JD000536, 2002.

Herman, J., Cede, A., Spinei, E., Mount, G., Tzortziou, M., and Abuhassan, N.: NO_2 column amounts from ground-based Pandora and MFDOAS spectrometers using the direct-sun DOAS technique: Intercomparisons and application to OMI validation, J. Geophys. Res., 114, doi:200910.1029/2009JD011848, 2009.

Hess, M., Koepke, P., and Schult, I.: Optical Properties of Aerosols and Clouds: The Software Package OPAC, B. Am. Meteorol. Soc., 79, 831–844, 1998.

Heue, K.-P., Richter, A., Bruns, M., Burrows, J. P., von Friedeburg, C., Platt, U., Pundt, I., Wang, P., and Wagner, T.: Validation of SCIAMACHY tropospheric NO_2-columns with AMAXDOAS measurements, Atmos. Chem. Phys., 5, 1039–1051, doi:10.5194/acp-5-1039-2005, 2005.

Hönninger, G., von Friedeburg, C., and Platt, U.: Multi axis differential optical absorption spectroscopy (MAX-DOAS), Atmos. Chem. Phys., 4, 231–254, doi:10.5194/acp-4-231-2004, 2004.

Honrath, R. E., Peterson, M. C., Guo, S., Dibb, J. E., Shepson, P. B., and Campbell, B.: Evidence of NO_x production within or upon ice particles in the Greenland snowpack, Geophys. Res. Lett., 26, P695–698, doi:10.1029/1999GL900077, 1999.

IBGE: La qualité de l'air en région de Bruxelles-Capitale, Tech. rep., Bruxelles Environment, 2009.

Ibrahim, O., Shaiganfar, R., Sinreich, R., Stein, T., Platt, U., and Wagner, T.: Car MAX-DOAS measurements around entire cities: quantification of NOx emissions from the cities of Mannheim and Ludwigshafen (Germany), Atmos. Meas. Tech., 3, 709–721, doi:10.5194/amt-3-709-2010, 2010.

IPCC: Contribution of Working Group I to the Fourth Assessment Report of the Intergovernmental Panel on Climate Change, Cambridge University Press, 2007.

Irie, H., Kanaya, Y., Akimoto, H., Iwabuchi, H., Shimizu, A., and Aoki, K.: First retrieval of tropospheric aerosol profiles using MAX-DOAS and comparison with lidar and sky radiometer measurements, Atmos. Chem. Phys., 8, 341–350, doi:10.5194/acp-8-341-2008, 2008.

Jacob, D.: Introduction to Atmospheric Chemistry, Princeton University Press, 1999.

Johansson, M., Rivera, C., de Foy, B., Lei, W., Song, J., Zhang, Y., Galle, B., and Molina, L.: Mobile mini-DOAS measurement of the outflow of NO_2 and HCHO from Mexico City, Atmos. Chem. Phys., 9, 5647–5653, doi:10.5194/acp-9-5647-2009, 2009a.

Johansson, M., Rivera, C., de Foy, B., Lei, W., Song, J., Zhang, Y., Galle, B., and Molina, L.: Mobile mini-DOAS measurement of the outflow of NO_2 and HCHO from Mexico City, Atmos. Chem. Phys., 9, 5647–5653, doi:10.5194/acp-9-5647-2009, 2009b.

Junkermann, W.: An Ultralight Aircraft as Platform for Research in the Lower Troposphere: System Performance and First Results from Radiation Transfer Studies in Stratiform Aerosol Layers and Broken Cloud Conditions, J. Atmos. Ocean. Tech., 18, 934, doi:10.1175/1520-0426(2001)018<0934:AUAAPF>2.0.CO;2, 2001.

Junkermann, W.: On the distribution of formaldehyde in the western Po-Valley, Italy, during FORMAT 2002/2003, Atmos. Chem. Phys., 9, 9187–9196, doi:10.5194/acp-9-9187-2009, 2009.

Kang, S. M., Polvani, L. M., Fyfe, J. C., and Sigmond, M.: Impact of Polar Ozone Depletion on Subtropical Precipitation, Science, 332, 951–954, doi:10.1126/science.1202131, 2011.

Kim, H., Song, Y., and Lee, K.: Inequality constraint in least-squares inversion of geophysical data, Earth Planets and Space, 51, 255âĂŞ260, 1999.

Kittaka, C., Winker, D. M., Vaughan, M. A., Omar, A., and Remer, L. A.: Intercomparison of column aerosol optical depths from CALIPSO and MODIS-Aqua, Atmos. Meas. Tech., 4, 131–141, doi:10.5194/amt-4-131-2011, 2011.

Kleipool, Q. L., Dobber, M. R., de Haan, J. F., and Levelt, P. F.: Earth surface reflectance climatology from 3 years of OMI data, J. Geophys. Res., 113, doi:10.1029/2008JD010290, 2008.

Koike, M., Kondo, Y., Kawakami, S., Nakajima, H., Gregory, G. L., Sachse, G. W., Singh, H. B., Browell, E. V., Merrill, J. T., and Newell, R. E.: Reactive nitrogen and its correlation with O_3 and CO over the Pacific in winter and early spring, J. Geophys. Res., 102, doi:10.1029/97JD02085, 1997.

Konovalov, I. B., Beekmann, M., Burrows, J. P., and Richter, A.: Satellite measurement based estimates of decadal changes in European nitrogen oxides emissions, Atmos. Chem. Phys., 8, 2623–2641, doi:10.5194/acp-8-2623-2008, 2008.

Koschmieder, H.: Theorie der horizontalen Sichtweite, Beitrag. Atm. Physik., 12, 33–55, 1926.

Kowalewski, M. G. and Janz, S. J.: Remote sensing capabilities of the Airborne Compact Atmospheric Mapper, in: Proc. SPIE 7452, Earth Observing Systems XIV, 74520Q, doi:10.1117/12.827035, 2009.

Kramer, L. J., Leigh, R. J., Remedios, J. J., and Monks, P. S.: Comparison of OMI and ground-based in situ and MAX-DOAS measurements of tropospheric nitrogen dioxide in an urban area, J. Geophys. Res., 113, 12 PP., doi:200810.1029/2007JD009168, 2008.

Kurucz, R.: The Solar Spectrum: Atlases and Line Identifications, in: Proceedings of ASP Conference, vol. 81, p. 17, 1995.

Lambert, J.-C., Pinardi, G., Granville, J., Clémer, K., Delcloo, A., Valks, P., and Hao, N.: O3M SAF Validation Report, Tech. Rep. SAF/O3M/IASB/VR/NO2/095, EUMETSAT, 2011.

Lamsal, L. N., Martin, R. V., van Donkelaar, A., Celarier, E. A., Bucsela, E. J., Boersma, K. F., Dirksen, R., Luo, C., and Wang, Y.: Indirect validation of tropospheric nitrogen dioxide retrieved from the OMI satellite instrument: Insight into the seasonal variation of nitrogen oxides at northern midlatitudes, J. Geophys. Res., doi:10.1029/2009JD013351, 2010.

Landulfo, E., Papayannis, A., Artaxo, P., Castanho, A. D. A., de Freitas, A. Z., Souza, R. F., Vieira Junior, N. D., Jorge, M. P. M. P., Sánchez-Ccoyllo, O. R., and Moreira, D. S.: Synergetic measurements of aerosols over São Paulo, Brazil using LIDAR, sunphotometer and satellite data during the dry season, Atmos. Chem. Phys., 3, 1523–1539, doi:10.5194/acp-3-1523-2003, 2003.

Latza, U., Gerdes, S., and Baur, X.: Effects of nitrogen dioxide on human health: systematic review of experimental and epidemiological studies conducted between 2002 and 2006, Int. J. Hyg. Environ. Health, 212, 271–287, doi:10.1016/j.ijheh.2008.06.003, 2009.

Law, K. and Stohl, A.: Arctic Air Pollution: Origins and Impacts, Science, 315, 1537–1540, doi:10.1126/science.1137695, 2007.

Lehn, W. and van der Werf, S.: Atmospheric refraction: a history, Appl. Optics., 44, doi:10.1364/AO.44.005624, 2005.

Lerner, J. and Thevenon, A.: The Optics of Spectroscopy: A Tutorial, Jobin Yvon/JY Optical System, 1998.

Lerot, C., Stavrakou, T., De Smedt, I., Müller, J.-F., and Van Roozendael, M.: Glyoxal vertical columns from GOME-2 backscattered light measurements and comparisons with a global model, Atmos. Chem. Phys., 10, doi:10.5194/acp-10-12059-2010, 2010.

Levelt, P., van den Oord, G., Dobber, M., Malkki, A., Visser, H., de Vries, J., Stammes, P., Lundell, J., and Saari, H.: The ozone monitoring instrument, IEEE T. Geosci. Remote., 44, doi:10.1109/TGRS.2006.872333, 2006.

Lin, J.-T. and McElroy, M. B.: Detection from space of a reduction in anthropogenic emissions of nitrogen oxides during the Chinese economic downturn, Atmos. Chem. Phys., 11, 8171–8188, doi:10.5194/acp-11-8171-2011, 2011.

Lin, P.-H.: OBSERVATIONS: The First Successful Typhoon Eyewall-Penetration Reconnaissance Flight Mission Conducted by the Unmanned Aerial Vehicle, Aerosonde, B. Am. Meteorol. Soc., 87, 1481–1483, 2006.

Liou, K.: An Introduction to Atmospheric Radiation, Academic Press, 2002.

Litwiller, D.: CMOS vs CCD: Maturing technologies, maturing markets, Photon Spectra, 2005.

Loyola, D., van Geffen, J., Valks, P., Erbertseder, T., Van Roozendael, M., Thomas, W., Zimmer, W., and Wißkirchen, K.: Satellite-based detection of volcanic sulphur dioxide from recent eruptions in Central and South America, Adv. Geosci., 14, 35–40, doi:10.5194/adgeo-14-35-2008, 2008.

Madsen, K., Nielsen, H. B., and Tingleff, O.: Methods for Non-Linear Least Squares Problems (2nd ed.), Tech. rep., Informatics and Mathematical Modelling, Technical University of Denmark, DTU, 2004.

Martin, S., Bange, J., and Beyrich, F.: Meteorological profiling of the lower troposphere using the research UAV "M^{2}AV Carolo", Atmos. Meas. Tech., 4, doi: 10.5194/amt-4-705-2011, 2011.

Mätzler, C.: Matlab functions for Mie scattering and absorption, Research report no. 2002-08, Institut für Angewandte Physik, Bern, 2002.

Mayer, B. and Kylling, A.: Technical note: The libRadtran software package for radiative transfer calculations - description and examples of use, Atmos. Chem. Phys., 5, 1855–1877, doi:10.5194/acpd-5-1319-2005, 2005.

McGonigle, A. J. S., Aiuppa, A., Giudice, G., Tamburello, G., Hodson, A. J., and Gurrieri, S.: Unmanned aerial vehicle measurements of volcanic carbon dioxide fluxes, Geophys. Res. Let., 35, L06 303, doi:10.1029/2007GL032508, 2008.

McLinden, C. A., McConnell, J. C., Strong, K., McDade, I. C., Gattinger, R. L., King, R., Solheim, B., Llewellyn, E. J., and Evans, W. J.: The impact of the OSIRIS grating efficiency on radiance and trace-gas retrievals, Can. J. Phys., 80, doi:10.1139/p01-151, 2002.

McPeters, R. D., Labow, G. J., and Logan, J. A.: Ozone climatological profiles for satellite retrieval algorithms, J. Geophys. Res., 112, doi:10.1029/2005JD006823, 2007.

Mellqvist, J., Samuelsson, J., Johansson, J., Rivera, C., Lefer, B., Alvarez, S., and Jolly, J.: Measurements of industrial emissions of alkenes in Texas using the solar occultation flux method, J. Geophys. Res., 115, doi:10.1029/2008JD011682, 2010.

Merlaud, A., Van Roozendael, M., Theys, N., Fayt, C., Hermans, C., Quennehen, B., Schwarzenboeck, A., Ancellet, G., Pommier, M., Pelon, J., Burkhart, J., Stohl, A., and De Mazière, M.: Airborne DOAS measurements in Arctic: vertical distributions of aerosol extinction coefficient and NO_2 concentration, Atmos. Chem. Phys., 11, 9219–9236, doi:10.5194/acp-11-9219-2011, 2011.

Merlaud, A., De Mazière, M., Hermans, C., and Cornet, A.: Equations for Solar Tracking, Sensors, 12, doi:10.3390/s120404074, 2012.

Milman, A.: Mathematical Principles of Remote Sensing, CRC Press, 2000.

Mitchell, J.: Visual range in the polar regions with particular reference to the Alaskan Arctic, J. Atmos. Terr. Phys. Special Suppl., 1, 195âĂŞ211, 1957.

Mount, G. H., Rusch, D. W., Noxon, J. F., Zawodny, J. M., and Barth, C. A.: Measurements of Stratospheric NO_2 from the Solar Mesosphere Explorer Satellite 1. An Overview of the Results, J. Geophys. Res., 89, 1327–1340, doi:10.1029/JD089iD01p01327, 1984.

Munro, R., Eisinger, M., Anderson, C., Callies, J., Corpaccioli, E., Lang, R., Lefebvre, A., Livschitz, Y., and Albinana, A. P.: GOME-2 on MetOp, in: The 2006 EUMETSAT Meteorological Satellite Conference, p. 48, 2006.

NARSTO: An Assessment of Tropospheric Ozone Pollution: A North American Perspective, NARSTO Management Office (Envair), Pasco, Washington, 2000.

Nebuloni, R.: Empirical relationships between extinction coefficient and visibility in fog, Appl. Opt., 44, 3795–3804, doi:10.1364/AO.44.003795, 2005.

Nédélec, P., Cammas, J.-P., Thouret, V., Athier, G., Cousin, J.-M., Legrand, C., Abonnel, C., Lecoeur, F., Cayez, G., and Marizy, C.: An improved infrared carbon monoxide analyser for routine measurements aboard commercial Airbus aircraft: technical validation and first scientific results of the MOZAIC III programme, Atmos. Chem. Phys., 3, 1551–1564, doi:10.5194/acp-3-1551-2003, 2003.

Nisbet, E.: Earth monitoring: Cinderella science, Nature, 450, doi:10.1038/450789a, 2007.

NOAA-NESDIS: Algorithm Theoretical Basis Document For Visibility, Tech. rep., Center for satellite applications and research, 2010.

Noxon, J.: Nitrogen Dioxide in the Stratosphere and Troposphere Measured by Ground-Based Absorption Spectroscopy, Science, 189, doi:10.1126/science.189.4202.547, 1975.

Olivier, J., Aardenne, J. V., Dentener, F., Pagliari, V., Ganzeveld, L., and Peters, J.: Recent trends in global greenhouse gas emissions: regional trends 1970-2000 and spatial distribution of key sources in 2000, Env. Sc., 2, 81–99, doi:10.1080/15693430500400345, 2005.

Palm, S. P., Benedetti, A., and Spinhirne, J.: Validation of ECMWF global forecast model parameters using GLAS atmospheric channel measurements, Geophys. Res. Lett., 32, doi:10.1029/2005GL023535, 2005.

Peng, F., Xie, P., Zhang, Y., Zhu, Y., Si, F., Liu, W., and Wang, J.: Effect of spectral resolution on the measurement of monoaromatic hydrocarbons by DOAS, J. Environ. Sci-China, 20, 632–640, 2008.

Petty, G.: A First Course in Atmospheric Radiation, Sundog Publishing, 2 edn., 2006.

Pinardi, G., Hendrick, F., Clémer, K., Lambert, J.-C., Bai, J., and Van Roozendael, M.: On the use of the MAX-DOAS technique for the validation of tropospheric NO_2 column measurements from satellite, in: EUMETSAT meteorological satellite conference, 2008.

Pinardi, G., Lambert, J.-C., Granville, J., Van Roozendael, M., Delcloo, A., De Backer, H., Valks, P., and Hao, N.: Overview of the validation of GOME-2 total and tropospheric NO_2 columns, in: EUMETSAT meteorological satellite conference, 2010.

Pinardi, G., Van Roozendael, M., Abuhassan, N., Adams, C., Cede, A., Clémer, K., Fayt, C., Frieß, U., Gil, M., Herman, J., Hermans, C., Hendrick, F., Irie, H., Merlaud, A., Navarro Comas, M., Peters, E., Piters, A. J. M., Puentedura, O., Richter, A., Schönhardt, A., Shaiganfar, R., Spinei, E., Strong, K., Takashima, H., Vrekoussis, M., Wagner, T., Wittrock, F., and Yilmaz, S.: MAX-DOAS formaldehyde slant column measurements during CINDI: intercomparison and analysis improvement, Atmos. Meas. Tech., 6, doi:10.5194/amt-6-167-2013, 2013.

Piters, A. J. M., Boersma, K. F., Kroon, M., Hains, J. C., Van Roozendael, M., Wittrock, F., Abuhassan, N., Adams, C., Akrami, M., Allaart, M. A. F., Apituley, A., Beirle, S., Bergwerff, J. B., Berkhout, A. J. C., Brunner, D., Cede, A., Chong, J., Clémer, K., Fayt, C., Frieß, U., Gast, L. F. L., Gil-Ojeda, M., Goutail, F., Graves, R., Griesfeller, A., Großmann, K., Hemerijckx, G., Hendrick, F., Henzing, B., Herman, J., Hermans, C., Hoexum, M., van der Hoff, G. R., Irie, H., Johnston, P. V., Kanaya, Y., Kim, Y. J., Klein Baltink, H., Kreher, K., de Leeuw, G., Leigh, R., Merlaud, A., Moerman, M. M., Monks, P. S., Mount, G. H., Navarro-Comas, M., Oetjen, H., Pazmino, A., Perez-Camacho, M., Peters, E., du Piesanie, A., Pinardi, G., Puentedura, O., Richter, A., Roscoe, H. K., Schönhardt, A., Schwarzenbach, B., Shaiganfar, R., Sluis, W., Spinei, E., Stolk, A. P., Strong, K., Swart, D. P. J., Takashima, H., Vlemmix, T., Vrekoussis, M., Wagner, T., Whyte, C., Wilson, K. M., Yela, M., Yilmaz, S., Zieger, P., and Zhou, Y.: The Cabauw Intercomparison campaign for Nitrogen Dioxide measuring Instruments (CINDI): design, execution, and early results, Atmos. Meas. Tech., 5, 457–485, doi:10.5194/amt-5-457-2012, 2012.

Platt, U. and Stutz, J.: Differential Optical Absorption Spectroscopy: Principles and Applications, Physics of Earth and Space Environments, Springer, Berlin, 2008.

Pommereau, J. and Goutail, F.: O_3 and NO_2 ground-based measurements by visible spectrometry during Arctic winter and spring 1988, Geophys. Res. Lett., 15, doi:10.1029/GL015i008p00891, 1988.

Pommier, M., McLinden, C., Neuman, J., and Nowak, J.: Biomass burning in Siberia as a source of BrO to the Arctic free troposphere, Atmos. Env., 62, 416 – 423, doi:10.1016/j.atmosenv.2012.08.070, 2012.

Popp, C., Brunner, D., Damm, A., Van Roozendael, M., Fayt, C., and Buchmann, B.: High-resolution NO_2 remote sensing from the Airborne Prism EXperiment (APEX) imaging spectrometer, Atmos. Meas. Techn., 5, doi:10.5194/amt-5-2211-2012, 2012.

Prados-Roman, C., Butz, A., Deutschmann, T., Dorf, M., Kritten, L., Minikin, A., Platt, U., Schlager, H., Sihler, H., Theys, N., Van Roozendael, M., Wagner, T., and Pfeilsticker, K.: Airborne DOAS limb measurements of tropospheric trace gas profiles: case studies on the profile retrieval of O_4 and BrO, Atmos. Meas. Tech., 4, 1241–1260, doi:10.5194/amt-4-1241-2011, 2011.

Prank, M., Sofiev, M., Denier van der Gon, H. A. C., Kaasik, M., Ruuskanen, T. M., and Kukkonen, J.: A refinement of the emission data for Kola Peninsula

based on inverse dispersion modelling, Atmos. Chem. Phys., 10, 10 849–10 865, doi:10.5194/acp-10-10849-2010, 2010.

Press, W. H., Flannery, B. P., Teukolsky, S. A., and Vetterling, W. T.: Numerical Recipes in C: The Art of Scientific Computing, Second Edition, Cambridge University Press, 2 edn., 1992.

Ramana, M., Ramanathan, V., Kim, D., Roberts, G., and Corrigan, C.: Albedo, atmospheric solar absorption and heating rate measurements with stacked UAVs, Q. J. Roy. Meteor. Soc., 133, 1913–1931, doi:10.1002/qj.172, 2007.

Raut, J.-C. and Chazette, P.: Radiative budget in the presence of multi-layered aerosol structures in the framework of AMMA SOP-0, Atmos. Chem. Phys., 8, 6839–6864, doi:10.5194/acp-8-6839-2008, 2008.

Richter, A., Burrows, J., Nusz, H., Granier, C., and Niemeier, U.: Increase in tropospheric nitrogen dioxide over China observed from space, Nature, 437, 129–132, doi:10.1038/nature04092, 2005.

Richter, A., Begoin, M., Hilboll, A., and Burrows, J. P.: An improved NO_2 retrieval for the GOME-2 satellite instrument, Atmos. Meas. Tech., 4, 1147–1159, doi: 10.5194/amt-4-1147-2011, 2011.

Ridley, B., Walega, J., Montzka, D., Grahek, F., Atlas, E., Flocke, F., Stroud, V., Deary, J., Gallant, A., Boudries, H., Bottenheim, J., Anlauf, K., Worthy, D., Sumner, A. L., Splawn, B., and Shepson, P.: Is the Arctic Surface Layer a Source and Sink of NOx in Winter/Spring?, Journal of Atmospheric Chemistry, 36, 1–22, doi:10.1023/A:1006301029874, 2000.

Rivera, C., Mellqvist, J., Samuelsson, J., Lefer, B., Alvarez, S., and Patel, M. R.: Quantification of NO_2 and SO_2 emissions from the Houston Ship Channel and Texas City industrial areas during the 2006 Texas Air Quality Study, J. Geophys. Res., 115, 10 PP., doi:10.1029/2009JD012675, 2010.

Rodgers, C.: Retrieval of atmospheric temperature and composition from remote measurements of thermal radiation, Rev. Geophys., 14, doi:197610.1029/RG014i004p00609, 1976.

Rodgers, C. D.: Inverse Methods for Atmospheric Sounding : Theory and Practice, World Scientific Publishing Company, 2000.

Roll, A.: PIC Based Serial Port Servo Controller, Electronics Australia, 2000.

Roscoe, H. K., Van Roozendael, M., Fayt, C., du Piesanie, A., Abuhassan, N., Adams, C., Akrami, M., Cede, A., Chong, J., Clémer, K., Friess, U., Gil Ojeda, M., Goutail, F., Graves, R., Griesfeller, A., Grossmann, K., Hemerijckx, G., Hendrick, F., Herman, J., Hermans, C., Irie, H., Johnston, P. V., Kanaya, Y., Kreher, K., Leigh, R., Merlaud, A., Mount, G. H., Navarro, M., Oetjen, H., Pazmino, A., Perez-Camacho, M., Peters, E., Pinardi, G., Puentedura, O., Richter, A., Schönhardt, A., Shaiganfar, R., Spinei, E., Strong, K., Takashima, H., Vlemmix, T., Vrekoussis, M., Wagner, T., Wittrock, F., Yela, M., Yilmaz, S., Boersma, F., Hains, J., Kroon, M., Piters, A., and Kim, Y. J.: Intercomparison of slant column measurements of NO_2 and O_4 by MAX-DOAS and zenith-sky UV and visible spectrometers, Atmos. Meas. Tech., 3, doi:10.5194/amt-3-1629-2010, 2010.

Sabbah, I. and Hasan, F. M.: Remote sensing of aerosols over the Solar Village, Saudi Arabia, Atmos. Res., 90, 170–179, doi:10.1016/j.atmosres.2008.02.004, 2008.

Sabins, F. F.: Remote Sensing: Principles and Interpretation, W.H. Freeman and Company, 1997.

Salawitch, R. J., Canty, T., Kurosu, T., Chance, K., Liang, Q., da Silva, A., Pawson, S., Nielsen, J. E., Rodriguez, J. M., Bhartia, P. K., Liu, X., Huey, L. G., Liao, J., Stickel, R. E., Tanner, D. J., Dibb, J. E., Simpson, W. R., Donohoue, D., Weinheimer, A., Flocke, F., Knapp, D., Montzka, D., Neuman, J. A., Nowak, J. B., Ryerson, T. B., Oltmans, S., Blake, D. R., Atlas, E. L., Kinnison, D. E., Tilmes, S., Pan, L. L., Hendrick, F., Van Roozendael, M., Kreher, K., Johnston, P. V., Gao, R. S., Johnson, B., Bui, T. P., Chen, G., Pierce, R. B., Crawford, J. H., and Jacob, D. J.: A new interpretation of total column BrO during Arctic spring, Geophys. Res. Lett., 37, 9 PP., doi:201010.1029/2010GL043798, 2010.

Schneider, M., Hase, F., and Blumenstock, T.: Water vapour profiles by ground-based ftir spectroscopy: study for an optimised retrieval and its validation, Atmos. Chem. Phys., 6, doi:10.5194/acp-6-811-200, 2006.

Seinfeld, J. H. and Pandis, S. N.: Atmos. Chem. Phys.: From Air Pollution to Climate Change, Wiley-Interscience, 1997.

Senten, C., De Mazière, M., Dils, B., Hermans, C., Kruglanski, M., Neefs, E., Scolas, F., Vandaele, A. C., Vanhaelewyn, G., Vigouroux, C., Carleer, M., Coheur, P. F., Fally, S., Barret, B., Baray, J. L., Delmas, R., Leveau, J., Metzger, J. M., Mahieu, E., Boone, C., Walker, K. A., Bernath, P. F., and Strong, K.: Technical Note: New ground-based FTIR measurements at Ile de La Réunion:

observations, error analysis, and comparisons with independent data, Atmos. Chem. Phys., 8, doi:10.5194/acp-8-3483-2008, 2008.

Shaiganfar, R., Beirle, S., Sharma, M., Chauhan, A., Singh, R. P., and Wagner, T.: Estimation of NO_x emissions from Delhi using Car MAX-DOAS observations and comparison with OMI satellite data, Atmos. Chem. Phys., 11, doi:10.5194/acp-11-10871-2011, 2011.

Shaw, G. E.: The Arctic Haze Phenomenon, B. Am. Meteorol. Soc., 76, 2403–2414, doi:10.1175/1520-0477(1995)076<2403:TAHP>2.0.CO;2, 1995.

Sinreich, R., Volkamer, R., Filsinger, F., Frieß, U., Kern, C., Platt, U., Sebastián, O., and Wagner, T.: MAX-DOAS detection of glyoxal during ICARTT 2004, Atmos. Chem. Phys., 7, doi:10.5194/acp-7-1293-2007, 2007.

Sluis, W. W., Allaart, M. A. F., Piters, A. J. M., and Gast, L. F. L.: The development of a nitrogen dioxide sonde, Atmos. Meas. Tech., 3, doi:10.5194/amt-3-1753-2010, 2010.

Solomon, S., Sanders, R. W., Carroll, M. A., and Schmeltekopf, A. L.: Visible and near-ultraviolet spectroscopy at McMurdo Station, Antarctica: 5. Observations of the diurnal variations of BrO and OClO, J. Geophys. Res-Atmos, 94, doi:10.1029/JD094iD09p11393, 1989.

Sportisse, B.: Pollution atmosphérique: Des processus à la modélisation, Springer, 2007.

Spurr, R.: LIDORT and VLIDORT: Linearized pseudo-spherical scalar and vector discrete ordinate radiative transfer models for use in remote sensing retrieval problems, in: Light Scattering Reviews 3, edited by Kokhanovsky, A., Springer Praxis Books, pp. 229–275, Springer Berlin Heidelberg, 2008.

Stamnes, K., Tsay, S., Wiscombe, W., and Jayaweera, K.: Numerically stable algorithm for discrete-ordinate-method radiative transfer in multiple scattering and emitting layered media, Appl. Optics, 27, 1988.

Stamnes, K., Tsay, S. C., Wiscombe, W., and Laszlo, I.: DISORT, a General-Purpose Fortran Program for Discrete-Ordinate-Method Radiative Transfer in Scattering and Emitting Layered Media: Documentation of Methodology, Tech. rep., Dept. of Physics and Engineering Physics Stevens Institute of Technology Hoboken, NJ 07030, 2000.

Stavrakou, T., Müller, J.-F., Boersma, K. F., De Smedt, I., and van der A, R. J.: Assessing the distribution and growth rates of NOx emission sources by inverting

a 10-year record of NO_2 satellite columns, Geophy. Res. Lett., 35, doi:10.1029/2008GL033521, 2008.

Stewart, J. E. and Gallaway, W. S.: Diffraction Anomalies in Grating Spectrophotometers, Appl. Opt., 1, doi:10.1364/AO.1.000421, 1962.

Stohl, A., Forster, C., Eckhardt, S., Spichtinger, N., Huntrieser, H., Heland, J., Schlager, H., Wilhelm, S., Arnold, F., and Cooper, O.: A backward modeling study of intercontinental pollution transport using aircraft measurements, J. Geophys. Res., 108, 18 PP., doi:10.1029/2002JD002862, 2003.

Stohl, A., Forster, C., Frank, A., Seibert, P., and Wotawa, G.: Technical note: The Lagrangian particle dispersion model FLEXPART version 6.2, Atmos. Chem. Phys., 5, 2461–2474, doi:doi:10.5194/acp-5-2461-2005, 2005.

Stohl, A., Forster, C., Huntrieser, H., Mannstein, H., McMillan, W. W., Petzold, A., Schlager, H., and Weinzierl, B.: Aircraft measurements over Europe of an air pollution plume from Southeast Asia - aerosol and chemical characterization, Atmos. Chem. Phys., 7, 913–937, doi:10.5194/acp-7-913-2007, 2007.

Stroud, C., Madronich, S., Atlas, E., Ridley, B., Flocke, F., Weinheimer, A., Talbot, B., Fried, A., Wert, B., Shetter, R., Lefer, B., Coffey, M., Heikes, B., and Blake, D.: Photochemistry in the arctic free troposphere: NOx budget and the role of odd nitrogen reservoir recycling, Atmos. Environ., 37, 3351–3364, doi:10.1016/S1352-2310(03)00353-4, 2003.

Stutz, J. and Platt, U.: Numerical analysis and estimation of the statistical error of differential optical absorption spectroscopy measurements with least-squares methods, Appl. Optics, 35, 6041–6053, 1996.

Svanberg, S.: Atomic and Molecular Spectroscopy: Basic Aspects and Practical Applications, Springer, 4th edn., 2004.

Taleb, N.: Le cygne noir : La puissance de l'imprévisible, Belles Lettres, 2008.

Tarantola, A.: Inverse Problem Theory and Methods for Model Parameter Estimation, SIAM: Society for Industrial and Applied Mathematics, 1 edn., 2004.

Tarantola, A.: Popper, Bayes and the inverse problem, Nat Phys, 2, 492–494, doi:10.1038/nphys375, 2006.

Theys, N.: Atmospheric Bromine Monoxide : multi-platform observations and model calculations, Ph.D. thesis, Université Libre De Bruxelles, 2010.

Theys, N., Van Roozendael, M., Hendrick, F., Yang, X., De Smedt, I., Richter, A., Begoin, M., Errera, Q., Johnston, P., Kreher, K., and De Mazière, M.: Global observations of tropospheric BrO columns using GOME-2 satellite data, Atmos. Chem. Phys., 11, 1791–1811, doi:10.5194/acp-11-1791-2011, 2011.

Tikhonov, A.: On the solution of incorrectly stated problems and a method of regularization, Dokl. Acad. Nauk SSSR, pp. 501–504, 1963.

Tomasi, C., Vitale, V., Lupi, A., Carmine, C. D., Campanelli, M., Herber, A., Treffeisen, R., Stone, R. S., Andrews, E., Sharma, S., Radionov, V., von Hoyningen-Huene, W., Stebel, K., Hansen, G. H., Myhre, C. L., Wehrli, C., Aaltonen, V., Lihavainen, H., Virkkula, A., Hillamo, R., Ström, J., Toledano, C., Cachorro, V. E., Ortiz, P., de Frutos, A. M., Blindheim, S., Frioud, M., Gausa, M., Zielinski, T., Petelski, T., and Yamanouchi, T.: Aerosols in polar regions: A historical overview based on optical depth and in situ observations, J. Geophys. Res., 112, doi:10.1029/2007JD008432, 2007.

van der A, R. J., Eskes, H. J., Boersma, K. F., van Noije, T. P. C., Van Roozendael, M., De Smedt, I., Peters, D. H. M. U., and Meijer, E. W.: Trends, seasonal variability and dominant NO_x source derived from a ten year record of NO_2 measured from space, J. Geophys. Res., 113, doi:200810.1029/2007JD009021, 2008.

Van Roozendael, M., Soebijanta, V., Fayt, C., and Lambert, J.-C.: Investigation of DOAS issues affecting the accuracy of the GDP version 3.0 total ozone product, Tech. rep., ESA/ESRIN, 2002.

Vandaele, A. C., Hermans, C., Simon, P. C., Carleer, M., Colin, R., Fally, S., Mérienne, M. F., Jenouvrier, A., and Coquart, B.: Measurements of the NO_2 absorption cross-section from 42 000 $cm^{âĹŠ1}$ to 10 000 $cm^{âĹŠ1}$ (238-1000 nm) at 220 K and 294 K, J. Quant. Spectrosc. Ra., 59, doi:10.1016/S0022-4073(97)00168-4, 1998.

Vanhellemont, F., Fussen, D., Mateshvili, N., Tétard, C., Bingen, C., Dekemper, E., Loodts, N., Kyrölä, E., Sofieva, V., Tamminen, J., Hauchecorne, A., Bertaux, J., Dalaudier, F., Blanot, L., d'Andon, O. F., Barrot, G., Guirlet, M., Fehr, T., and Saavedra, L.: Optical extinction by upper tropospheric/stratospheric aerosols and clouds: GOMOS observations for the period 2002-2008, Atmos. Chem. Phys., 10, 7997–8009, doi:10.5194/acp-10-7997-2010, 2010.

Vautard, R., Beekmann, M., Roux, J., and Gombert, D.: Validation of a hybrid forecasting system for the ozone concentrations over the Paris area, Atmos. Environ., 35, doi:10.1016/S1352-2310(00)00466-0, 2001.

Vigouroux, C., Hendrick, F., Stavrakou, T., Dils, B., De Smedt, I., Hermans, C., Merlaud, A., Scolas, F., Senten, C., Vanhaelewyn, G., Fally, S., Carleer, M., Metzger, J.-M., Müller, J.-F., Van Roozendael, M., and De Mazière, M.: Ground-based FTIR and MAX-DOAS observations of formaldehyde at Réunion Island and comparisons with satellite and model data, Atmos. Chem. Phys., 9, 9523–9544, doi:10.5194/acp-9-9523-2009, 2009.

Villani, P., Picard, D., Michaud, V., Laj, P., and Wiedensohler, A.: Design and Validation of a Volatility Hygroscopic Tandem Differential Mobility Analyzer (VH-TDMA) to Characterize the Relationships Between the Thermal and Hygroscopic Properties of Atmospheric Aerosol Particles, Aerosol. Sci. Tech., 42, doi:10.1080/02786820802255668, 2008.

Vinuesa, J. and Galmarini, S.: Turbulent Dispersion of Non-uniformly Emitted Passive Tracers in the Convective Boundary Layer, Boundary-Layer Meteorology, 133, 1–16, doi:10.1007/s10546-009-9416-0, 2009.

Vlemmix, T.: Tropospheric nitrogen dioxide inversions based on spectral measurements of scattered sunlight, Ph.D. thesis, Technische Universiteit Eindhoven, 2011.

Vlemmix, T., Piters, A. J. M., Stammes, P., Wang, P., and Levelt, P. F.: Retrieval of tropospheric NO_2 using the MAX-DOAS method combined with relative intensity measurements for aerosol correction, Atmos. Meas. Tech., 3, doi:10.5194/amt-3-1287-2010, 2010.

Vlemmix, T., Piters, A. J. M., Berkhout, A. J. C., Gast, L. F. L., Wang, P., and Levelt, P. F.: Ability of the MAX-DOAS method to derive profile information for NO_2: can the boundary layer and free troposphere be separated?, Atmos. Meas. Tech., 4, doi:10.5194/amt-4-2659-2011, 2011.

Volten, H., Brinksma, E., Berkhout, A., Hains, J., Bergwerff, J., Van der Hoff, G., Apituley, A., Dirksen, R., Calabretta-Jongen, S., and Swart, D.: NO_2 lidar profile measurements for satellite interpretation and validation, J. Geophys. Res., 114, D24 301, doi:10.1029/2009JD012441, 2009.

Volz, A. and Kley, D.: Evaluation of the Montsouris series of ozone measurements made in the nineteenth century, Nature, 332, 240–242, doi:10.1038/332240a0, 1988.

von Neumann, J.: Can we survive technology?, Fortune, 91, 1955.

Wagner, T., Dix, B., Friedeburg, C. v., Friess, U., Sanghavi, S., Sinreich, R., and Platt, U.: MAX-DOAS O_4 measurements: A new technique to derive information on atmospheric aerosols: 1. Principles and information content, J. Geophys. Res., 109, D22 205, doi:10.1029/2004JD004904, 2004.

Wagner, T., Burrows, J. P., Deutschmann, T., Dix, B., von Friedeburg, C., Frieß, U., Hendrick, F., Heue, K., Irie, H., Iwabuchi, H., Kanaya, Y., Keller, J., McLinden, C. A., Oetjen, H., Palazzi, E., Petritoli, A., Platt, U., Postylyakov, O., Pukite, J., Richter, A., Van Roozendael, M., Rozanov, A., Rozanov, V., Sinreich, R., Sanghavi, S., and Wittrock, F.: Comparison of box-air-mass-factors and radiances for Multiple-Axis Differential Optical Absorption Spectroscopy (MAX-DOAS) geometries calculated from different UV/visible radiative transfer models, Atmos. Chem. Phys., 7, 1809–1833, 2007.

Wagner, T., Ibrahim, O., Shaiganfar, R., and Platt, U.: Mobile MAX-DOAS observations of tropospheric trace gases, Atmos. Meas. Tech., 3, doi:10.5194/amtd-2-2851-2009, 2010.

Wagner, T., Andreae, M. O., Beirle, S., Dörner, S., Mies, K., and Shaiganfar, R.: MAX-DOAS observations of the total atmospheric water vapour column and comparison with independent observations, Atmos. Meas. Tech., 6, doi:10.5194/amt-6-131-2013, 2013.

Weibring, P., Edner, H., and Svanberg, S.: Versatile Mobile Lidar System for Environmental Monitoring, Appl. Opt., 42, doi:10.1364/AO.42.003583, 2003.

WHO: Health aspects of air pollution with particulate matter, ozone, and nitrogen dioxide, Report on a WHO working group, World Health Organization, 2003.

Wittrock, F., Oetjen, H., Richter, A., Fietkau, S., Medeke, T., Rozanov, A., and Burrows, J.: MAX-DOAS measurements of atmospheric trace gases in Ny-Alesund - Radiative transfer studies and their application, Atmos. Chem. Phys., 4, 955–966, doi:10.5194/acp-4-955-2004, 2004.

WMO: Scientific Assessment of Ozone Depletion: 2010, Global ozone research and monitoring project report no.52, World Meteorological Organization, 2011.

Zahn, A., Brenninkmeijer, C. A. M., Maiss, M., Scharffe, D. H., Crutzen, P. J., Hermann, M., Heintzenberg, J., Wiedensohler, A., Güsten, H., Heinrich, G., Fischer, H., Cuijpers, J. W. M., and van Velthoven, P. F. J.: Identification of extratropical two-way troposphere-stratosphere mixing based on CARIBIC measurements of O_3, CO, and ultrafine particles, J. Geophys. Res., 105, 1527–1535, doi:10.1029/1999JD900759, 2000.

Zhou, Y., Brunner, D., Boersma, K. F., Dirksen, R., and Wang, P.: An improved tropospheric NO_2 retrieval for OMI observations in the vicinity of mountainous terrain, Atmos. Meas. Tech., 2, 401–416, doi:10.5194/amt-2-401-2009, 2009.

Zieger, P., Weingartner, E., Henzing, J., Moerman, M., de Leeuw, G., Mikkilä, J., Ehn, M., Petäjä, T., Clémer, K., van Roozendael, M., Yilmaz, S., Frieß, U., Irie, H., Wagner, T., Shaiganfar, R., Beirle, S., Apituley, A., Wilson, K., and Baltensperger, U.: Comparison of ambient aerosol extinction coefficients obtained from in-situ, MAX-DOAS and LIDAR measurements at Cabauw, Atmos. Meas. Tech. Discuss., 10, 29 683–29 734, doi:10.5194/acpd-10-29683-2010, 2010.

Zong, Y., Brown, S. W., Johnson, B. C., Lykke, K. R., and Ohno, Y.: Simple spectral stray light correction method for array spectroradiometers, Appl. Opt., 45, 1111–1119, 2006.